NONLINEAR ULTRASONIC EVALUATION FOR CORROSION ASSESSMENT OF STEEL PLATES EMBEDDED IN CONCRETE
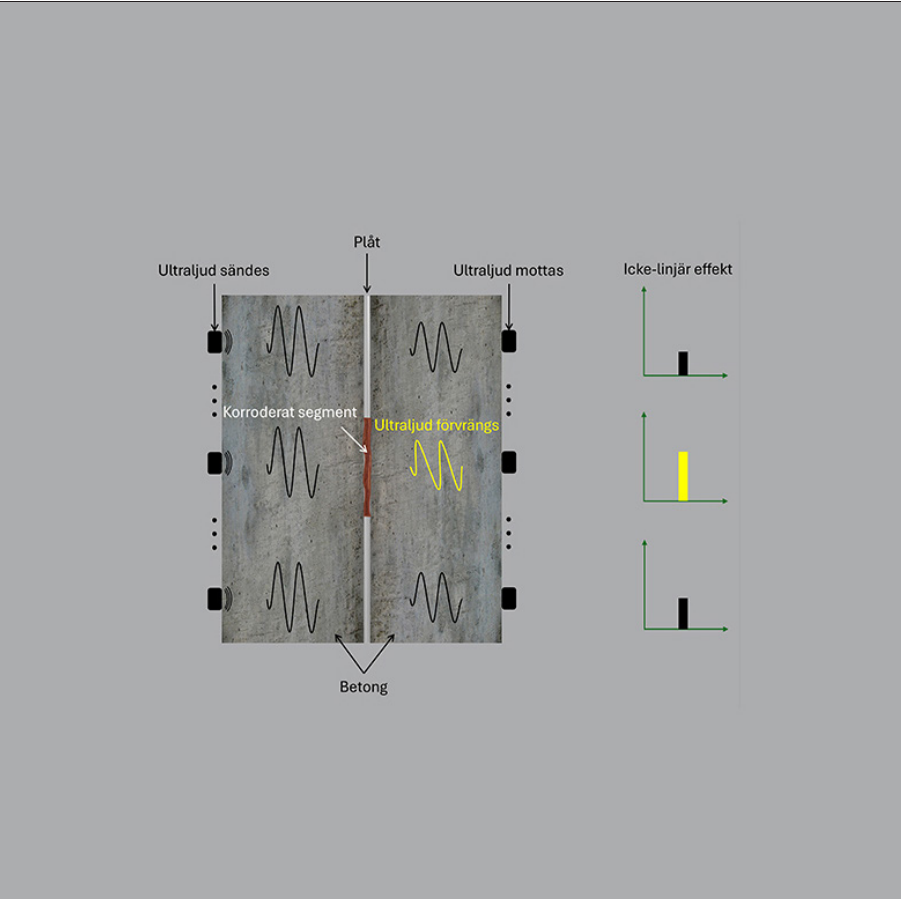
HYDROPOWER CONCRETE PROGRAMME

Energiforsk

LUND UNIVERSITY

Nonlinear Ultrasonic Evaluation for Corrosion Assessment of Steel Plates Embedded in Concrete

Nilsson, Markus

2024

[Link to publication](#)

Total number of authors:
1

Nonlinear Ultrasonic Evaluation for Corrosion Assessment of Steel Plates
Embedded in Concrete

Nonlinear Ultrasonic Evaluation for Corrosion Assessment of Steel Plates Embedded in Concrete

Markus Nilsson

LUND UNIVERSITY

DOCTORAL THESIS

Doctoral thesis for the degree of Doctor of Philosophy (PhD) at the Faculty of Engineering at Lund University to be publicly defended at V-huset, Klas Anshelms väg 14, Lund, Sweden, in hall V:D, on December 6, 2024, at 09:00.

Faculty opponent
Dr. Odile Abraham, Senior Researcher, Université Gustave Eiffel, Champs-sur-Marne, France

Organization: LUND UNIVERSITY

Document name: Doctoral thesis

Author(s): Markus Nilsson

Date of issue 2024-11-01

Sponsoring organizations: Swedish radiation safety authority, and the Swedish Energy Research Centre

Title and subtitle: Nonlinear Ultrasonic Evaluation for Corrosion Assessment of Steel Plates Embedded in Concrete

Abstract: The growing demand for sustainable electricity production, coupled with global uncertainties, highlights the need for nations to achieve self-sufficiency in producing electricity. Nuclear power, which provides around 30% of Sweden's electricity, plays a critical role in delivering fossil-free electricity. As many nuclear plants are near the end of their designated lifespans, extending their operational periods is crucial to meeting current and future demands.

Ensuring safe nuclear operations is vital. To address this, the Swedish Energy Research Centre, along with the Swedish Radiation Safety Authority and other industry partners, runs a research program focusing on concrete-related challenges in nuclear power. A significant issue within this program is detecting corrosion in containment liners – welded plate constructions that serve as gas-tight barriers to prevent the release of radioactive particles. These liners, sometimes embedded in thick concrete walls of reactor containment buildings, are difficult to inspect. Corrosion can compromise their structural integrity long before visible damage appears, making early detection essential for planning preventive measures.

This thesis evaluates nonlinear ultrasonic methods for detecting and assessing corrosion in embedded containment liners. Ultrasonic testing uses sound waves above the human audible range to image internal structures. However, in concrete, high-frequency sound waves are quickly absorbed, necessitating the use of low-frequency waves, which reduces the ability to resolve small defects. Nonlinear ultrasonic evaluation offers a solution. Defects like cracks cause elastic nonlinearity, leading to waveform distortion. This distortion creates new frequency components in the sound wave, allowing for the detection of defects regardless of the wave's frequency. The strength of these new components relative to the original frequency provides a measure of damage in the material.

The research, conducted on small-scale laboratory specimens, primarily focused on pre-corroded steel plates. The results demonstrate that nonlinear evaluation can locate and assess corrosion in embedded plates, with more severe corrosion yielding stronger nonlinear indications. Additionally, the method shows potential for detecting embedded foreign objects, such as wood, and separations between the plate and concrete. The findings suggest that combining conventional and nonlinear ultrasonic imaging techniques can provide a better understanding of a structure's damage state. However, further experiments on more realistic specimens are necessary to fully evaluate the methods' detection capabilities. These experiments should consider the challenges posed by intrinsic concrete micro-cracking, coarse aggregates, reinforcement, and large dimensions typical in nuclear power plants.

Key words: Nuclear, NDT, Ultrasound, nonlinearity

Classification system and/or index terms (if any)   Supplementary bibliographical information

Language: English

ISBN LU: 978-91-8104-205-4 (print), 978-91-8104-206-1 (electronic version)

ISBN Energiforsk: 978-91-89919-22-8   **Energiforsk Report**: 2024:1022

Recipient's notes   **Number of pages**:

I, the undersigned, being the copyright owner of the abstract of the above-mentioned thesis, hereby grant to all reference sources permission to publish and disseminate the abstract of the above-mentioned thesis.

Signature   Date 2024-11-01

Nonlinear Ultrasonic Evaluation for Corrosion Assessment of Steel Plates Embedded in Concrete

Markus Nilsson

LUND
UNIVERSITY

To my wonderful daughter

"One must pay dearly for immortality; one has to die several times while one is still alive."
(Friedrich Nietzsche, *Ecce Homo: How One Becomes What One Is.* 1908)

Preface

I was introduced to the concept of nonlinear ultrasonics in nondestructive testing (NDT) during my master's program, where I was immediately fascinated by the operating principles, complexity, and potential applications of related methods. I was fortunate to work with the subject during my degree project and later as an NDT engineer, which further deepened my interest in the field. Then came the COVID-19 pandemic, which led to the termination of my position as an NDT engineer. I was nearly certain that I would never have the opportunity to work with nonlinear ultrasonics again. Little did I know that my journey had only just begun.

When I saw a posting for a doctoral student position focused on using nonlinear ultrasonics to evaluate concrete-embedded corrosion, I immediately jumped at the chance. Knowing this would be an incredibly challenging topic, I was concerned, to say the least. The years that followed my admission were often frustrating, extremely challenging, and incredibly educational. However, perseverance and hard work pay off – this thesis is definite proof of that.

Throughout my journey as a doctoral student, I have been fortunate to encounter many helpful and inspiring people – far more than I can mention. However, certain individuals deserve special thanks. First, to my unofficial super-supervisor, Docent Peter Ulriksen, I extend my deepest gratitude for our many engaging discussions on all topics imaginable and for truly encouraging me to pursue my ideas. I would also like to thank my official supervisor, Docent Nils Rydén, whose invaluable support has elevated my studies immensely. To all my colleagues in the Division of Engineering Geology, thank you for creating a welcoming work environment filled with interesting discussions.

Finally, to my family and friends, thank you for your continuous support and encouragement. Special thanks to my dear brother, who has been very supportive and provided a language review on my first manuscript. I am also sincerely grateful to my fishing partner and uncle; our time spent with tight lines and near-death experiences has made incredibly challenging times manageable – here's to many more!

Markus Nilsson

Lund, October 2024.

Table of Contents

Popular science summary

The growing demand for sustainable electricity production, coupled with global uncertainties, highlights the need for nations to achieve self-sufficiency in producing electricity. Nuclear power, which provides around 30% of Sweden's electricity, plays a critical role in delivering fossil-free electricity. As many nuclear plants are near the end of their designated lifespans, extending their operational periods is crucial to meeting current and future demands.

Ensuring safe nuclear operations is vital. To address this, the Swedish Energy Research Centre, along with the Swedish Radiation Safety Authority and other industry partners, runs a research program focusing on concrete-related challenges in nuclear power. A significant issue within this program is detecting corrosion in containment liners – welded plate constructions that serve as gas-tight barriers to prevent the release of radioactive particles. These liners, sometimes embedded in thick concrete walls of reactor containment buildings, are difficult to inspect. Corrosion can compromise their structural integrity long before visible damage appears, making early detection essential for planning preventive measures.

This thesis evaluates nonlinear ultrasonic methods for detecting and assessing corrosion in embedded containment liners. Ultrasonic testing uses sound waves above the human audible range to image internal structures. However, in concrete, high-frequency sound waves are quickly absorbed, necessitating the use of low-frequency waves, which reduces the ability to resolve small defects. Nonlinear ultrasonic evaluation offers a solution. Defects like cracks cause elastic nonlinearity, leading to waveform distortion. This distortion creates new frequency components in the sound wave, allowing for the detection of defects regardless of the wave's frequency. The strength of these new components relative to the original frequency provides a measure of damage in the material.

The research, conducted on small-scale laboratory specimens, primarily focused on pre-corroded steel plates. The results demonstrate that nonlinear evaluation can locate and assess corrosion in embedded plates, with more severe corrosion yielding stronger nonlinear indications. Additionally, the method shows potential for detecting embedded foreign objects, such as wood, and separations between the plate and concrete. The findings suggest that combining conventional and nonlinear ultrasonic imaging techniques can provide a better understanding of a structure's damage state. However, further experiments on more realistic specimens are necessary to fully evaluate the methods' detection capabilities. These experiments should consider the challenges posed by intrinsic concrete micro-cracking, coarse aggregates, reinforcement, and large dimensions typical in nuclear power plants.

Populärvetenskaplig sammanfattning

Den växande efterfrågan på hållbar och miljövänlig elproduktion, tillsammans med globala osäkerheter, understryker behovet för nationer att uppnå självförsörjande produktion av el. Kärnkraft, som står för cirka 30% av Sveriges elproduktion, spelar en avgörande roll i att leverera fossilfri el. Eftersom många kärnkraftverk närmar sig slutet av sin planerade livslängd är det avgörande att förlänga deras driftsperioder för att möta nuvarande och framtida behov.

Att säkerställa säker drift av kärnkraftverk är av yttersta vikt. För att hantera detta driver Energiforsk AB, tillsammans med Strålsäkerhetsmyndigheten och andra branschpartners, ett forskningsprogram som fokuserar på betongtekniska utmaningar inom kärnkraft. En viktig fråga inom detta program är att upptäcka korrosion i tätplåtar – svetsade plåtkonstruktioner som fungerar som gastäta barriärer för att förhindra utsläpp av radioaktiva partiklar. Dessa tätplåtar, som ofta är ingjutna i tjocka betongväggar i reaktorinneslutningarna, är svåra att inspektera. Korrosion kan äventyra deras täthet långt innan synliga skador uppstår, vilket gör tidig upptäckt avgörande för att planera förebyggande åtgärder.

Denna avhandling utvärderar icke-linjära ultraljudsmetoder för att upptäcka och utvärdera korrosion i ingjutna tätplåtar. Ultraljudsprovning använder ljudvågor över det mänskliga hörbara området för att avbilda inre strukturer. I betong dämpas dock högfrekventa ljudvågor effektivt, vilket nödvändiggör användning av förhållandevis lågfrekventa vågor, vilket minskar förmågan att upptäcka små defekter. Icke-linjär utvärdering erbjuder en lösning. Defekter som sprickor orsakar elastisk icke-linjäritet, vilket leder till vågformsförvrängning. Denna distorsion skapar nya frekvenskomponenter i ljudvågen, vilket möjliggör detektering av defekter oavsett vågens frekvens. Styrkan hos dessa nya komponenter i förhållande till den ursprungliga frekvensen ger ett mått på skadeläget i materialet.

Forskningen, som genomfördes på småskaliga laboratorieprover, fokuserade främst på förkorroderade stålplåtar. Resultaten visar att icke-linjär utvärdering kan lokalisera och utvärdera korrosion i ingjutna plåtar, där allvarligare korrosion ger starkare icke-linjära indikationer. Dessutom visar metoden potential för att upptäcka ingjutna främmande föremål, såsom trä, och separationer mellan plåten och betongen.

Resultaten tyder på att en kombination av konventionell och icke-linjär utvärdering vid avbildning kan ge en god förståelse för en strukturs skadeläge. Ytterligare experiment på mer realistiska prover är dock nödvändiga för att fullt ut utvärdera metodernas detektionsförmåga. Dessa experiment bör beakta de utmaningar som ställs av naturliga mikrosprickor i betong, grova ballastmaterial, rikhaltig armering och stora dimensioner typiska för faktiska kärnkraftverk.

List of Papers

Paper I

Nilsson, M., Ulriksen, P. and Rydén, N., (2023). Nonlinear ultrasonic characteristics of a corroded steel plate. *Nondestructive Testing and Evaluation*. Taylor & Francis, *38(3),* pp. 456–479, doi: 10.1080/10589759.2022.2123481

Paper II

Nilsson, M., Huttunen-Saarivirta, E., Bohner, E. and Ferreira, M., (2023). Non-destructive evaluation of corrosion in steel liner plates embedded in concrete using nonlinear ultrasonics. *Construction and Building Materials*. Elsevier Ltd, *408(September),* p. 133691, doi: 10.1016/j.conbuildmat.2023.133691

Paper III

Nilsson, M., Ulriksen, P. and Rydén, N. (2024). Nonlinear Wave Modulation for the Evaluation of Corroded Steel Plates Embedded in Concrete. *Journal of Advanced Concrete Technology*. Japan Concrete Institute, Vol. 22, pp. 545 – 560, doi:10.3151/jact.22.545

Paper IV

Nilsson, M., Ulriksen, P. and Rydén, N. (2024). Ultrasonic imaging of concrete-embedded corroded steel liners using linear and nonlinear evaluation. *Nondestructive Testing and Evaluation*. Taylor & Francis, 1-29, doi: 10.1080/10589759.2024.2402889

Author's contribution to the papers

Paper I

I conceptualized the paper. I designed and performed the necessary experiments, analysed, and visualised the data that are presented in the paper. As the main author I wrote the original draft and lead the submission and revision process.

Paper II

I conceptualized the paper. I designed and performed the necessary experiments concerning non-destructive evaluation (NDE), analysed, and visualised the data that are related to the NDE. I did not design the specimens or the ageing process, neither did I perform any of the corrosion characterization post concrete removal. As the main author I wrote most of the original draft and lead the submission and revision process.

Paper III

I conceptualized the paper. I designed and performed the necessary experiments, analysed, and visualised the data that are presented in the paper. As the main author I wrote the original draft and lead the submission and revision process.

Paper IV

I conceptualized the paper. I designed and performed the necessary experiments, analysed, and visualised the data that are presented in the paper. As the main author I wrote the original draft and lead the submission and revision process.

Abbreviations

ADC	Analogue to Digital Converter
AM	Amplitude-modulation/modulated
AWG	Arbitrary Waveform Generator
CAN	Contact Acoustic Nonlinearity
CLP	Containment Liner Plate
DAQ	Data Acquisition
DPC	Dry-Point-Contact
EMD	Empirical Mode Decomposition
FFT	Fast Fourier Transform
HHT	Hilbert-Huang Transform
HT	Hilbert Transform
IMF	Intrinsic Mode Function
IQHS	In-phase/Quadrature Homodyne Separation
LDR	Local Defect Resonance
LG	Luxembourg-Gorky
MI	Modulation Index
NDE	Non-Destructive Evaluation
NDT	Non-Destructive Testing
NIRAS	Nonlinear Impact Resonance Acoustic Spectroscopy
NME	Nonlinear Mesoscopic Elasticity
NPP	Nuclear Power Plant
NRUS	Nonlinear Resonant Ultrasound Spectroscopy
NWMS	Nonlinear Wave Modulation Spectroscopy
OCP	Open-Circuit Potential
RC	Reinforced Concrete
SHG	Second Harmonic Generation
SNR	Signal-to-Noise Ratio
SPC	Sideband Peak Count

SPI   Sideband Peak Index

SPACE   Subharmonic Phased Array for Crack Evaluation

TDI   Total Damage Index

VAM   Vibro-Acoustic Modulation

1. Introduction

1.1.　Background

Given the societal shift towards sustainability and the increasing urgency for nations to possess self-sufficient and eco-friendly electricity production, the role of nuclear power becomes even more critical. Nuclear power contributes to about 30% of Sweden's electricity output, providing abundant fossil-free energy that is essential for meeting current and future energy demands. As many Nuclear Power Plants (NPPs) approach their designated lifespan, extending their operational duration becomes imperative. This necessitates maintaining and upgrading the concrete structures that house these reactors to ensure their continued safety and efficiency. To ensure the safe operation of nuclear energy, the Swedish Energy Research Centre (Energiforsk AB), in collaboration with entities such as the Swedish Radiation Safety Authority and various partners in the nuclear industry, conduct a research program addressing concrete-related challenges in nuclear power.

Concrete is the most common man-made building material by a large margin. A study from 2020 estimated that the mass of concrete represents about 60% of all anthropogenic mass, and that the total mass of dry concrete may surpass the total biomass on earth by 2035 (Elhacham et al., 2020). Infrastructure that is crucial for our society today is composed of concrete to a large extent. A few examples of such infrastructure would be high-rise buildings, bridges, hydropower dams, and NPPs These large and important structures must withstand heavy loads and in the case of power-related infrastructure they must also be able to withstand loads resulting from catastrophic accidents and missile attacks to ensure safe operation. To meet these needs and in addition to large dimensions, the concrete itself must be of a specific strength class according to the application, and the members must be heavily reinforced by embedding steel bars. The containment buildings that house the nuclear reactors in NPPs employ several protective barriers to shield the exterior from radioactive particle release. One of the barriers is the leak-tight Containment Liner Plate (CLP) which in certain containment structures is embedded between two thick layers of heavily reinforced concrete. It is therefore safe to assume that most concrete structures have various embedded steel components that are crucial to the structural strength, and safety of the surrounding environment.

Concrete is an alkaline material meaning it has a high pH, typically 12 to 14 (Sumra et al., 2020). When steel is embedded in concrete, a passive iron oxide film is formed

on the surface of the steel component due to complex physiochemical phenomena (Saha et al., 2023). This property implies that concrete is an excellent material for steel embedment as it protects the steel from corroding severely. However, the concrete curing process may produce pores near the steel component which facilitates the ingress of corrosive agents such as chloride ions and carbon dioxide. The process of carbonation, which is the reaction between carbon dioxide and calcium hydroxide in the cement paste, lowers the pH to ~8 by the formation of calcium carbonate (Broomfield, 2022). This locally reduced pH compromises the passivity, potentially leading to severe corrosion of the steel member over time. Additional risks include embedded foreign materials such as wooden struts, and large cavities around the steel components (Dunn et al., 2011; Sandberg et al., 2019). For thick concrete walls, the drying of the concrete may not occur until several decades after construction (Oxfall, 2016), which means that cavities may be partially filled with water which further increases the corrosion risk. The matter of steel corrosion becomes even more important to consider as the industry moves towards sustainable concrete with binders that reduce the resistance against carbonation and have lower pH compared to conventional concrete. Because of these factors, steel corrosion can be viewed as being the Achilles' heel for sustainable concrete (Angst, 2023).

The formation of corrosion products on a steel surface causes a volumetric expansion and a multi-layered composition of various elements (Köliö et al., 2015). The swelling causes cracks and delaminations to form within the corrosion products and between the layers. When the steel is embedded in concrete, the swelling may cause significant concrete cracking due to the resulting stress (Neff et al., 2011). When considering steel plate corrosion, it is interesting to note that plates are commonly manufactured by rolling, a processing method that presses raw material through a series of rolls to reduce the thickness of the material. The rolling process is illustrated in Figure 1 where it is highlighted that rolling affects the grains and causes grain boundaries in the rolling direction to be elongated (Ahmad et al., 2014; Krishna et al., 2018). For materials that are cold rolled i.e., rolled below the recrystallization temperature, the grain structure is permanently elongated. Otherwise, the grain structure returns to its original state but any defects that have been elongated will remain so. It is hypothesized that when steel plate corrosion occurs, the elongated grain boundaries and defects, that are surface-plane parallel, separate which induces delaminations and cracks in the corroded material.
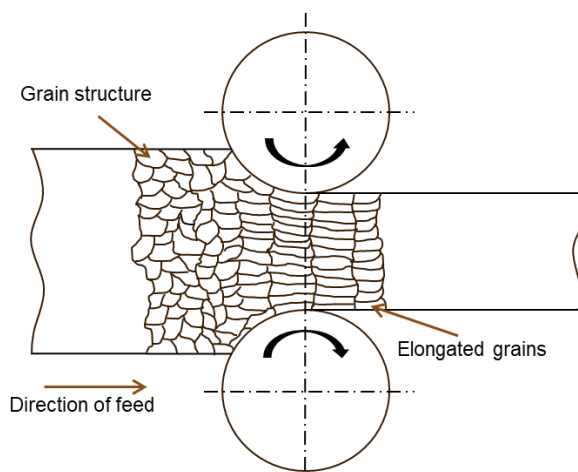
Figure 1. Illustration of the rolling process and the grain elongation it induces in the case of cold rolling.

Such characteristics are found in corroded steel plates regardless of the nature of the corrosion, i.e., if it has occurred in a high- or low-oxygen environment and with or without pre-stress. This delamination and crack characteristic can be observed in Figure 2 where X-ray tomographies of two corrosion products are shown. The bulk of common red rust (shell corrosion) in (a) is shown to exhibit surface-plane parallel defects and so does the dark corrosion product shown in (b) which is from an authentic CLP from an NPP that has corroded while being embedded in concrete, thus subjected to a low oxygen and a pre-stressed environment.
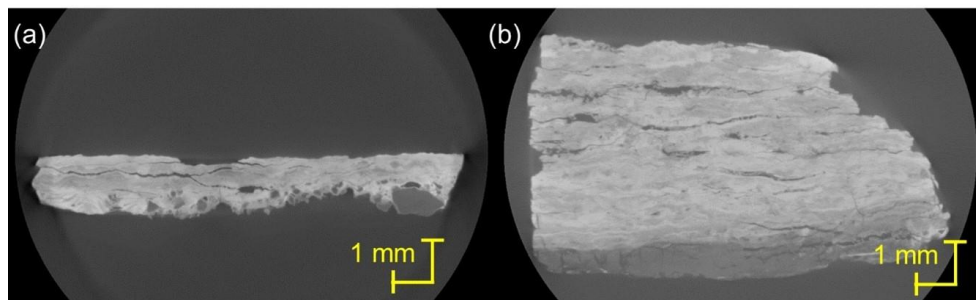
Figure 2. X-ray tomography of (a) red (oxide and moisture rich) corrosion product found on a scrap yard steel plate. (b) Corrosion product from a concrete-embedded containment liner plate (dark, indicating low oxygen and moisture environment). Figure from (Nilsson et al., 2024a).

The corrosion products viewed in Figure 2 are severe and imply that well before through-wall corrosion occurs, the strength of the steel plate may be significantly reduced which poses a threat to the structural integrity of the CLP in NPPs. This is also indicated by simulations on the matter (Li & Gong, 2023). Similarly, well before concrete cover cracking occurs due to corroding near-surface reinforcement bars, the corrosion-related degradation is in a propagation phase (Otieno et al., 2019)

and adequate remedial measures may require extensive and lengthy repairs. It is therefore important to detect the corrosion at an initiation phase to plan and implement maintenance when possible.

To detect embedded corrosion, Non-Destructive Testing and Evaluation (NDT & E) must be performed. This involves inspection techniques that do not affect the serviceability of the structure post-inspection. There exist numerous methods and techniques for NDT & E, but the most common can be grouped into electromagnetic methods, e.g., radar and eddy current, electrochemical, and elastic (or stress) wave methods, e.g., impact echo and ultrasonics. Ultrasound has the capability of resolving small defects given that the probing wavelength is on the same order of magnitude as the defect dimensions. This generally poses an issue in concrete inspection due to the heterogeneous nature of concrete. The various constituents vary in size and create complex scattering and attenuation effects that increase with decreasing wavelength (increasing frequency) which results in weak signals and large amounts of structural noise. This limits the use of high frequencies and thus the capability of resolving small defects that may be linked to the initiation of concrete-embedded steel corrosion. However, methods based on nonlinear evaluation of ultrasound are not as wavelength-dependent compared to the conventional methods and may serve as a promising tool for concrete-embedded corrosion detection.

Nonlinear ultrasonics is based on analysing waveform distortion caused by the presence of defects. These techniques are generally very sensitive to contact-type defects, i.e., small cracks, due to the mechanical behaviour of complex contacts. However, interatomic anharmonicity and weak nonlinear elastic behaviour also cause waveform distortion, which elevates the complexity of analysis using these methods. Waveform distortion manifests by the generation of new spectral components that are dependent on the excitations being used during the measurement. These techniques are generally much less restricted to the probing wavelength compared to conventional techniques which makes them particularly interesting to evaluate for concrete NDT & E, especially when it comes to the detection of small incipient defects in general. One such case is the detection and evaluation of concrete-embedded steel corrosion. Due to the heterogeneity of concrete, the application of nonlinear techniques may be challenging due to a high level of intrinsic distortion of the waves propagating in the material. Additionally, since lower frequencies are typically employed, the ability to very accurately localize defects is affected. In other words, nonlinear ultrasonics excel at *detecting* defects, but when using lower frequencies, *localization* may be challenging.

1.2.   Motivation

According to the NACE report on the International Measures of Prevention, Application, and Economics of Corrosion Technologies (IMPACT) the corrosion-related costs globally for 2013 were US$2.5 trillion (Bowman et al., 2016), which is roughly 4.3 times greater than the Swedish Gross Domestic Product for the same year. This indicates an economic motivation for proceeding with the expansion of knowledge within the corrosion field at large to reduce these costs. In civil engineering, advancing corrosion detection and evaluation is highly incentivized by safety concerns, as structural failures can result in significant losses of human and animal life.

Civil engineering has lagged behind other industries when it comes to performing and researching NDT (Grosse et al., 2023). Due to concrete being a relatively low-cost material, it is sometimes less expensive to perform destructive testing than NDT. However, since sustainable and efficient material usage must be prioritized, and due to the rise of digitalization in the sector, there is a large need to advance the topic of civil engineering NDT. One of the many important topics is detecting corrosion of concrete-embedded steel members. Particularly detection of steel liner corrosion as NPPs with embedded steel liners built in the 1970s and 1980s are approaching or have reached their designed lifetime. Due to the increasing demands on abundant fossil-free energy, it is important to consider the prolongated use of existing reactors.

Corrosion of steel reinforcements is a topic that has received a lot of attention from various disciplines, especially NDT & E. As concrete-embedded steel plates are not as common occurrence as reinforcement bars (rebars) considerably less attention has been given to the evaluation of corrosion in liner plates embedded in concrete. However, when extending the operating life of NPPs globally this becomes an important issue to tackle, and the results may carry significance for future designs.

The assessment of nonlinear ultrasonic techniques for the detection and evaluation of concrete-embedded corrosion has been mainly focused on the case of rebar corrosion. These studies have focused on small laboratory-scale specimens where the corrosion has been highly accelerated, thus resulting in gross uniform corrosion and several studies have been published on the matter, indicating a clear interest for the topic worldwide (Antonaci et al., 2013; Arumaikani et al., 2022; Climent-Llorca et al., 2020; M.-Á. Climent et al., 2022; M. Á. Climent et al., 2019; Miró et al., 2021).

The content within this thesis aims to contribute to the field of corrosion evaluation using nonlinear ultrasonics. To the author's knowledge, no prior work has reported the evaluation of liner plate corrosion using nonlinear ultrasonics.

1.3.   Aim, objective, and limitations

The Nuclear Power Concrete Technology programme, managed by the Swedish Energy Research Centre, aims to provide new knowledge to assist in managing concrete structures at Swedish and international nuclear power plants. The intention is to safeguard the longevity of the structures and ensure their safe operation. As a part of this programme, the work disseminated herein aims to investigate the potential of using nonlinear ultrasonic techniques for the detection and evaluation of concrete-embedded steel liner plate corrosion. Such liners are found in the containment buildings of nuclear power plants.

The general scope is limited to experiments on small laboratory-scaled specimens with no reinforcement and small aggregates, i.e., the experiments were not performed on real containment buildings or mock-ups. Most of the experiments performed within the scope of the work put an emphasis on embedded corrosion where the concrete is unaffected, which is realized by having pre-corroded plates embedded in concrete. By embedding steel plates with known corrosion, it is possible to isolate the effects of corrosion itself. However, one experiment covers the evaluation of specimens that have undergone weakly accelerated corrosion. This enables the evaluation of the effects of corrosion at an initiation stage and before critical loss of leak tightness occurs.

As the focus of this thesis is the evaluation of nonlinear ultrasonic techniques for NDT & E, no emphasis is placed on the corrosion mechanisms or concrete properties. This means that phenomena such as carbonation, pore-formation, and more are not evaluated using nonlinear ultrasonic techniques, although such research is acknowledged.

1.4.   Thesis contributions

Paper I presents a novel investigation of the nonlinear ultrasonic characteristics of a steel plate with varying degrees of corrosion using high-frequency (MHz-range) tone-burst excitation. The steel plate was submerged in water to eliminate the influence of heterogeneity that would otherwise be present in concrete while still having the plate embedded in some medium. This study shows that when immersed in a homogeneous medium (water) the corroded regions increase signal attenuation and when the corrosion is of the type including bulk cracks and delaminations, pronounced energy transfer to the second harmonic is observed when using a pitch-catch measurement scheme. Increased intermodulation is observed when conducting contact-type through-transmission measurements. Increased attenuation is a known phenomenon for corrosion, however, the results from the nonlinear evaluations are novel.

The evaluation of specimens that have undergone weakly accelerated corrosion under various circumstances is investigated in Paper II where it is revealed that when the contact in the steel-concrete interface is challenged, regardless of corrosion, nonlinear parameters are affected. These novel experiments were performed using continuous ultrasound and an impact source to modulate the probing ultrasound. The instantaneous modulation characteristics were analysed using the Hilbert-Huang Transform which gave particularly interesting results as frequency modulation was observed to be very sensitive to specifically corrosion-related defects. The study included the evaluation of several damage indices based on harmonic generation, modulation spectroscopy, and instantaneous characteristics. I proposed a novel Total Damage Index which combines several parameters related to waveform distortion into a single index. This novel parameter can be combined with other inspection methods to achieve a comprehensive qualitative damage index.

The interesting findings regarding instantaneous frequency modulation reported in Paper II are further investigated in Paper III where cylindrical concrete specimens with steel plates embedded in their center are studied. In addition to performing measurements to evaluate the instantaneous modulation characteristics, the nonclassical Luxembourg-Gorky (LG) modulation., i.e., cross-modulation, was studied as there have been reports on the remarkable sensitivity of nonclassical methods for particularly the detection of crack-like defects. The results did not confirm the sensitivity to corrosion defects using instantaneous frequency modulation analysis reported in Paper II. This indicates that when the concrete remains unaffected by corrosion it may be challenging to detect corrosion at an early stage. Furthermore, the results do confirm that LG modulation is remarkably sensitive to cracks regardless of origin, which may not be optimal for the current application as it is observed that concrete cracking yields strong LG modulation.

Paper IV builds upon the results in Paper I and presents an investigation into using nonlinear ultrasonic evaluation to image corrosion inside a concrete slab. The measurements were performed using both compression waves and horizontally polarized shear waves. The results indicate that the shear waves are significantly more sensitive to interfaces that are perpendicular to the incidence inside the concrete, compared to the longitudinal waves. Additionally, the same corrosion type that exhibited elevated nonlinearity in Paper I when immersed in water, shows elevated levels of attenuation and nonlinearity even when covered by 0.4 m concrete. These novel results indicate the benefits of using horizontally polarized shear waves over longitudinal waves in concrete-embedded steel plate inspection. Furthermore, the results also highlight reasons to include nonlinear evaluation of ultrasonic signals in concrete inspection to complement the conventional analysis.

1.5.   Thesis outline

A literature review on nonlinear ultrasonic evaluation in general will be provided in Chapter 2 along with some mentioning of promising electrical methods for corrosion evaluation. Chapter 3 delves into some basic theoretical background for elastic waves with an emphasis on nonlinear phenomena. Additionally, Chapter 3 also covers some important experimental considerations for nonlinear ultrasonic NDT & E and notes on signal processing. The methodology used and obtained results are provided in Chapter 4. Conclusions that cover the main scientific contributions and suggestions for future work are provided in Chapter 5.

2. Related research

This chapter provides a literature review on nonlinear ultrasonic methods for NDT & E, and a brief review of some electrical methods as well. The provided background into the various methods and applications is crucial as readers proceed to Chapter 3, where the related theoretical background for nonlinear ultrasonics with an emphasis on elastic wave theory in NDT & E is provided.

2.1. Higher- and subharmonic analysis

As an elastic wave propagates through a nonlinearly elastic solid, the waveform is distorted due to the nonlinear stress-strain relationship. The distortion can be intuitively described as being caused by amplitude-dependent stiffness which naturally affects the propagation speed of sound in the given material. As such, the initial, perhaps sinusoidal waveform, is skewed into resembling more of a sawtooth. This waveform distortion causes the generation of harmonics, which are integer multiples of the fundamental (first harmonic) frequency of the excitation waveform (Kyung-Young Jhang et al., 2020). Figure 3 illustrates such waveform distortion by studying a sinusoidal waveform with the fundamental frequency (f) of 2 (black line) using a multi-frequency solution to Burger's equation proposed by (C. M. Hedberg, 1999) and MATLAB scripts generously provided by Prof. Hedberg. After the wave has propagated some distance, the waveform is distorted (magenta), thus generating integer multiples of the fundamental frequency ($nf, n = 2, 3, ...$). The magnitude spectrum corresponding to these waveforms can be viewed in the bottom half of Figure 3.
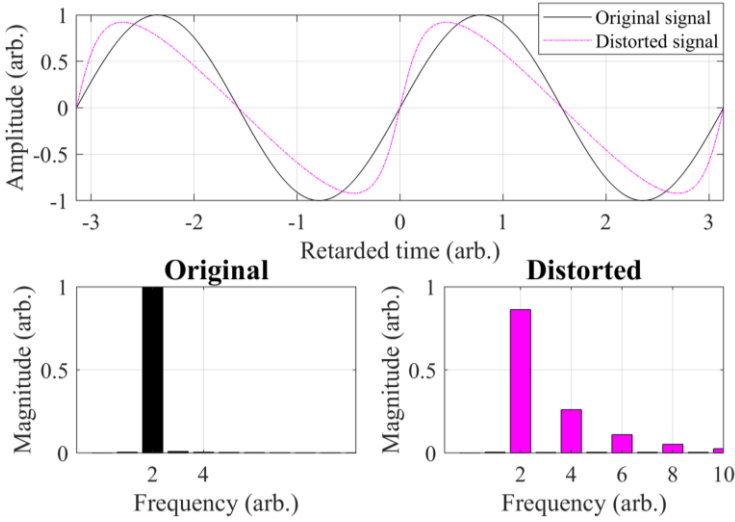
Figure 3. Top: Initially sinusoidal waveform (black) and the distorted counterpart (magenta). Bottom: Magnitude spectra for the original signal (black, left), and for the distorted signal (magenta, right).

Observations of the harmonic generation in solids have been reported extensively since the 1960's (Hikata et al., 1963). The most common technique for nonlinear ultrasonic evaluation relies on the generation of higher harmonics. The scientific community has mainly focused on the use of second harmonic generation (SHG) (Jhang, 2017; Matlack et al., 2015; Williams et al., 2024).

The method relies on the manifestation of the harmonic component that corresponds to the double fundamental frequency. The parameter used for damage evaluation is called the *quadratic parameter* of nonlinearity, commonly denoted β and given by Eq. (2.1). Here, A_1 is the particle displacement of the fundamental frequency component, A_2 is the corresponding displacement for the second harmonic, k is the wavenumber, and x is the propagation distance. The form given in Eq. (2.1) is sometimes called the absolute parameter of quadratic nonlinearity as it is a material parameter typically on the order of several units. However, the absolute parameter is difficult to evaluate experimentally as the second-order displacement, A_2, can be difficult to measure. The displacement may be in the nm-range and requires calibrated transfer functions for reliable extraction (Kyung-Young Jhang et al., 2020). To cope with such experimental challenges, a relative parameter has been proposed that only takes the voltage magnitudes of the respective components into account (Kim et al., 2017). The relative parameter of quadratic nonlinearity, denoted β', is given by Eq. (2.2) where A'_1 and A'_2 are the voltage magnitudes of the first and second harmonic as given by the magnitude spectrum. To use the relative parameter, the propagation distance and wavenumber, i.e., frequency must be constant during the experiments. The derivation and presentation of some additional properties of the quadratic (and higher order) parameter of molecular elastic nonlinearity will be discussed in further detail in Chapter 3.2.1.

$$\beta = \frac{8A_2}{A_1^2 k^2 x} \tag{2.1}$$

$$\beta' = \frac{A_2'}{A_1'^2} \tag{2.2}$$

Some examples of the application of the SHG technique include evaluation of concrete carbonation (Zhao, Wu, & Chen, 2022), evaluation of the effects of temperature on concrete carbonation (Zhao, Wu, Chen, et al., 2022), concrete cracking using embedded sensors (J. Chen et al., 2020), intergranular corrosion (Zhong et al., 2016), stress-corrosion cracking (Zeitvogel et al., 2014), and concrete reinforcement corrosion (Climent-Llorca et al., 2020). To the author's knowledge, there have been no reports of imaging of corrosion using SHG on steel plates regardless of the state of embedment. Paper I partially bridges this gap by presenting coarse imaging of corrosion-induced harmonic distortion on a steel plate immersed in water. To build upon the results in Paper I, fine-grid SHG imaging of corroded steel plates embedded in a concrete slab is presented in Paper IV.

Although evaluation methods based on the SHG are quite common in the literature, there are several instances where the use of higher-order harmonics has been reported. The third harmonic has been utilized for purposes such as the evaluation of concrete damage (Xie et al., 2016), and fatigue damage in rail specimens (Zhu & Lee, 2019). Even the use of the tenth harmonic has been reported (I. Solodov, 2019; I. Solodov et al., 2004).

Measurements of harmonic generation typically utilize a sinusoidal tone-burst excitation, and the spectral content of the received waveform is studied in a frequency spectrum. Additionally, harmonic generation may be studied via the principle of phase inversion, a technique which superimposes two signals that are 180° phase-shifted in relation to each other (Choi et al., 2019). This eliminates the fundamental frequency component and doubles the second harmonic. Harmonic generation must not necessarily originate from waveform interactions with inhomogeneities within the solid under investigation but may occur in the measurement equipment, such as the transducer or amplifier (Kyung-Young Jhang et al., 2020), or the coupling agent being used (Stuber Geesey et al., 2019). Even surface roughness may affect the harmonic generation when using contact transducers (Chakrapani et al., 2018). Furthermore, the generation of higher harmonics is an effect that can be attributed to lattice anharmonicity which is described by the classical theory of elasticity proposed by Landau and Lifshitz (Landau & Lifshitz, 1986), a topic that will be discussed in greater detail in Chapter 3.2. In practice, this means that harmonic generation is expected to occur to a certain extent in almost all solids because most materials are interatomically imperfect. These considerations imply that the manifestation of harmonics does not necessarily mean that the object under investigation is contains unwanted defects. Because of this and in contrast to biomedical applications (Lee & Chang, 2019), imaging

internal anomalies using strictly the magnitude of the higher harmonics, may not be particularly sensitive due to the possibility of spurious harmonic generation. The exception would be very high-order harmonics, such as the tenth harmonic used in (I. Solodov et al., 2004) as the generation of such high-order harmonics requires strong nonlinearity. Interestingly, there exist nonclassical phenomena that are expected to only occur in objects containing contact-type defects such as closed cracks and imperfect bond interfaces (I. Y. Solodov et al., 2002). One such phenomenon is subharmonics.

In contrast to the higher harmonics that are integer multiples of the fundamental frequency (f), subharmonics are fractions of the fundamental, i.e., f/2, 3f/4, and so on (Korshak et al., 2002; I. Y. Solodov & Korshak, 2002). The emergence of subharmonics can be used to image closed cracks and similar defects because subharmonics do not manifest when the crack is opened (Yamanaka et al., 2004), whereas the integer harmonics would manifest (to a certain extent) regardless of the crack state. Because of the remarkable sensitivity to closed cracks, the method Subharmonic Phased Array for Crack Evaluation (SPACE) has been proposed (Ohara et al., 2007, 2008) and it has been used to image closed stress-corrosion cracks (Ohara et al., 2009; Ohara, Shintaku, et al., 2010) and fatigue cracks (Ohara et al., 2019; Ohara, Endo, et al., 2010).

2.2. Modulation-based methods

When an object undergoes ultrasonic testing with a single-frequency excitation and the object exhibits elastic nonlinearity, the only spectral components generated due to classic nonlinearity are higher harmonics, as discussed in the previous section (Chapter 2.1). However, if multiple excitation frequencies are used simultaneously the various waves will interact which causes nonlinear wave mixing. Wave mixing is a type of modulation, thus energy is exchanged between the various spectral components which will manifest as the generation of sidebands in the frequency spectrum (D. Donskoy et al., 2001). The phenomenon is illustrated in Figure 4 where a waveform with the frequencies 1 and 7 initially only contains these two frequencies, however, as the waveform distorts due to nonlinearity, both higher harmonics and modulation frequencies are generated. Nonlinear wave modulation can be generated by different means and analysed in many ways. What follows are brief descriptions of various methods related to nonlinear wave modulation and examples of reported applications.
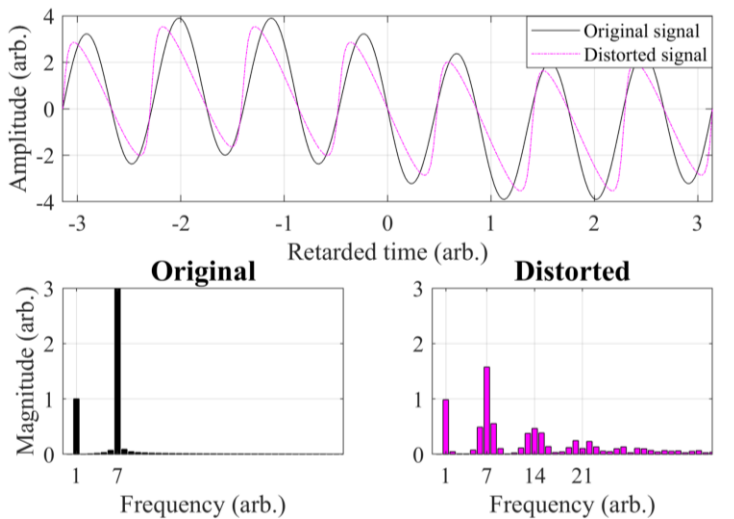
Figure 4. Top: Sinusoidal waveform of frequencies 1 and 7 (black), and the corresponding distorted waveform (magenta). Bottom: magnitude spectra of the original signal (black, left), for the distorted signal (magenta, right).

2.2.1. Nonlinear modulation spectroscopy

The nonlinear ultrasonic methods initially proposed utilizing modulation phenomena were called Vibro-Acoustic Modulation (VAM) (D. M. Donskoy & Sutin, 1998), and Nonlinear Wave Modulation Spectroscopy (NWMS) (K. E.-A. Van Den Abeele et al., 2000). The techniques are essentially identical as they are

both based on the principle of modulation of sound (high-frequency elastic wave) by vibration (comparatively low-frequency perturbation), commonly referred to as pump-probe measurements (Terzi et al., 2019). A continuous ultrasonic sinusoidal probe wave is typically used to probe the modulation effects, and its frequency is generally significantly greater than the modulating pump frequency to ensure adequate separation in the magnitude spectrum that is used for analysis. Continuous excitation is used to ensure that the probing component is narrowband which allows for greater separation between the probing component and the sidebands generated by the pump excitation. The pump is a second comparatively strong excitation whose purpose is to perturb the defects within the material to enhance the nonlinear effects. The pump source may be an impact from an instrumented hammer (X. J. Chen et al., 2008; D. Donskoy et al., 2001; Kober et al., 2020), vibrations from a shaker (Aymerich & Staszewski, 2010; Pieczonka et al., 2015; Terzi et al., 2019), or a second ultrasonic excitation (Aymerich & Staszewski, 2010; Hilloulin et al., 2016; V. Y. Zaitsev et al., 2005).

The modulation intensity is typically presented as a modulation index (MI) which is usually given in the form in Eq. (2.3) (D. Donskoy & Liu, 2021), where A_- is the magnitude of the first-order sideband corresponding to the difference frequency ($f_1 - f_0$) between the probe frequency (f_1) and the pump (f_0), A_+ is the magnitude of the sideband for the sum frequency ($f_1 + f_0$), and A is the magnitude of the probing component, all of which are extracted from a magnitude spectrum of the received waveform.

$$MI = \frac{A_- + A_+}{2A} \qquad (2.3)$$

Although Eq. (2.3) only takes the first-order sidebands into account, if the higher-order sidebands are strong it can improve the sensitivity of the method to include those terms as well. This is because the presence of higher-order sidebands indicates more severe defects. Although the input frequencies may be arbitrary, the probe wave frequency selection has been shown to greatly affect the results (D. Liu & Donskoy, 2023). The robustness of the methods can be improved by using several probe frequencies and average the MI values. The MI then takes the form of Eq. (2.4), as suggested by (D. Donskoy et al., 2003).

$$MI_{avg} = \frac{1}{q} \sum_{m=1}^{q} \frac{A_{m-n} + A_{m+n}}{2A_m} \qquad (2.4)$$

where A_m is the magnitude of the fundamental frequency f_m, $A_{m\pm n}$ is the magnitude at the combination frequencies $f_m \pm f_n$, f_n is the frequency of the n:th modulation frequency, and q is the total number of fundamental frequency steps.

Modulation spectroscopy has been successfully employed for the evaluation of reinforcement corrosion using VAM (D. M. Donskoy et al., 1998), difference

frequency between two ultrasonic perturbations (Korenska et al., 2009), intermodulation (Climent-Llorca et al., 2020; M.-Á. Climent et al., 2022). To the author's knowledge there have been no studies reporting on modulation experiments for concrete-embedded steel liner evaluation.

When using a wideband modulating input, such as a hammer blow, when inspecting high-attenuating materials such as concrete then it may be difficult to discern discrete peaks which is required for the MI calculation. To overcome this, researchers (X. J. Chen et al., 2008) have proposed the use of integration to acquire the energy of the sidebands and the probing component to estimate the modulation intensity. This method was utilized in Paper II, which is to the author's knowledge the first of its kind to apply nonlinear wave modulation measurements for the evaluation of concrete specimens containing steel liner plates that have undergone accelerated corrosion.

2.2.2. Sideband peak count

Two (or more) sources are not required to investigate the modulation phenomena for NDT & E purposes. Researchers have proposed the use of a single excitation in the form of transients to achieve self-interaction between multiple modes generated by the pulse, a method commonly referred to as Sideband Peak Count (SPC) (Eiras et al., 2013; Kundu et al., 2019; P. Liu et al., 2014). The SPC is defined as the number of nonlinearly generated frequency components (N) above a moving threshold (th) governed by the weakest dominant peak from the excitation (Hafezi et al., 2017). An illustration of the principle of the SPC technique is shown in Figure 5 where the excitation has generated 3 dominant peaks, and in the linear case in (a) these are the only spectral components present. In Figure 5 (b) the nonlinear case is illustrated, observe the generated sidebands. The sum of the sideband peaks in relation to the dominant peaks gives the SPC.
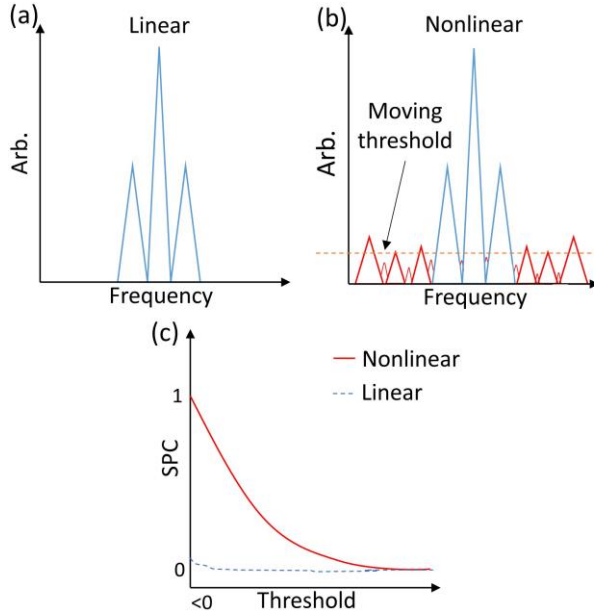
Figure 5. Illustration of the SPC technique in the frequency domain for (a) a linearly elastic medium with no distortion, and (b) for a nonlinearly elastic medium with accompanied distortion. The resulting SPC is illustrated in (c). Figure from (Nilsson et al., 2023a).

Expressed in mathematical terms, the SPC is given by Eq. (2.5) where N_{tot} is the total number of peaks that are greater than the lower limit (*LL*) but weaker than the dominant peaks (*UL*) for the specimen population. It is important to use the same N_{tot} for all datasets within a specimen population or measurement locations on a larger specimen. This is required for facilitating comparisons between the specimens or measurement points. Alternatively, the SPC is only given by the number of peaks per threshold, i.e., *N(th)* (M. Sun et al., 2024)

$$SPC(th) = \frac{N(th)}{N_{tot}}, LL \leq th \leq UL \qquad (2.5)$$

The SPC for a certain threshold range is illustrated in Figure 5 (c) where the linear (dashed line) example generates a small response at very low threshold levels, typically because of spurious noise. The nonlinear case generates a substantial number of sideband peaks, and the number of peaks diminishes as the threshold increases.

As the SPC is a function of a moving threshold, the SPC index (SPC-I) has been proposed as an alternative to SPC (Alnuaimi et al., 2021). The SPC-I is defined as the average number of peaks and the divisor is the number of threshold steps between LL and UL. This gives a number instead of a function which makes SPC-I more appropriate as a damage index compared to SPC.

The number of peaks is expected to increase with increasing nonlinearity, however, to study the modulation intensity the energy distribution to the sidebands from the dominant peaks should be considered. Based on work by (X. J. Chen et al., 2008) the authors of (Arumaikani et al., 2022) have proposed to use the energy ratio between the sidebands (W_{NL}) to the dominant peaks (W_L), as given by Eq. (2.6). An index corresponding to magnitude instead of energy is called the Sideband Peak Index (SPI) (M. Sun et al., 2024), is given by Eq. (2.7), which is practically similar to the MI given by Eq. (2.4).

$$\alpha = \frac{W_{NL}}{W_L} \tag{2.6}$$

$$SPI = \frac{\sum A_{sidebands}}{A_{fundamental}} \tag{2.7}$$

The SPC and related techniques have been used to evaluate the progression of corrosion-induced damage in concrete (Arumaikani et al., 2022; Basu et al., 2021), porosity in additive manufactured parts (S. Park et al., 2022), and impact damage in steel (S. H. Park & Kundu, 2023) and more (Hafezi et al., 2017; P. Liu et al., 2014). The SPC technique with the related energy distribution estimation by Eq. (2.6) was used to confirm the observations of increased nonlinearity in the severely corroded plate region in Paper I via contact through-transmission measurements. This is to the author's knowledge the first report of the use of SPC to directly evaluate the nonlinear ultrasonic characteristics of a corroded steel plate. An SPI C-scan of a concrete slab containing embedded corroded steel liners is presented in Chapter 4.4.1, which is a novel application of the technique.

2.2.3. Demodulation analysis

Although the analysis of the modulation intensity is commonly done in the frequency domain typically by the Fourier transform, there is a drawback of the method because the dominating type of modulation, i.e. amplitude or frequency modulation, cannot be discerned from the analysis. To demodulate the nonlinear waveforms and acquire instantaneous modulation characteristics, the Hilbert transform (HT) can be applied (Huang et al., 1998). However, the HT is mostly suitable for narrowband and monofrequency signals which is not the case of nonlinearly modulated waveforms. To overcome this limitation, the nonlinearly distorted waveform can be decomposed into intrinsic mode functions (IMF) via empirical mode decomposition (EMD), as proposed by (Huang et al., 1998; Huang & Wu, 2008). The method will be presented in greater detail in Chapter 3.6.2 but the core principle is to decompose the wideband signal into several IMF each representing some dominant frequency in the original signal. Because the IMF is a narrowband mode of the original signal, it admits a more suitable HT which is then used to acquire the instantaneous amplitude and frequency.

The use of the HHT to study nonlinear wave modulation was proposed by (H. F. Hu et al., 2010) to evaluate crack detection in an aluminium plate. The damage indices that the authors proposed (see Eqs. (2.8) & (2.9)) differ from previous indices as they are based on the standard deviation of the instantaneous amplitude and frequency, respectively. Indeed, the standard deviation certainly is a measure of the deviation from a mean that the nonlinear modulation would attribute to. The damage indices are given by:

$$DI_A = \frac{\sqrt{\frac{1}{N}\sum_{i=1}^{N}[IA(i) - \mu_A]^2}}{\mu_A} \tag{2.8}$$

$$DI_F = \frac{\sqrt{\frac{1}{N}\sum_{i=1}^{N}[IF(i) - \mu_F]^2}}{F_{probe}} \tag{2.9}$$

Where N is the number of digitized samples being analysed, IA and IF are the instantaneous amplitude and frequency, μ_A and μ_F are the mean instantaneous amplitude and frequency. When determining these damage indices, it is important to consider that the HHT process may induce erroneous end-effects in the instantaneous amplitude and frequency waveforms. The end-effects must be omitted from the calculations or be mitigated by various techniques (Z. He et al., 2012).

In-phase/Quadrature Homodyne Separation (IQHS) has been proposed as an alternative to Hilbert-Huang Transform (HHT) or Hilbert Transform (HT) demodulation, particularly in applications involving well-defined carrier frequencies and periodic modulation (D. M. Donskoy & Ramezani, 2018; Ehsani et al., 2023). IQHS is computationally efficient compared to the HHT. It is also more robust to multipath interference, as its carrier-based demodulation can mitigate phase shifts and frequency spreading caused by reflections. In contrast, HHT is better suited for nonlinear and non-stationary signals, e.g., an impulse-modulated waveform. However, HHT struggles in multipath scenarios where it does not distinguish between modulated and unmodulated parts of the received waveform, leading to potential demodulation errors (D. M. Donskoy & Ramezani, 2018). In-depth discussions of IQHS for demodulation is outside of the scope of this thesis but the interested reader is referred to (D. M. Donskoy & Ramezani, 2018) for the original IQHS and to (Ehsani et al., 2023) for the modified IQHS which is more suitable for high-frequency pump excitation.

To the author's knowledge, no reports of the evaluation of concrete-embedded steel plate corrosion using instantaneous modulation have previously been published. Paper II and Paper III cover this topic where, among others, the application of the demodulation analysis for the evaluation of concrete-embedded corrosion for specimens that have undergone accelerated corrosion is reported.

2.2.4. Nonclassical modulation transfer

Wave-mixing between two or more elastic waves can be described using the classical theory of elasticity (see e.g. Chapter 3.2.2) and is therefore associated with phenomena that are not strictly related to the presence of defects. Wave-mixing can also occur due to waveform distortion that occurs in the electronics. Conversely, the transfer of bulk wave modulation from an initially amplitude-modulated (AM) wave onto an initially monochromatic wave, so-called cross-modulation (V. Y. Zaitsev et al., 2002), cannot typically be explained by classical theory (Yin et al., 2023) and is suspected to be caused by non-frictional non-hysteretic nonlinear dissipation (Osika et al., 2023; V. Zaitsev et al., 2002) that is remarkably sensitive to the presence of crack-like defects due to their intrinsically dissipative nature (V. Zaitsev et al., 2006). Interestingly, for elastic codirectional guided wave mixing the cross-modulation can be described by classical cubic nonlinear wave mixing and is therefore not necessarily related to nonlinear dissipation (Shan et al., 2024). The most interesting observation regarding this particular fact is that codirectional cross-modulation using guided waves is therefore one of the few methods capable of evaluating material nonlinearity without the influence of instrument nonlinearity.

The principle of the phenomenon is as follows: assume that a medium is excited by two bulk waves; a *pump* wave and a *probe* wave. Let the *pump* wave with the *carrier frequency* F_{pump} be amplitude-modulated at a frequency F_m, i.e., the AM pump-wave is given by:

$$s_{pump}(t) = (A + m_0 \sin(2\pi F_m t))\sin(2\pi F_{pump} t) \qquad (2.10)$$

where A is the carrier amplitude and m_0 is the modulation depth. If Eq. (2.10) is expanded using trigonometric identities, it is shown that the AM pump-wave contains three spectral components: F_{pump}, and $F_{pump} \pm F_m$.

Additionally, assume that the monofrequency elastic *probe* wave has the frequency F_{probe}. If the medium being perturbed by the waves is linear, it is only these four spectral components that would be present in a spectrum of a response, which is illustrated in Figure 6 (a). If the medium is nonlinear of the classical type(s), then harmonics of the initial frequency components will be generated as well as certain sidebands, however, no cross-modulation components of the type $F_{probe} \pm F_m$ are generated. This case is illustrated in Figure 6 (b) for the representation of quadratic nonlinearity. However, if the medium contains cracks certain nonclassical nonlinear phenomena might manifest in the generation of cross-modulation components, as shown in Figure 6 (c). By basing the modulation index (Eq. (2.11)) on these nonclassical components ($A_{cross\text{-}mod}$) the impact from classical material nonlinearity can be reduced and higher sensitivity can be achieved.

$$MI = \frac{\sum A_{cross-mod}}{A_{probe}} \qquad (2.11)$$
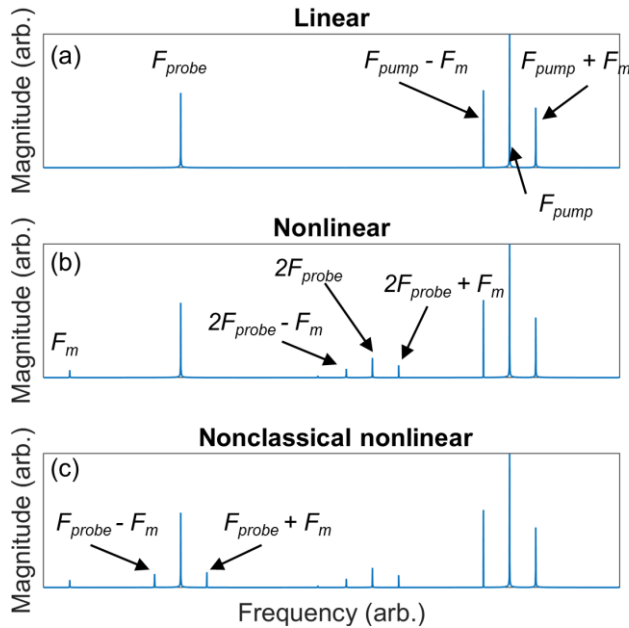
Figure 6. Spectral representation of the cross-modulation phenomenon. (a) Linear case without nonlinear wave modulation. (b) Quadratically nonlinear case, no cross-modulation. (c) Nonclassical nonlinear case where cross-modulation occurs.

The phenomenon is an acoustic analogue to the Luxembourg-Gorky (LG) effect observed for radio waves in the 1930s (Tellegen, 1933) when Tellegen was listening to Radio Beromünster at ~650 kHz, he simultaneously heard audio from radio Luxembourg, transmitted at ~250 kHz which at the time had a powerful 150 kW transmitter (Carozzi, 2000). The phenomenon was observed in Nizhny Novgorod (formerly Gorky), hence the term Luxembourg-Gorky. It is believed that the powerful transmissions from Luxembourg and Gorky heated the ionosphere which causes nonlinear dissipative effects on weaker radio waves propagating in the same medium (Carozzi, 2000; V. Zaitsev et al., 2002). This phenomenon is an excellent example of the universality of nonclassical nonlinearity (Delsanto, 2007).

Reports of the application of cross-modulation include the detection of cracks in glass rods (V. Zaitsev et al., 2006; V. Y. Zaitsev et al., 2002), probing material state perturbations in a granular material (V. Y. Zaitsev et al., 2005), detection of impact-damage in composites (Aymerich & Staszewski, 2010), fatigue cracks (Trojniar et al., 2014), and debonding in concrete strengthened by fibre-reinforced polymer laminate (T. Wang et al., 2024). Cross-modulation to evaluate concrete-embedded steel plate corrosion has been investigated in Paper III (Nilsson et al., 2024a).

2.3. Resonance shift

Nonlinear ultrasonics for NDT & E are typically based on analysing the generation of new spectral components, i.e., higher harmonics and modulation frequencies. These effects are typically dependent on the excitation amplitude. Another such phenomenon is the amplitude-dependent resonance frequency, i.e., the global stiffness of the object under inspection (Johnson et al., 1996). The stiffness decreases, i.e., downwards resonant shift, with accumulated damage due to material weakening.

The global inspection technique called Nonlinear Resonant Ultrasound Spectroscopy (NRUS) relies on exciting an object around a known resonant frequency (Muller et al., 2006). The excitation form is typically sinusoidal with a frequency that is swept around the resonant frequency of interest. An example of the phenomenon is shown in Figure 7 where frequency sweeps with increasing excitation levels are performed around the second longitudinal eigenmode for an aluminium 6082-T6 cylinder in (a) and a concrete cylinder with a corroded steel plate in its centre is shown in (b). Figure 7 (c) shows the frequency shift relative to the resonant frequency at the lowest excitation level for the specimens. Both specimens exhibit a softening (reduction of the resonant frequency) at increasing excitation levels, but the effect is much more pronounced in the concrete specimen.

The resonances of a body may also be excited by an impact from an instrumented hammer, this technique is typically called Nonlinear Impact Resonance Acoustic Spectroscopy (NIRAS) (Leśnicki et al., 2011), but has many variations (Carrión et al., 2021; Dahlen et al., 2015; K. Van Den Abeele et al., 2001). An advantage of the impact-based resonance methods is that the measurements do not require prior knowledge of the object's resonant frequencies which is advantageous for specimens with complex geometry. It is also more practical to excite resonances on large structures using impacts compared to using shakers.

Common for all nonlinear resonant methods is that the resonant frequency at the lowest excitation level, f_0, is used together with the corresponding frequency at the highest excitation, f, to estimate a parameter of hysteretic nonlinearity, α. The frequency shift is directly proportional to the parameter of nonlinearity and the average strain:

$$\frac{f - f_0}{f_0} \approx \alpha \Delta\epsilon \qquad (2.12)$$

Nonlinear resonance shift methods have been applied to inspect various materials and types of defects. Some examples are micro-cracking in bone (Muller et al., 2006), stress-corrosion cracking in stainless steel (Remillieux et al., 2020), defects (Haller et al., 2010) electron beam welds (Kober et al., 2020), and distributed damage in concrete (Jin et al., 2017). The methods are global, meaning that an entire

object is being inspected and no information regarding defect location can be ascertained.
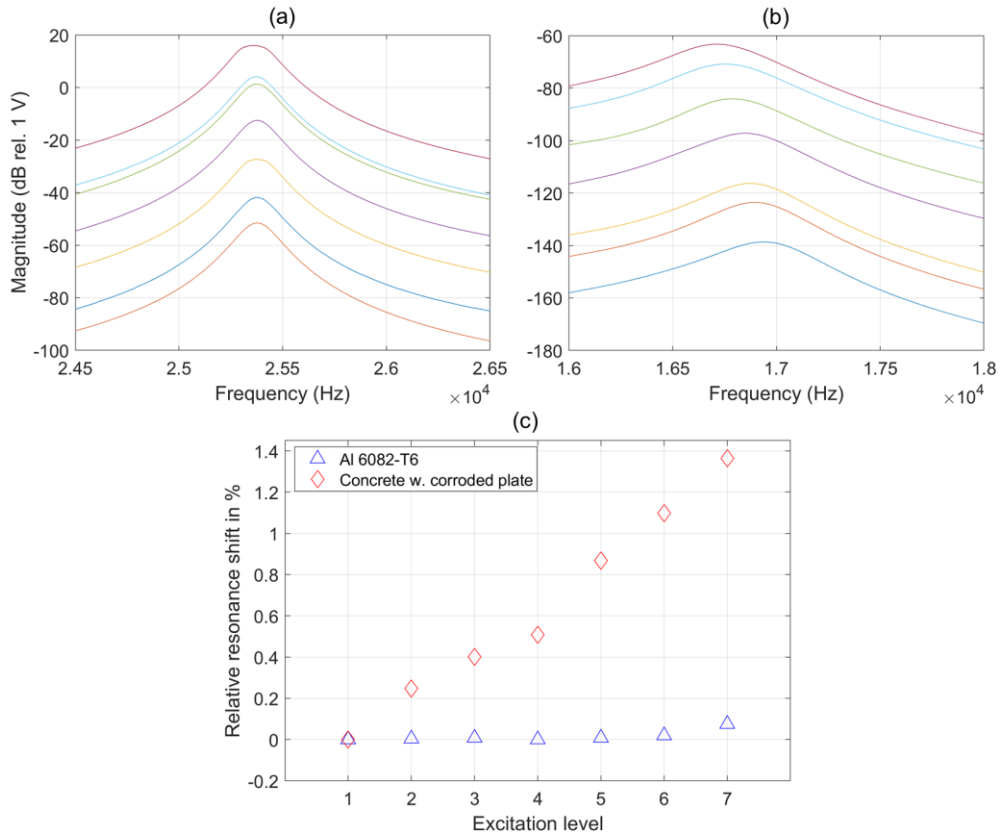

Figure 7. Nonlinear properties for the second longitudinal mode for (a) AL 6082-T6 cylinder, (b) concrete cylinder with embedded shell-corroded plate. (c) shows the frequency shift relative to the resonance at the weakest excitation level.

2.4.   Nonequilibrium recovery

There is a class of time-dependent effects that are attributable to material nonlinearity, namely *Slow Dynamics*. In essence, when a material in thermodynamic equilibrium is perturbed by an external influence, e.g., a change in pressure, temperature, or electrical currents, the material is forced into a state of nonequilibrium. When the perturbation stops, a recovery process towards equilibrium begins which is typically linear with logarithmic time. The recovery can be studied by probing *material state indicators* (C. M. Hedberg et al., 2013) such as stiffness and sound velocity (TenCate, 2000) and electrical properties (Haller et al., 2010).

Slow Dynamics Diagnostics (Guyer & Johnson, 2009, Ch. 13.4.7), is employed for global, i.e., triage-type inspection. The method typically utilizes a weak ultrasonic signal to probe the deviations from an equilibrium. The probing wave must be sufficiently weak to not induce a pronounced nonlinear response (Haller & Hedberg, 2012). The Slow Dynamics are activated by *conditioning* (TenCate et al., 2000) the material by employing a strong excitation, such as an impulse, or a high-power tone burst.

The short-time magnitude of the probing component can be used to study the recovery process. This is illustrated in Figure 8 where the nonequilibrium recovery is probed after an impulse perturbation for an undamaged (a) and a damaged (b) elastomer component, the figure is adapted from (Nilsson & Carlén, 2019). The probe component is at a steady state before the impulse perturbation which abruptly affects the magnitude of the probe component. This characteristic is shared between the specimens. When the perturbation has stopped, the recovery begins and there are pronounced differences between the recovery characteristics. The undamaged specimen almost reaches equilibrium during the measurement window; however, the damaged counterpart is far from reaching equilibrium. This longer recovery period is indicative of a damaged specimen. Linear regression can be used to obtain qualitative damage indices (Nilsson & Carlén, 2019), however, pristine reference specimens are required to set a baseline.
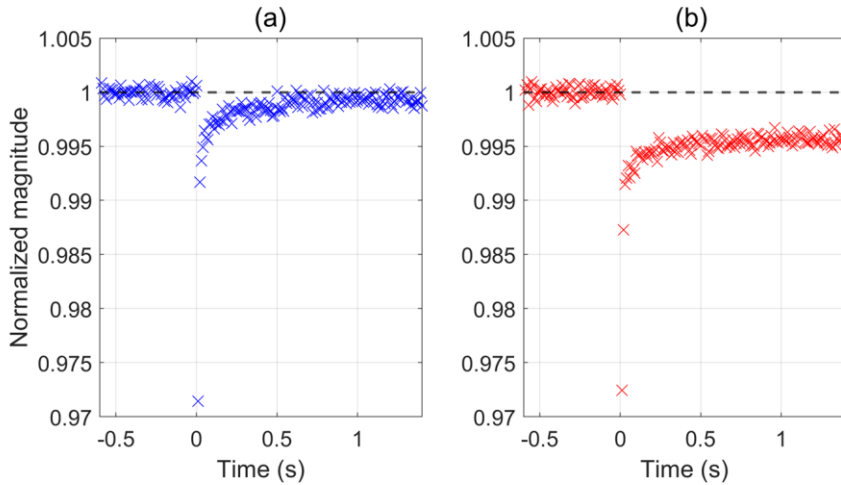
Figure 8. Examples of nonequilibrium recovery for (a) undamaged and (b) damaged complex elastomer components, results from (Nilsson & Carlén, 2019).

Reports of the use of slow dynamics diagnostics show successful applications for evaluating concrete damage (Bentahar et al., 2020), thermal damage in asphalt (Bekele et al., 2017), rock softening due to ultrasonic conditioning (C. M. Hedberg et al., 2013). The study of slow dynamics has been proposed to evaluate building damage due to earthquakes (Astorga et al., 2018), and it is hypothesized that monitoring the softening of the Earth's crust may play an important role in deterministically predicting earthquakes (C. Hedberg, 2014).

2.5.   Electrical methods for corrosion evaluation

Previous sections have focused on various nonlinear ultrasonic techniques. To provide a comprehensive review of methods and techniques for detecting embedded corrosion some alternative electrical methods are briefly presented in the following sub-sections.

2.5.1. Half-cell potential (Open-Circuit Potential)

Half-cell potential techniques (Francois et al., 1994; Garcia & Deby, 2019; Huttunen-Saarivirta et al., 2023; Reichling & Raupach, 2014) are well-established for corrosion evaluation. The methods typically measure the Open-Circuit Potential (OCP) difference between a concrete-embedded steel component and a reference electrode placed on the concrete surface or embedded inside the concrete.

The OCP can be considered an indication of the thermodynamic driving force for corrosion (Huttunen-Saarivirta et al., 2023). The lower the potential difference, the greater the driving force for corrosion. Typically, the OCP is measured in negative units, thus higher negative values mean higher corrosion risk. Although the OCP indeed measures a driving force for corrosion, it cannot deterministically indicate that corrosion indeed has occurred or give quantitative information on the current corrosion rate (Rodrigues et al., 2021). Half-cell potential measurements are fast and not particularly complex; however, they typically require contact with the steel member of interest. The technique is therefore valuable for monitoring and mapping the corrosion risk for specific embedded components given that it is possible to access the component.

2.5.2. Linear Polarization Resistance

The instantaneous corrosion rate can be estimated using linear polarization resistance (LPR) measurements (Broomfield, 2022 Ch. 4.12), a technique that was proposed in the 1950s (Stern & Geary, 1957). The technique most commonly utilizes a three-electrode configuration where the working electrode is the steel component of interest, a reference electrode that measures the potential or current, and a counter electrode to close the circuit (Rodrigues et al., 2021). The measurements are performed by perturbing the steel component (working electrode) with a potential sweep around the OCP and measuring the resulting current with a reference electrode (Millard et al., 2001), or by measuring the change in potential due to an applied current (Broomfield, 2022). The applied perturbation (potential or current) must be kept constant for an adequate duration to reach a steady state. The applied potential is typically in the order of OCP $\pm$ 10 mV (Rodrigues et al., 2021) which results in a linear polarization resistance (R_p), hence the name of the method.

The polarization resistance is used to estimate the corrosion current via the Stern–Geary formula:

$$I_{corr} = \frac{B}{R_p},\qquad(2.13)$$

where I_{corr} is the corrosion current, B is the Stern–Geary constant which is assumed to be 25 mV for actively corroding steel in concrete, and 50 mV for passive steel (Millard et al., 2001). The LPR (R_p) is given by:

$$R_p = \frac{\Delta V}{\Delta I},\qquad(2.14)$$

where ΔV is the change in potential, and ΔI is the change in current (Rodrigues et al., 2021). The instantaneous corrosion rate in $\mu m/year$ is then given by (Broomfield, 2022):

$$x = 11 \cdot 10^6 \cdot \frac{B}{R_p A},\qquad(2.15)$$

where A is the surface area of the steel component measured in cm^2.

The drawback of the method is that the surface area being electrically perturbed is not easily determined under field conditions and that it requires electrical contact with the steel component that is going to be monitored. This implies that the technique is not truly nondestructive as concrete needs to be removed to access the steel component. However, there have been some developments in four-electrode configurations that do not require a connection to the steel component (Fahim et al., 2019; Lim et al., 2009). The measurements can be made using direct–current (Andrade et al., 2008) or alternating–current (Alexander & Orazem, 2020a, 2020b; Keddam et al., 2011; Yu et al., 2019). The interested reader is referred to (Rodrigues et al., 2021) for a comprehensive review of these techniques.

2.5.3. Resistivity measurements

Electrical resistivity is a material property that describes its ability to withstand the transfer of electrical charge (Hornbostel et al., 2013). Concrete resistivity can vary over several orders of magnitude depending on the moisture content of the concrete. This means that at a saturated state the higher the water-to-cement ratio (w/c) the lower the resistivity. It is therefore important to consider the moisture content when interpreting the measurements (J. Su et al., 2002). Additionally, high water content facilitates efficient ion transport which is required for steel corrosion in concrete (Robles et al., 2022). The degree of saturation is therefore a key parameter in evaluating corrosion risks for concrete–embedded steel components.

An additional factor that affects the concrete resistivity is the level of chloride penetration, which also affects the corrosion risks as chloride lowers the pH and therefore might challenge the passivity of the steel component. Concrete conductivity, i.e., the inverse of resistivity, has been shown to increase with increasing chloride diffusivity (Robles et al., 2022). The many factors that affect the measured resistivity have resulted in a large scatter of resistivity values that may or may not indicate corrosion (Hornbostel et al., 2013). However, it is generally assumed that a resistivity of less than 100 Ωm indicates a high probability of corrosion (James et al., 2019).

Resistivity measurements for corrosion evaluation are typically performed using a four-electrode Wenner configuration (C.-T. Chen et al., 2014; Hornbostel et al., 2013; Robles et al., 2022) where the outer electrodes inject current into the specimen and the inner two electrodes measure the resulting potential. The ratio of the induced potential to the injected current gives the resistance, which is then converted to resistivity by a geometrical constant:

$$\rho = kR = k\left(\frac{V}{I}\right), \tag{2.16}$$

where ρ is the resistivity in Ωm, k is the geometrical factor which depends on the size of the specimen, its shape, and the electrode spacing (Minagawa et al., 2023), V is the induced potential by the injected current I.

The interesting aspect of resistivity measurements is that they allow for tomographic assessment of the distribution of resistivity within the specimens (Karhunen et al., 2010; Reichling et al., 2015), and possibly an indication of the corrosion risk and localization of components of interest (Jeon et al., 2022). This is particularly interesting considering steel liner corrosion as embedded liners may be covered by several dm concrete. However, there appears to be a lack of studies covering electrical resistivity tomography for the evaluation of corrosion risk for concrete–embedded steel components.

3. Nonlinear ultrasonics for NDT & E

Most applications of acoustics in general assume that the systems considered are linear, which practically means the characteristics of the displacement are unaffected by the amplitude of the perturbing wave. In mathematical terms, this is a result of assuming that the elastic waves that perturb the media are infinitesimal, thus making the higher-order terms in the differential equations that describe the wave propagation negligible. However, most applications use waves of finite amplitude which may lead to manifestations of waveform distortion, such as the generation of higher harmonics, nonlinear wave mixing, nonlinear resonance, and more. This nonlinear behaviour is typically described by including higher-order terms in the governing equations. However, certain phenomena cannot be explained by *classical* theory and require additional phenomenological models, these are typically called *nonclassical* which describe anomalous nonlinear effects.

Apart from the techniques for NDT & E dealt within this thesis, acoustical phenomena that are governed by nonlinear effects are the sonic boom (Rudenko & Makov, 2021), acoustic levitation (Brandt, 1989), and of course music where nonlinearity is essential to produce pleasant sounds from instruments such as the violin (Fletcher, 1999), and to produce digitally distorted kick-drums for electronic dance music. The examples are many, but this thesis will present phenomena related to NDT & E. To get a basic understanding of these phenomena, we must revisit the theory of elasticity (Chapters 3.1 – 3.3), and to apply the phenomena for NDT & E we must grasp the necessary experimental considerations (3.4), and some basic signal processing (3.6).

3.1. Fundamentals of elastic waves and ultrasonics

Elastic waves are mechanical waves that propagate within elastic media, causing perturbations and perturbations in the particles within. These waves are characterized by their amplitude, frequency, phase, and wavelength. The wavelength (λ) is inversely proportional to the frequency (f) and directly proportional to the velocity at which the wave propagates (c), see Eq. (3.1). The relationship between the wavelength and the thickness of a layer determines how the wave reflects and transmits when encountering a layer, such as a plate.

When the thickness of a layer (d) is a multiple of half the wavelength, i.e., $d = n\lambda/2$, where n is an integer, constructive interface from the layer can occur which facilitates strong reflections. If reflections are unwanted, then the wavelength should be matched to the thickness by the quarter wavelength rule, i.e., $d = n\lambda/4$. This causes destructive interference which minimizes reflections. The quarter wavelength rule is important to consider in transducer design when making impedance-matching layers. If the layer thickness is comparable to the wavelength, i.e., $d \approx \lambda$, then multiple reflections (reverberation) can occur which may cause artifacts in an ultrasound image.

$$\lambda = \frac{c}{f} \tag{3.1}$$

Furthermore, the polarization of the wave has important implications for its propagation characteristics. There are mainly two types of bulk (body) waves: longitudinal and transverse. Longitudinal waves, sometimes called pressure or compression waves (P-waves), can propagate in fluid and solid media, but transverse, i.e., shear waves (S-waves), can only propagate in solid media. Figure 9 shows the displacement characteristics for a longitudinal wave (a) and a horizontally polarized shear wave (b). In addition to bulk waves, there are Rayleigh waves that are formed by a combination of P- and S-waves that only travel along the surface or between interfaces of semi-infinite, i.e., thick, solids (Rayleigh, 1885). Such waves are called *surface waves*. Waves that are guided by the geometrical boundaries in plate-like structures are called *guided waves,* such as Lamb and Love waves (Z. Su & Ye, 2009). The scope of this thesis only deals with the analysis of bulk waves and in-depth discussion about surface and guided waves will be omitted. However, nonlinear ultrasonic guided waves have received significant attention in the field of NDT & E and the interested reader is referred to (Lissenden & Hasanian, 2020) and (Lissenden, 2021) for theoretical discussions and measurement principles concerning the matter.

Ultrasound employs high-frequency elastic waves to examine various materials such as concrete, steel, and biological tissues. The process begins with an electrical pulse sent to a transducer, typically comprised of a piezoelectric material, which converts the electrical charge into mechanical stress, thereby deforming the material and generating elastic waves. The characteristics of these waves depend on the design of the transducer. To achieve spatial resolution, the excitation must be transient. The generated waves are then directed into the object being examined. When these waves encounter interfaces with different acoustic impedances compared to the host material, they partially reflect and transmit. In heterogeneous materials like concrete, which contains randomly arranged constituents of varying sizes (such as aggregates and pores), the ultrasound experiences significant absorption and scattering. This leads to effective attenuation of the ultrasound and the generation of many spurious reflections, often referred to as *structural noise*.

When a plane wave at normal incidence encounters an interface between two media, the energy of the incident (I) wave is partially reflected (R) and transmitted (T). The displacement at the boundary is the same on both sides of the interface, which gives:

$$u_T = u_I + u_R \tag{3.2}$$

where u_I, u_R, and u_T are the displacements by the incident and reflected wave in medium 1, and the displacement of the transmitted wave in medium 2, respectively. The stress ratios for reflection and transmission in relation to the incident wave are given by (Ensminger & Bond, 2023):

$$\frac{\sigma_R}{\sigma_I} = \frac{Z_2 - Z_1}{Z_1 + Z_2} \tag{3.3}$$

$$\frac{\sigma_T}{\sigma_I} = \frac{2Z_2}{Z_1 + Z_2} \tag{3.4}$$

where $Z_1 = \rho_1 c_1$ and $Z_2 = \rho_2 c_2$ are the specific acoustic impedances in media 1 and 2, respectively, and ρ is the density of each medium. If we assume that an incident longitudinal wave is interacting with a concrete-steel interface, we have impedances 9.6 and 47 MRayl for concrete and steel, respectively. This gives a reflection coefficient of 66% and transmission of 34%. This shows that more energy is reflected from the interface than is transmitted through the steel. It is therefore safe to assume that reflection measurements from a steel surface embedded in concrete can yield information regarding its condition. It is important to note that reality rarely offers ideal conditions which complicates the matter. This includes non-normal incidence, refraction, mode conversion, and more. Describing these phenomena in detail is beyond the scope of this thesis, but the interested reader is referred to (Ensminger & Bond, 2023).
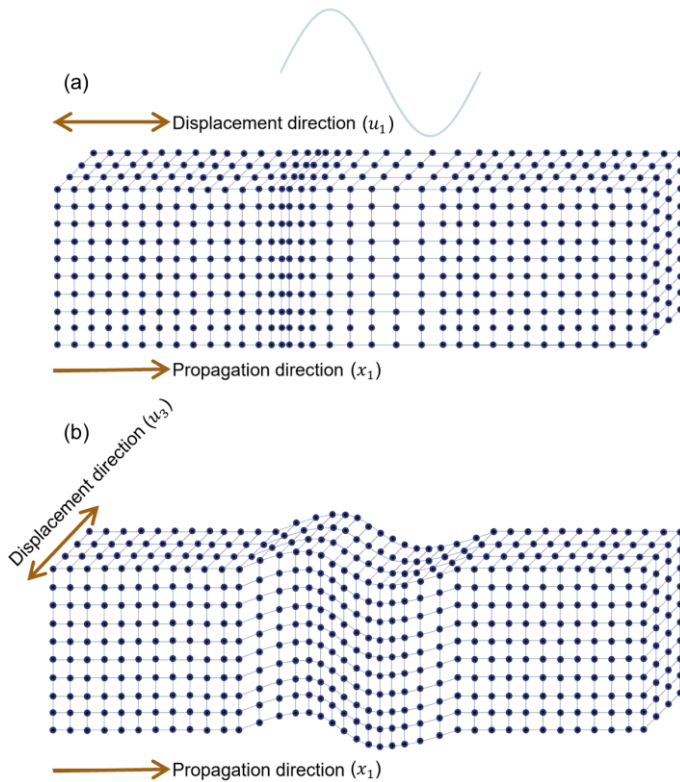
Figure 9. Illustrations of (a) longitudinal wave displacement and (b) shear-horizontal wave displacement. The single-period sinusoid at the top illustrates the excitation waveform for the different wave types.

3.1.1. Ultrasonic imaging

An ultrasonic image is produced by performing a multitude of measurements, each producing a single waveform (including reflections) called an *A-scan (z)*, which is typically presented as the waveform envelope. When multiple A-scans have been acquired along a line, these can be combined to form a vertical slice which is called a *B-scan* (xz or yz image). When multiple lines within a region have been scanned, then a horizontal slice at a certain depth (time) can be extracted to create a *C-scan* (xy image). An illustration clarifying these *scans* can be viewed in Figure 10.
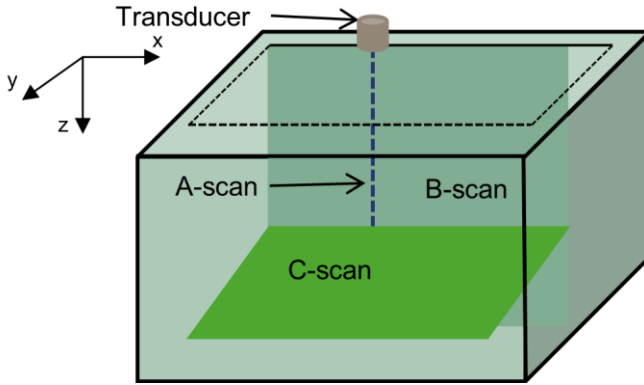
Figure 10. Illustration of A-, B-, and C-scans.

3.2.   Classical theory of nonlinear elasticity

The *classical* theory of nonlinear elasticity describes deviations from Hooke's law, which states that the force required to deform some object scales linearly with the elongation by the stiffness of the material. More commonly, it is said that the stress (σ) is equal to the stiffness (typically Young's modulus) multiplied by the relative deformation, i.e., strain. If we assume a plane elastic wave we get $\sigma_{ij} = E_0 \frac{\partial u_i}{\partial x_j}$, where subscripts *i, j = 1, 2, 3* denote the direction of propagation of a displacement field, i.e., *(x₁, x₂, x₃) = (x, y, z)*, and the direction of the displacement *u*, i.e., *(u₁, u₂, u₃)* are displacements in *(x, y, z)*, see Figure 11.
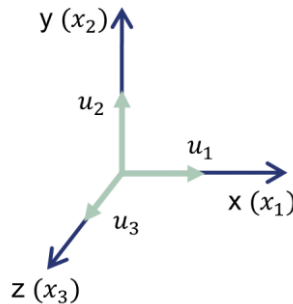
Figure 11. Coordinate system.

For homogeneous isotropic media, the deviation from Hooke's law can be formulated by developing expressions of the elastic energy density as a function of the strain field (F. D. Murnaghan, 1937; Landau & Lifshitz, 1986; McCall & Guyer, 1996). The third-order internal elastic energy due to deformation can be described as

33

$$W = \mu u_{ij}^2 + \left(\frac{K}{2} - \frac{\mu}{3}\right) u_{kk}^2 + \frac{\mathcal{A}}{3} u_{ij} u_{ij} u_{kl} + \mathcal{B} u_{ik}^2 u_{jj} + \frac{\mathcal{C}}{3} u_{jj}^3, \qquad (3.5)$$

where the constants μ, K, $\mathcal{A}$, $\mathcal{B}$, and $\mathcal{C}$, are the members of the so-called five-constant theory of elasticity (Broda et al., 2014; McCall & Guyer, 1996) of which $\mu = E_0/2(1 + \nu)$ and $K = E_0/3(1 - 2\nu)$ are the bulk shear and compression moduli respectively (second-order elastic moduli), E_0 is Young's modulus, ν is Poisson's ratio and $\mathcal{A}$, $\mathcal{B}$ and $\mathcal{C}$ are the third-order elastic moduli (Landau & Lifshitz, 1986). The displacement of the material when perturbed is described by the strain tensor u_{ij} (Landau & Lifshitz, 1986):

$$u_{ij} = \frac{1}{2}\left(\frac{\partial u_i}{\partial x_j} + \frac{\partial u_j}{\partial x_i} + \frac{\partial u_k}{\partial x_i}\frac{\partial u_k}{\partial x_j}\right). \qquad (3.6)$$

Observe that large strains may cause nonlinear interactions between the components of the strain tensor u_{ij} and the displacement vector u by, e.g., large deformations. This type of nonlinearity is independent of the physical properties of the perturbed medium, it is therefore termed *geometrical nonlinearity* (Zarembo & Krasilnikov, 1971). Of course, the deformation itself is dependent on the mechanical properties of the medium. When considering the application of ultrasonics for NDT & E, the geometric nonlinearity in solids will often be negligible due to the small strains normally exerted on the specimens, which are typically in the range of micro-strain.

As we are interested in the dynamics of displacement, we must express the equation of motion. We begin by finding the stress associated with the strain (Guyer & Johnson, 2009):

$$\sigma_{ij} = \frac{\partial W}{\partial\left(\frac{\partial u_i}{\partial x_j}\right)}, \qquad (3.7)$$

and Newton's second law of motion (*F* = *ma*)

$$\rho_0 \frac{\partial^2 u_i}{\partial t^2} = \sum_{k=1}^{3} \frac{\partial \sigma_{ik}}{\partial x_k}, \qquad (3.8)$$

where ρ_0 is the mass density at an unperturbed state. By combining Eqs. (3.5) – (3.7) into (3.8) we can formulate the dynamics of the displacement of a longitudinal wave ($u_2 = u_3 = 0, u = u_1$) propagating in x, which gives the one-dimensional nonlinear wave equation excluding attenuation (Gusev et al., 2009):

$$\frac{\partial^2 u}{\partial t^2} - c_0^2 \left[1 - \beta\frac{\partial u}{\partial x} + \delta\left(\frac{\partial u}{\partial x}\right)^2\right]\frac{\partial^2 u}{\partial x^2} = 0 \qquad (3.9)$$

where c_0 is the longitudinal wave velocity at equilibrium, β and δ are the classical *quadratic* and *cubic* parameters of nonlinearity respectively. There are no universal expressions for the parameters β and δ as solids facilitate the interaction of different wave types (Rudenko, 2006). For the case of longitudinal waves in isotropic solids,

the parameters are related to the third- and fourth-order elastic moduli and the Lamé coefficients λ, and μ (shear modulus) as follows (Kube & Arguelles, 2017; Landau & Lifshitz, 1986):

$$\beta = -\frac{[3(\lambda + 2\mu) + (2\mathcal{A} + 6\mathcal{B} + 2\mathcal{C})]}{\lambda + 2\mu},$$

$$\delta = -\frac{[3(\lambda + 2\mu) + 6(2\mathcal{A} + 6\mathcal{B} + 2\mathcal{C}) + 24(\mathcal{E} + \mathcal{F} + \mathcal{G} + \mathcal{H})}{2(\lambda + 2\mu)},$$

(3.10)

where $\mathcal{E}, \mathcal{F}, \mathcal{G},$ and $\mathcal{H}$ are the fourth-order elastic moduli (Landau & Lifshitz, 1986). This type of nonlinearity that is directly linked to the elastic properties of the material is called *physical nonlinearity* and is typically attributed to the anharmonic characteristics of the interatomic forces (Zarembo & Krasilnikov, 1971). Indeed, the presence of defects, dislocations, and discontinuities affect the characteristics of interatomic forces and therefore cause increased nonlinearity. This is why the parameters of classical nonlinearity can be used for the nondestructive evaluation of solids. Moreover, due to the scale of nonlinear interactions that are indeed probed (interatomic), remarkable sensitivity may be provided regardless of probing wavelength.

To illustrate the two phenomena that are most commonly exploited for nonlinear ultrasonic NDT & E, derivations of approximate solutions for Eq. (3.9) are given in sections 3.2.1 where higher-harmonic generation for monochromatic excitation is expressed, and 3.2.2 where the nonlinear wave mixing, i.e., nonlinear wave modulation by classical nonlinearity is formulated.

3.2.1. Higher-harmonic generation for isotropic solids with cubic nonlinearity

We proceed by investigating the case of a monochromatic excitation perturbing a body, then the quadratic nonlinearity would produce both even and odd higher harmonics, whereas the cubic nonlinearity only generates odd harmonics (K. E.-A. Van Den Abeele et al., 2000). This can be shown by solving the nonlinear wave equation (3.9) by perturbation theory.

Let's represent the longitudinal displacement u as a sum of multiple perturbations:

$$u = u_0 + u_1 + u_2 + \cdots \qquad (3.11)$$

where the subscript denotes the order of smallness of the perturbation, i.e., $u_0 \gg u_1 \gg u_2$. We can therefore reduce Eq. (3.8) into a set of quasi-linear equations by applying the method of successive approximations (Kube & Arguelles, 2017):

$$u_{0,tt} - c_0^2 u_{0,xx} = 0 \qquad (3.12)$$

35

$$u_{1,tt} - c_0^2 u_{1,xx} = -\beta c_0^2 u_{0,xx} u_{0,x} \tag{3.13}$$

$$u_{2,tt} - c_0^2 u_{2,xx} = -\beta c_0^2 (u_{0,xx} u_{1,x} + u_{1,xx} u_{0,x})$$
$$+ \frac{1}{2} \delta c_0^2 u_{0,xx} (u_{0,x})^2 \tag{3.14}$$

Where the subscripts *tt, xx,* denote the second-order differentiation with respect to (w.r.t) *t* and *x*, and the subscript *x* is the first-order differentiation w.r.t *x*. Equation (3.12) is the linear homogeneous wave equation excluding attenuation, the solution for which is given by the boundary condition, i.e., the excitation signal, which in the case of monochromatic plane wave excitation has the form (Marion, 1965):

$$u_0 = A_0 \sin(\tau) \tag{3.15}$$

where A_0 is the initial amplitude at the source $x=0$, $\tau = (kx - \omega t)$, x is the propagation distance, $k = \omega/c_0$ is the wave number, $\omega = 2\pi f$ is the angular frequency of the excitation waveform, and f is the frequency. We may find the solution for Eq. (3.13) by using the trial solution (Green, 1973)

$$u_1 = b_1 x \sin(2\tau) + b_2 x \cos(2\tau) \tag{3.16}$$

where b_1 and b_2 are constants that are to be determined. Inserting the trial solution (3.16) and the solution for the linear equation (3.15) into (3.13) we get:

$$b_1 = 0, b_2 = \beta \frac{A_0^2 k^2}{8} \tag{3.17}$$

Equation (3.14) can also be solved by the method of undetermined coefficients. Knowing the form of u_1 we can see from Eq. (3.14) that u_2 only contains terms with τ and 3τ due to the products of the first- and second-order derivatives. This suggests that a trial solution may have the form

$$u_3 = h_1 x \cos(\tau) + h_2 x \sin(\tau)$$
$$+ h_3 x^2 \cos(\tau) + h_4 x^2 \sin(\tau)$$
$$+ h_5 x \cos(3\tau) + h_6 x \sin(3\tau)$$
$$+ h_7 x^2 \cos(3\tau) + h_8 x^2 \sin(3\tau) \tag{3.18}$$

where $h_1, h_2, …, h_8$ are constants that are determined by substituting the trial solution into Eq. (3.14), which gives:

$$h_1 = -\frac{A_0^3 k^3}{8}\left(\frac{\beta^2}{2} + \delta\right), \qquad h_4 = h_8 = \frac{\beta^2 k^4 A_0^3}{32},$$

$$h_5 = -\frac{k^3 A_0^3}{24}(\beta^2 + \delta), \tag{3.19}$$

$$h_2 = h_3 = h_6 = h_7 = 0$$

Thus, the approximative perturbation solution (3.11) for Eq. (3.9) is given by:

$$u(\tau) = A_0 \sin(\tau) + \beta \frac{A_0^2 k^2 x}{8} \cos(2\tau)$$

$$-\frac{\beta^2 A_0^3 k^3 x}{8} \left[\frac{1}{2} \cos(\tau) + \frac{1}{3} \cos(3\tau) \right]$$

$$+\frac{\beta^2 A_0^3 k^4 x^2}{32} [\sin(\tau) + \sin(3\tau)]$$

$$-\frac{\delta A_0^3 k^3 x}{24} [3 \cos(\tau) + \cos(3\tau)]$$

(3.20)

From which it follows that the amplitude of the second harmonic (A_2) only depends on β in the following manner:

$$A_2 = \beta \frac{A_0^2 k^2 x}{8} \tag{3.21}$$

Which is almost equivalent to Eq. (2.1). If only quadratic order was considered, then the two expressions would be equal as the quadratic order does not include β^2, which indeed affects the amplitude of the fundamental harmonic, something the observant reader may have noticed in Eq. (3.20). If we assume that the $\sin(\tau)$-term is dominating, then the fundamental amplitude is approximately given by:

$$A_1 \approx A_0 \left(1 + \frac{\beta^2 A_0^2 k^4 x^2}{32} \right) \tag{3.22}$$

This suggests that β may be estimated by only measuring the received fundamental harmonic and the source excitation amplitude (Kube & Arguelles, 2017). It is important to remember that the above derivation does not include attenuation effects, it is therefore erroneous to assume that $A_0 = A_1$ even in the case of strictly quadratic nonlinearity. This is most important when considering absolute parameters of nonlinearity.

The solution (Eq. (3.20)) also implies that the second and third harmonic amplitudes may be estimated by the measurement of the fundamental as the third harmonic depends on both β and δ. An interesting observation made by (K. Van Den Abeele & Breazeale, 1996) is that the amplitude of the third harmonic (A_3) can be approximately given by

$$A_3 \approx \beta^2 \frac{A_0^3 k^4 x^2}{32} \tag{3.23}$$

when $(kx)^2$ is large, which is not uncommon for ultrasonic inspections. For example, assuming concrete with a longitudinal wave velocity of 4000 m/s and the inspection frequency 100 kHz, with a propagation distance of 1 m, then $(kx)^2 \approx$

25 000 *rad*. However, if the cubic nonlinearity, i.e., δ is large, then (Na & Breazeale, 1994) found that

$$A_3 \approx \delta \frac{A_0^3 k^3 x}{24} \qquad (3.24)$$

This is why some care is needed when evaluating absolute values of δ from the third harmonic. Regardless, it is evident that the third harmonic is related to the fundamental harmonic cubed which enables the application of a relative parameter analogous to the relative parameter for quadratic nonlinearity given by Eq. (2.2).

3.2.2. Nonlinear wave modulation by classical quadratic nonlinearity

To express the nonlinear wave mixing phenomenon, also known as nonlinear wave modulation, we consider only quadratic nonlinearity for the sake of simplicity. The manner of derivation is analogous to the previous section; the solution is found via successive approximations, however, as only terms of up to quadratic nonlinearity are considered we only need to include the zeroth- and first-order perturbations u_0 and u_1, respectively. Thus, only equations (3.12) and (3.13) need to be solved. For a rigorous analysis of the phenomenon for up to cubic nonlinearity, the reader is referred to (M. Sun et al., 2023).

The zeroth-order solution is once again found by formulating the excitation waveform, i.e. the source boundary condition. Let the exciting waveform(s) be given by:

$$u_0 = A_1 \sin(\tau_1) + A_2 \sin(\tau_2), \qquad (3.25)$$

where $\tau_1 = k_1 x - \omega_1 t$, and $\tau_2 = k_2 x - \omega_2 t$. The amplitudes A_1 and A_2 are not equal to those in the previous section. From Eqs. (3.16) and (3.17) we can see that u_1 is given on the form $u_1 = xg(\tau)$. Given the conditions in the present example, this implies that:

$$u_1 = m_1 x cos(2\tau_1) + m_2 x cos(2\tau_2) + m_3 x cos(\tau_1 + \tau_2) \\ + m_4 x cos(\tau_1 - \tau_2). \qquad (3.26)$$

Proceeding, we get the following by inserting (3.25) and (3.27) into (3.13):

$$-4k_1 m_1 \sin(2\tau_1) - 4k_2 m_2 \sin(2\tau_2)$$
$$-2(k_1 + k_2)m_3 \sin(\tau_1 + \tau_2) - 2(k_1 - k_2)m_4 \sin(\tau_1 - \tau_2)$$
$$= \beta \frac{A_1^2 k_1^3}{2} \sin(2\tau_1) + \beta \frac{A_2^2 k_2^3}{2} \sin(2\tau_2)$$
$$+\beta \frac{A_1 k_1^2 A_2 k_2}{2} [\sin(\tau_1 - \tau_2) + \sin(\tau_1 + \tau_2)]$$
$$+\frac{\beta A_1 k_1 A_2 k_2^2}{2} [\sin(\tau_1 + \tau_2) - \sin(\tau_1 - \tau_2)]$$

(3.27)

which gives the constants:

$$m_1 = -\beta \frac{A_1^2 k_1^2}{8}, m_2 = -\beta \frac{A_2^2 k_2^2}{8},$$
$$m_3 = m_4 = -\beta \frac{A_1 k_1 A_2 k_2}{4}.$$

(3.28)

Insertion of the determined coefficients into the trial solution (3.26) gives the total solution:

$$u = A_1 \sin(\tau_1) + A_2 \sin(\tau_2)$$
$$-\beta \frac{A_1^2 k_1^2 x}{8} \cos(2\tau_1)$$
$$-\beta \frac{A_2^2 k_2^2 x}{8} \cos(2\tau_2)$$
$$-\beta \frac{A_1 k_1 A_2 k_2 x}{4} [\cos(\tau_1 - \tau_2) + \cos(\tau_1 + \tau_2)]$$

(3.29)

By this example we can see that the parameters of nonlinearity not only govern the amplitude of the higher harmonics but also the modulation components. By including higher-order nonlinearity, we would naturally also get higher-order modulation components, i.e., $p\tau_1 \pm q\tau_2$, where $p,q = n - 1$ and n is the order of nonlinearity. For example, quadratic nonlinearity ($n = 2$) gives $p, q = 1$.

The classical parameters of nonlinearity mentioned here are typically not used to evaluate the nonlinearity of an object under test when utilizing modulation measurements because the classical parameters are not strictly dependent on the modulation magnitudes, but also the magnitudes of the present harmonics, as seen in Eq. (3.29). Instead, as discussed in Section 2.2, it is common to employ various modulation indices to evaluate the level of nonlinearity by modulation measurements. However, just as the relative parameters of nonlinearity, the modulation indices are given by the ratio of the nonlinear component over the fundamental.

3.3.   Nonclassical nonlinear elasticity

Classical nonlinear elasticity accounts for geometrical, i.e., related to finite strains, and physical, i.e., nonlinear stress-strain due to nonlinear characteristics of interatomic forces (nonlinear elastic energy). These effects generally only cause weak nonlinearity. However, materials with inhomogeneous microstructure such as concrete, and objects containing defects such as cracks and delaminations, may exhibit anomalously strong nonlinear behaviour that cannot be explained by classical sources of nonlinearity. To explain certain observed phenomena the development of various *nonclassical* models of nonlinear elasticity has been pursued since the late 1990's (Guyer & Johnson, 1999) and continues today (Osika et al., 2023). These models introduce the concept of *structural* nonlinearity (Rudenko, 2006), i.e., nonlinear effects caused by the interaction of structural elements, such as contacts, within the material. What follows is a very brief presentation of the two commonly discussed types of nonclassical nonlinearity in the literature, namely *nonlinear mesoscopic elasticity* and *contact acoustic nonlinearity*.

3.3.1. Nonlinear mesoscopic elasticity

Materials that are intrinsically heterogeneous, e.g., concrete, rocks, and soils can be said to be composed of building blocks, e.g., silicate crystals in rocks and cement, and mortar, e.g., asperities in rocks that cause friction locking. These components typically have diametrically different elastic properties which gives the resulting heterogeneous material complex elastic behaviour. Such materials exhibit what is called nonlinear *mesoscopic* elasticity (NME) and they are modelled as consisting of a collection of elastic hysteretic elements (hysterons) by using Preisach-Mayergoyz (PM) space (Guyer & Johnson, 1999, 2009).

These materials exhibit very high strain dependency on the stiffness. When the elastic contacts compress, they become stiffer, they are therefore strongly nonlinear. They also exhibit hysteresis, an effect which causes strain history (magnitude and rate) to affect the response of a system to an external stimulus. Another interesting phenomenon that is strongly observed in materials with NME is a slow response to transient excitation, i.e., *slow dynamics.* This is typically observed as a nonequilibrium recovery of initial properties that is logarithmic in time. Observe that most, if not all, solid materials that exist exhibit a certain degree of slow dynamics (C. Hedberg, 2014). All these effects are anomalous considering that no classical nonlinearity can describe the observed phenomena. The NME model successfully describes these anomalous phenomena, however, it does not provide any physical data related to the material. (Berjamin et al., 2019).

3.3.2. Contact acoustic nonlinearity

Structural discontinuities within a material, such as the contact interface of a closed crack or delamination, react differently to compressive stimuli compared to tensile. Nonbonded interfaces are typically more difficult to compress, as the stiffness at the interface increases with increasing load due to the expanding contact area of the asperities. Conversely, when subjected to tensile stress, such interfaces weaken as the asperities separate. This phenomenon forms the basis of Contact Acoustic Nonlinearity (CAN), whose simplest representations include linear bimodular stiffness (I. Y. Solodov et al., 2002). In contrast, the transitional bilinear stiffness model (Lu et al., 2023; J. Wang et al., 2021) introduces a more sophisticated approach by incorporating a transitional phase between the compressive and tensile states. In this model, stiffness changes continuously but nonlinearly as the interface moves from a fully closed (compressed) state to a partially or fully open (tensile) state. For interfaces with rough asperities, the nonlinear response can be modelled using Hertzian contact mechanics (Y. He et al., 2022), where the contact area grows nonlinearly with applied load. The Hertzian model complements the transitional bilinear stiffness model by linking the nonlinear stiffness variation to the physical contact mechanics of asperities.

The bilinear stiffness models describe the efficient generation of higher harmonics of orders much greater than those typically expected for classical nonlinearity, i.e., greater than cubic (3f). The stiffness asymmetry that is achieved via bilinear stiffness also results in the generation of subharmonics (Korshak et al., 2002), DC, i.e., zero-frequency components (X. Sun et al., 2020), and dynamic instability (I. Y. Solodov & Korshak, 2002), effects that are indeed anomalous, hence nonclassical. Moreover, the change in stiffness at a contact anomaly creates *Local Defect Resonance* (LDR), a phenomenon that can be exploited for defect localization (I. Solodov, 2014; I. Solodov & Kreutzbruck, 2019).

3.4.   An overview of nonlinear ultrasonic phenomena and associated physical models

Following the presentation of fundamental equations and terminology in nonlinear ultrasonics, a comprehensive overview of physical phenomena and their corresponding nonlinear ultrasonic manifestations illustrates the complexity of nonlinear ultrasonic methods in NDT&E, particularly for corrosion assessment of steel plates embedded in concrete. Table 1 provides a non-exhaustive compilation of these phenomena, their manifestations, and some associated theoretical frameworks that can be used to model the phenomena.

As evident from Table 1, multiple physical phenomena can manifest through similar nonlinear ultrasonic indicators, such as the generation of higher harmonics, nonlinear modulation, and resonant frequency shift. This overlapping nature stems from the fundamental similarities in the underlying nonlinear stress-strain relationships that govern these phenomena. For instance, both corrosion layer interfaces and concrete-steel boundaries can generate higher harmonics, albeit through different mechanical processes: the former via contact nonlinearity at the corrosion-steel interface, and the latter through degraded interfacial stiffness mechanisms. This overlap in these effects presents a significant challenge in corrosion characterization, as it complicates the isolation and identification of specific damage mechanisms. This is true for most cases of nonlinear ultrasonic evaluation regardless of defect type.

The challenge is further exacerbated by the fact that real corrosion scenarios in concrete-embedded steel plates often involve multiple concurrent physical phenomena. For example, corrosion-related defects typically encompass several mechanisms including corrosion layer formation, pitting, interfacial degradation, and stress due to corrosion expansion, each contributing to the overall nonlinear ultrasonic response. Additionally, the presence of concrete introduces its own nonlinear signatures through its intrinsic heterogeneity and mechanisms such as micro-cracking and the presence of pores. Consequently, the interpretation of nonlinear ultrasonic measurements requires careful consideration of multiple potential contributing factors and their interactions.

Table 1. Physical phenomena related to nonlinear ultrasonic manifestations and their associated theoretical models.

Physical Phenomena	Nonlinear Ultrasonic Manifestation	Theoretical Model
Contact interfaces (cracks, corrosion layers, steel-concrete interfaces)	- Higher harmonics - Subharmonics - Modulation - Slow dynamics - Resonance shift	Clapping/breathing crack model with bilinear stiffness (Lu et al., 2023; I. Y. Solodov et al., 2002). Hertzian contact model modified for multiple asperities (Broda et al., 2014; Korobov et al., 2015).
Dislocation dynamics	- Higher harmonics - Modulation - Slow dynamics - Resonance shift	Granato-Lücke theory modified for nonlinear effects (Nazarov, 2016). Amplitude-dependent internal friction (Nazarov & Kiyashko, 2014).
Anharmonic lattice potential	- Second and third harmonics - Modulation	Landau-Lifshitz nonlinear elasticity theory (Landau & Lifshitz, 1986). Phonon-phonon interaction (Taylor & Rollins, 1964).
Friction at interfaces	- Higher harmonics - Modulation - Slow dynamics	Coulomb friction model with rate and state variables (Li & Dwyer-Joyce, 2020).
Hysteretic behavior	- Slow dynamics - Memory effects	Preisach-Mayergoyz space model (Guyer & Johnson, 1999).
Thermal effects	- Higher harmonics - Modulation - Slow dynamics - Resonance shift	Coupled thermomechanical equations (V. Zaitsev et al., 2003).
Material fatigue	- Higher harmonics - Modulation - Slow dynamics	Ultrasonic wave–dislocation dipole interaction (Cantrell, 2009).
Residual stress	- Higher harmonics - Modulation - Resonance shift	Landau-Lifshitz nonlinear elasticity theory (H. Hu et al., 2019; Landau & Lifshitz, 1986). Acoustoelasticity (Kube et al., 2022).

3.5. Measurement equipment and experimental considerations

In order to perform nonlinear evaluation of ultrasonic signals they must be generated, transmitted, received, and digitized. Each step in the chain of measurement requires specific instrumentation and certain important considerations. This section discusses the various steps required to make nonlinear ultrasonic measurements and some related experimental considerations.

3.5.1. Signal generation and amplification

The first step in making any nonlinear ultrasonic measurement is to generate the electrical signal used to excite the transmitter. This is generally done by using an arbitrary waveform generator (AWG) which allows precise setup of the waveform parameters such as the type of waveform, frequency, amplitude, and more. For nonlinear ultrasonics, it is generally preferable to use sinusoidal probe signals over square waves or spike pulses because it facilitates precise control of the frequency content of the generated wave. However, the sinusoid may be continuous, or a tone burst depending on the application.

Continuous waves offer narrow frequency peaks which facilitates the resolution of sidebands around the probing frequency that are generated by a low-frequency perturbation. Moreover, continuous excitation insonify a comparatively large volume which facilitates the inspection of an entire object, given reasonable size as to not completely attenuate the signals. This is helpful when triage-type inspections are wanted. However, continuous excitation measurements do not yield any spatial information. If modulation methods are employed, spatial information may be achieved by varying the point of modulator excitation. The benefit of using tone burst sinusoids is that such transient excitations offer spatial information which is generally required for imaging purposes. Although measurements using mainly transient excitation enable the localization of defects, many measurements are required which complicates matters due to the factors involving coupling, which is discussed in Chapter 3.5.2. Additionally, tone bursts generate comparatively wide frequency peaks which can make the separation of sought-after components difficult. Spectral leakage also becomes a more pronounced issue when studying tone bursts.

When the waveform has been configured, the signal from the AWG, typically voltage, is fed through an amplifier. High excitation levels are required to reach the adequate signal-to-noise ratio (SNR) required to resolve the nonlinearly generated spectral components. This is the first step where spurious nonlinearity might occur as amplifiers are known to cause various types of waveform distortion (Collins & Runton, 2007). It is therefore important to monitor the output from the amplifier to

ensure that the excitation signal is not contaminated prior to the measurement. If a monofrequency signal is amplified, it may undergo harmonic distortion. Similarly, any modulated signal may suffer from additional modulation and harmonic distortion. Analogue low-pass filtering can be used to suppress spurious harmonics that may have arisen during the amplification process, and bandpass filtering can be used to suppress spurious modulation frequencies.

3.5.2. Transmitting and receiving ultrasound

There are various transducer configurations used for actuating and sensing ultrasound in nondestructive testing.

1) Pulse-echo measurements: This configuration employs a single reciprocal probe that both transmits an ultrasonic pulse and senses the reflected waves. It is commonly used for flaw detection and thickness measurements.

2) Pitch-catch: In pitch-catch measurements, transient signals are transmitted using a separate emitter and receiver, typically located on the same side of the specimen. This configuration allows for the detection of certain types of flaws and material properties assessment.

3) Through-transmission: Measurements involve transmitting signals through the specimen and sensing them at the opposite side of the transmitter. This configuration is widely used in nonlinear ultrasonic testing.

4) Array transducers: Array transducers consist of multiple elements arranged in a linear or matrix configuration. They offer the advantage of beam steering, focusing, and extended imaging capabilities, making them particularly suitable for imaging purposes.

Each transducer configuration has its advantages and limitations, and the choice depends on the specific application requirements and the type of information needed for analysis. Nonlinear ultrasonics typically employ pitch-catch or through-transmission configurations with contact transducers. Transducers that are used for contact measurements typically consist of piezoelectrical element(s) that convert electrical charge into mechanical strain and are therefore capable of transmitting ultrasonic elastic waves into materials. Naturally, in a reciprocal manner, piezoelectrical elements can convert elastic waves into electrical signals. Transducer selection must be made based on the sought-after frequency range. For studies of higher harmonics, it is recommended that a narrowband transducer at frequency F is used to excite the specimen and a broadband transducer that is efficient on sensing frequencies $\geq 2F$ to receive the signal. When performing modulation measurements, a broadband receiver at around F is preferred.

An additional important consideration regarding transducer selection is its linearity at high excitation levels. The elements may act in a nonlinear fashion when excited

by the very high-amplitude signals required to resolve nonlinearly generated spectral components. Evaluating the limits of the transmitting transducer is therefore important to eliminate the risks of contaminating the measurement, and of course to avoid damaging the equipment.

When performing contact measurements on solids it is important to remember that most surfaces are not perfectly smooth, which means that there will be air between the face of the transducer and the specimen. Air has a significantly lower acoustic impedance than most solid materials. This means that the energy from the transducer will not be efficiently transmitted into the specimen, and vice versa. This is why it is it is generally recommended to use a coupling agent to reduce the impedance difference and facilitate efficient transmission. Typical couplants include various gels, grease, adhesives such as cyanoacrylate or silicone, and wax. It is important to note that nonlinear ultrasonic measurements require uniform coupling, meaning that the coupling layer must be homogeneous and preferably thin. Additionally, the couplant must not behave nonlinearly when excited by high-amplitude ultrasound. Thus, a third possible source of spurious nonlinearity has been identified. The fortunate invention of dry-point-contact (DPC) transducers (Shevaldykin et al., 2002) has made concrete inspections less reliant on the use of couplants.

When the signal has propagated through the specimen it is received at a significantly reduced level, possibly also with new spectral components. Depending on application it may be required to perform additional analogue signal conditioning before digitizing the signal. If the signal is very weak then pre-amplifiers can be used. To remove unwanted components various types of filtering can be employed.

3.5.3. Analogue to digital conversion

When the received ultrasonic signal has undergone signal conditioning it needs to be digitized to facilitate post-processing. Digitizing is performed using an analogue to digital converter (ADC) typically included in a data acquisition (DAQ) unit or an oscilloscope. To properly digitize the ultrasonic signals for nonlinear evaluation there are several key properties that must be considered for the ADC. First, the sampling rate must adhere to the Nyquist criterion which states that any harmonic waveform can be reconstructed only if the sampling rate is greater than double the highest frequency component of interest. However, it is generally recommended to have a sampling rate that is 10 times higher than the wanted components to ensure that the digitized waveform maintains the shape of the analogue wave.

Another very important property of the ADC is its amplitude resolution, given as the number of bits used to digitize the signal. As the spectral components that are generated due to material nonlinearity often are many times smaller than the fundamental component it is important to consider the minimum quantization voltage in the ADC. The quantization voltage is equal to the maximum measurement

range (full-scale) divided by the number of quantization intervals. The number of intervals is given by 2^n where n is the resolution in a number of bits. For example, an ADC with a full-scale of 10 V, and 16 bits resolution would have a minimum quantization voltage of roughly 0.15 mV. The minimum quantization voltage can be lowered by lowering the full-scale voltage. However, care must be taken to ensure that the lowered full-scale still captures the maximum amplitudes of the signal to not induce signal clipping. For a rigorous analysis of the impact of quantization voltage on the estimation of parameters of nonlinearity, the interested reader is referred to (Kyung-Young Jhang et al., 2020).

3.6. Signal processing

The ultrasonic signals that have been digitized must undergo certain post-processing to perform nonlinear evaluation, i.e., to study the generation of new spectral components or anomalous behaviour of the received signal(s). The typical signal processing includes digital filtering, windowing, and the application of transforms to conduct various types of spectral analysis. The result of the signal processing is the value of some damage index that is related to the waveform distortion caused by material or structural nonlinearity. Brief discussions regarding windowing and the Hilbert-Huang transform will be provided in the following sub-sections. The presentation of the novel *Total Damage Index*, which combines multiple damage indices into one is also given.

3.6.1. Windowing effects in spectral analysis

Nonlinear evaluation of ultrasonic signals typically relies on extracting weak components from various spectra. The discrete Fourier transforms such as the fast Fourier transform (FFT) algorithm operate on the assumption that the time record extends to past and future infinity, when only a discrete, finite time record is studied. As the record is finite there are discontinuities at its ends. This induces a glitch where energy from the fundamental frequency component leaks over to all other frequency bins. Additionally, spectral leakage might occur due to frequency resolution mismatch when sampling the DFT, and due to improperly time-limited observations. The latter occurs when spectral analysis is performed on a signal that contains a non-integer number of periods and/or non-zero endpoints. Spectral leakage can be reduced by applying suitable window functions to the signals of interest and by using zero-padding. Windowing can also be used to discard unwanted portions of a digitized signal.

An example of leakage reduction using windowing is shown in Figure 12 where (a) illustrates the time-domain representation of a sinusoid with a fundamental

frequency of 50 kHz and a second harmonic at 100 kHz whose amplitude is 0.5 % of the fundamental. The signal is sampled at 2 MS/s. Observe that the measurement contains a non-integer number of periods. The window function that is selected for the comparison is the Hanning window, which has been shown to be most efficient at reducing the level of spectral leakage for higher harmonic extraction (Kyung-Young Jhang et al., 2020). The zero-padded spectra are shown in (b). The second harmonic is completely hidden when applying the rectangular window, i.e., no window on a finite number of samples, but the Hanning window effectively reduces the spectral leakage which facilitates the extraction of the harmonic. However, observe that the main lobe is considerably widened by windowing the signal. When studying modulation phenomena this is particularly important to consider.
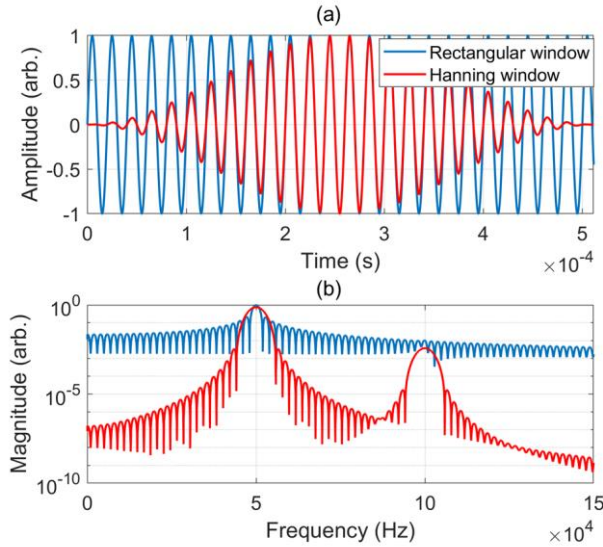
Figure 12. Effects of windowing on a signal containing a second harmonic. (a) signals in time domain, (b) frequency spectra of the signals from (a).

3.6.2. Hilbert-Huang transform

The generation of new spectral components is typically studied in frequency spectrum acquired by the discrete Fourier transform or by using Welch's estimation method. The spectrum practically shows the distribution of energy per frequency bin. This is excellent for extracting the magnitudes of specific spectral components. However, the frequency spectrum does not facilitate the separation of amplitude- and frequency modulation, i.e., demodulation. Neither does the typical implementation of the FFT enable the study of changes over time (excluding short-time Fourier transform). Fortunately, the Hilbert transform (HT) can be applied to extract instantaneous amplitude and frequency which facilitates the study of

amplitude and frequency changes over time. However, the HT is typically only suitable for narrowband signals which nonlinear ultrasonic signals intrinsically are not. To overcome this limitation the implementation of a decomposition process was suggested by Huang et al. and the term Hilbert-Huang transform was coined (Huang et al., 1998; Huang & Wu, 2008).

The Hilbert-Huang transform (HHT) utilizes a procedure called empirical mode decomposition (EMD) to decompose an initially broadband signal into several of its intrinsic mode functions (IMF), each representing a distinct frequency component. An IMF is generally a narrowband signal that admits a proper HT and therefore facilitates the study of the instantaneous characteristics of a certain mode (frequency). The EMD process, which is called *sifting* is schematically described by the block diagram in Figure 13 and essentially comprises the following 5 steps:

1) Identify all local extrema of the input signal $x(t)$. Connect all maxima and minima with two separate spines. These two curves define an upper and lower envelope.

2) Calculate the average of the two envelopes to obtain the *local mean* (m_i).

3) Subtract the local mean from the original signal to obtain the first IMF candidate EMD component (c_1). If $c_1(t)$ contains an equal number of local extrema and zero-crossing or differs by at most one, and if the component has zero mean, it is considered an IMF.

4) If no IMF, repeat steps 1) – 3) by using the residual $r_1 = x(t) - c_1(t)$ instead of the signal $x(t)$. For iterations >1, repeat the steps using the n:th residual given by $r_n = r_{n-1} - c_n$.

5) The mode decomposition is completed when certain stoppage criteria have been met. The criteria can be set by the user, such as a fixed number of IMFs to extract. A general criterion is to continue the decomposition until the residual is a monotonic function, meaning it no longer contains oscillatory features.

The first IMF should contain the highest carrier frequency. It is therefore recommended to perform suitable filtering to ensure that the frequency component of interest is extracted first (Y. Chen & Feng, 2003), although not required as the sifting process can be run until the desired IMF has been extracted.
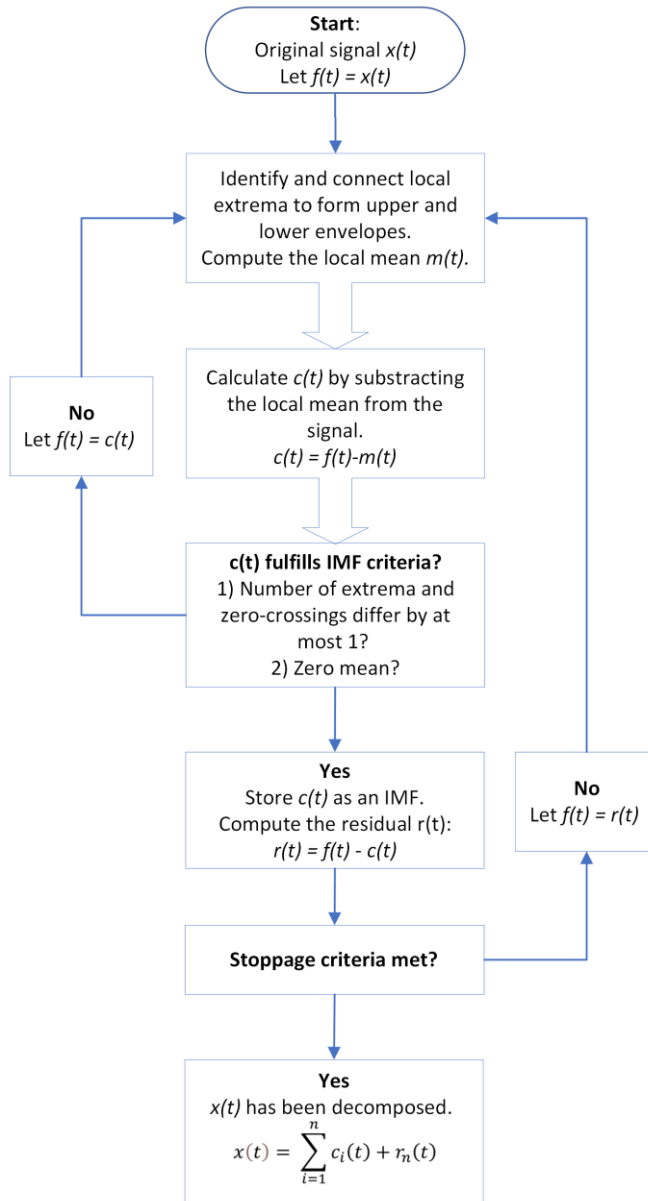
```
        ┌──────────────────────────┐
        │ Start:                   │
        │ Original signal x(t)     │
        │ Let f(t) = x(t)          │
        └──────────────────────────┘
                    │
                    ▼
        ┌──────────────────────────┐
        │ Identify and connect local│
        │ extrema to form upper and │
        │ lower envelopes.          │
        │ Compute the local mean m(t)│
        └──────────────────────────┘
                    │
                    ▼
        ┌──────────────────────────┐
        │ Calculate c(t) by         │
        │ substracting the local    │
        │ mean from the signal.     │
        │ c(t) = f(t)-m(t)          │
        └──────────────────────────┘
```

No
Let $f(t) = c(t)$

c(t) fulfills IMF criteria?
1) Number of extrema and zero-crossings differ by at most 1?
2) Zero mean?

Yes
Store $c(t)$ as an IMF.
Compute the residual r(t):
$r(t) = f(t) - c(t)$

No
Let $f(t) = r(t)$

Stoppage criteria met?

Yes
$x(t)$ has been decomposed.

$$x(t) = \sum_{i=1}^{n} c_i(t) + r_n(t)$$

Figure 13. Block diagram for the process of empirical mode decomposition. From (Nilsson et al., 2023b).

3.6.3. Total Damage Index

Regardless of NDT modality, some damage index is typically extracted from the measurements which may act as a qualitative or quantitative material state indicator. There is currently no method that can utilize all physical phenomena at once to investigate the condition of a structure. There is therefore a need to perform testing with multiple methods that utilize various phenomena in order to get a full investigation. To get the most out of such comprehensive investigations, the data should be analysed separately but the evaluation should be of the combined results. Efforts towards the use of data fusion, i.e., to integrate multiple datasets into a comprehensive and accurate description of the investigated structure, are therefore greatly encouraged.

One way to combine results from multiple damage indices related to acoustic nonlinearity, and perhaps other methods, is proposed herein; the *Total Damage Index* (TDI). Assume that we have a specimen or a measurement point, both denoted as S, and that K damage indices $(DI_k, k = 1, 2, ..., K)$ have been extracted from the testing of the specimens. The TDI is then given by normalizing each the damage index for each S by the maximum DI_k for the entire range of S and performing summation for all indices, in other words:

$$TDI(S) = \frac{1}{K} \sum_{k=1}^{K} \frac{DI_k(S)}{\max(DI_k)} \qquad (3.30)$$

where $TDI(S)$ is a value from 0 to 1, where 0 denotes pristine (no damage) and 1 means severe damage. The TDI allows damage classifications from 0% to 100% where acceptable levels can be set after having acquired a statistically significant amount of data. This is excellent for monitoring damage progression over time, as well as for triage-type inspections in production lines. The TDI was introduced and utilized in Paper II, and results using the TDI are presented in Chapters 4.2 and 4.4.1.

4. Methodology and results

This chapter will briefly describe the experiments carried out within the scope of the thesis. Each experiment is described in further detail in the appended papers. The overall conclusions based on the work and some suggestions for future research are provided in Chapter 5.

4.1. Investigation of the nonlinear ultrasonic behavior of a corroded steel plate

Before examining the ultrasonic response of steel plates embedded in concrete, it's wise to first understand their isolated characteristics to clarify the expected response. This was the motivation behind the work presented in Paper I and the work is briefly summarized here. Two experiments were carried out, the first experiment utilized pitch-catch measurements on a steel plate that was submerged in water. This enables the use of a narrowband transmitter and a broadband receiver to sense second harmonic generation, described in Chapter 2.1. The second experiment utilized through-transmission measurements to study intermodulation by employing the SPC method described in Chapter 2.2.2. Through-transmission measurements are particularly interesting as they most certainly measure the mechanical waves that have propagated through the material of interest, thus interacting with defects within.

Both experiments investigated the same specimen, which can be seen in Figure 14. The steel plate, 225x260 mm, was originally uniformly corroded with the shell corrosion product described in Chapter 1.1. The severe corrosion product was removed to expose the uniform corrosion (COR), which in turn was mechanically removed to get a clean surface free from corrosion to act as a reference region (OK). A part of the shell corrosion (SCOR) was reattached to maintain a region with severe corrosion.

What follows are brief descriptions of the SHG measurements and the associated results (Chapter 4.1.1), and the corresponding results for the SPC measurements (Chapter 4.1.2).
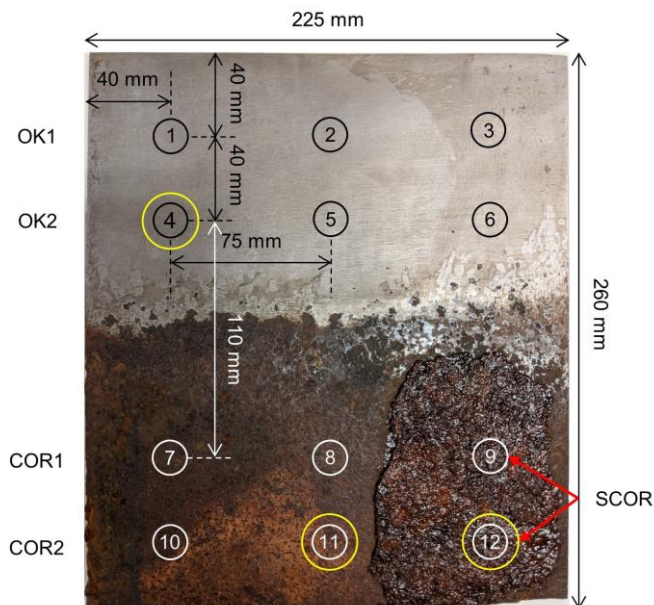
Figure 14. Corroded plate specimen. The approximate placement of the measurement points is shown. Points highlighted by the yellow circle were used for the SPC measurements. OK is the reference, COR is uniform corrosion, SCOR is shell corrosion. Figure from (Nilsson et al., 2023a).

4.1.1. Second harmonic generation due to corrosion

The nonlinear response from a corroded plate subjected to transient excitation was investigated by using a 4-cycle sinusoidal tone burst at 4.5 MHz generated from an Agilent 33500B AWG. A schematic of the entire experimental setup can be viewed in Figure 15. A total of 6 excitation levels from $14 - 80$ V_{pp} were used to investigate the amplitude dependence of the relative quadratic nonlinearity parameter (β'), as described in Eq. (2.2). For the analysis to be valid, β' should remain constant across all excitation levels; any variation would indicate the presence of spurious effects, such as influence from the measurement system.

The plate was submerged in water and the plate rested on a foam board to reduce spurious effects from the bottom of the water tank. A manual XY-scanner was used to move the probe. The beam width (full width at half-maximum) at the surface of the plate was estimated to be approximately 5 mm, which is reflected in Figure 14 where the measurement points are marked to scale. The reflected waves were received by a needle hydrophone was placed as close as possible to the transmitter, marked **R** and **T** in Figure 15.
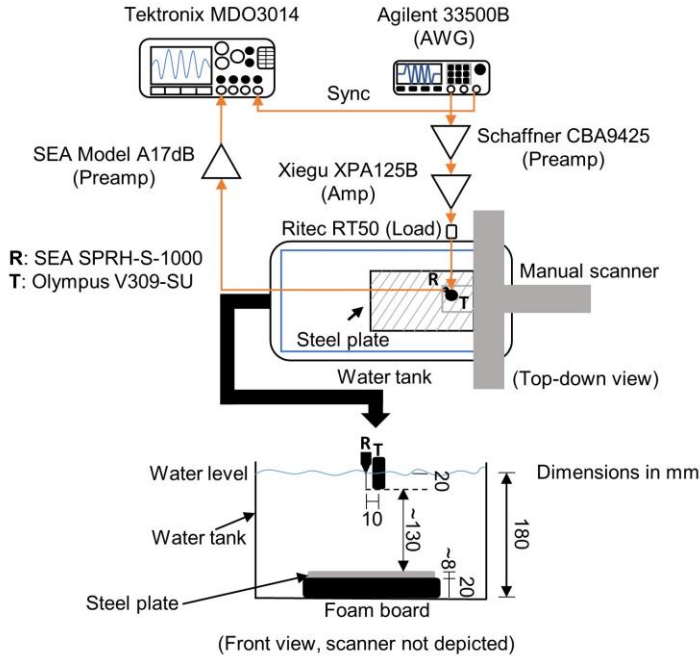
Figure 15. Setup for pitch-catch measurements of the SHG. Figure from (Nilsson et al., 2023a)

The resulting frequency spectra for measurements at points #4 (a), #11 (b), and #12 (c) are shown in Figure 16. It is very clear that attenuation increases with corrosion severity, an expected result considering attenuation measurements are often used to evaluate corrosion in conventional testing. However, although the SCOR measurement exhibits the strongest level of attenuation, its second harmonic is on a comparable level to COR. This result shows that nonlinearity cannot be estimated by the magnitude of the nonlinear components alone. The magnitude of the probing component must be considered as well.

To check if spurious effects are present, and to obtain β' averaged over several excitation levels, the magnitudes of the second harmonic are plotted against the fundamental magnitude squared in Figure 17. Regression lines are fitted to the data points and the slope of the respective lines gives an average of the β'. This is highlighted by the equations in Figure 17. The y-intercept in the linear functions is on a similar level and a low order of magnitude, indicating that there is only a weak offset in the nonlinearity. Ideally, the intercept should be 0 to fit Eq. (2.2). Regardless, it is clear that #12, i.e., the shell corrosion product, exhibits the strongest level of nonlinearity. This is even more clear when plotting the distribution of the average β'-values for all measurement points, which is shown in Figure 18 where points #4, #11, and #12 are highlighted in green. The shell-corroded region exhibits significantly elevated levels of nonlinearity compared to the other points. Moreover, it is not possible to distinguish the uniformly corroded region from the region with

55

no corrosion by looking at nonlinearity alone. This indicates that SHG might only be able to detect severe corrosion.
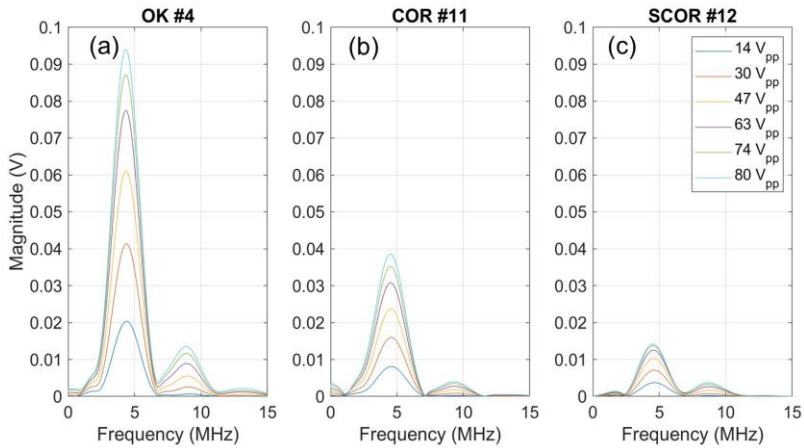

Figure 16. Frequency spectrum of the received signals for measurement points (a) #4, (b) #11, and (c) #12. Figure from (Nilsson et al., 2023a).
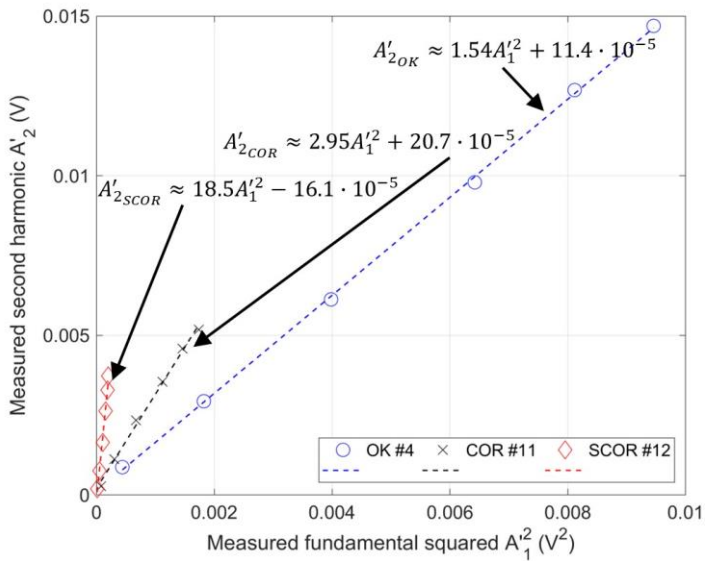

Figure 17. Magnitudes of the second harmonic plotted versus the fundamental magnitude squared. Dashed lines are regression lines given by the equations in the figure. Figure from (Nilsson et al., 2023a).
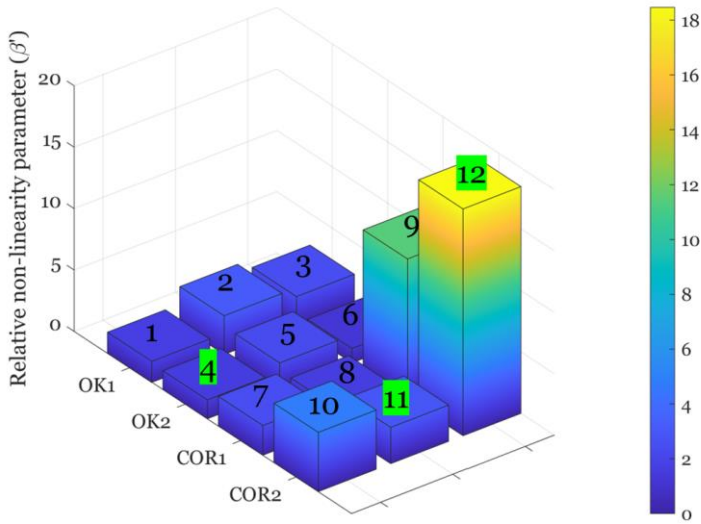
Figure 18. Distribution of β' over the 12 measurement points in Figure 14.

4.1.2. Sideband peak count for corrosion detection

A schematic for the through-transmission SPC measurements is shown in Figure 19. The same transmitter used in the SHG measurements is used here and is coupled to the plate by an aqueous ultrasonic gel. The receiver was a magnetic contact transducer with a nominal frequency of 5 MHz coupled to the plate using the ultrasonic gel and by magnetic contact. A Hanning-windowed 4-cycle sinusoidal tone burst at 4.5 MHz was used as the excitation signal. The SPC measurements were only conducted at measurement points #4, #11, and #12 on the plate shown in Figure 14.
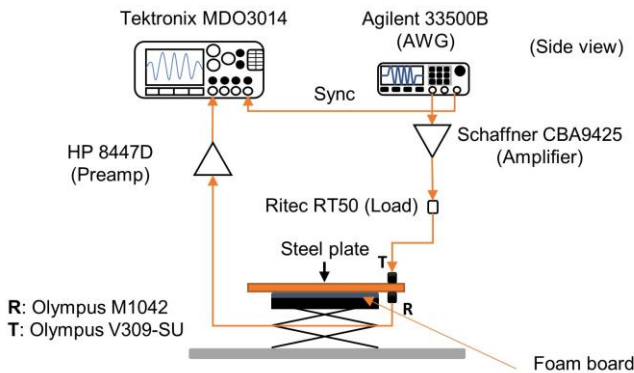

Figure 19. Schematic of the SPC-measurements. From (Nilsson et al., 2023a).

The resulting spectra that are shown in Figure 20 were normalized with respect to each respective maximum magnitude to enable a comparison of relative energy transfer. The maximum threshold for SPC evaluation was set to 6% of the maximum magnitude, i.e. 0.06 as this was the level of the weakest dominant peak. The threshold was varied with increments of 0.5%. The SPC was determined by recording the number of peaks whose magnitudes were greater than the noise level but weaker than the maximum threshold. The SPC was then normalized with respect to the number of sidebands for the reference region, i.e., the measurement at OK #4. That means that N_{tot} in Eq. (2.5) was equal for all measurements. The SPC as a function of the threshold value is plotted in Figure 21 (a). Observe that the SPC at SCOR is initially almost double compared to OK. The measurement at COR exhibits slightly fewer peaks, but comparatively higher magnitude than OK, which is observed because of the lack of a sharp drop at the second threshold level. At higher thresholds, the SPC for COR and SCOR are very similar, indicating that many of the intermodulation sidebands for SCOR are quite weak but numerous.
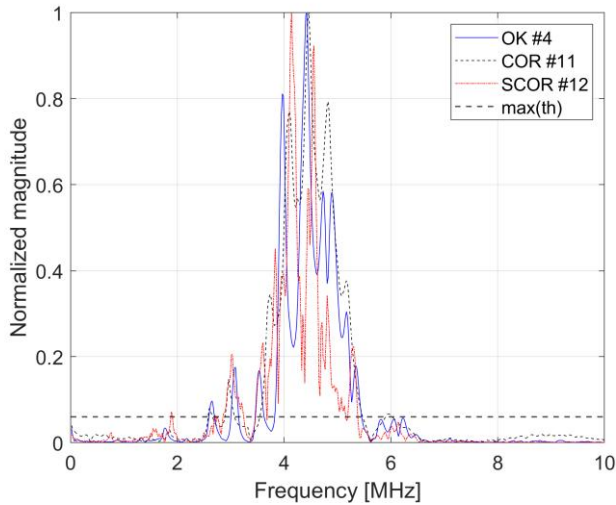

Figure 20. Normalized frequency spectra for the SPC measurements. From (Nilsson et al., 2023a).

In addition to studying the number of sidebands via the SPC index, it is interesting to look at the energy distribution in the sidebands in relation to the dominant peaks. This is because, indeed, the number of sidebands is expected to grow with increasing nonlinearity, however, the bandwidth of transducers is limited. With increasing nonlinearity, it is also expected that more energy is transferred onto these nonlinearly generated components, which is what most modulation indices evaluate. The sum of the sidebands over the sum of the dominant peaks gives α in accordance with Eq. (2.6). The α plotted in Figure 21 (b) were normalized with respect to the maximum value for OK. It is observed that SCOR exhibited more than double to

comparative energy transfer than OK, and COR was slightly greater than OK. Compared to the SPC, α indicated much stronger nonlinearity for SCOR for most of the threshold range. This suggests that this index may be more suitable for evaluation than SPC and the results follow those from the SHG analysis. Namely, the methods may only be suitable for severe corrosion detection as there is no large difference between OK and COR.
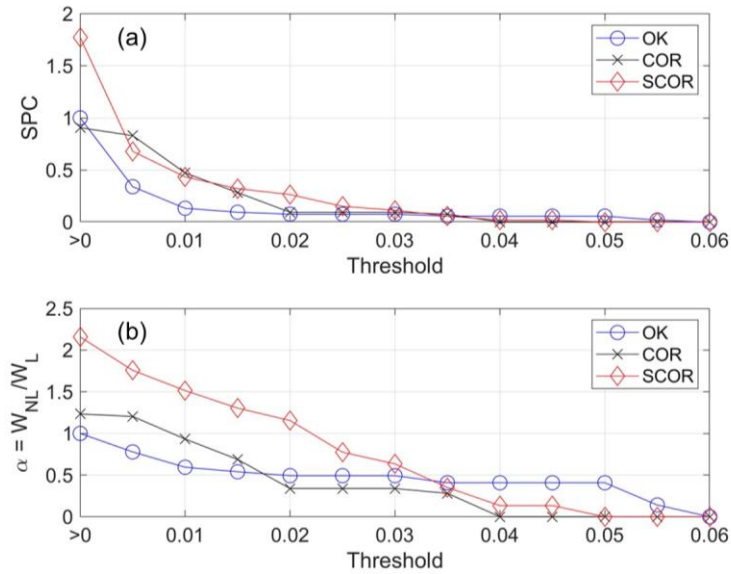

Figure 21. Normalized SPC and the energy distribution parameter α. From (Nilsson et al., 2023a).

4.2. Assessing concrete-embedded steel plates subjected to weakly accelerated corrosion

Steel plates that corrode while being embedded in concrete are suspected to affect the contact interface and possibly the concrete surrounding the plates due to the volumetric expansion of corrosion products and chemical reactions in the interface. If the contact interface is challenged and complex contact mechanics become dominant, then nonlinear ultrasonics can be a suitable contender to evaluate the conditions of the embedded steel plates.

A list of the specimens that were examined can be found in Table 2 along with the estimated surface coverage of the resulting corrosion. The specimens were cured for 8 weeks before they were stored under constant climatic conditions of 20° C and 65% RH for approximately two years. During this period, the specimens were subjected to periodic wetting and drying to facilitate accelerated corrosion. An in-depth description of the manufacturing, electrochemical methods, and corrosion characterisation is presented in (Huttunen-Saarivirta et al., 2023) whereas Paper II (Nilsson et al., 2023b) reports on ultrasonic NDE of the specimens and is summarized here.

Table 2. List of specimens.

Specimen	Variable	Conditions	Corrosion (% of total surface)
R	Reference	Normal concrete	0.12
RC	R. with chlorides	Concrete inlay with added chlorides	0.51
PH	Concrete pH	Carbonated concrete inlay	0.82
PHI	Concrete pH, electrochemical acceleration	Carbonated concrete inlay, impressed current	**51.4**
PHCl	Concrete pH, chlorides, electrochemical acceleration	Carbonated concrete inlay with added chlorides, impressed current	**76.9**
WC	Embedded wood, chlorides	Piece of wood soaked in chloride-rich solution	3.1
D	Delamination in steel-concrete interface	Delamination gap formed between the concrete inlay and steel plate	0.08
DC	Delamination, chlorides	Delamination inlay with added chlorides.	0.59

Continuous ultrasound was emitted and sensed diagonally across the concrete inlays, and the specimen was impacted at two locations to introduce low-frequency perturbations, see Figure 22. This facilitated the evaluation of higher harmonics

(Chapter 2.1), modulation spectroscopy (Chapter 2.2.1), and instantaneous modulation characteristics (Chapter 2.2.3) from a single measurement.
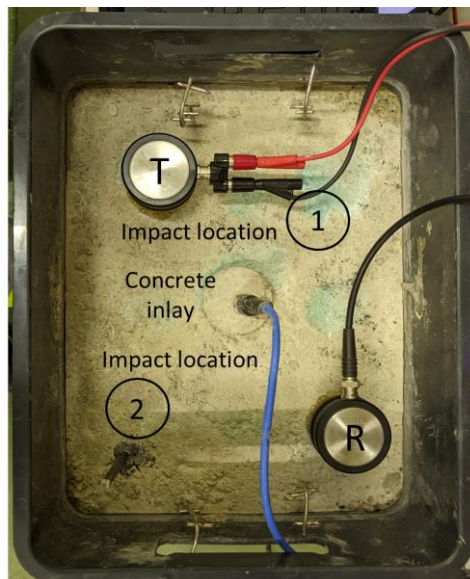

Figure 22. View of the transmitter (T) and receiver (R) placement on the specimens. Figure from (Nilsson et al., 2023b).

Results for the higher harmonic analysis can be viewed in Figure 23. These results indicate the strongest nonlinear response for specimens PHCI, DC, and WC. Interestingly, neither DC nor WC exhibited pronounced corrosion, see Table 2. However, both DC and WC offer completely different contact interfaces than the remaining samples do. PHCI exhibits the strongest quadratic and cubic nonlinearity, which successfully indicates that this is the most severely corroded specimen. There are also slight variations in the parameter values between the two successive measurements, possibly indicating some nonequilibrium phenomena considering that the sensors were not reattached. PHI, the specimen which has the second highest corrosion extent, did not exhibit strong higher harmonic generation as it is on the same order as the reference specimen.

Proceeding with the modulation spectroscopy, the results of which are shown in Figure 24, where γ is a modulation index given by integrating the sidebands instead of summation. Additional information is provided in Paper II (Nilsson et al., 2023b). Interestingly, the spectroscopy results only indicate elevated levels for DC, and WC, however, also D when the impact was done at location 2. PHCI and PHI had similar parameter values as R. When compared to the corrosion extent presented in Table 2, the γ does not appear to correctly evaluate the corrosion condition.
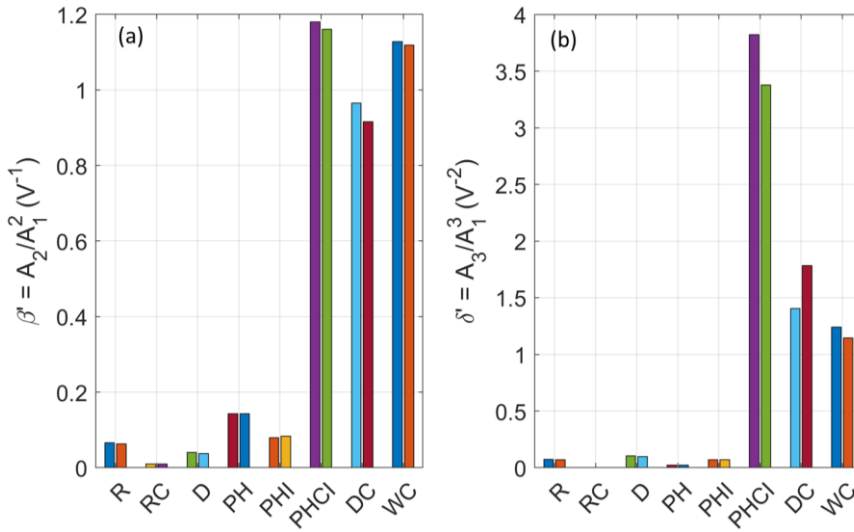
Figure 23. Results for the higher harmonic analysis. (a) Relative quadratic parameter. (b) Relative cubic parameter. Figure from (Nilsson et al., 2023b).
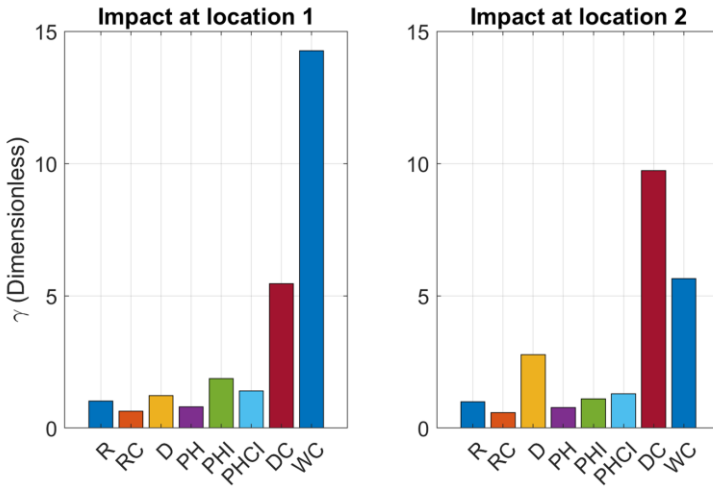

Figure 24. Results for the modulation spectroscopy using the integration modulation index, γ. Figure from (Nilsson et al., 2023b).

When studying the modulation from a different perspective, namely by using the HHT to examine the instantaneous modulation characteristics (see Chapters 2.2.3 and 3.6.2), we obtained very interesting results. Figure 25 shows the damage indices for amplitude (a – b) and frequency modulation (c – d), respectively. The trends for amplitude modulation appear very similar to the γ-results in Figure 24. However, the corresponding damage index for frequency modulation indicates a strong

nonlinear response for PHI, PHCI, DC, and WC, at location 1, and a particularly elevated response for D when impacted at location 2. This indicates that isolated frequency modulation appears sensitive to changes to the contact mechanics due to delamination, the presence of foreign matter, and corrosion. This is a promising result for corrosion evaluation when compared to the other indices that were studied from the same measurement.
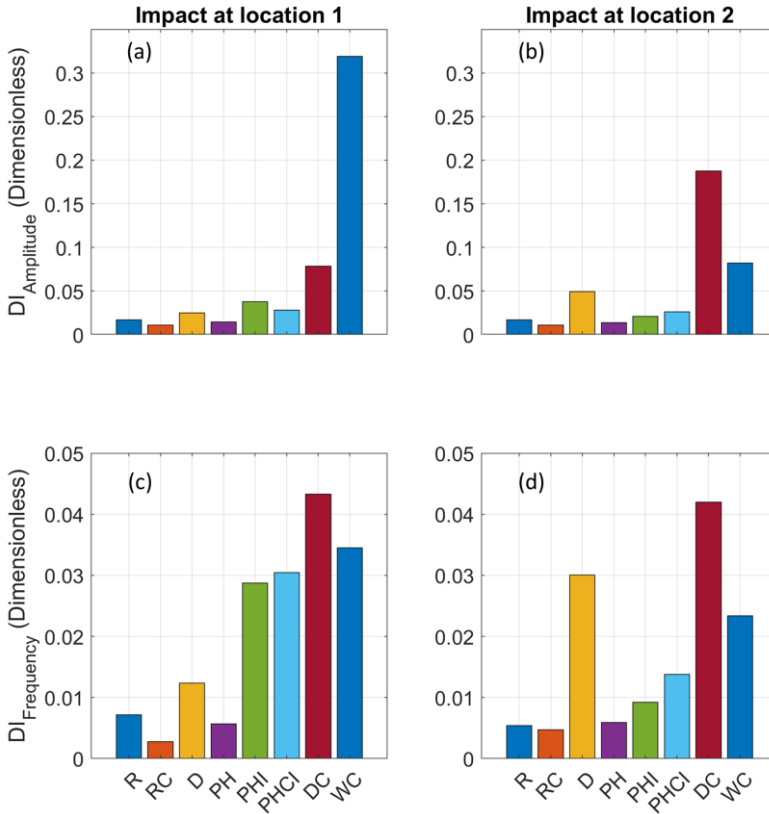

Figure 25. Damage indices based on instantaneous amplitude (a – b), and instantaneous frequency (c – d). Figure from (Nilsson et al., 2023b).

Analysing each index individually is interesting as it enables the evaluation of the defect contribution to each phenomenon. However, when evaluating the condition, it is advantageous to integrate the data into a single comprehensive index, such as the TDI (see Chapter 3.6.3). The TDI which combines the results from both impact locations can be studied in Figure 26. There is no new trend to the results as PHCI, DC, and WC stand out among the inspected samples. Although it is interesting to observe that D and PHI exhibit comparable levels of TDI as D has no corrosion (0.08% surface coverage) but PHI has over 50% surface coverage. Once again, this illustrates how sensitive these methods are for changes to the contact interface

between two solids. The TDI offers a comprehensive metric for the evaluation and presentation of the condition of the specimens and structures that have been investigated.
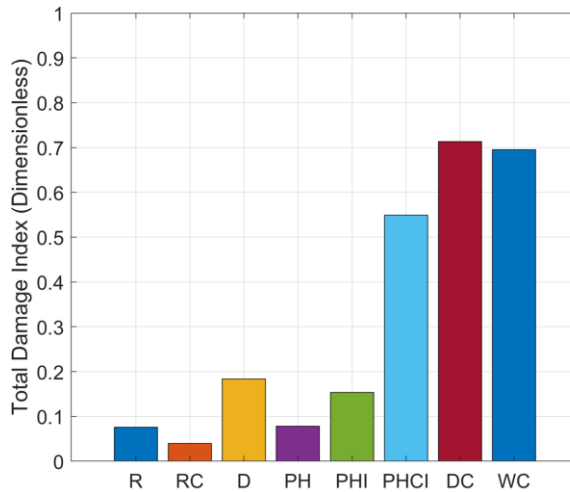

Figure 26. Levels of TDI within the specimen population.

The results from this novel investigation indicate the potential of utilizing several modalities of nonlinear evaluation from a single measurement and raise the question if frequency modulation is particularly sensitive to corrosion-related defects.

4.3. Evaluation of pre-corroded steel plates embedded in concrete using modulation techniques

Nonclassical nonlinear ultrasonic methods for NDE have been claimed to be remarkably sensitive to crack-like defects (Rudenko, 2006), which severe corrosion products have been shown to contain. One such method discussed in Chapter 2.2.4 is cross-modulation. Additionally, previous experiments indicated the promising potential of isolating frequency modulation using the HHT to detect corrosion-related defects (Nilsson et al., 2023b). Therefore, assessing the applicability of the cross-modulation method and verifying if isolating frequency modulation for corrosion detection is as sensitive as previous work indicated are of interest. Furthermore, it is also important to understand the capabilities of detecting the mere presence of corrosion products embedded in concrete. This can be achieved by embedding steel plates that were corroded before being embedded. That way, the corrosion should not affect the surrounding concrete, and it is mostly the effects of the corrosion itself that are probed. This motivation led to the experiments reported in Paper III, which are summarized below: details can be found in the manuscript (Nilsson et al., 2024a).

Five cylindrical specimens were manufactured, four of which contained steel plates and corrosion product discs with a diameter of 90 mm, seen in Figure 27, while the fifth only contained concrete. The discs were a pristine steel plate (OK), uniformly corroded (COR), uniformly corroded with shell corrosion (SCOR), and the shell corrosion only (Shell). Unfortunately, the Shell disc disintegrated during casting which was evidenced when pouring the concrete. The steel plates were centred and held in place by a steel mesh and a silicone adhesive, this can be viewed in Figure 28 (a – b). After curing for 4 weeks, the ends were sawed off to create smooth surfaces and a precise length of 200 mm, the diameter of the concrete was 100 mm.
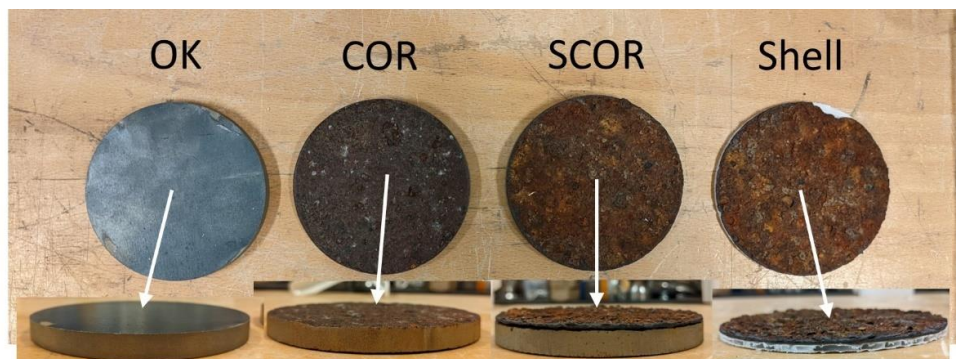

Figure 27. Steel plate discs to be embedded in concrete. Figure from (Nilsson et al., 2024a).

Figure 28. Cylindrical specimens. (a – b) Steel mesh and centred plate. (c) Specimen after casting. (d) Specimen after curing. Figure from (Nilsson et al., 2024a).

The specimen containing only concrete, the reference (OK) and uniform with shell corrosion (SCOR) were X-rayed to investigate if any significant cracking had occurred in the concrete. It was observed that only specimen OK contained cracks, these are shown in an X-ray slice close to the edge of the specimen (Figure 29). The zig-zag pattern observed in the figure is simply the steel mesh.
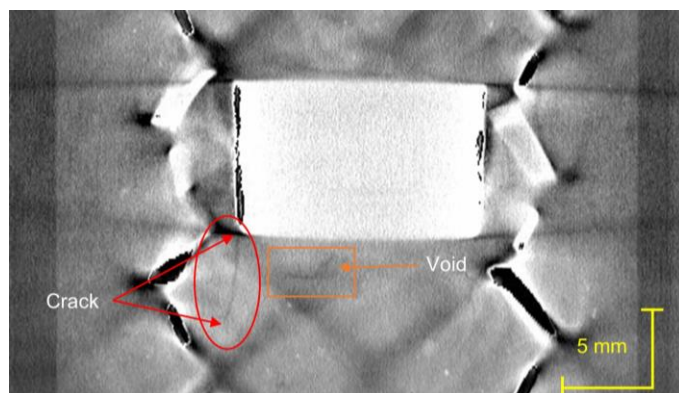
Figure 29. X-ray slice revealed cracks near the OK plate. Observe that the slice is close to the edge of the specimen. Figure from (Nilsson et al., 2024a).

Schematics of the experimental setups for the nonclassical cross-modulation measurements and for the instantaneous modulation characteristics can be seen in Figure 30 (a) and (b), respectively. The ultrasonic probing wave was a continuous sinusoid at a frequency (F_{probe}) of 52380 Hz for both measurements. The modulator for the nonclassical measurements was a continuous amplitude-modulated sinusoid

with a carrier frequency of 178 kHz and a modulation frequency (F_{mod}) of 100 Hz. The modulation depth was set to full modulation, i.e., 100%. The modulator in the second experiment was an instrumented hammer to facilitate broadband modulation.
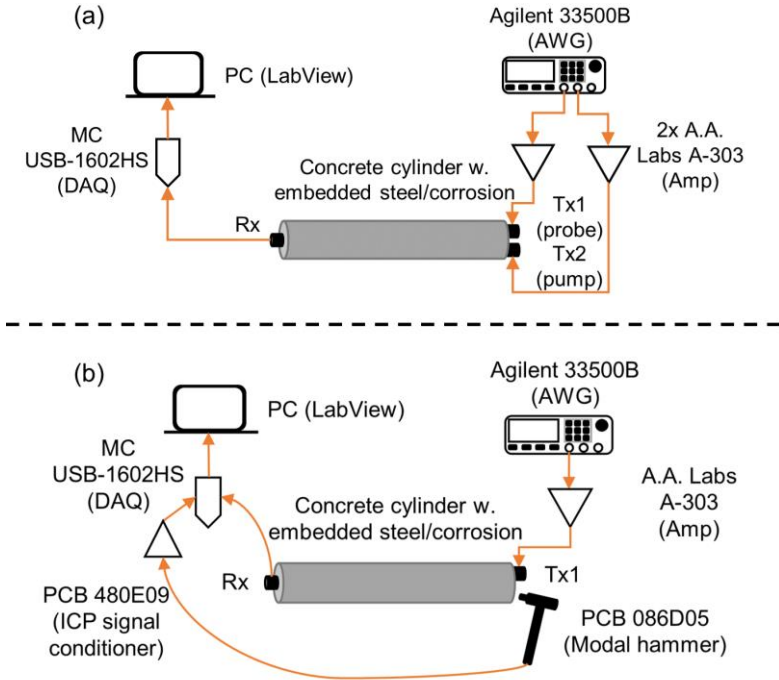
Figure 30. Experimental setup for the (a) cross-modulation measurements, and (b) for the evaluation of instantaneous modulation. Figure adopted from (Nilsson et al., 2024a).

4.3.1. Nonclassical cross-modulation results

The spectra resulting from the cross-modulation measurements can be viewed in Figure 31. Observe that the plot is focused on the probing frequency. It is immediately observed that all specimens generate a first-order cross-modulation frequency at $F_{probe} \pm F_{mod}$, whereas only SCOR generates second-order modulation ($\pm 2F_{mod}$). This, along with the observation that SCOR also has the strongest first-order modulation components indicates that SCOR exhibits the strongest level of nonclassical nonlinearity out of the examined specimens. To quantify the modulation intensity, the modulation index is determined by the sum of the magnitudes of the modulation components taken over the probing component. The results are shown in Figure 32 which confirms the observation made from the spectrum regarding SCOR exhibiting the strongest nonlinearity. However, the modulation index indicates that OK also exhibits very strong nonclassical

nonlinearity. It is suspected that the cracks that were revealed by X-ray tomography (see Figure 29) are the culprit behind this effect, indicating that cross-modulation may not be optimal for the evaluation of embedded components, but rather efficient at detecting concrete cracking overall. This is something that can be investigated further within the scope of concrete evaluation.
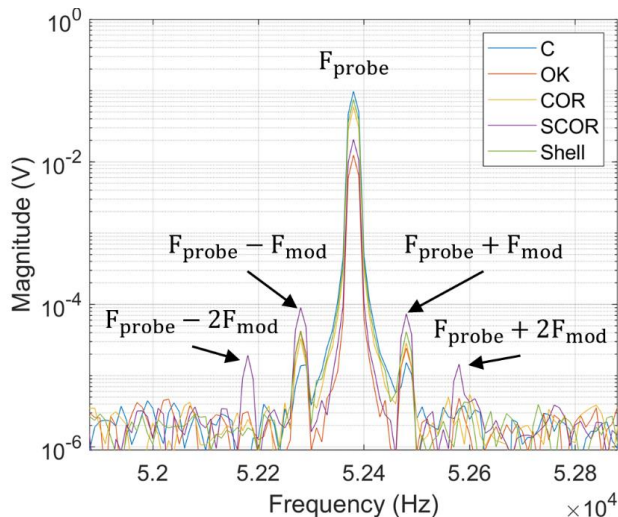

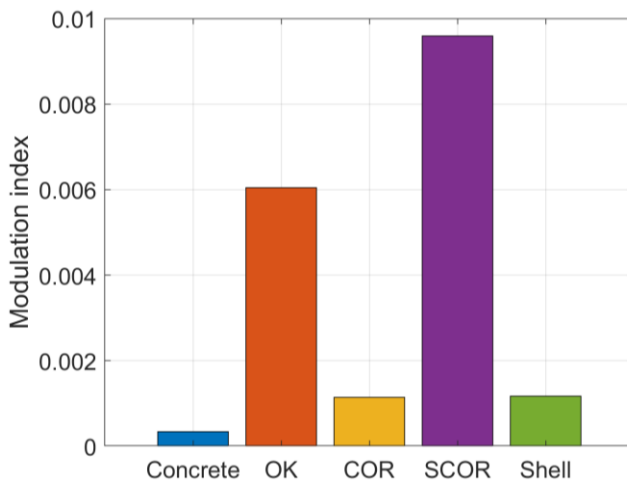**Figure 31.** Spectrum zoomed in in at the probing frequency. Figure from (Nilsson et al., 2024a).

Figure 32. Cross-modulation index considering only the probing magnitude as the denominator. Figure from (Nilsson et al., 2024a).

4.3.2. Corrosion assessment using instantaneous modulation

The extraction of instantaneous modulation characteristics by employing the HHT (covered in Chapter 3.6.2) resulted in the damage indices (explained in Chapter 2.2.3) plotted in Figure 33, where (a) shows the index for amplitude modulation, and (b) shows the corresponding index for frequency modulation. Amplitude modulation directly indicates strong nonlinearity for SCOR. Interestingly though, OK appears to be modulated much weaker than SCOR, even though the nonclassical cross-modulation reported in the previous section indicated strong nonlinearity. Granted, OK appears more nonlinear than COR and Shell, albeit by a small margin. Looking at the maximum impact force recorded for each measurement (Figure 34) we see that this might partly be explained by the impact force being slightly higher for OK compared to COR.

When studying the damage index for frequency modulation, we once again observe strong indication for SCOR. However, the remaining specimens that contain corrosion, i.e., COR and Shell, does not exhibit strong nonlinearity. Observe that since the corroded plates are embedded post-corrosion the concrete should be unaffected. This result indicates that the findings in Paper II indicating that frequency modulation is particularly sensitive to corrosion-related defects perhaps is only valid when the steel-concrete interface is affected by the corrosion.

The nonlinear response for OK in terms of frequency modulation follows the same trend as the amplitude modulation. This result highlights the difficulties of inspecting concrete-embedded members using nonlinear ultrasonics as cracks due to concrete curing or aging may affect the measurements greatly. It is therefore clear that the instantaneous modulation method needs additional verification before its ultimate sensitivity to concrete-embedded corrosion can be determined.
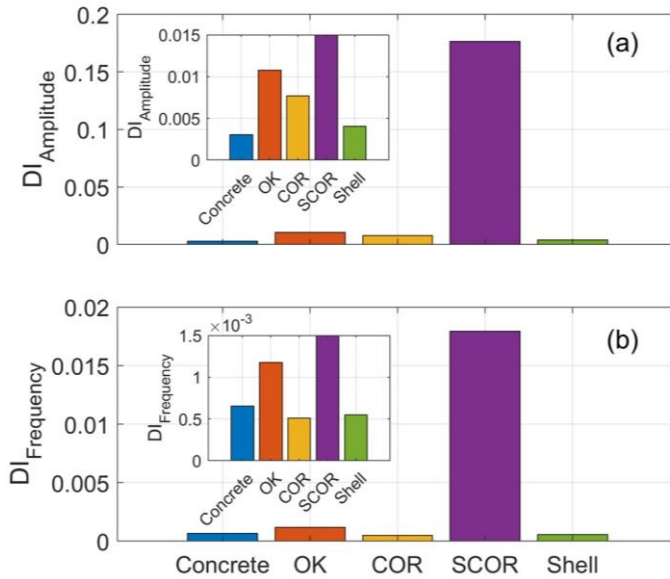
Figure 33. Damage indices for amplitude (top) and frequency modulation (bottom). Figure from (Nilsson et al., 2024a).
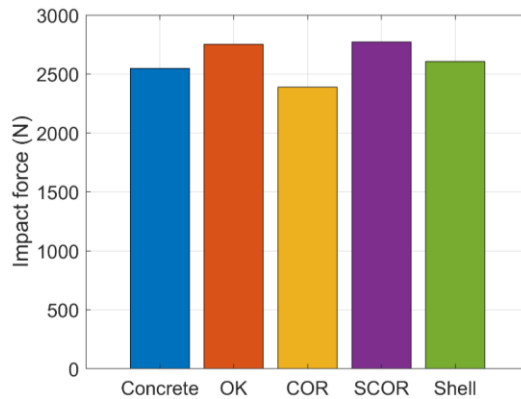
Figure 34. Peak impact force. Figure from (Nilsson et al., 2024a)**.**

4.4. Linear and nonlinear ultrasonic imaging of concrete-embedded corroded steel liners

Previous work has indicated that severe corrosion regardless of its state of embedment induces elevated levels of waveform distortion compared to non-corroded regions. To build upon the work presented in Paper I (Nilsson et al., 2023a), the work reported in Paper IV aimed to investigate the feasibility of using ultrasonic imaging to detect corrosion when covered by a ~40 cm concrete cover. This work is briefly summarized below, and additional details are provided in the paper.

The specimen that was examined was a concrete slab measuring 1100x710x420 mm (~790 kg) contained within a heavy-duty plastic container capable of withstanding a maximum load of 4300 kg, see Figure 35. Three steel plates were placed on the bottom of the plastic tub as seen in Figure 35 (a). The plates were one reference plate with no corrosion, one uniformly corroded with shell corrosion, and a uniformly corroded plate, see Figure 36. After the concrete had cured, the surface was ground to achieve a comparatively smooth surface, which can be viewed in Figure 35 (b). The bottom of the plastic container is shown in Figure 35 (c) where no buckling can be visually evidenced. This ensures that the back wall is horizontal, and that no anomalous behaviour of the backscattered signals is to be expected.

Figure 35. Concrete slab specimen. (a) Heavy-duty plastic container before casting. (b) Slab after curing and surface removal. (c) Reinforced bottom showing no signs of buckling. Figure from (Nilsson et al., 2024b).
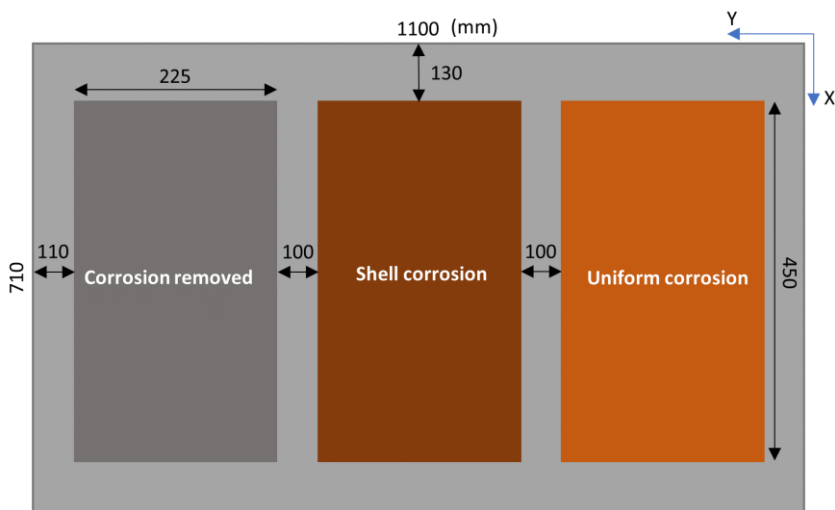
Figure 36. Schematic of the placement of the embedded liners. Figure from (Nilsson et al., 2024b).

Three types of measurements were conducted within the scope of this subproject: fine-grid scanning using longitudinal (P-waves), and horizontally polarized shear waves (SH-waves) with the LTH scanner; and the application of the ACS1040 MIRA ultrasonic tomographer which utilizes Synthetic Aperture Focusing Technique (SAFT). The MIRA ultrasonic tomographer was supplied by Allan Lion Kristensen and Mette Steinlein Christensen from FORCE Technology for the duration of the subproject, to whom I express sincere gratitude. The core of the analysis is performed by studying *C-scans*, i.e., the top view of slices of data at a certain instance in time corresponding to a certain depth within the specimen. Essentially an ultrasonic analogue of a slice of cheese.

The experimental specifics are listed in Chapters 4.4.1 and 4.4.2 for the fine scanning and for the measurements utilizing the ultrasonic tomographer with the built-in SAFT, respectively.

4.4.1. Fine-grid measurements using the LTH Scanner

The LTH scanner uses two servo motors that facilitate translation in local X- and Y-axes that are illustrated in Figure 36. Movement is enabled via two sets of wheels (Y), a linear arm (X), and a pneumatic cylinder which facilitates vertical (Z) movement of the mounted probe(s). The LTH scanner can be viewed in Figure 37. The scanner allows computerized scanning and precise control of the probe placement which eliminates operator dependency. The measurement grid was 98x62 cm with each measurement spaced 1 cm apart on both axes. This resulted in a total of 6076 measurement points within the grid.

72

Figure 37. LTH Scanner in action. Figure from (Nilsson et al., 2024b).

The measurements utilized ultrasonic antennae with 4x6 spring-loaded DPC transducers, see Figure 38. The antennae were of a fixed dual aperture array type, meaning that half of the array (4x3) transmitted ultrasound whereas the other half received it. Switching between the apertures can only be done by switching cables, hence a *fixed* dual aperture. Two types of these antennae were used, one that transmits and receives P-waves (ACS M2503), and the other SH-waves (ACS M2502). The specified nominal frequencies were 100 kHz for the P-wave array and 50 kHz for the corresponding SH antenna. However, the SH-wave array generated the strongest response at 40 kHz, and the P-wave array at 80 kHz which were selected as the excitation frequencies. This means that the wavelengths are on the order of 5 cm. The waveform was a sinusoidal tone burst with 5 cycles. The excitations were amplified by a gated amplifier (RITEC GA-2500) to a level of approximately 550 V_{p-p} for the SH-waves, and 700 V_{p-p} for the P-wave measurements. The received signals were band-pass filtered and pre-amplified by a Krohn-Hite 3905B programmable filter. The cutoff frequencies were 20 kHz and 150 kHz for the SH-wave measurements, and 60 kHz and 300 kHz for the P-wave measurements. The filter steepness was 48 dB/octave.
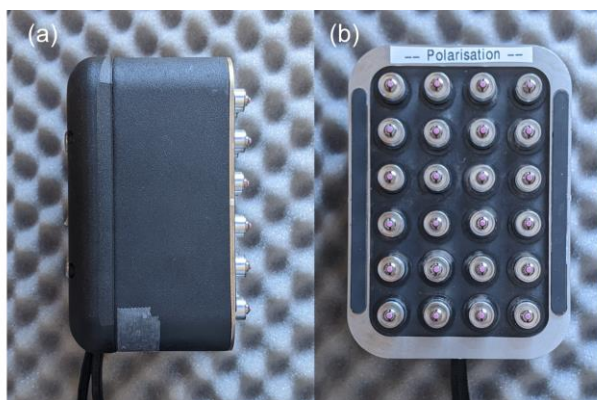
Figure 38. Fixed dual aperture array with 4x12 spring-loaded DPC transducers.

The C-scans that correspond to the maximum envelope magnitude of the first echo from the backwall can be seen in Figure 39 where the dashed rectangles show the approximate location of the embedded plates. The results for the SH-wave measurements in (a) clearly indicate the locations of the uniformly corroded plate (top) and the plate from which corrosion was mechanically removed (bottom). The middle plate is not resolved as clearly and appears to have a ridge-like structure along its centre. As the middle plate does not have a pronounced ridge, this result is believed to indicate that the corrosion product is delaminated along the edges of the plate, whereas the middle part is in contact. Without knowledge of the plate, this would be difficult to assess, but it is clear that some anomaly is present. When studying the corresponding P-wave C-scan (b) there is only some indication for the top plate. It appears as if the P-wave measurement mostly reflects the conditions of the back wall rather than the plates, whereas the SH-wave measurements reflect the condition of the plate surfaces. This result is very interesting due to the similar wavelength of the wave types, which suggests that the SH-waves are significantly more sensitive to the condition of reflectors perpendicular to their incidence compared to P-waves. At least when assessing surface conditions of the reflectors, such as corrosion, using normal incidence.

Figure 39. Envelope C-scans for SH-wave (a) and P-wave (b) measurements. Dashed rectangles show the approximate location of the embedded steel plates. Figure from (Nilsson et al., 2024b).

By performing a nonlinear evaluation of the signals corresponding to the echoes in Figure 39, some additional information can be extracted. In Figure 40, C-scans of the parameter of nonlinearity based on the second harmonic are shown. The results appear as if they are the inverse of th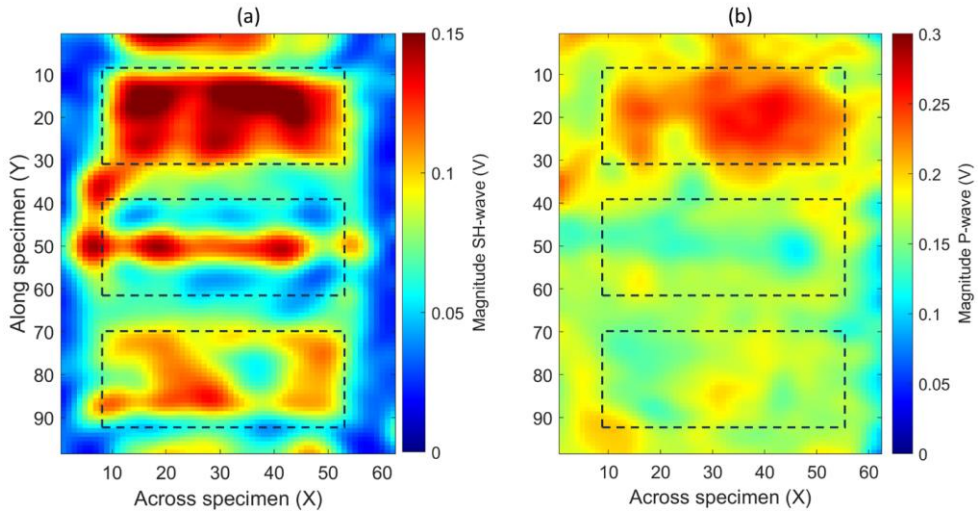e C-scans in Figure 39, which is true to a certain extent as the fundamental component is squared in the denominator for β' (see Eq. (2.2)). What we observe in Figure 40 (a) is that the shell-corroded plate appears to distort the SH-waves, in particular along its edges. This strengthens the hypothesis of delamination along its edges. Delaminations are known to exhibit strong nonlinearity, particularly partial delaminations. There also appears to be strong distortion along the boundaries of the specimen, likely due to geometrical effects. There are no indications of elevated nonlinearity when studying the P-wave nonlinearity which indicates that it is indeed the back wall of the plastic container, essentially air because the plastic is even thinner than the plates, that is assessed.

Waveform distortion can manifest in many different ways. In addition to higher harmonics, intermodulation may occur. This can be studied via the SPI (see Eq. (2.7)). SPI C-scans are shown in Figure 41 and they show quite similar patterns as the β' C-scans in Figure 40. The SH-wave SPI exhibits a stronger response at the bottom plate from which corrosion was mechanically removed. It is possible that certain pitting in the plate was not removed which causes elevated levels of waveform distortion. Regardless, it is evident that the shell-corroded plate once again exhibits the strongest levels of waveform distortion along with the boundaries. The P-wave SPI still does not show any clear pattern that can be attributed to the embedded plates. It is therefore challenging to draw any conclusions from those results.
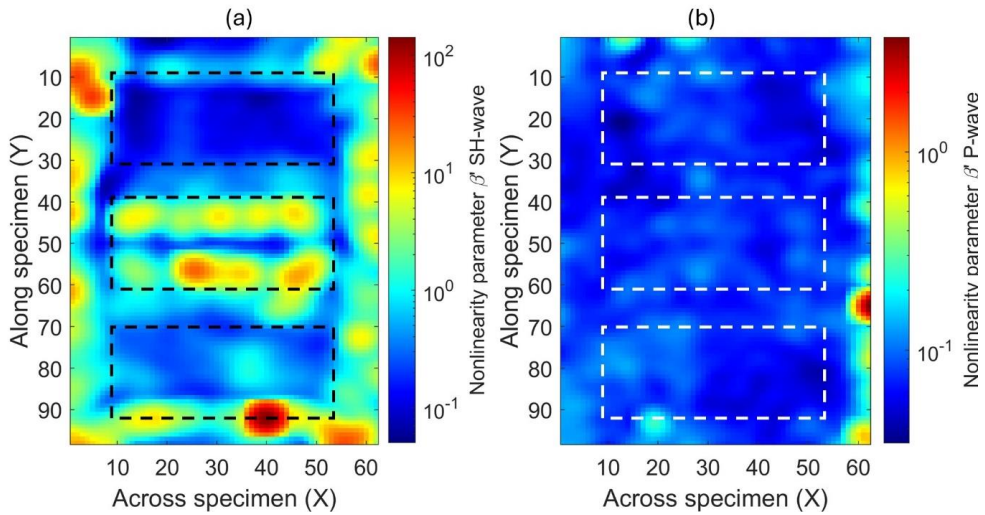
Figure 40. Nonlinearity C-scan based on β' for SH (a) and P-wave measurements (b). Figure from (Nilsson et al., 2024b).
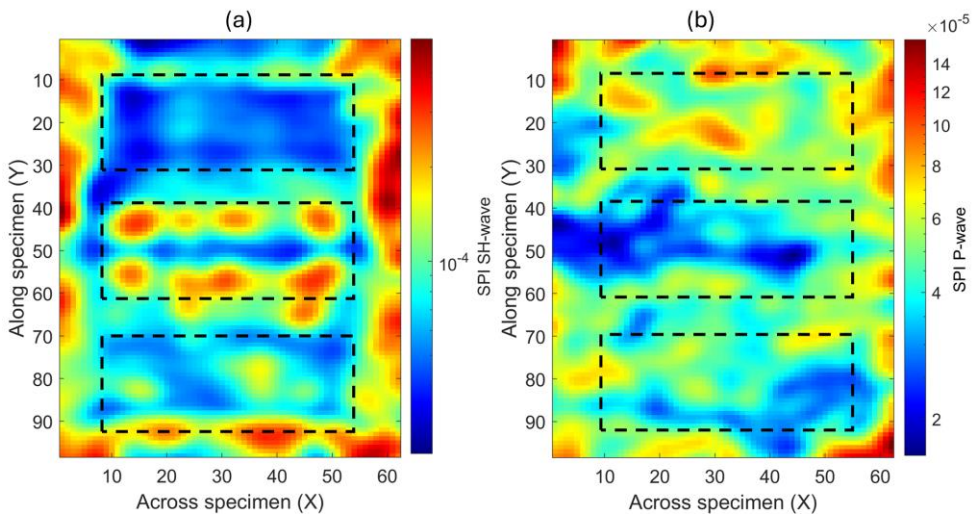
Figure 41. SPI C-scans for (a) SH-wave and (b) P-wave measurements.

To emphasize the fact that nonlinear evaluation should be performed together with conventional linear analysis we can combine the results into a TDI (see Chapter 3.6.3) C-scan for each wave type. This is viewed in Figure 42 where the responses for each index, i.e. envelope magnitude, β', and SPI were normalized and summed to create a TDI from 0 to 3. In Figure 42 (a) we can see that the TDI for the SH-wave measurements indicate that the presence of the uniformly corroded plate induces an intermediate-level response, and the bottom plate has very little response apart from a very strong anomaly near its edge. The shell-corroded plate clearly

creates a very strong response. Hence, by integrating the results into a single index we have achieved a classification of the corrosion severity of the embedded plates. However, the comparative P-wave measurements do not yield any conclusive evidence of plate location or condition. These results highlight to the highest degree that SH-waves are much more sensitive to corrosion-related degradation for reflectors that are oriented perpendicular to its incidence compared to P-waves of similar wavelength.
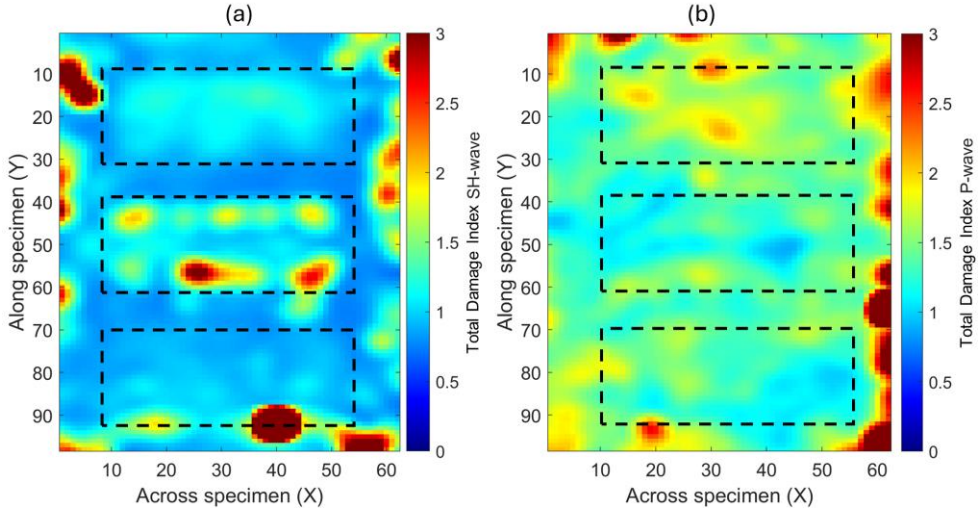
Figure 42. Combined response. (a) SH-wave and (b) P-wave.

4.4.2. Ultrasonic tomography with ACS 1040 MIRA

The ACS 1040 MIRA (2nd gen) system has 4x12 spring-loaded DPC transducers that emit and sense SH-waves. The MIRA (Spanish for 'look') device has a set of 48 spring-loaded DPC transducers with a specified nominal frequency of 50 kHz arranged in 4 rows and 12 columns (see Figure 43 (b)) acting in a pitch-catch fashion. The transducers in the MIRA are of the same type as those used in the M2502 antenna. The MIRA device uses a linear array firing sequence which operates by having one column transmit while the others listen. This results in a total of 66 signal combinations used in the 2D SAFT-C algorithm implemented in the device. In-depth discussions of SAFT are beyond the scope of this thesis. However, the interested reader is referred to the doctoral thesis by (Lingvall, 2004) for time-domain SAFT and the thesis by (Skjelvareid, 2012) for frequency-domain SAFT.

The measurement grid used is shown in Figure 44. This grid is significantly sparser than the scanner grid presented in Chapter 4.4.1 as we used 10 cm (compared to 1

cm) steps in X and Y, here with a total of 4 steps in X and 11 in Y. This equals a total of 2904 measurements for the MIRA. The post-processing is conducted in a software called IDealViewer which stitches the individual B-scans by interpolation into a volume from which C-scans can be extracted. The entire scan was conducted in approximately 10 minutes using MIRA. The system excites the transducers with a low-frequency pulse, specified to 40 kHz for the measurements conducted here.

Figure 43. Ultrasonic tomographer ACS 1040 MIRA (2nd gen). (a) Operator view, (b) bottom view showing the 48 spring-loaded DPC transducers.

The SAFT-C C-scan is shown in Figure 45 where the displayed result lacks the separation between plate and non-plate regions that were shown in Figure 39 (a) for the SH scan results. This is likely due to two reasons: 1) the grid for the MIRA measurements was significantly sparser than the scanner measurements, however, the MIRA utilizes 48 transducers, each individually acting as transmitter/receiver. This higher number, in contrast to the 12 transducers for transmitting and receiving for the dual aperture arrays gives significantly better coverage per measurement. Another advantage of the MIRA is its internal optimized signal processing and 2D SAFT-C algorithm which should indeed contribute to increased measurement quality and resolution. 2) the process of stitching B-scans in the IDealViewer software to acquire the C-scan uses interpolation which causes the observed smearing effect. As a result of this effect, it is challenging to ascertain the exact location of the plates from the tomogram in Figure 45 alone.

Figure 44. Measurement grid for the MIRA.

A noticeable difference is observed between the middle of the C-scan and its top and bottom parts, suggesting the presence of some anomaly. This agrees with the observations from the LTH Scanner measurements. Considering the significant difference in inspection time between the automated scans (approximately 20 hours each) and the MIRA measurements (approximately 10 minutes), the MIRA results are indeed impressive and very similar to the SH C-scan. Newer generations of the MIRA system use Full Matrix Capture meaning that all possible element combinations in transmit-receive are utilized for subsequent reconstruction (Holmes et al., 2005). Advanced reconstruction algorithms including 3D SAFT (Dinh et al., 2021), and Total Focusing Method (Zhang et al., 2010) are implemented which indeed should improve its performance compared to earlier generations.
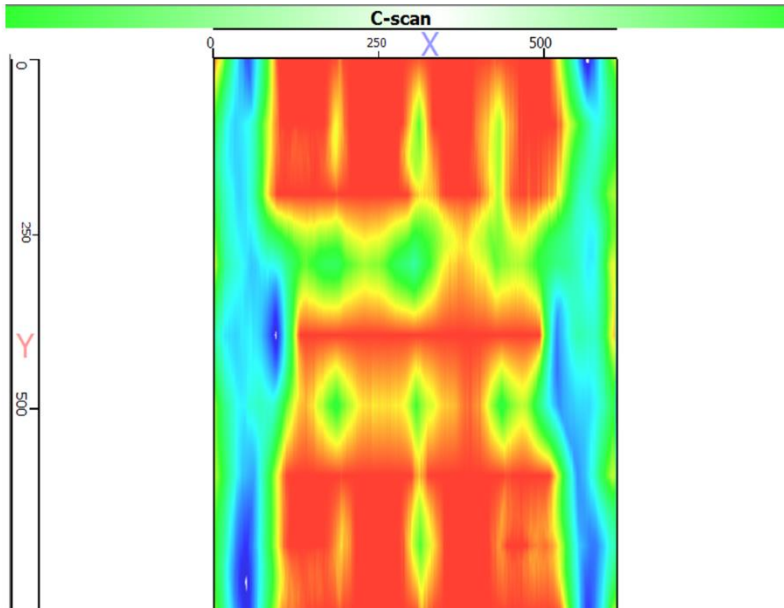
Figure 45. SAFT C-scan from IDealViewer.

5. Conclusions and future work

5.1. Main scientific contributions

This thesis synthesizes four novel studies on the detection of corrosion in concrete-embedded steel plates using nonlinear ultrasonic techniques. The research demonstrates the effectiveness of nonlinear ultrasound in detecting severe corrosion products with internal defects such as cracks and delaminations on their own (Paper I) and whilst being embedded in concrete (Paper III + Paper IV). The research also demonstrates the feasibility of evaluating corrosion, delamination in the steel-concrete interface, and the presence of foreign matter in concrete slabs with embedded steel liners (Paper II).

The studies have mainly examined three acoustic nonlinearity parameters; β', which is related to the second harmonic generation (Paper I+ Paper II+ Paper IV), sideband peak count and related indices (Paper I), and various modulation indices related to the magnitudes of the generated sidebands over the fundamental component (Paper II + Paper III). The work highlights the capability to indicate significant increases in nonlinearity in regions containing corroded steel liners, and defects related to corrosion such as delaminations and the presence of foreign matter. The novel investigations reported in Paper II, Paper III, and Paper IV show that although concrete is a highly heterogeneous material which exhibits strong intrinsic nonlinearity, corrosion and related defects induce comparatively stronger waveform distortion than areas and specimens with no corrosion do. This holds true for cases where the concrete was not affected by the corrosion, as shown in Paper III and Paper IV.

The study in Paper II is the first of its kind to report on the nonlinear ultrasonic evaluation of slowly accelerated corrosion of concrete-embedded steel liners. By combining higher-harmonic analysis, impact-based modulation spectroscopy, and the instantaneous modulation characteristics into a Total Damage Index (TDI), this approach provided a promising method of data fusion for classifying damage levels. High TDI values consistently indicated the presence of discontinuities such as foreign matter, delamination gaps, or severe corrosion. This lays a strong foundation for future studies on larger and more complex structures and suggests that data fusion of multiple methods may yield a more complete picture of the condition of the inspected structures.

In addition to the novel TDI, it was shown for the first time in Paper II that isolated frequency modulation, studied via the Hilbert-Huang transform, indicated very high sensitivity to corrosion-related defects. However, a second study in Paper III examined specimens containing pre-corroded steel plates and the results did not confirm the observations made in Paper II. In contrast, instantaneous frequency modulation appeared to be insensitive to corrosion when the concrete remains unaffected. The ultimate sensitivity to corrosion-related defect therefore remains unknown. However, the initial findings suggest that the method of instantaneous modulation analysis would be interesting to investigate further for more realistic conditions.

Nonclassical cross-modulation was investigated in Paper III as a means to evaluate concrete specimens with various corrosion conditions. Nonclassical nonlinearity typically only occurs for structural nonlinearity, i.e., cracks and contact-type defects. The results confirm this by showing that both corrosion and concrete cracking impact the monitored modulation index greatly, whereas intact concrete shows comparably weak nonclassical nonlinearity. However, the cross-modulation technique was less effective for uniformly corroded steel plates or thin shell corrosion, suggesting its optimal use for detecting more advanced stages of degradation and concrete cracking.

The use of horizontally polarized shear (SH) waves was reported in Paper IV. The results demonstrated that SH-waves are more suitable for ultrasonic inspection of concrete-embedded steel liners, particularly for detecting corrosion, compared to longitudinal (P) waves. SH-waves effectively located and facilitated dimensioning of the embedded plate-like structures in traditional envelope magnitude C-scans, unlike comparable P-waves. The study also for the first time explored second harmonic generation (SHG) for SH-waves for imaging purposes, revealing that contact-type defects might facilitate this phenomenon. Although conclusive evidence for SHG due to corrosion was not obtained, the parameter maps of nonlinearity accurately indicated the location of severely corroded plates. These findings suggest promising applications of SH-waves for detecting and localizing corrosion in concrete structures, with further research needed to refine the techniques and develop suitable instrumentation.

5.2.   Suggestions for future work

5.2.1. Evaluation of realistic structures

The research conducted within the scope of this thesis has highlighted the potential use of nonlinear ultrasonics for evaluating corrosion in concrete-embedded steel liner plates through experiments on lab-scaled specimens. However, to truly assess the applicability of such methods, it is essential to extend the experiments to realistic structures. These structures should include reinforcements, coarse aggregates, and possess large dimensions to closely mimic real-world conditions. Both single-sided access and through-transmission experiments should be conducted to thoroughly evaluate the strengths and limitations of each measurement modality.

It is crucial to examine the impact of corrosion-related concrete defects on nonlinear evaluations in such realistic environments. These defects may include embedded foreign materials and cavities near the steel liner. Understanding how these imperfections affect the measurements will provide a more comprehensive insight into the reliability and accuracy of nonlinear ultrasonics for corrosion assessment in complex structures, such as containment buildings.

5.2.2. Corrosion monitoring using nonlinear ultrasonics

To fully understand the limitations of nonlinear ultrasonics and its capabilities in detecting ongoing corrosion, it is crucial to conduct experiments throughout the corrosion process. Performing daily measurements during the corrosion process facilitates tracking the progression of various damage indices in real time. While this approach has been explored to some extent with specimens subjected to reinforcement bar corrosion, no such experiments have been conducted on large structures with corroding steel liners embedded in concrete. Achieving this understanding is essential for accurately evaluating results from realistic structures.

Additionally, continuous monitoring is vital for accounting for normal variations due to operational and climatic conditions over time. Continuous data collection allows for the differentiation between corrosion-related changes and those caused by environmental factors, thereby improving the reliability and accuracy of corrosion assessments in real-world scenarios.

5.2.3. Data fusion and AI

In addition to continuing the work on using nonlinear ultrasonic evaluation for corrosion evaluation, additional effort is encouraged to be oriented towards integrating data fusion to a larger extent in civil engineering NDT & E. Data fusion

involves combining results from various NDT methods, such as ultrasonic testing, ground-penetrating radar (GPR), and infrared thermography, to achieve a more comprehensive understanding of the condition of the investigated structure. This multi-modal data integration combines the unique strengths and abilities of each technique which may enhance defect detection, localization, and characterization.

Furthermore, the incorporation of machine learning and artificial intelligence can automate and optimize the analysis process, detecting patterns and anomalies more effectively than traditional techniques. However, the application of AI technology requires a lot of data. It is therefore advantageous to integrate AI evaluation in monitoring systems, which coincides with the previous suggestion regarding the extended scope of monitoring.

References

Abeele, K. E.-A. Van Den, Johnson, P. A., & Sutin, A. (2000). Nonlinear Elastic Wave Spectroscopy (NEWS) Techniques to Discern Material Damage, Part I: Nonlinear Wave Modulation Spectroscopy (NWMS). *Research in Nondestructive Evaluation*, *12*(1), 17–30. https://doi.org/10.1080/09349840008968159

Ahmad, E., Karim, F., Saeed, K., Manzoor, T., & Zahid, G. H. (2014). Effect of cold rolling and annealing on the grain refinement of low alloy steel. *IOP Conference Series: Materials Science and Engineering*, *60*. https://doi.org/10.1088/1757-899X/60/1/012029

Alexander, C. L., & Orazem, M. E. (2020a). Indirect electrochemical impedance spectroscopy for corrosion detection in external post-tensioned tendons: 1. Proof of concept. *Corrosion Science*, *164*(November 2019), 108331. https://doi.org/10.1016/j.corsci.2019.108331

Alexander, C. L., & Orazem, M. E. (2020b). Indirect Impedance for Corrosion Detection of External Post-tensioned Tendons: 2. Multiple Steel Strands. *Corrosion Science*, *164*(November 2019), 108330. https://doi.org/10.1016/j.corsci.2019.108330

Alnuaimi, H., Amjad, U., Russo, P., Lopresto, V., & Kundu, T. (2021). Monitoring damage in composite plates from crack initiation to macro-crack propagation combining linear and nonlinear ultrasonic techniques. *Structural Health Monitoring*, *20*(1), 139–150. https://doi.org/10.1177/1475921720922922

Andrade, C., Martínez, I., & Castellote, M. (2008). Feasibility of determining corrosion rates by means of stray current-induced polarisation. *Journal of Applied Electrochemistry*, *38*(10), 1467–1476. https://doi.org/10.1007/s10800-008-9591-6

Angst, U. M. (2023). Steel corrosion in concrete – Achilles' heel for sustainable concrete? *Cement and Concrete Research*, *172*(February), 107239. https://doi.org/10.1016/j.cemconres.2023.107239

Antonaci, P., Bruno, C. L. E., Scalerandi, M., & Tondolo, F. (2013). Effects of corrosion on linear and nonlinear elastic properties of reinforced concrete. *Cement and Concrete Research*, *51*, 96–103. https://doi.org/10.1016/j.cemconres.2013.04.006

Arumaikani, T., Sasmal, S., & Kundu, T. (2022). Detection of initiation of corrosion induced damage in concrete structures using nonlinear ultrasonic techniques. *The Journal of the Acoustical Society of America*, *151*(2), 1341–1352. https://doi.org/10.1121/10.0009621

Astorga, A., Guéguen, P., & Kashima, T. (2018). Nonlinear elasticity observed in buildings during a long sequence of earthquakes. *Bulletin of the Seismological Society of America*, *108*(3), 1185–1198. https://doi.org/10.1785/0120170289

Aymerich, F., & Staszewski, W. J. (2010). Experimental study of impact-damage detection

in composite laminates using a cross-modulation vibro-acoustic technique. *Structural Health Monitoring*, *9*(6), 541–553. https://doi.org/10.1177/1475921710365433

Basu, S., Thirumalaiselvi, A., Sasmal, S., & Kundu, T. (2021). Nonlinear ultrasonics-based technique for monitoring damage progression in reinforced concrete structures. *Ultrasonics*, *115*(April), 106472. https://doi.org/10.1016/j.ultras.2021.106472

Bekele, A., Birgisson, B., Ryden, N., & Gudmarsson, A. (2017). Slow dynamic diagnosis of asphalt concrete specimen to determine level of damage caused by static low temperature conditioning. *AIP Conference Proceedings*, *1806*. https://doi.org/10.1063/1.4974637

Bentahar, M., Di Bella, A., Mechri, C., Montresor, S., Scalerandi, M., & Yu, X. (2020). Exploiting Slow Dynamics Effects for Damage Detection in Concrete. *Frontiers in Built Environment*, *6*(June), 1–10. https://doi.org/10.3389/fbuil.2020.00064

Berjamin, H., Chiavassa, G., Favrie, N., Lombard, B., & Payan, C. (2019). A Unified Treatment of Nonlinear Viscoelasticity and Non-equilibrium Dynamics. In T. Kundu (Ed.), *Nonlinear Ultrasonic and Vibro-Acoustical Techniques for Nondestructive Evaluation* (pp. 471–486). Springer Nature Switzerland.

Bowman, E., Jacobson, G., Koch, G., Varney, J., Thopson, N., Moghissi, O., Gould, M., & Payer, J. (2016). International Measures of Prevention, Application, and Economics of Corrosion Technologies Study. In *NACE International*.

Brandt, E. H. (1989). Levitation in Physics. *Science*, *243*(4889), 349–355. http://www.jstor.org/stable/1702871

Broda, D., Staszewski, W. J., Martowicz, A., Uhl, T., & Silberschmidt, V. V. (2014). Modelling of nonlinear crack-wave interactions for damage detection based on ultrasound - A review. *Journal of Sound and Vibration*, *333*(4), 1097–1118. https://doi.org/10.1016/j.jsv.2013.09.033

Broomfield, J. P. (2022). *Corrosion of Steel in Concrete* (Third Edit). CRC Press. https://doi.org/10.1201/9781003223016

Cantrell, J. H. (2009). Ultrasonic harmonic generation from fatigue-induced dislocation substructures in planar slip metals and assessment of remaining fatigue life. *Journal of Applied Physics*, *106*(9). https://doi.org/10.1063/1.3254223

Carozzi, T. D. (2000). Radio Waves in the Ionosphere : Propagation , Generation , and Detection [Uppsala University]. In *IRF Scientific Report 272* (Issue August). http://www.diva-portal.org/smash/get/diva2:160737/FULLTEXT01.pdf

Carrión, A., Genovés, V., Pérez, G., Bittner, J., Popovics, J. S., Payá, J., & Gosálbez, J. (2021). Effects of slow dynamics and conditioning on non-linear hysteretic material assessment using impact resonance acoustic spectroscopy. *Mechanical Systems and Signal Processing*, *150*. https://doi.org/10.1016/j.ymssp.2020.107273

Chakrapani, S. K., Howard, A., & Barnard, D. (2018). Influence of surface roughness on the measurement of acoustic nonlinearity parameter of solids using contact piezoelectric transducers. *Ultrasonics*, *84*, 112–118. https://doi.org/10.1016/j.ultras.2017.10.022

Chen, C.-T., Chang, J.-J., & Yeih, W. (2014). The effects of specimen parameters on the resistivity of concrete. *Construction and Building Materials*, *71*, 35–43.

https://doi.org/10.1016/j.conbuildmat.2014.08.009

Chen, J., Yang, C., Wang, Q., Xu, N., & Zhang, T. (2020). Nonlinear Ultrasonic Second Harmonic Assessment of Concrete Defects Based on Embedded Piezoelectric Sensors. *Research in Nondestructive Evaluation*, *31*(4), 254–270. https://doi.org/10.1080/09349847.2020.1797255

Chen, X. J., Kim, J. Y., Kurtis, K. E., Qu, J., Shen, C. W., & Jacobs, L. J. (2008). Characterization of progressive microcracking in Portland cement mortar using nonlinear ultrasonics. *NDT and E International*, *41*(2), 112–118. https://doi.org/10.1016/j.ndteint.2007.08.009

Chen, Y., & Feng, M. Q. (2003). A technique to improve the empirical mode decomposition in the Hilbert-Huang transform. *Earthquake Engineering and Engineering Vibration*, *2*(1), 75–85. https://doi.org/10.1007/BF02857540

Choi, S., Lee, P., & Jhang, K. Y. (2019). A Pulse Inversion-Based Nonlinear Ultrasonic Technique using a Single-Cycle Longitudinal Wave for Evaluating Localized Material Degradation in Plates. *International Journal of Precision Engineering and Manufacturing*, *20*(4), 549–558. https://doi.org/10.1007/s12541-019-00093-1

Climent-Llorca, M. Á., Miró-Oca, M., Poveda-Martínez, P., & Ramis-Soriano, J. (2020). Use of Higher-Harmonic and Intermodulation Generation of Ultrasonic Waves to Detecting Cracks due to Steel Corrosion in Reinforced Cement Mortar. *International Journal of Concrete Structures and Materials*, *14*(1). https://doi.org/10.1186/s40069-020-00432-x

Climent, M.-Á., Miró, M., Eiras, J.-N., Poveda, P., de Vera, G., Segovia, E.-G., & Ramis, J. (2022). Early Detection of Corrosion-Induced Concrete Micro-cracking by Using Nonlinear Ultrasonic Techniques: Possible Influence of Mass Transport Processes. *Corrosion and Materials Degradation*, *3*(2), 235–257. https://doi.org/10.3390/cmd3020014

Climent, M. Á., Miró, M., Carbajo, J., Poveda, P., de Vera, G., & Ramis, J. (2019). Use of non-linear ultrasonic techniques to detect cracks due to steel corrosion in reinforced concrete structures. *Materials*, *12*(5). https://doi.org/10.3390/MA12050813

Collins, G., & Runton, D. (2007). Nonlinear analysis of power amplifiers. *Microwave Journal*, *50*(September 2007).

Dahlen, U., Ryden, N., & Jakobsson, A. (2015). Damage identification in concrete using impact non-linear reverberation spectroscopy. *NDT and E International*, *75*, 15–25. https://doi.org/10.1016/j.ndteint.2015.04.002

Delsanto, P. P. (Ed.). (2007). *Universality of Nonclassical Nonlinearity - Applications to Non-Destructive Evaluations and Ultrasonics*. Springer Science + Business Media.

Dinh, K., Gucunski, N., Tran, K., Novo, A., & Nguyen, T. (2021). Full-resolution 3D imaging for concrete structures with dual-polarization GPR. *Automation in Construction*, *125*(February), 103652. https://doi.org/10.1016/j.autcon.2021.103652

Donskoy, D., Ekimov, A., Luzzato, E., Lottiaux, J.-L., Stoupin, S., & Zagrai, A. (2003). N-SCAN: new vibromodulation system for detection and monitoring of cracks and other contact-type defects. In S.-C. Liu (Ed.), *Smart Structures and Materials 2003: Smart Systems and Nondestructive Evaluation for Civil Infrastructures* (Vol. 5057, p. 400). https://doi.org/10.1117/12.484635

Donskoy, D., & Liu, D. (2021). Vibro-acoustic modulation baseline-free non-destructive testing. *Journal of Sound and Vibration*, *492*, 115808. https://doi.org/10.1016/j.jsv.2020.115808

Donskoy, D. M., Ferroni, K., Sutin, A., & Sheppard, K. (1998). A Nonlinear Acoustic Technique for Crack and Corrosion Detection in Reinforced Concrete. In *Nondestructive Characterization of Materials VIII* (pp. 555–560). Springer US. https://doi.org/10.1007/978-1-4615-4847-8_87

Donskoy, D. M., & Ramezani, M. (2018). Separation of amplitude and frequency modulations in Vibro-Acoustic Modulation Nondestructive Testing Method. *Proceedings of Meetings on Acoustics*, *34*(1), 045002. https://doi.org/10.1121/2.0000831

Donskoy, D. M., & Sutin, A. M. (1998). Vibro-Acoustic Modulation Nondestructive Evaluation technique. *Journal of Intelligent Material Systems and Structures*, *9*(9), 765–771.

Donskoy, D., Sutin, A., & Ekimov, A. (2001). Nonlinear acoustic interaction on contact interfaces and its use for nondestructive testing. *NDT & E International*, *34*(4), 231–238. https://doi.org/10.1016/S0963-8695(00)00063-3

Dunn, D., Pulvirenti, A., & Klein, P. (2011). Containment Liner Corrosion. In *Proceedings of the 15th International Conference on Environmental Degradation of Materials in Nuclear Power Systems — Water Reactors* (Vol. 2, pp. 1037–1049). Springer International Publishing. https://doi.org/10.1007/978-3-319-48760-1_63

Ehsani, M., Sepehry, N., Shamshirsaz, M., Sadighi, M., & Loendersloot, R. (2023). Demodulation-derived damage metrics for nonlinear wave modulation-based health monitoring of structures. *Mechanical Systems and Signal Processing*, *204*(March 2022), 110749. https://doi.org/10.1016/j.ymssp.2023.110749

Eiras, J. N., Kundu, T., Bonilla, M., & Payá, J. (2013). Nondestructive monitoring of ageing of alkali resistant glass fiber reinforced cement (GRC). *Journal of Nondestructive Evaluation*, *32*(3), 300–314. https://doi.org/10.1007/s10921-013-0183-y

Elhacham, E., Ben-Uri, L., Grozovski, J., Bar-On, Y. M., & Milo, R. (2020). Global human-made mass exceeds all living biomass. *Nature*, *588*(7838), 442–444. https://doi.org/10.1038/s41586-020-3010-5

Ensminger, D., & Bond, L. J. (2023). *Ultrasonics*. CRC Press. https://doi.org/10.1201/9780429286964

F. D. Murnaghan. (1937). Finite Deformations of an Elastic Solid. *American Journal of Mathematics*, *59*(2), 235–260.

Fahim, A., Ghods, P., Alizadeh, R., Salehi, M., & Decarufel, S. (2019). CEPRA: A New Test Method for Rebar Corrosion Rate Measurement. In *Advances in Electrochemical Techniques for Corrosion Monitoring and Laboratory Corrosion Measurements* (Issue September, pp. 59–80). ASTM International. https://doi.org/10.1520/STP160920170227

Fletcher, N. H. (1999). The nonlinear physics of musical instruments. *Reports on Progress in Physics*, *62*(5), 723–764. https://doi.org/10.1088/0034-4885/62/5/202

Francois, R., Arliguie, G., & Bardy, D. (1994). Electrode potential measurements of

concrete reinforcement for corrosion evaluation. *Cement and Concrete Research*, *24*(3), 401–412. https://doi.org/10.1016/0008-8846(94)90127-9

Garcia, S., & Deby, F. (2019). Numerical and Experimental Development of Gradient Potential Measurement for Corrosion Detection in Reinforced Concrete. In C. Andrade, J. Gulikers, & E. Marie-Victoire (Eds.), *Service Life and Durability of Reinforced Concrete Structures* (pp. 71–86). Springer Cham. https://doi.org/10.1007/978-3-319-90236-4_6

Green, R. E. (1973). Ultrasonic investigation of mechanical properties. In H. Herbert (Ed.), *Treatise on Materials Science and Technology Volume 3*. Academic Press.

Grosse, C. U., Algernon, D., Arndt, R., Feistkorn, S., Niederleithinger, E., & Taffe, A. (2023). Some developments in the field of non-destructive testing - new devices and techniques, industrial training and academic education. *Ce/Papers*, *6*(6), 1443–1451. https://doi.org/10.1002/cepa.2875

Gusev, V., Tournat, V., & Castagnède, B. (2009). Nonlinear Acoustic Phenomena in Micro-inhomogenous Media. In *Materials and Acoustics Handbook* (pp. 431–471). Wiley. https://doi.org/10.1002/9780470611609.ch17

Guyer, R. A., & Johnson, P. A. (1999). Nonlinear Mesoscopic Elasticity: Evidence for a New Class of Materials. *Physics Today*, *52*(4), 30–36. https://doi.org/10.1063/1.882648

Guyer, R. A., & Johnson, P. A. (2009). *Nonlinear Mesoscopic Elasticity: The Complex Behaviour of Granular Media including Rocks and Soil*. Wiley-VCH.

Hafezi, M. H., Alebrahim, R., & Kundu, T. (2017). Peri-ultrasound for modeling linear and nonlinear ultrasonic response. *Ultrasonics*, *80*, 47–57. https://doi.org/10.1016/j.ultras.2017.04.015

Haller, K. C. E., & Hedberg, C. M. (2012). Method for monitoring slow dynamics recovery. *Acoustical Physics*, *58*(6), 713–717. https://doi.org/10.1134/S1063771012060061

Haller, K. C. E., Hedberg, C. M., & Rudenko, O. V. (2010). Slow variations of mechanical and electrical properties of dielectrics and nonlinear phenomena at ultrasonic irradiation1. *Acoustical Physics*, *56*(5), 660–664. https://doi.org/10.1134/S1063771010050118

He, Y., Xiao, Y., Su, Z., Pan, Y., & Zhang, Z. (2022). Contact acoustic nonlinearity effect on the vibro-acoustic modulation of delaminated composite structures. *Mechanical Systems and Signal Processing*, *163*(June 2021), 108161. https://doi.org/10.1016/j.ymssp.2021.108161

He, Z., Shen, Y., & Wang, Q. (2012). Boundary extension for Hilbert–Huang transform inspired by gray prediction model. *Signal Processing*, *92*(3), 685–697. https://doi.org/10.1016/j.sigpro.2011.09.010

Hedberg, C. (2014). Rock Softening with Consequences for Earthquake Science. In *Springer Proceedings in Physics* (Vol. 150, pp. 159–178). https://doi.org/10.1007/978-3-319-02207-9_17

Hedberg, C. M. (1999). A multi-frequency solution for the Burgers equation. *Nonlinear Acoustics at the Turn of the Millenium, Proceedings of 15th International Symposium on Nonlinear Acoustics*.

Hedberg, C. M., Andersson, S. A. K., & Haller, K. C. E. (2013). Deflection dynamics of rock beam caused by ultrasound. *Mechanics of Time-Dependent Materials*, *17*(4), 597–604. https://doi.org/10.1007/s11043-012-9207-8

Hikata, A., Chick, B. B., & Elbaum, C. (1963). Effect of dislocations on finite amplitude ultrasonic waves in aluminum. *Applied Physics Letters*, *3*(11), 195–197. https://doi.org/10.1063/1.1753845

Hilloulin, B., Legland, J. B., Lys, E., Abraham, O., Loukili, A., Grondin, F., Durand, O., & Tournat, V. (2016). Monitoring of autogenous crack healing in cementitious materials by the nonlinear modulation of ultrasonic coda waves, 3D microscopy and X-ray microtomography. *Construction and Building Materials*, *123*, 143–152. https://doi.org/10.1016/j.conbuildmat.2016.06.138

Holmes, C., Drinkwater, B. W., & Wilcox, P. D. (2005). Post-processing of the full matrix of ultrasonic transmit–receive array data for non-destructive evaluation. *NDT & E International*, *38*(8), 701–711. https://doi.org/10.1016/j.ndteint.2005.04.002

Hornbostel, K., Larsen, C. K., & Geiker, M. R. (2013). Relationship between concrete resistivity and corrosion rate – A literature review. *Cement and Concrete Composites*, *39*, 60–72. https://doi.org/10.1016/j.cemconcomp.2013.03.019

Hu, H. F., Staszewski, W. J., Hu, N. Q., Jenal, R. B., & Qin, G. J. (2010). Crack detection using nonlinear acoustics and piezoceramic transducers—instantaneous amplitude and frequency analysis. *Smart Materials and Structures*, *19*(6), 065017. https://doi.org/10.1088/0964-1726/19/6/065017

Hu, H., Zou, Z., Jiang, Y., Wang, X., & Yi, K. (2019). Finite element simulation and experimental study of residual stress testing using nonlinear ultrasonic surface wave technique. *Applied Acoustics*, *154*, 11–17. https://doi.org/10.1016/j.apacoust.2019.04.014

Huang, N. E., Shen, Z., Long, S. R., Wu, M. C., Snin, H. H., Zheng, Q., Yen, N. C., Tung, C. C., & Liu, H. H. (1998). The empirical mode decomposition and the Hilbert spectrum for nonlinear and non-stationary time series analysis. *Proceedings of the Royal Society A: Mathematical, Physical and Engineering Sciences*, *454*(1971), 903–995. https://doi.org/10.1098/rspa.1998.0193

Huang, N. E., & Wu, Z. (2008). A review on Hilbert-Huang transform: Method and its applications to geophysical studies. *Reviews of Geophysics*, *46*(2), RG2006. https://doi.org/10.1029/2007RG000228

Huttunen-Saarivirta, E., Bohner, E., Trentin, A., & Ferreira, M. (2023). A closer look at the corrosion of steel liner embedded in concrete. *Cement and Concrete Composites*, *105280*, 105280. https://doi.org/10.1016/j.cemconcomp.2023.105280

James, A., Bazarchi, E., Chiniforush, A. A., Panjebashi Aghdam, P., Hosseini, M. R., Akbarnezhad, A., Martek, I., & Ghodoosi, F. (2019). Rebar corrosion detection, protection, and rehabilitation of reinforced concrete structures in coastal environments: A review. *Construction and Building Materials*, *224*, 1026–1039. https://doi.org/10.1016/j.conbuildmat.2019.07.250

Jeon, D., Kim, M. K., Jeong, Y., Oh, J. E., Moon, J., Kim, D. J., & Yoon, S. (2022). High-accuracy rebar position detection using deep learning–based frequency-difference electrical resistance tomography. *Automation in Construction*, *135*(December 2021),

104116. https://doi.org/10.1016/j.autcon.2021.104116

Jhang, K.-Y. (2017). Nonlinear ultrasonic techniques for nondestructive assessment of micro damage in material: A review. *International Journal of Precision Engineering and Manufacturing*, *18*(1), 139–139. https://doi.org/10.1007/s12541-017-0018-3

Jin, J., Moreno, M. G., Riviere, J., & Shokouhi, P. (2017). Impact-Based Nonlinear Acoustic Testing for Characterizing Distributed Damage in Concrete. *Journal of Nondestructive Evaluation*, *36*(3), 51. https://doi.org/10.1007/s10921-017-0428-2

Johnson, P. A., Zinszner, B., & Rasolofosaon, P. N. J. (1996). Resonance and elastic nonlinear phenomena in rock. *Journal of Geophysical Research B: Solid Earth*, *101*(5), 11553–11564. https://doi.org/10.1029/96jb00647

Karhunen, K., Seppänen, A., Lehikoinen, A., Monteiro, P. J. M., & Kaipio, J. P. (2010). Electrical Resistance Tomography imaging of concrete. *Cement and Concrete Research*, *40*(1), 137–145. https://doi.org/10.1016/j.cemconres.2009.08.023

Keddam, M., Ramon Novoa, X., Puga, B., & Vivier, V. (2011). Impedance based method for non-contact determination of the corrosion rate in buried metallic structures. *European Journal of Environmental and Civil Engineering*, *15*(7), 1097–1103. https://doi.org/10.3166/ejece.15.1097-1103

Kim, J., Song, D.-G., & Jhang, K.-Y. (2017). Absolute Measurement and Relative Measurement of Ultrasonic Nonlinear Parameters. *Research in Nondestructive Evaluation*, *28*(4), 211–225. https://doi.org/10.1080/09349847.2016.1174322

Kober, J., Kirchner, A., Kruisova, A., Chlada, M., Hirsekorn, S., Weißgärber, T., & Prevorovsky, Z. (2020). Assessing Porosity in Selective Electron Beam Melting Manufactured Ti–6Al–4V by Nonlinear Impact Modulation Spectroscopy. *Journal of Nondestructive Evaluation*, *39*(4), 1–8. https://doi.org/10.1007/s10921-020-00731-z

Köliö, A., Honkanen, M., Lahdensivu, J., Vippola, M., & Pentti, M. (2015). Corrosion products of carbonation induced corrosion in existing reinforced concrete facades. *Cement and Concrete Research*, *78*, 200–207. https://doi.org/10.1016/j.cemconres.2015.07.009

Korenska, M., Matysik, M., Vyroubal, P., & Pospisil, K. (2009). Assessment of reinforcement corrosion using nonlinear ultrasonic spectroscopy. *NDT in Progress 2009 - 5th International Workshop of NDT Experts, Proceedings*, 143–151.

Korobov, A. I., Shirgina, N. V., & Kokshaiskii, A. I. (2015). A pressure effect on the nonlinear reflection of elastic waves from the boundary of two solid media. *Acoustical Physics*, *61*(2), 165–172. https://doi.org/10.1134/S1063771015020074

Korshak, B. A., Solodov, I. Y., & Ballad, E. M. (2002). DC effects, sub-harmonics, stochasticity and "memory" for contact acoustic non-linearity. *Ultrasonics*, *40*(1–8), 707–713. https://doi.org/10.1016/S0041-624X(02)00241-X

Krishna, S. C., Karthick, N. K., Jha, A. K., Pant, B., & Cherian, R. M. (2018). Effect of Hot Rolling on the Microstructure and Mechanical Properties of Nitrogen Alloyed Austenitic Stainless Steel. *Journal of Materials Engineering and Performance*, *27*(5), 2388–2393. https://doi.org/10.1007/s11665-018-3317-7

Kube, C. M., & Arguelles, A. P. (2017). Ultrasonic harmonic generation from materials with up to cubic nonlinearity. *The Journal of the Acoustical Society of America*,

142(2), EL224–EL230. https://doi.org/10.1121/1.4998139

Kube, C. M., Roy, A., Jensen, D. S., & Branch, D. W. (2022). A unifying model of weakly nonlinear elastic waves; large on large theory. *The Journal of the Acoustical Society of America*, *151*(2), 1294–1310. https://doi.org/10.1121/10.0009376

Kundu, T., Eiras, J. N., Li, W., Liu, P., Sohn, H., & Payá, J. (2019). Fundamentals of Nonlinear Acoustical Techniques and Sideband Peak Count. In T. Kundu (Ed.), *Nonlinear Ultrasonic and Vibro-Acoustical Techniques for Nondestructive Evaluation* (pp. 1–88). Springer Nature Switzerland.

Kyung-Young Jhang, Lissenden, C. J., Solodov, I., Ohara, Y., & Gusev, V. (2020). *Measurement of Nonlinear Ultrasonic Characteristics* (K.-Y. Jhang, C. J. Lissenden, I. Solodov, Y. Ohara, & V. Gusev (Eds.)). Springer Singapore. https://doi.org/10.1007/978-981-15-1461-6

Landau, L. D., & Lifshitz, E. M. (1986). Theory of Elasticity. In *Theory of Elasticity* (2nd ed.). Elsevier. https://doi.org/10.1016/C2009-0-25521-8

Lee, J., & Chang, J. H. (2019). Dual-Element Intravascular Ultrasound Transducer for Tissue Harmonic Imaging and Frequency Compounding: Development and Imaging Performance Assessment. *IEEE Transactions on Biomedical Engineering*, *66*(11), 3146–3155. https://doi.org/10.1109/TBME.2019.2901005

Leśnicki, K. J., Kim, J. Y., Kurtis, K. E., & Jacobs, L. J. (2011). Characterization of ASR damage in concrete using nonlinear impact resonance acoustic spectroscopy technique. *NDT and E International*, *44*(8), 721–727. https://doi.org/10.1016/j.ndteint.2011.07.010

Li, X., & Dwyer-Joyce, R. S. (2020). Measuring friction at an interface using ultrasonic response. *Proceedings of the Royal Society A: Mathematical, Physical and Engineering Sciences*, *476*(2241). https://doi.org/10.1098/rspa.2020.0283

Li, X., & Gong, J. (2023). Effects of steel liner corrosion on the leak-tightness of prestressed concrete containment structure under severe accident loads. *Annals of Nuclear Energy*, *180*(October 2022), 109487. https://doi.org/https://doi.org/10.1016/j.anucene.2022.109487

Lim, Y.-C., Noguchi, T., & Shin, S.-W. (2009). Formulation of a Nondestructive Technique for Evaluating Steel Corrosion in Concrete Structures. *ISIJ International*, *49*(2), 275–283. https://doi.org/10.2355/isijinternational.49.275

Lingvall, F. (2004). Time-domain Reconstruction Methods for Ultrasonic Array Imaging: A Statistical Approach. In *Signals*. Uppsala University.

Lissenden, C. J. (2021). Nonlinear ultrasonic guided waves—Principles for nondestructive evaluation. *Journal of Applied Physics*, *129*(2), 021101. https://doi.org/10.1063/5.0038340

Lissenden, C. J., & Hasanian, M. (2020). Measurement of Nonlinear Guided Waves. In K.-Y. Jhang, C. J. Lissenden, I. Y. Solodov, Y. Ohara, & V. Gusev (Eds.), *Measurement of Nonlinear Ultrasonic Characteristics* (pp. 61–108). Springer Nature Singapore.

Liu, D., & Donskoy, D. (2023). Vibroacoustic modulation method with arbitrary probe wave frequency based on machine learning algorithms. *Nondestructive Testing and Evaluation*, *38*(5), 845–860. https://doi.org/10.1080/10589759.2023.2173751

Liu, P., Sohn, H., Kundu, T., & Yang, S. (2014). Noncontact detection of fatigue cracks by

laser nonlinear wave modulation spectroscopy (LNWMS). *NDT and E International*, *66*, 106–116. https://doi.org/10.1016/j.ndteint.2014.06.002

Lu, R., Shen, Y., Zhang, B., & Xu, W. (2023). Nonlinear Electro-Mechanical Impedance Spectroscopy for fatigue crack monitoring. *Mechanical Systems and Signal Processing*, *184*(August 2022), 109749. https://doi.org/10.1016/j.ymssp.2022.109749

Marion, J. B. (1965). The Wave Equation in One Dimension. In *Classical Dynamics of Particles and Systems* (pp. 478–521). Elsevier. https://doi.org/10.1016/B978-1-4832-5676-4.50019-6

Matlack, K. H., Kim, J. Y., Jacobs, L. J., & Qu, J. (2015). Review of Second Harmonic Generation Measurement Techniques for Material State Determination in Metals. *Journal of Nondestructive Evaluation*, *34*(1). https://doi.org/10.1007/s10921-014-0273-5

McCall, K. R., & Guyer, R. A. (1996). A new theoretical paradigm to describe hysteresis, discrete memory and nonlinear elastic wave propagation in rock. *Nonlinear Processes in Geophysics*, *3*(2), 89–101. https://doi.org/10.5194/npg-3-89-1996

Millard, S. ., Law, D., Bungey, J. ., & Cairns, J. (2001). Environmental influences on linear polarisation corrosion rate measurement in reinforced concrete. *NDT & E International*, *34*(6), 409–417. https://doi.org/10.1016/S0963-8695(01)00008-1

Minagawa, H., Miyamoto, S., Kurashige, I., & Hisada, M. (2023). Appropriate geometrical factors for four-probe method to evaluate electrical resistivity of concrete specimens. *Construction and Building Materials*, *374*(March), 130784. https://doi.org/10.1016/j.conbuildmat.2023.130784

Miró, M., Eiras, J. N., Poveda, P., Climent, M. Á., & Ramis, J. (2021). Detecting cracks due to steel corrosion in reinforced cement mortar using intermodulation generation of ultrasonic waves. *Construction and Building Materials*, *286*, 122915. https://doi.org/10.1016/j.conbuildmat.2021.122915

Muller, M., Tencate, J. A., Darling, T. W., Sutin, A., Guyer, R. A., Talmant, M., Laugier, P., & Johnson, P. A. (2006). Bone micro-damage assessment using non-linear resonant ultrasound spectroscopy (NRUS) techniques: A feasibility study. *Ultrasonics*, *44*(SUPPL.), 245–249. https://doi.org/10.1016/j.ultras.2006.06.043

Na, J. K., & Breazeale, M. A. (1994). Ultrasonic nonlinear properties of lead zirconate-titanate ceramics. *The Journal of the Acoustical Society of America*, *95*(6), 3213–3221. https://doi.org/10.1121/1.409985

Nazarov, V. E. (2016). Dislocation nonlinearity and nonlinear wave processes in polycrystals with dislocations. *Physics of the Solid State*, *58*(9), 1719–1728. https://doi.org/10.1134/S1063783416090249

Nazarov, V. E., & Kiyashko, S. B. (2014). Amplitude-Dependent Internal Friction and Harmonic Generation in Media with Hysteresis Nonlinearity and Linear Dissipation. *Radiophysics and Quantum Electronics*, *56*(10), 686–696. https://doi.org/10.1007/s11141-014-9473-1

Neff, D., Harnisch, J., Beck, M., L'Hostis, V., Goebbels, J., & Meinel, D. (2011). Morphology of corrosion products of steel in concrete under macro-cell and self-corrosion conditions. *Materials and Corrosion*, *62*(9), 861–871.

https://doi.org/10.1002/maco.201005861

Nilsson, M., & Carlén, T. (2019). *Quality Assessment of Thin Polymer Components using NonDestructive Testing*. Blekinge Institute of Technology.

Nilsson, M., Huttunen-Saarivirta, E., Bohner, E., & Ferreira, M. (2023). Non-destructive evaluation of corrosion in steel liner plates embedded in concrete using nonlinear ultrasonics. *Construction and Building Materials*, *408*(September), 133691. https://doi.org/10.1016/j.conbuildmat.2023.133691

Nilsson, M., Ulriksen, P., & Rydén, N. (2023). Nonlinear ultrasonic characteristics of a corroded steel plate. *Nondestructive Testing and Evaluation*, *38*(3), 456–479. https://doi.org/10.1080/10589759.2022.2123481

Nilsson, M., Ulriksen, P., & Rydén, N. (2024). Ultrasonic imaging of concrete-embedded corroded steel liners using linear and nonlinear evaluation. *Nondestructive Testing and Evaluation*, *00*(00), 1–29. https://doi.org/10.1080/10589759.2024.2402889

Nilsson, M., Ulriksena, P., & Rydén, N. (2024). Nonlinear Wave Modulation for the Evaluation of Corroded Steel Plates Embedded in Concrete. *Journal of Advanced Concrete Technology*, *22*(9), 545–560. https://doi.org/10.3151/jact.22.545

Ohara, Y., Endo, H., Hashimoto, M., Shintaku, Y., Yamanaka, K., Thompson, D. O., & Chimenti, D. E. (2010). MONITORING GROWTH OF CLOSED FATIGUE CRACK USING SUBHARMONIC PHASED ARRAY. *AIP Conference Proceedings*, *1211*, 903–909. https://doi.org/10.1063/1.3362519

Ohara, Y., Endo, H., Mihara, T., & Yamanaka, K. (2009). Ultrasonic measurement of closed stress corrosion crack depth using subharmonic phased array. *Japanese Journal of Applied Physics*, *48*(7 PART 2). https://doi.org/10.1143/JJAP.48.07GD01

Ohara, Y., Mihara, T., Sasaki, R., Ogata, T., Yamamoto, S., Kishimoto, Y., & Yamanaka, K. (2007). Imaging of closed cracks using nonlinear response of elastic waves at subharmonic frequency. *Applied Physics Letters*, *90*(1). https://doi.org/10.1063/1.2426891

Ohara, Y., Nakajima, H., Haupert, S., Tsuji, T., & Mihara, T. (2019). Nonlinear ultrasonic phased array with fixed-voltage fundamental wave amplitude difference for high-selectivity imaging of closed cracks. *The Journal of the Acoustical Society of America*, *146*(1), 266–277. https://doi.org/10.1121/1.5116017

Ohara, Y., Shintaku, Y., Horinouchi, S., Hashimoto, M., Yamaguchi, Y., Tagami, M., & Yamanaka, K. (2010). Ultrasonic imaging of stress corrosion crack formed in high temperature pressurized water using subharmonic phased array. *Proceedings of Meetings on Acoustics*, *10*(2010). https://doi.org/10.1121/1.3533836

Ohara, Y., Yamamoto, S., Mihara, T., & Yamanaka, K. (2008). Ultrasonic evaluation of closed cracks using subharmonic phased array. *Japanese Journal of Applied Physics*, *47*(5 PART 2), 3908–3915. https://doi.org/10.1143/JJAP.47.3908

Osika, M., Ziaja–Sujdak, A., Radecki, R., & Staszewski, W. J. (2023). The Luxembourg–Gorky effect for elastic shear horizontal guided waves — Analytical and numerical modelling. *International Journal of Engineering Science*, *193*(May), 103933. https://doi.org/10.1016/j.ijengsci.2023.103933

Otieno, M., Ikotun, J., & Ballim, Y. (2019). Experimental investigations on the influence of cover depth and concrete quality on time to cover cracking due to carbonation-

induced corrosion of steel in RC structures in an urban, inland environment. *Construction and Building Materials*, *198*, 172–181. https://doi.org/10.1016/j.conbuildmat.2018.11.215

Oxfall, M. (2016). *Climatic conditions inside nuclear reactor containments - Evaluation of moisture condition in the concrete within reactor containments and interaction with the ambient compartments*. Lund University.

Park, S., Alnuaimi, H., Hayes, A., Sitkiewicz, M., Amjad, U., Muralidharan, K., & Kundu, T. (2022). Nonlinear Acoustic Technique for Monitoring Porosity in Additively Manufactured Parts. *Journal of Nondestructive Evaluation, Diagnostics and Prognostics of Engineering Systems*, *5*(2), 1–6. https://doi.org/10.1115/1.4053252

Park, S. H., & Kundu, T. (2023). A modified sideband peak count based nonlinear ultrasonic technique for material characterization. *Ultrasonics*, *128*(September 2022), 106858. https://doi.org/10.1016/j.ultras.2022.106858

Pieczonka, L., Klepka, A., Martowicz, A., & Staszewski, W. J. (2015). Nonlinear vibroacoustic wave modulations for structural damage detection: an overview. *Optical Engineering*, *55*(1), 011005. https://doi.org/10.1117/1.oe.55.1.011005

Rayleigh, Lord. (1885). On Waves Propagated along the Plane Surface of an Elastic Solid. *Proceedings of the London Mathematical Society*, *s1-17*(1), 4–11. https://doi.org/10.1112/plms/s1-17.1.4

Reichling, K., & Raupach, M. (2014). Method to determine electrochemical potential gradients without reinforcement connection in concrete structures. *Cement and Concrete Composites*, *47*, 3–8. https://doi.org/10.1016/j.cemconcomp.2013.12.007

Reichling, K., Raupach, M., & Klitzsch, N. (2015). Determination of the distribution of electrical resistivity in reinforced concrete structures using electrical resistivity tomography. *Materials and Corrosion*, *66*(8), 763–771. https://doi.org/10.1002/maco.201407763

Remillieux, M. C., Kaoumi, D., Ohara, Y., Stuber Geesey, M. A., Xi, L., Schoell, R., Bryan, C. R., Enos, D. G., Summa, D. A., Ulrich, T. J., Anderson, B. E., & Shayer, Z. (2020). Detecting and imaging stress corrosion cracking in stainless steel, with application to inspecting storage canisters for spent nuclear fuel. *NDT and E International*, *109*(September 2019). https://doi.org/10.1016/j.ndteint.2019.102180

Robles, K. P. V., Yee, J.-J., & Kee, S.-H. (2022). Electrical Resistivity Measurements for Nondestructive Evaluation of Chloride-Induced Deterioration of Reinforced Concrete—A Review. *Materials*, *15*(8), 2725. https://doi.org/10.3390/ma15082725

Rodrigues, R., Gaboreau, S., Gance, J., Ignatiadis, I., & Betelu, S. (2021). Reinforced concrete structures: A review of corrosion mechanisms and advances in electrical methods for corrosion monitoring. *Construction and Building Materials*, *269*, 121240. https://doi.org/10.1016/j.conbuildmat.2020.121240

Rudenko, O. V. (2006). Giant nonlinearities in structurally inhomogeneous media and the fundamentals of nonlinear acoustic diagnostic techniques. *Physics-Uspekhi*, *49*(1), 69–87. https://doi.org/10.1070/PU2006v049n01ABEH005876

Rudenko, O. V., & Makov, Y. N. (2021). Sonic Boom: From the Physics of Nonlinear Waves to Acoustic Ecology (a Review). *Acoustical Physics*, *67*(1), 1–25. https://doi.org/10.1134/S1063771021010036

Saha, S. K., Takano, T., Fushimi, K., Sakairi, M., & Saito, R. (2023). Passivity of iron surface in curing cement paste environment investigated by electrochemical impedance spectroscopy and surface characterization techniques. *Surfaces and Interfaces*, *36*(December 2022), 102549. https://doi.org/10.1016/j.surfin.2022.102549

Sandberg, B., Sederholm, B., Taxen, C., Trägårdh, J., & Tidblad, J. (2019). Genomgång av potentiella korrosionsrisker för ingjuten tätplåt i reaktorinneslutningar. *Energiforsk Rapport*, *2019:581*.

Shan, S., Zhang, Y., Liu, Z., Wen, F., Cheng, L., & Staszewski, W. J. (2024). Cross-modulation in guided wave propagation: how does it relate to the Luxemburg-Gorky effect? *Journal of Sound and Vibration*, *568*(July 2023), 117961. https://doi.org/10.1016/j.jsv.2023.117961

Shevaldykin, V. G., Samokrutov, A. A., & Kozlov, V. N. (2002). Ultrasonic low-frequency transducers with dry dot contact and their applications for evaluation of concrete structures. *2002 IEEE Ultrasonics Symposium, 2002. Proceedings.*, *1*(c), 793–798. https://doi.org/10.1109/ULTSYM.2002.1193518

Skjelvareid, M. H. (2012). *Synthetic aperture ultrasound imaging with application to interior pipe inspection* (Issue September). University of Tromsø.

Solodov, I. (2014). Resonant ultrasonic imaging of defects for advanced non-linear and thermosonic applications. *International Journal of Microstructure and Materials Properties*, *9*(3–5), 261–273. https://doi.org/10.1504/IJMMP.2014.066909

Solodov, I. (2019). Nonlinear Acoustic Response of Damage Applied for Diagnostic Imaging. In T. Kundu (Ed.), *Nonlinear Ultrasonic and Vibro-Acoustical Techniques for Nondestructive Evaluation* (pp. 301–343). Springer Nature Switzerland.

Solodov, I., & Kreutzbruck, M. (2019). Mode matching to enhance nonlinear response of local defect resonance. *Journal of Sound and Vibration*, *461*, 114916. https://doi.org/10.1016/j.jsv.2019.114916

Solodov, I., Wackerl, J., Pfleiderer, K., & Busse, G. (2004). Nonlinear self-modulation and subharmonic acoustic spectroscopy for damage detection and location. *Applied Physics Letters*, *84*(26), 5386–5388. https://doi.org/10.1063/1.1767283

Solodov, I. Y., & Korshak, B. A. (2002). Instability, Chaos, and "Memory" in Acoustic-Wave–Crack Interaction. *Physical Review Letters*, *88*(1), 3. https://doi.org/10.1103/PhysRevLett.88.014303

Solodov, I. Y., Krohn, N., & Busse, G. (2002). CAN: an example of nonclassical acoustic nonlinearity in solids. *Ultrasonics*, *40*, 621–625.

Stern, M., & Geary, A. L. (1957). Electrochemical Polarization. *Journal of The Electrochemical Society*, *104*(1), 56. https://doi.org/10.1149/1.2428496

Stuber Geesey, M. A., Aristorenas, B., Ulrich, T. J., & Donahue, C. M. (2019). Investigation of the nonlinearity of transducer acoustic couplants for nonlinear elastic measurements. *NDT and E International*, *104*(October 2018), 10–18. https://doi.org/10.1016/j.ndteint.2019.03.004

Su, J., Yang, C., Wu, W., & Huang, R. (2002). Effect of moisture content on concrete resistivity measurement. *Journal of the Chinese Institute of Engineers*, *25*(1), 117–122. https://doi.org/10.1080/02533839.2002.9670686

Su, Z., & Ye, L. (2009). Fundamentals and Analysis of Lamb Waves. In *Lecture Notes in Applied and Computational Mechanics* (Vol. 48, pp. 15–58). https://doi.org/10.1007/978-1-84882-784-4_2

Sumra, Y., Payam, S., & Zainah, I. (2020). The pH of Cement-based Materials: A Review. *Journal of Wuhan University of Technology-Mater. Sci. Ed.*, *35*(5), 908–924. https://doi.org/10.1007/s11595-020-2337-y

Sun, M., Li, X., & Kube, C. M. (2023). Interaction of elastic waves in solids with quadratic and cubic nonlinearity. *The Journal of the Acoustical Society of America*, *154*(5), 3285–3309. https://doi.org/10.1121/10.0022381

Sun, M., Zhang, S., Zhang, G., Li, X., & Kundu, T. (2024). Detection and evaluation of fatigue cracks using a nonlinear ultrasonic sideband peak count technique with a pulse-echo experimental method. *Journal of Sound and Vibration*, *583*(July 2023), 118429. https://doi.org/10.1016/j.jsv.2024.118429

Sun, X., Liu, H., Zhao, Y., Qu, J., Deng, M., & Hu, N. (2020). The zero-frequency component of bulk waves in solids with randomly distributed micro-cracks. *Ultrasonics*, *107*(April), 106172. https://doi.org/10.1016/j.ultras.2020.106172

Taylor, L. H., & Rollins, F. R. (1964). Ultrasonic Study of Three-Phonon Interactions. I. Theory. *Physical Review*, *136*(3A), A591–A596. https://doi.org/10.1103/PhysRev.136.A591

Tellegen, B. D. H. (1933). Interaction Between Radio-Waves? *Nature*, *131*, 840.

TenCate, J. A. (2000). *Slow dynamics experiments in solids with nonlinear mesoscopic elasticity*. *July 2000*, 303–306. https://doi.org/10.1063/1.1309228

TenCate, J. A., Smith, E., & Guyer, R. A. (2000). Universal slow dynamics in granular solids. *Physical Review Letters*, *85*(5), 1020–1023. https://doi.org/10.1103/PhysRevLett.85.1020

Terzi, M., Chehami, L., Moulin, E., Aleshin, V., & Smagin, N. (2019). Baseline-free repetitive pump-probe experiment for structural health monitoring. *Proceedings of the International Congress on Acoustics*, *2019-Septe*(1), 8193–8200. https://doi.org/10.18154/RWTH-CONV-239742

Trojniar, T., Klepka, A., Pieczonka, L., & Staszewski, W. J. (2014). Fatigue crack detection using nonlinear vibro-acoustic cross-modulations based on the Luxemburg-Gorky effect. *Health Monitoring of Structural and Biological Systems 2014*, *9064*(March 2014), 90641F. https://doi.org/10.1117/12.2046471

Van Den Abeele, K., & Breazeale, M. A. (1996). Theoretical model to describe dispersive nonlinear properties of lead zirconate–titanate ceramics. *The Journal of the Acoustical Society of America*, *99*(3), 1430–1437. https://doi.org/10.1121/1.414722

Van Den Abeele, K., Carmeliet, J., & Van De Velde, K. (2001). Inferring the degradation of pultruded composites from dynamic nonlinear resonance measurements. *Polymer Composites*, *22*(4), 555–567. https://doi.org/10.1002/pc.10559

Wang, J., Shen, Y., Rao, D., & Xu, W. (2021). An instantaneous-baseline multi-indicial nonlinear ultrasonic resonance spectral correlation technique for fatigue crack detection and quantification. *Nonlinear Dynamics*, *103*(1), 677–698. https://doi.org/10.1007/s11071-020-06128-x

Wang, T., Yin, T., Ng, C. T., Cao, Y., & Kotousov, A. (2024). Debonding detection of

FRP-strengthened reinforced concrete using a novel amplitude modulated vibro-acoustic method. *NDT & E International*, *145*(November 2023), 103121. https://doi.org/10.1016/j.ndteint.2024.103121

Williams, C. L., Lear, M. H., & Shokouhi, P. (2024). A review of the microstructural contributions to the acoustic nonlinearity parameter measured with longitudinal and Rayleigh wave second harmonic generation in metals. *NDT & E International*, *142*(November 2023), 103027. https://doi.org/10.1016/j.ndteint.2023.103027

Xie, X., Xu, D., Guo, X., Sha, F., & Huang, S. (2016). Nonlinear Ultrasonic Nondestructive Evaluation of Damaged Concrete Based on Embedded Piezoelectric Sensors. *Research in Nondestructive Evaluation*, *27*(3), 125–136. https://doi.org/10.1080/09349847.2015.1012247

Yamanaka, K., Mihara, T., & Tsuji, T. (2004). Evaluation of closed cracks by model analysis of subharmonic ultrasound. *Japanese Journal of Applied Physics, Part 1: Regular Papers and Short Notes and Review Papers*, *43*(5 B), 3082–3087. https://doi.org/10.1143/JJAP.43.3082

Yin, T., Ng, C. T., Vidler, J., Ho, V. D., & Kotousov, A. (2023). Amplitude-Modulation Vibro-Acoustic Technique for Damage Evaluation. *Structural Health Monitoring*, *22*(2), 1399–1420. https://doi.org/10.1177/14759217221106209

Yu, J., Sasamoto, A., & Iwata, M. (2019). Wenner method of impedance measurement for health evaluation of reinforced concrete structures. *Construction and Building Materials*, *197*, 576–586. https://doi.org/10.1016/j.conbuildmat.2018.11.121

Zaitsev, V., Gusev, V., & Castagnede, B. (2002). Luxemburg-Gorky Effect Retooled for Elastic Waves: A Mechanism and Experimental Evidence. *Physical Review Letters*, *89*(10), 2–5. https://doi.org/10.1103/PhysRevLett.89.105502

Zaitsev, V., Gusev, V., & Castagnede, B. (2003). Thermoelastic Mechanism for Logarithmic Slow Dynamics and Memory in Elastic Wave Interactions with Individual Cracks. *Physical Review Letters*, *90*(7), 4. https://doi.org/10.1103/PhysRevLett.90.075501

Zaitsev, V., Nazarov, V., Gusev, V., & Castagnede, B. (2006). Novel nonlinear-modulation acoustic technique for crack detection. *NDT & E International*, *39*(3), 184–194. https://doi.org/10.1016/j.ndteint.2005.07.007

Zaitsev, V. Y., Gusev, V., & Castagnède, B. (2002). Observation of the "Luxemburg-Gorky effect" for elastic waves. *Ultrasonics*, *40*, 627–631.

Zaitsev, V. Y., Nazarov, V. E., Tournat, V., Gusev, V. E., & Castagnède, B. (2005). Luxemburg-Gorky effect in a granular medium: Probing perturbations of the material state via cross-modulation of elastic waves. *Europhysics Letters*, *70*(5), 607–613. https://doi.org/10.1209/epl/i2005-10023-5

Zarembo, L. K., & Krasilnikov, V. A. (1971). Nonlinear Phenomena in the Propagation of Elastic Waves in Solids. *Soviet Physics Uspekhi*, *13*(6), 778–797.

Zeitvogel, D. T., Matlack, K. H., Kim, J.-Y., Jacobs, L. J., Singh, P. M., & Qu, J. (2014). Characterization of stress corrosion cracking in carbon steel using nonlinear Rayleigh surface waves. *NDT & E International*, *62*, 144–152. https://doi.org/10.1016/j.ndteint.2013.12.005

Zhang, J., Drinkwater, B. W., Wilcox, P. D., & Hunter, A. J. (2010). Defect detection

using ultrasonic arrays: The multi-mode total focusing method. *NDT & E International*, *43*(2), 123–133. https://doi.org/10.1016/j.ndteint.2009.10.001

Zhao, J., Wu, J., & Chen, K. (2022). Feasibility of Application for the SHG Technology of Longitudinal Wave in Quantitatively Evaluating Carbonated Concrete. *Applied Sciences (Switzerland)*, *12*(24). https://doi.org/10.3390/app122413009

Zhao, J., Wu, J., Chen, X., & Zeng, R. (2022). Effect of Temperature on Ultrasonic Nonlinear Parameters of Carbonated Concrete. *Materials*, *15*(24), 8797. https://doi.org/10.3390/ma15248797

Zhong, F., Zhang, C., Li, W., Jiao, J., & Zhong, L. (2016). Nonlinear ultrasonic characterization of intergranular corrosion damage in super 304H steel tube. *Anti-Corrosion Methods and Materials*, *63*(2), 145–152. https://doi.org/10.1108/ACMM-05-2014-1390

Zhu, B., & Lee, J. (2019). A study on fatigue state evaluation of rail by the use of ultrasonic nonlinearity. *Materials*, *12*(7). https://doi.org/10.3390/ma12172698

Appendices

Brief overview

Paper I studies a corroded steel plate immersed in water to isolate the nonlinear ultrasonic characteristics of corrosion. Several nonlinear ultrasonic methods are studied in Paper II to evaluate concrete slabs with steel liners that have undergone slowly accelerated corrosion. Two types of nonlinear wave modulation methods are studied in Paper III to investigate the feasibility of detecting corrosion while the concrete interface is unaffected by corrosion. Paper IV builds upon the results of Paper I and studies ultrasonic imaging of steel liners embedded in concrete using horizontally polarized shear waves and compressional waves, with evaluations done based on linear and nonlinear parameters.

Appendix A

<div align="right">

Paper I

</div>

Nilsson, M., Ulriksen, P. and Rydén, N., (2023). Nonlinear ultrasonic characteristics of a corroded steel plate. *Nondestructive Testing and Evaluation*. Taylor & Francis, *38(3),* pp. 456–479, doi: 10.1080/10589759.2022.2123481

Taylor & Francis
Taylor & Francis Group

Nonlinear ultrasonic characteristics of a corroded steel plate

Markus Nilsson 📵, Peter Ulriksen and Nils Rydén 📵

Division of Engineering Geology, Department of Biomedical Engineering, Lund University, Lund, Sweden

ABSTRACT

Corrosion in leak-tight plate structures, such as the containment liner in Nuclear Power Plants (NPPs), is detrimental to their operational state. To tackle this issue, the present work aims to assess the feasibility of using nonlinear ultrasound to detect corrosion. The corrosion product of main concern in the present study contains several microscopic and macroscopic cracks and delaminations. Three parameters based on nonlinear acoustics were studied by using two types of measurements on a uniformly corroded steel plate. The relative parameter of quadratic nonlinearity (β'), given by the ratio between the second harmonic amplitude and the fundamental amplitude squared, was measured using indexed measurements with a pitch-catch setup while the specimen was immersed in water. The sideband peak count (SPC), which is a measure of the number of sidebands generated from a wide band excitation, was extracted from through-transmission measurements. The third parameter studied is a measure of the energy distributed in the sidebands over the energy at the excitation frequencies (a). This parameter is determined for the same datasets used for SPC. All three parameters increased in the severely corroded region of the inspected steel plate, indicating the potential use of nonlinear ultrasonics to detect corrosion.

1. Introduction

Nuclear power plants (NPPs) provide a significant portion of electricity in our societies. In Sweden, about 30% of the electricity comes from nuclear power [1]. The reactor containment buildings usually consist of one thick heavily reinforced concrete wall, shielding the reactor from an external threat, and a leak-tight steel plate construction called a containment liner plate (CLP) [2,3]. The purpose of the CLP is to stop radioactive particles from contaminating the surrounding environment if an accident occurs. The CLP typically consists of 6–10-mm-thick pressure vessel quality steel plates. CLP inspection can normally be done by visual inspection [2], thermography [4], and conventional thickness gauging using ultrasound. However, in certain NPPs the CLP is embedded in concrete, thus making it inaccessible which makes Non-Destructive Testing (NDT) of the CLP very challenging.

Due to the global impact of corrosion damage, multiple ways have been devised to inspect different structures for corrosion. For structures that may suffer from corrosion

CONTACT Markus Nilsson ✉ Markus.nilsson@tg.lth.se

damage beneath their accessible surface, for example concrete structures, proposed methods of inspection include electromagnetic methods such as radar [5] and X-ray [6], and acoustical methods such as acoustic emission [7], guided wave testing [8] and ultrasonics [9]. Metal plates are conventionally manufactured by rolling, a metalworking process that relies on passing the material through a series of rolls to reduce the thickness of the material. This process is assumed to form surface-plane parallel internal structures in the plate. When the steel plate then corrodes, such layers are separated, thus creating delaminations and cracks, as seen in Figure 1. Structurally inhomogeneous media, such as metals containing cracks, are known to exhibit strong nonlinear phenomena when excited by elastic waves [10]. In cracked or delaminated media, elastic nonlinearity is caused by effects such as stress concentration at crack tips [11], and stiffness asymmetry (bi-modular elasticity) [12]. Acoustically nonlinear phenomena include the generation of new spectral components in the received acoustic signal. The most commonly studied components are the generation of higher-harmonics and modulation frequencies [13]. Studies into the detection of corrosion-based defects using nonlinear acoustical methods have largely focused on detecting stress corrosion cracking [14–16], intergranular corrosion [17,18], and cracks in concrete structures due to rebar corrosion [19–22]. As shown, several studies into the degradation of reinforced concrete due to rebar corrosion have been carried out. These studies have established that concrete may crack due to embedded elements corroding, and that this cracking can be detected effectively by using nonlinear ultrasonics. However, these studies does not study the nonlinearity of the corroded elements themselves. Instead, the focus is put on the elastic nonlinearity caused by micro-cracks in the surrounding concrete. As this has evidently already been studied extensively, the present work aims to take a different approach.
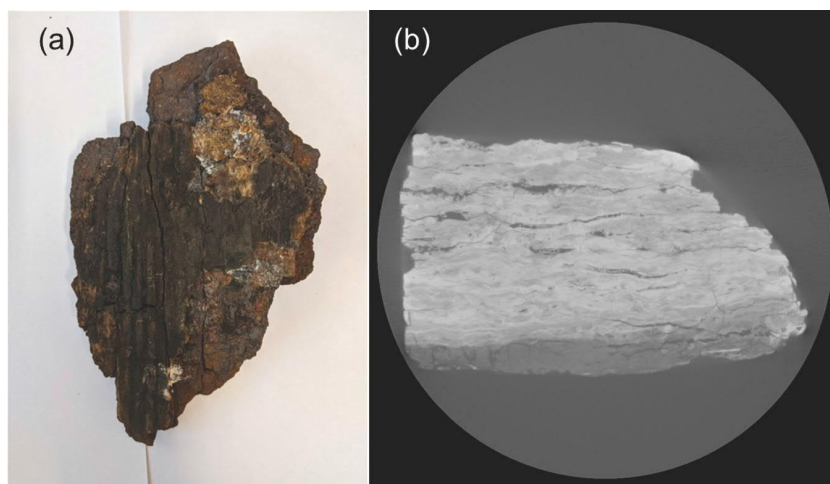

Figure 1. (a) Embedded CLP corrosion product. (b) X-ray tomography showing the cross-section of a piece of the corrosion product shown in (a).
An embedded CLP corrosion product is shown along with X-ray tomography of the corrosion product. The tomography reveals several cracks and delaminations in the cross-section of the corrosion product.

Studies into the detection of general corrosion, also called uniform corrosion [23], using nonlinear acoustical methods are lacking. Uniform corrosion rarely leads to failure and is easily detected visually, which is likely part of the reason why there is a lack of studies on the matter. However, if detection of corrosion attacks at early stages in inaccessible structures is sought, then the detection of gross uniform corrosion must be considered. This is particularly important for structures such as the CLP where the loss of leak tightness is detrimental to the surrounding environment. This study aims to investigate the plausibility of using nonlinear acoustical methods to detect such gross corrosion. Due to the heterogeneity of concrete, it must first be established that corrosion induces significant acoustical nonlinearity on its own before any meaningful conclusions can be drawn from inspection of embedded specimens. This is important because it is not certain that corrosion of plate-like structures embedded in concrete will induce micro-cracking in the concrete. The present work employs two different experimental methods based on probing effects from elastic nonlinearity. To assess the feasibility of using a pitch-catch setup to inspect embedded specimens, the relative parameter of quadratic nonlinearity (β') is measured in an immersed plate using a pitch-catch configuration. The specimen is immersed in water to ensure uniform coupling. The pitch-catch setup is chosen because it is probable that only the inner (or outer) containment wall will be accessible for CLP inspection. It is therefore unlikely that through-transmission will be applicable due to accessibility issues. However, through-transmission measurements can be used to complement the pitch-catch experiment. By applying the Sideband Peak Count (SPC) method [24] in through-transmission experiments, we ensure that energy is transmitted through the corrosion, thus exciting the defects within. The SPC technique relies on using a single wide band excitation to produce and probe intermodulation frequencies, that is, sidebands. Two parameters related to acoustic nonlinearity can be extracted from SPC measurements. These are the SPC itself, which is a measure of the number of sidebands generated, and the nonlinearity parameter α, which is a measure of the energy contained in the sidebands relative to the energy at the excitation components [22].

This study shows that severe uniform corrosion can create crack-like defects (such as delaminations) in the corrosion products. The corrosion also induces severe surface roughness that may affect the measured nonlinearity. Our experiments show that the three parameters of nonlinearity we have studied increase in the severely corroded region of the inspected plate. This indicates that the corrosion-induced defects yield a local increase in elastic nonlinearity.

2. Parameters of acoustic nonlinearity

Conventional ultrasonic methods used for NDT operate on the assumption that linear approximations of the stress–strain relationship hold [25, Ch. 1] due to sufficiently weak excitations. Then, higher-order terms in the governing differential equations can be ignored. However, research has shown that defects such as cracks [26], delaminations [12], and corrosion [17], locally affect the elastic properties to such an extent that this assumption no longer holds, even for low excitation levels. It is well known that crack tips induce stress concentrations that cause acoustic excitations to be locally amplified by several orders of magnitude, thus causing an increase in acoustical nonlinearity [11]. It is

also known that cracks cause stiffness asymmetry in their region as the tensile half-periods of an acoustic excitation will force the crack walls apart, thus weakening the region [12]. Nonlinear acoustical methods for NDT have shown great applicability to monitor progressive damage [27]. However, when cracks grow from microscopic to macroscopic, the measured nonlinearity has been shown to decrease in some instances [28]. This could render some difficulty in detecting gross damage using methods based on probing the effects of elastic nonlinearity.

2.1. Extraction of the relative parameter of quadratic elastic nonlinearity

A simple representation of a nonlinear approximation of a stress–strain relationship that includes classical quadratic nonlinearity can be formulated in terms of Hooke's Law in one-dimension [29]:

$$\sigma(\in) = E(\in + \beta \in^2 + \ldots) \tag{1}$$

where σ is stress; $\in$ is strain; E is the linear elastic modulus; and β is the quadratic parameters of nonlinearity. To examine the differences in material nonlinearity between a pristine specimen and a damaged specimen, β can be used. For longitudinal waves travelling in a solid, β is given by Equation (2) [30], where A_i denotes the displacement amplitude for harmonic component i; x is the propagation distance; $k = f \frac{2\pi}{c}$ is the wave number, where f is the fundamental wave frequency; and c is the sound velocity in the inspected medium. For water, it has been shown [31] that a similar expression, which is half of Equation (2), holds.

$$\beta = \frac{8A_2}{A_1^2 k^2 x} \tag{2}$$

If the transfer functions of the transducers used are not known, then it might be cumbersome to translate the voltage signal into displacement, making it difficult to determine the true parameter of quadratic nonlinearity. In such cases, it might be advantageous to determine the relative parameter of quadratic nonlinearity instead. Given that displacement is proportional to the received voltage signal amplitude, the true quadratic parameter must be proportional to the ratio of the second harmonic amplitude and the fundamental component squared, as given by Equation (3) [13, Ch. 2.2]. When comparing parameter values between different measurements, it is important to either use the same transmitter/receiver pair, or be aware of the acoustic-electric transfer function absolute values at the first and second harmonic for the transducers used. Not adjusting for sensitivity differences could yield erroneous comparisons.

$$\beta \propto \frac{A'_2}{{A'_1}^2} = \beta' \tag{3}$$

Here, $'$ indicates the usage of the measured voltage signal amplitude of the fundamental and second harmonic extracted from the magnitude spectrum of the received signal. As indicated by Equation (2), the parameter does not only vary with displacement amplitudes but varies also with the propagation distance and the wavelength. It is

therefore important to maintain a fixed propagation distance and as similar a wavelength as possible during experiments. Assuming that the frequency is fixed, it is important to note any differences in the sound velocity in each respective specimen. Not correcting for differences might yield erroneous conclusions when comparing parameter values. If the propagation distances in the inspected specimens are not held constant, for example when a plate with varying thickness is inspected, a correction factor must be applied when comparing parameter values. Assuming that the plate has a uniform sound velocity (wave number held constant), then a correction factor can be applied to the areas with differing thickness with respect to a reference thickness x_0. If Equation (2) is studied, it is evident that a large x-value (here plate thickness) will render the lowest β-value. By choosing $x_0 = x_{max}$, this relation is maintained. The corrected β' is then given by Equation (4) where i is the measurement point notation:

$$\beta'_{corr} = \frac{x_{max}}{x_i}\beta'_i = K_i\beta'_i \tag{4}$$

To ensure that the parameters have been measured successfully one of the three input variables can be varied, as discussed extensively in Ref [13, Ch. 2.3.4]. As propagation distance and wave number might be difficult to vary in a controlled manner, varying the excitation amplitude is recommended. For example, if β' is measured successfully, A'_2 should increase linearly with A'^2_1, as seen from Equation (3). The values of the relative quadratic parameter in a measurement point can be extracted by fitting a line to the acquired data points. The slope of the regression line will yield the relative parameter value ($A'_2 = A'^2_1\beta' + m$) as an average of the input amplitudes, given that the correlation coefficient R^2 is high, indicating a good fit. Ideally, the intercept term in the regression-line formulation should be equal to zero, but due to parasitic nonlinearity from the electrical equipment, some offset is expected.

2.2. Sideband peak count

When a structure is subjected to a transient excitation, a wide band of frequency components is excited. If the medium that is being excited is strongly scattering and/or nonlinear, the frequency components contained in the transient will start to interact, thus generating intermodulation components, that is, sidebands. For rigorous mathematical derivations of the generation of modulation components, the reader is referred to Refs [24,32,33]. The Sideband Peak Count (SPC) is defined as the number of sideband peaks above a threshold governed by the weakest dominant peak [32] (Equation (5)). Let the weakest dominant peak be 0.1 times the strongest peak (1 in the normalised spectrum). The sidebands are then assumed to be weaker than 0.1, thus the threshold maximum would be undefined.1. The SPC is defined as the ratio of peaks in the normalised frequency spectrum above the moving threshold ($N(th)$) over the total number of peaks (N_{tot}) greater than the noise level but weaker than the dominant peaks. An illustration of the modulation phenomenon and the SPC method is shown in Figure 2. Here, the excitation is illustrated as having three dominant peaks. When interacting with a linear medium, these are the only frequencies present in the spectrum ((a) in Figure 2). In the nonlinear medium ((b) in Figure 2), the three dominant peaks interact which
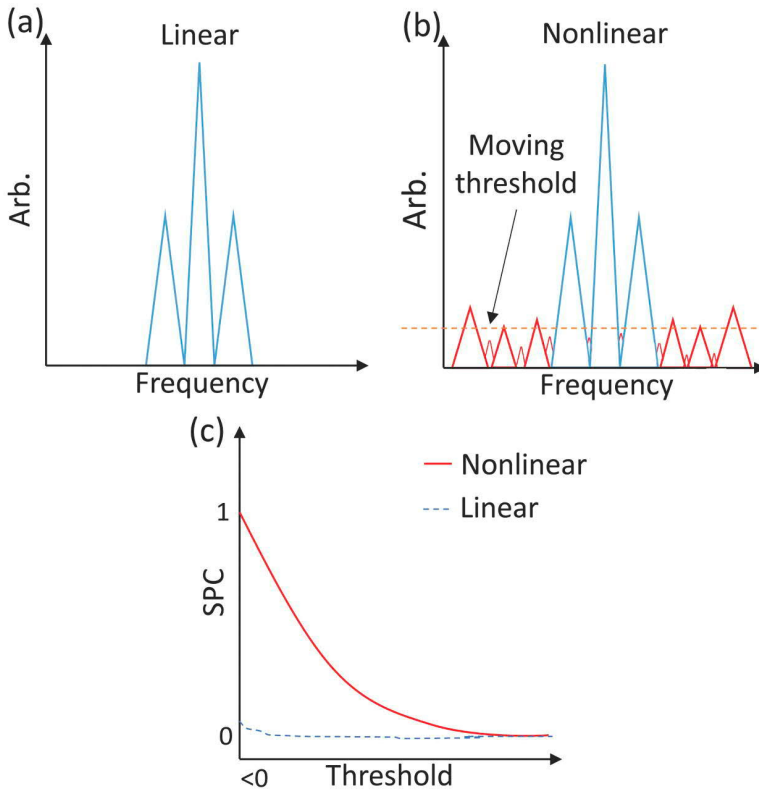
Figure 2. Illustration of the Sideband Peak Count method. (a) a linear response only contains the excitation frequencies, i.E. dominant peaks (blue). (b) the nonlinear response contains the dominant peaks, as well as sidebands generated by intermodulation of the excitation frequencies and nonlinear components (red). (c) the SPC is defined as the ratio between the number of peaks above a moving threshold over the total number of peaks. The SPC approaches zero as the threshold value increases. When a linear medium is excited by a wideband excitation, only the excitation frequencies, that is, dominant peaks, are represented in the frequency spectrum. Here indicated by three peaks. When a nonlinear medium is excited in a similar fashion, additional frequency components are generated, so-called sidebands. In addition to the three dominant peaks, the frequency spectrum now contains several sideband peaks. The sideband peak count (SPC) is a measure of the number of sideband peaks whose magnitudes are greater than some threshold value. At low threshold values, the SPC is greatest, and the SPC will gradually decrease as the threshold value increases.

generates intermodulation components, that is, sidebands. As the wave propagates, the nonlinear effects accumulate and more nonlinear interactions arise, thus generating more sidebands. The moving threshold will then start at some value > 0 and move towards the maximum threshold value, which is given by the weakest dominant peak. At the lowest threshold value, the number of sideband peaks will be the greatest which means that the SPC will start at 1 for the measurement acting as reference. In Figure 2(c) this would be the nonlinear case. As the threshold increases, the SPC will decrease and approach zero, which is illustrated in Figure 2(c). Observe that the illustration in Figure 2(c) shows non-zero SPC for the linear case at low threshold values. This is because there is always some

nonlinearity to be expected, even in pristine specimens due to inherent atomic non-linearity and/or parasitic nonlinearity from the electrical equipment. Note that the dominant peaks are excluded in the SPC, which means that peaks above the maximum threshold will be ignored in the computation.

$$SPC(th) = \frac{N(th)}{N_{tot}} \tag{5}$$

The number of sidebands grows with increasing nonlinearity, but it may be advantageous to compare the energy distributed in the sidebands rather than the number of sidebands. There is always some inherent nonlinearity to be expected due to weak atomic nonlinearity and parasite nonlinearity from the equipment used, and thus, some sidebands will be generated. The authors of [22] proposed a nonlinearity parameter α based on work from [34] that is defined as the energy contained in the nonlinear components, that is, sidebands (W_{NL}), over the linear components, that is, the excitation frequencies (W_L), as given by Equation (6). The energy is conventionally given by the integral of the squared magnitude, but such integrals would also contain energy from noise. The possible impact from noise can be reduced by instead of using the conventional energy, using the sum of the magnitudes of the linear components as W_L, and the sum of magnitudes of the nonlinear components as W_{NL}. Henceforth, the term energy will therefore be used interchangeably with magnitude. This measure of energy distribution is likely more sensitive to structural damage than the SPC as the generation of sideband components might be saturated, meaning that no additional sidebands are detected with increased nonlinearity. However, the increased energy distributed from the fundamental components to the sidebands yields greater magnitudes at these peaks, thus greater α. This is particularly important for experimental considerations as transducers have limited bandwidth, and are therefore only capable of adequately detecting sidebands in a limited frequency band.

$$\alpha = \frac{W_{NL}}{W_L} \tag{6}$$

3. Experimental investigation

3.1. Inspected specimen

The plate inspected in the present work (see Figure 3) was composed of ordinary construction steel and had the approximate dimensions $225 \times 260x8$ *mm*. Initially, it was uniformly sheet corroded over its entire surface, but the sheet corrosion was separated from the plate during handling. A piece of the top sheet corrosion layer with approximate dimensions $90 \times 115x2$ *mm* was reattached to the plate by gluing it using superglue (ethyl 2-cyanoacrylate). Before being glued, the corrosion shell was painted with water-resistant varnish to avoid the dissolution of the corrosion product when immersed in water. The glue was spread evenly across the contact area of the corrosion shell before the shell was placed on the corroded side of the plate (see Figure 3). Gluing likely affects the contact-coupling in the region, as it might induce air bubbles and other inhomogeneities. The corrosion shell was included because, upon an investigation of other pieces of the corrosion product, a large number of delaminations of varying sizes were found. Optical microscopy using a Keyence
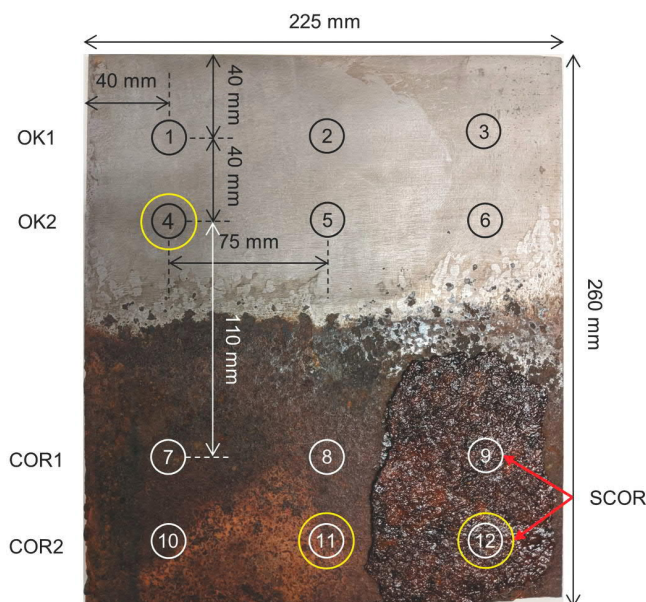
Figure 3. The steel plate used in the present work. Half of the plate was ground with a belt grinder to remove the top corrosion layer. This area is called OK and contains two measurement rows with three measurement points each (OK #1 - #6). The uniformly corroded area is called COR with a measurement point notation of COR #7, #8, #10, and #11. The third area contains the shell-type corrosion product and is denoted SCOR with measurement points SCOR #9 and #12. Data for measurement points highlighted with yellow circles are presented in Figures 8–10 and are used for the SPC measurements presented in Section 4.2.

A steel plate with three distinct regions, one from which corrosion has been removed by means of belt grinding. One uniformly corroded region which is about two-thirds in size of the non-corroded region. The third region is uniformly corroded and contains a reattached corrosion shell. The size of this area is a third of the non-corroded region.

VHX-6000 revealed several surface cracks and delaminations in the bulk of the corrosion shell (Figure 4). X-ray tomography (Figure 5) of a piece of corrosion shell with dimensions $15 \times 15x2 \; mm$ was conducted at the 4D-imaging lab at the division of Solid Mechanics at Lund University using a Zeiss Xradia XRM520 with 13 resolution. The tomography revealed delaminations and cracks in the micro- to macro-scale throughout the cross-section of the corrosion product (Figure 5). Similar delamination characteristics have been found in other corrosion products, as seen in Figure 1 and Refs [35–37]. It is suspected that this delamination characteristic can be found in most corrosion products that are severe enough to be of interest to detect, which makes it interesting to study the feasibility of using nonlinear ultrasound to detect them.

The uniform corrosion on the surface of half the plate area was removed by using a belt grinder to ensure that the only property changes in the plate were due to corrosion. This allowed the plate to have an area deemed undamaged. Due to the grinding and corrosion, the plate had varying thicknesses (6.13–8.67 mm). Table 1 shows the thicknesses at the measurement points as determined using a caliper. The values in
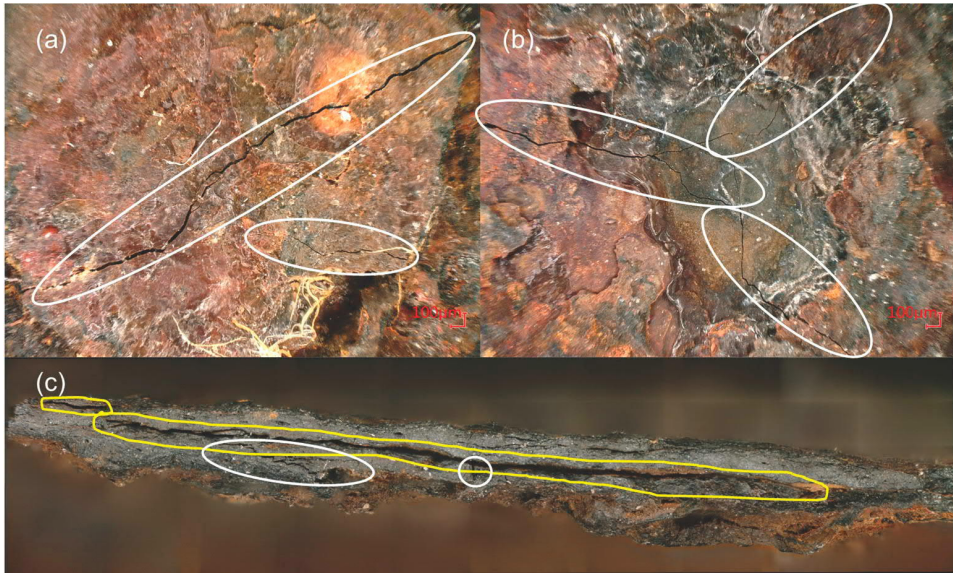
Figure 4. Optical microscopy (Keyence VHX-6000) of a corrosion shell. (a), (b) Cracks in the surface of the corrosion product indicated by white circles. (c) Stitching of several images acquired over the bulk of the corrosion product, indicating severe delaminations (yellow markings) and several cracks (white circles).

Several cracks are noticed on the surface of a sheet corrosion product. The corrosion product also contains delaminations seen in the bulk of the corrosion product.
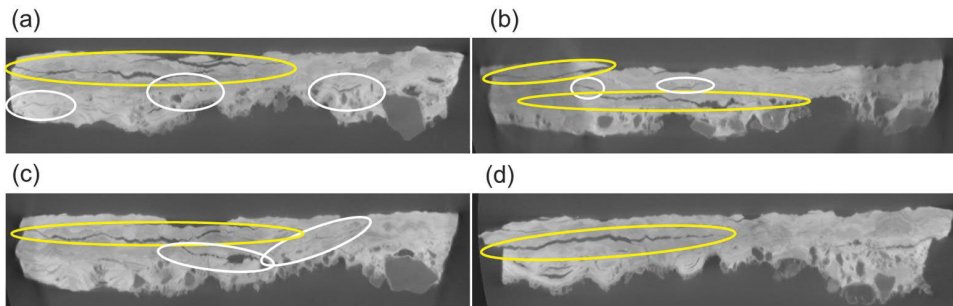

Figure 5. X-Ray tomography showing several delaminations (yellow circles) in the cross-section of a small piece of a corrosion shell. (a) Two clearly visible delaminations and several less visible cracks (white circles). (b) Two large delaminations and several cracks. (c) One large and one less severe delamination. (d) a delamination that is almost perfectly parallel with the surface plane of the corrosion product.

X-ray tomography reveals several cracks and delaminations in the cross-section of a sheet corrosion product.

parentheses are the measured thicknesses before attaching the corrosion shell. Points 5 and 8 were not possible to reach with the caliper, therefore, the thicknesses at these points were estimated by taking an average of the points next to them, that is, points 4 and 6 for

Table 1. Plate thickness at the measurement points.

Measurement point (#)	Plate thickness x_i (mm)
1	6.13
2	6.29
3	7.28
4	7.08
5	*7.36*
6	7.63
7	8.28
8	*8.30*
9	10.7 (8.32)
10	8.62
11	8.67
12	**11.0** (8.53)

point 5 and points 7 and 9 (before the corrosion shell) for point 8. The sound velocity was estimated to be undefined 000 m/s in all regions of the plate. This measurement used a Lecoeur US-key USB ultrasound device coupled with a 5 MHz transducer (Olympus M1042) in a pulse-echo configuration, using the same transducer as a receiver. It is likely that the measured sound velocity is only valid for the bulk of the material and that local velocity variations would occur in the corroded volume.

Since the severity of corrosion-induced damage might vary over the corroded area, the inspection was performed at several measurement points. As can be seen in Figure 3, the entire inspection area was split into 4 rows, 2 in each area of interest, with a total of 12 measurement points. The ground area is called OK, hence OK1 and OK2 describe the rows in the plate area without corrosion. The uniformly corroded area is called COR (for corroded), with measurement rows COR1 and COR2. COR also includes the corrosion shell and measurement points associated with the shell are denoted SCOR. Figure 3 shows the spacing between each measurement point using correct scaling; 75 mm in the horizontal direction and 40 mm in the vertical direction between adjacent rows. The spacing between OK2 and COR1 was 110 mm.

3.2. Determining β' using immersed pitch-catch

A schematic for the pitch-catch configuration used in the present work can be seen in Figure 6. A 4.5 MHz sine-burst with four cycles was generated by an Agilent 33250A waveform generator (AWG). The voltage signal from the AWG was amplified in two steps: first pre-amplified by the Schaffner CBA9425 to reach higher voltage levels than those generated by the AWG, then final amplification using a Xiegu XPA125B amplifier. A total of 6 excitation levels were used: 14, 30, 47, 63, 74, and 80 V_{pp}. Some of these excitation levels could be reached without the two-step amplification. However, the amplification process was kept throughout all measurements to keep potential errors, such as parasitic nonlinearity, constant. The output from the XPA125B amplifier was terminated into a high-power 50 Ω load (Ritec RT50) before the amplified signal was sent to the transmitter. The transmitter was an Olympus V309-SU immersion transducer (**T** in Figure 6) with a centre frequency of 4.5 MHz and a beamwidth (full width at half maximum) of 5 mm measured 130 mm away from the transducer. The number of cycles used was determined by using the thickness of the plate as guidance. The spatial length of the sine-burst must be less than the specimen thickness to avoid generating
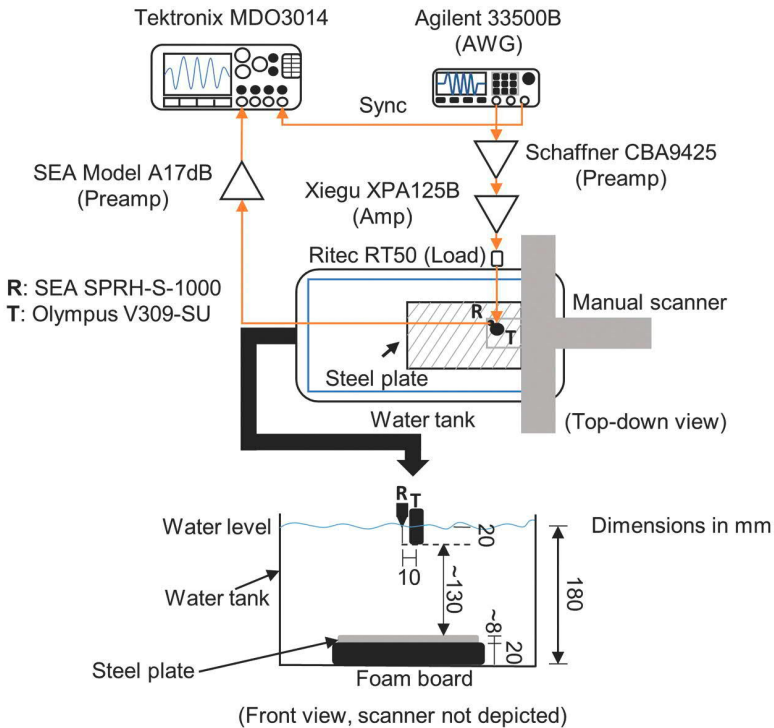
Figure 6. Schematic for the experimental setup used in the reported work.
Decorative schematic of the pitch-catch setup used for the immersion experiment.

spurious harmonics due to interference between incident and reflected waves within the specimen. In the present case, the sound velocity in the bulk material was estimated to be 6000 m/s, which yields a spatial resolution of approximately 5.3 mm for the 4.5 MHz 4-cycle tone-burst. This is less than the thinnest part of the plate (see Table 1). The distance between the plate and the transducer/receiver was kept at approximately 130 mm. As the plate thickness varies, so does this distance. To minimise reflections from the bottom of the water tank, the plate was placed on a 20 mm thick high-density foam board with similar dimensions as the plate. The water temperature was $20 \pm 0.2^\circ$ C. The reflected wave was received by a SEA SPRH-S-1000 needle hydrophone (**R** in Figure 6) with high sensitivity in the frequency band 1.5 MHz to 10 MHz. This frequency range covers both the fundamental frequency (4.5 MHz) and the second harmonic (9 MHz). The hydrophone was placed next to the transducer with an offset of 10 mm measured from the centre of the transducer. As the measured beam width is half of the offset, it is possible that the setup records side-lobes of the reflected signal. Thus, the recorded second harmonics might be weaker than those if the main lobe was recorded. Given that the placement of the transducers is constant, the error is also constant and should not severely impact the parameter comparison between regions. The transducer and hydrophone were placed approximately 20 mm under the water surface as measured from their faces. This implies a total water level of 180 mm relative to the bottom of the water tank. The received signal was pre-amplified with a SEA Model A17 dB before being acquired by a Tektronix MDO3014 oscilloscope. A sync signal from the AWG was used to trigger the

measurement. Each measurement was repeated 16 times for averaging purposes. A manual XY-scanner was used to move the transducer and hydrophone pair to ensure equal and consistent movement of both parts. Post-processing (windowing, DFT, and more) was done on a PC in the MATLAB environment. Measurements were not taken until the plate had been submerged for several minutes to reduce the most immediate effects caused by the effects of thermodynamic perturbation (slow dynamics [38,39]) due to the immersion. The surface of the transducers was carefully wiped with a sponge cloth after moving the transducer-pair to a new point in order to remove any bubbles that may introduce spurious harmonics.

3.3. Through-transmission for SPC

A schematic for the through-transmission setup for the SPC measurements is shown in Figure 7. The steel plate was placed on a foam board resting on a tabletop scissor lift. The purpose of the foam board is to reduce noise from environmental vibrations. A 4.5 MHz 4-cycle Hanning-windowed sine-burst is used to excite the plate which is amplified by a Schaffner CBA9425 amplifier which is terminated by a high-power 50 Ω load (Ritec RT-50). The transmitter (Olympus V309-SU) is pressed to the plate and held by a clamp on a laboratory stand. The receiver (Olympus M1042) is mounted on the plate by magnetic contact. The transducers are coupled to the plate by using ultrasound gel. Both transmitter and receiver have a centre frequency of 4.5 MHz. The received signal is pre-amplified by an HP 8447D Dual pre-amp (25 dB gain) before being collected in an oscilloscope. The data was transferred from the oscilloscope to a PC for post-processing. The SPC measurements were carried out at three points, OK #4, COR #11, and SCOR #12 seen in Figure 3.
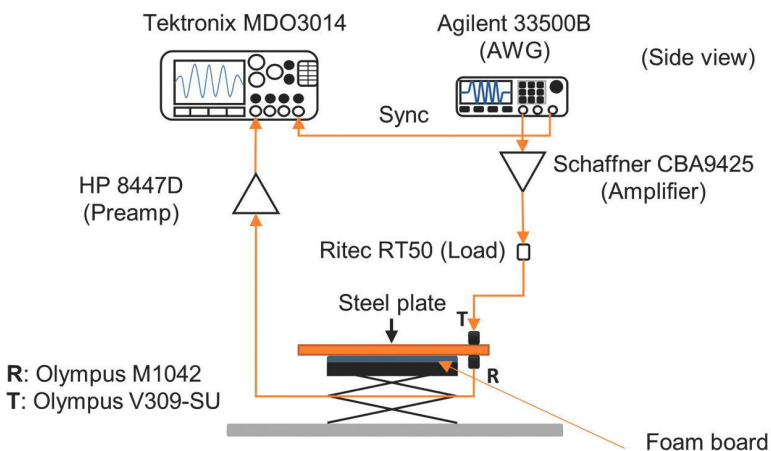

Figure 7. Schematic for the experimental setup used in the SPC measurements (side view). Decorative schematic of the through-transmission experiment.

4. Results and discussion

4.1. Relative quadratic nonlinearity

Figure 8 shows typical time signals at the highest excitation levels for measurement points in each inspected region: OK #4, COR #11, and SCOR #12. The x-markings and vertical dashed lines in the plots indicate the data intervals used for amplitude extraction. The intervals are selected by neglecting the initial and final transient responses to achieve the most stable amplitude level possible for the echo of interest. A steady-state interval would be optimal but would require many more cycles. The time-of-arrival of the echo of interest is estimated by the time-of-arrival for the first echo at region OK, which here is approximately 173.8 μs as seen in Figure 8. As the COR and SCOR regions are both thicker than the OK region, it is expected that echoes from these regions arrive earlier, which is seen in Figure 8. Note that the signals for COR #11 and SCOR #12 both have echoes before the echo of interest. These might originate
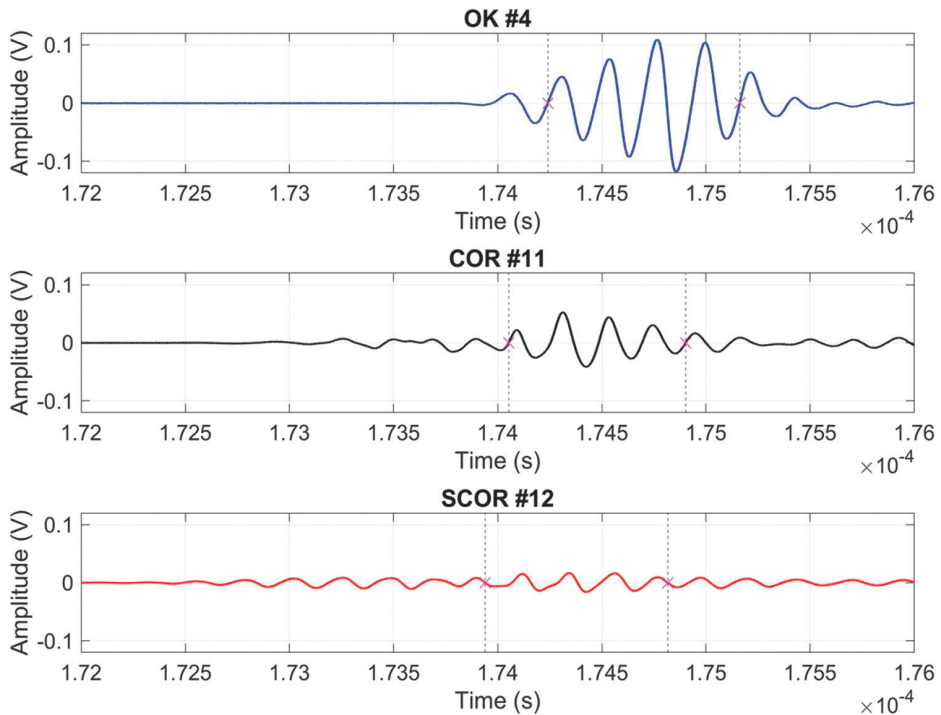

Figure 8. Time signals for measurement points #4 (top, blue line), #11 (middle, black line), and #12 (bottom, red line) at the highest excitation level ($80V_{pp}$). The 'x' markings and vertical dashed lines indicate the intervals extracted for further analysis. Data within these intervals are windowed with a Hanning window before the amplitude spectra are obtained. Note the clear differences in amplitude between the three regions. The inset figures and vertical dashed line show that the time of arrival is slightly faster for the signals collected in the corroded areas.
Time signals represented in voltage versus time plots at measurement points four (OK), eleven (COR), and twelve (SCOR). The intervals extracted for analysis are: OK; one hundred seventy-two and two tenths to one hundred seventy-five and two tenths microseconds. COR; one hundred seventy-four and one tenth to one hundred seventy-four and nine tenths microseconds. SCOR; one hundred seventy-three and nine tenths to one hundred seventy-four and eight tenths microseconds.

from layers in the corroded structure, or they are due to the significant surface roughness in the respective regions. For SCOR #12, likely, the first echo seen in the bottom plot in Figure 8 is caused by the interaction between the glue and corrosion shell. The additional echoes make it difficult to separate successive reflections accurately which in turn makes attenuation correction very challenging. Because of this, no efforts have been made to correct attenuation differences in the regions.

After the data within the marked intervals are extracted, a Hanning window is applied without overlap before amplitude spectra are obtained. The Hanning window is used because it has been shown [13, Ch. 2.4.4] that it causes less intense side-lobes than, for example, the Tukey window does. The magnitude spectra for the time signals in Figure 8 are shown in Figure 9 along with the magnitude spectra for the remaining five excitation levels. The colours represent the six excitation levels as seen in the legend in Figure 9(c). All measurements generated second harmonics. A step-wise attenuation is clearly seen in Figure 9 (a–). The amplitude levels are reduced by more than 50% at each stage of corrosion. The most interesting observation in Figure 9 is the similarity in the second harmonic levels between (b) and (c), corresponding to COR #11 and SCOR #12, respectively. The levels of the second harmonics are almost equal, but the levels of the fundamental components in (c) are less than
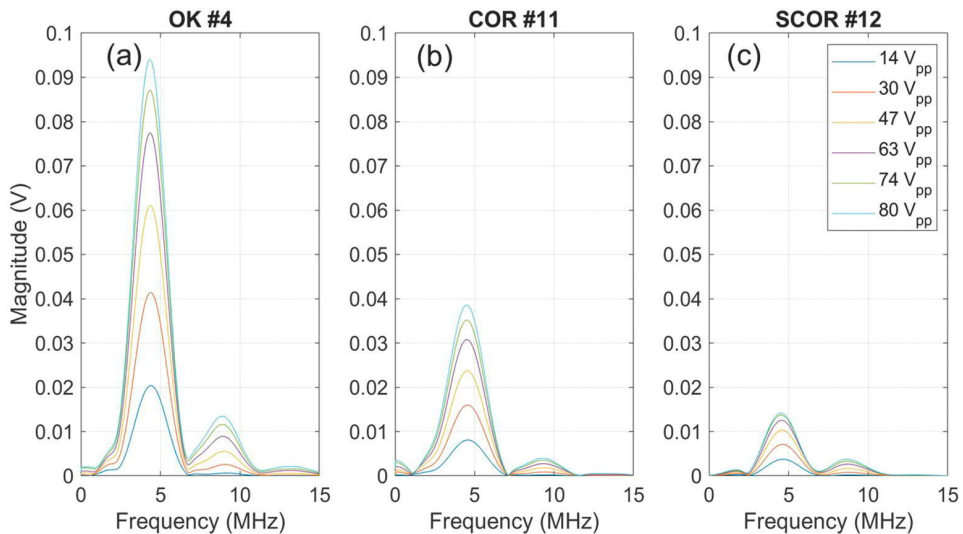

Figure 9. Magnitude spectra obtained at all six excitation levels for the measurement points shown in Figure 8. The spectra corresponding to the time signals shown in Figure 8. are the cyan lines with the highest magnitude. (a) Spectra for measurement point #4 (no corrosion). (b) Spectra for point #11 (uniform corrosion). (c) Spectra for #12 (shell-type corrosion). The amplitude levels decrease at each stage of corrosion. Note the similar level of the second harmonics in (b) and (c), while the level of the fundamental frequency of (c) is less than half of (b). Colours represent the different excitation levels: blue is $14V_{pp}$, orange is $30V_{pp}$, yellow is $47V_{pp}$, purple is $63V_{pp}$, green is $74V_{pp}$, and cyan is $80V_{pp}$. Magnitude in volts plotted versus frequency for the measurements carried out at points four (OK), eleven (COR), and twelve (SCOR). The maximum magnitude at point four was ninety-four millivolts, and the second harmonic magnitude was thirteen millivolts. At point eleven, the corresponding maximums were approximately thirty-nine and four millivolts respectively. At point twelve the maximum values were fourteen and four millivolts.
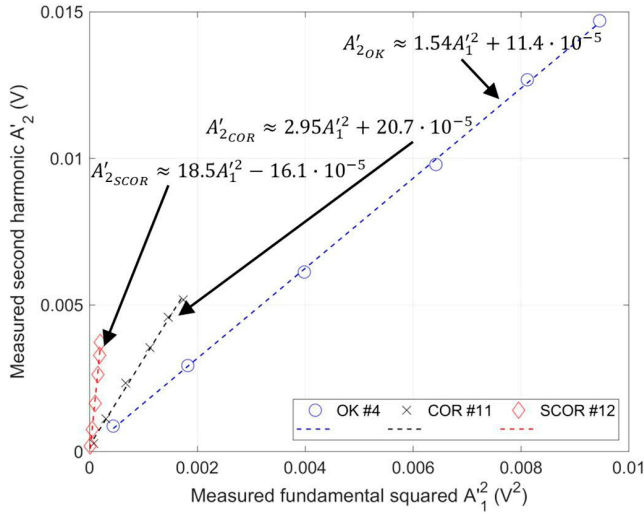
Figure 10. A'_2 plotted versus A'^2_1. Dashed lines are regression lines for the data points (blue circles for #4, black crosses for #11, and red diamonds for #12). The expressions for the regression lines are shown. Note the increase in inclination of the regression lines with increasing grade of corrosion damage.

The magnitudes of the second harmonics for six excitation levels are plotted versus the corresponding magnitude of the fundamental component squared. Data is presented from the measurement points four (OK), eleven (COR), and twelve (SCOR).

half of the corresponding levels in (b). It is also worth mentioning that very clear harmonics are generated for the measurements in OK #4. These could perhaps have been reduced by using a low-pass filter between the XPA125B amplifier and the transmitter, given that the observed harmonics were not generated by small internal defects or inherent atomic nonlinearity.

To determine β', the fundamental (A'_1) and second harmonic (A'_2) amplitudes were extracted from the magnitude spectra as described in Section 2.1. The amplitudes obtained (and squared in the case for A'_1) from the spectra seen in Figure 9 were plotted in Figure 10 along with regression lines fit to the data. By plotting the extracted amplitudes in this manner, the most interesting observation made is the slope of the regression lines. A gradual increase in the slope is seen for increasing grade of corrosion. The slope for OK #4, which is equivalent to β' before the application of correction factor K, is approximately 1.54. The corresponding value is 2.95 for COR #11, and 18.5 for SCOR #12. The computed regression lines for all measurement points have a correlation coefficient (R^2) exceeding 0.99, which indicates a good fit. Table 2 presents β'-values scaled with K given by Eq. ((2.4)). By using $x_{max} = 11.0$ mm (thickness at point #12 from Table 1), the corrected β' for OK #4 is 2.39 ($K_4 = 1.55$) and $\beta'_{11} = 3.74$ ($K_{11} = 1.27$). β'_{12} is still approximately 18.5 as $K_{12} = 1$. The intercept is small and similar for all measurements, which indicates a low level of parasitic nonlinearity from the electrical equipment.

Figure 11(a,b) show A'_1 for all measurement points (refer to Figure 3 for measurement point locations) across the plate and the average A'_1 for each inspected region. The significant difference in attenuation between the three regions is made apparent by plotting the amplitude

Table 2. Thickness correction factors K_i and corrected β' values for all measurement points.

Measurement point (#)	K_i	Corrected β'_i
Region **OK**	-	-
1	1.80	3.08
2	1.75	5.50
3	1.51	3.68
4	1.55	2.39
5	1.49	3.39
6	1.44	1.70
Region **COR & SCOR**	-	-
7	1.33	3.2
8	1.32	2.16
9	1.03	11.7
10	1.28	6.15
11	1.27	3.74
12	1.00	18.5

distribution. Studies of the average A'_1 for each region show that the amplitude levels are reduced by approximately 50% going from OK to COR, and when going from OK to SCOR, the corresponding reduction is 86% on average (72% for COR – SCOR). Granted, there are only two measurement points for SCOR taken into account, which might make the average values less accurate than those for OK and COR, respectively. These results indicate an increase in attenuation with increasing deterioration, which is to be expected as the thickness of the corrosion is largest in this area due to the added corrosion shell. Moreover, it is well-known that corrosion induces significant acoustic attenuation [40]. When studying the levels of A'_2 in Figure 11(c,d) similar contrasts are seen. By looking at A'_2 alone, erroneous conclusions concerning the material state might be drawn if high harmonic amplitudes are assumed to indicate damage. The region with removed corrosion exhibits significantly higher harmonic amplitudes than the corroded region. If β' is studied instead, a similar but inverted contrast is acquired, as indicated by Figure 11(e,f) where the β' values from Table 2 are used. Even if attenuation differences likely also affect the β' values, it would seem that the parameter is sensitive to the damage type induced by the shell-type corrosion product. As indicated by Figures 4 and 5, the shell-type corrosion products likely contain several severe delaminations and cracks, which could explain the vast increase in β'. This result shows the importance of quantifying the nonlinear response in other ways than harmonic amplitudes. Direct use of harmonic imaging for detecting uniform corrosion damage might give false indications of damage in pristine areas of a specimen. This is because the strong attenuation might cause low harmonic levels in the corroded regions. Furthermore, the result also indicates the importance of indexed measurements or scanning techniques to detect corrosion, as single-point measurements might not be sufficient to detect corrosion defects.

It is clear that corrosion induces significant acoustic attenuation, which is likely at least partially due to the diffraction caused by increased surface roughness. The beamwidth in the configuration used in the pitch-catch measurements was 5 mm, which is greater than the diameters of most of the peaks and troughs caused by increased roughness in the corroded regions. When the sound beam hits the surface, it is likely partially scattered, which ultimately leads to a less intense sound wave being recorded by the hydrophone. This would likely not be an issue if the corrosion is embedded in concrete as concrete itself is a heterogeneous material, thus effectively scattering internal vibrations.
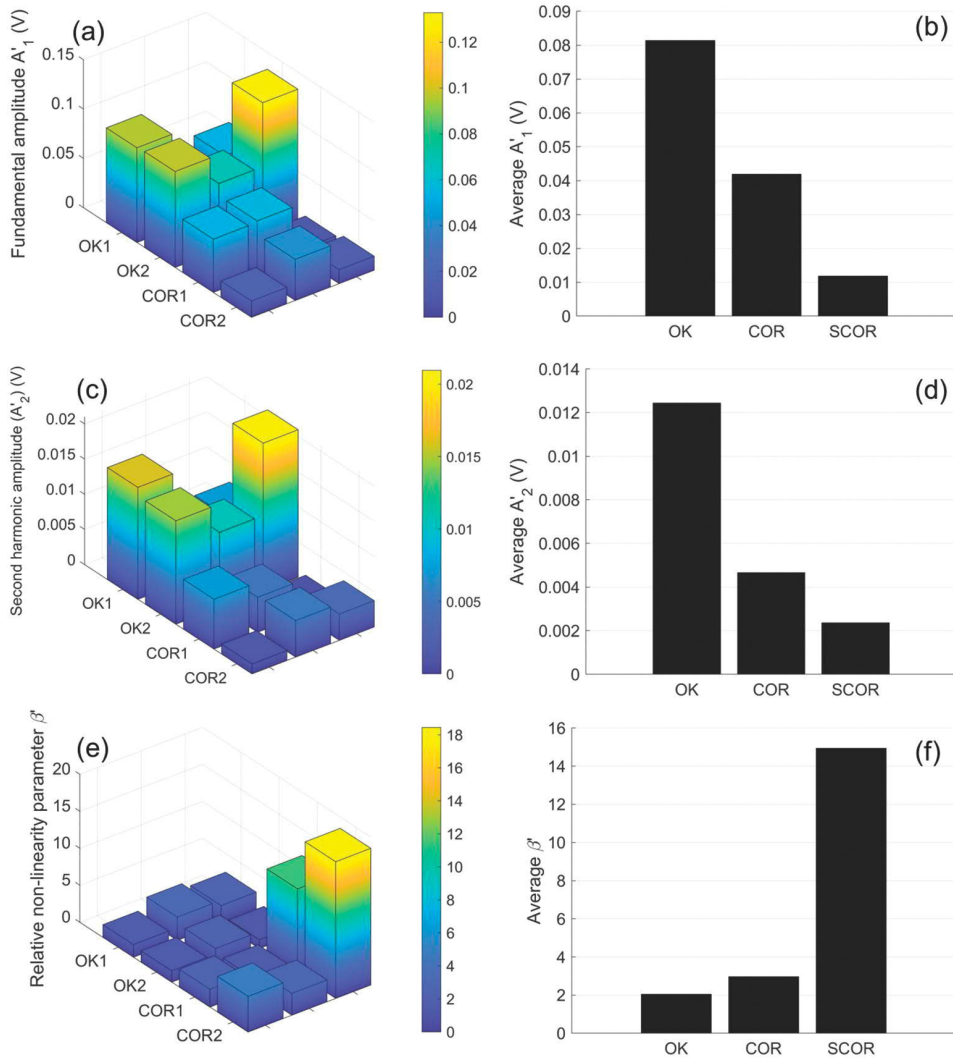
Figure 11. (a) A'_1 levels at the highest excitation level for each measurement point on the plate. A sudden decrease in amplitude level is displayed between the OK and COR regions, with an even more significant decrease in the SCOR area. (b) Average A'_1 at each region. (c) Corresponding A'_2 levels and the clear contrast between OK and COR. (d) the average A'_2 levels. (e) β' values obtained for each measurement point with applied correction factors (values presented in Table 2). The difference between OK and COR is not as significant as in (a) and (c), and no contrast between the two main regions (OK and COR) is observed. However, β' values at the SCOR region clearly stand out from all other measurement points. Refer to Figure 3 for measurement point locations. f) Average β'.

(a) Isometric three-dimensional bar plot of the amplitudes of the fundamental component at each measurement point. (b) Bar plot of the average fundamental amplitudes at regions OK, COR, and SCOR respectively. The levels are approximately eighty-one millivolts at OK, forty-two millivolts at COR, and twelve millivolts at SCOR. (c) Isometric three-dimensional bar plot of the amplitudes of the second harmonics generated at each measurement point. (d) Bar plot of the average second harmonic magnitudes at each measurement region. The levels are approximately twelve millivolts at OK, four and seven tenths of a millivolt at COR, and two and four tenths of a millivolt at SCOR. (e) Isometric three-dimensional bar plot of the β prime distribution. (f) Bar plot showing the average β prime values at each region. The values are three and three tenths at OK, three and eight tenths at COR, and fifteen at SCOR.

Moreover, the offset of the receiver hydrophone might result in side-lobes of the reflected signals being recorded. This could affect the recorded harmonic levels, as they are expected to be highest in the main lobe. The surface roughness in the corroded region and the small slopes in the ground area (OK) likely also affects the measurements as it induces mode conversion. The experimental setup could be further optimised by using a low-pass filter before the transmitter to reduce parasite nonlinearities originating from the electronics, and by using a broadband transducer capable of both acting as transmitter and receiver with adequate sensitivity at the second harmonic.

4.2. Sideband peak count and a

The received signals from the transmission measurements in points OK#4, COR#11, and SCOR#12 are shown in Figure 12. By simply looking at the signals, it is evident that SCOR induces greater self-interaction than at the other two measurement points. This is likely caused by reflections in the top corrosion layer and these reflections cause challenges if echoes were to be separated for accurate attenuation correction. Because of this, efforts towards attenuation correction are not made.

To determine the number of sideband peaks for each measurement, the magnitude spectrum is computed over the entire time signal with a rectangular window. The spectra
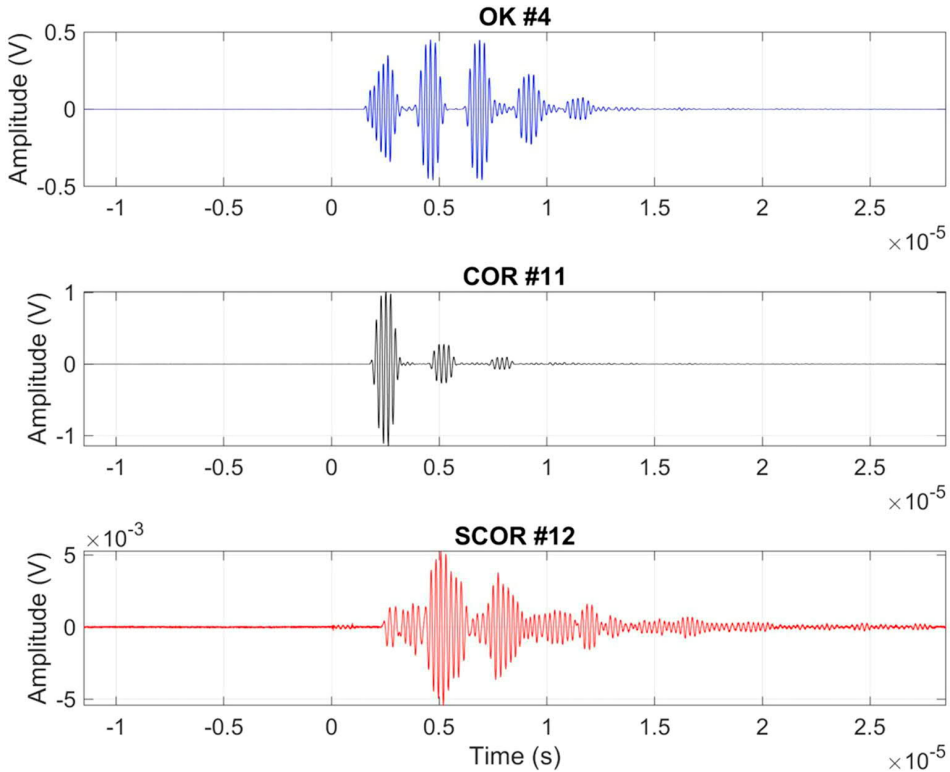

Figure 12. Received voltage signals at points OK #4 (upper), COR #11 (middle), and SCOR #12 (bottom). Voltage signals versus time acquired from the through-transmission measurements. The signals from points four and eleven indicate clear separation between echoes. The signal acquired at point twelve has no clear separation between echoes, indicating self-interaction.
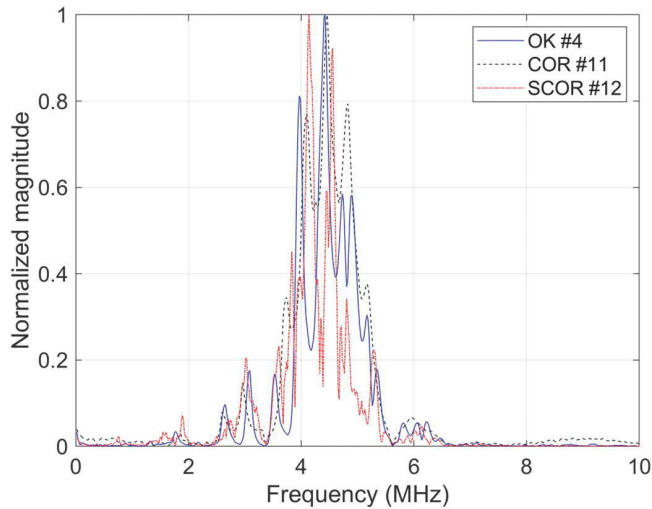
Figure 13. Normalised frequency spectra for the time signals at OK #4 (blue line), COR #11 (black dashed), and SCOR #12 (red dash-dotted).
Normalized spectra indicating that the weakest dominant peak to be around six percent of the strongest dominant peak.

are then self-normalised with respect to their maximum magnitude. The spectra are shown in Figure 13. The majority of energy is found in the detection bandwidth 0–10 MHz and is thus the band of main concern for the sideband analysis. By studying Figure 13, the dominant peaks, i.e. linear components, are found to be as weak as 6% of the maximum magnitude. This yields the maximum threshold of 0.06. The SPC (Figure 14 upper) is determined by Equation (5) with the threshold varying from > 0 to 0.06 at steps of 0.005. It is evident that if Equation (5) is applied, the SPC will always start at 1 as the SPC is normalised for the total number of peaks for each measurement. In the present work, the SPC is instead normalised for the maximum number of peaks found at the reference region, and the same N_{tot} is used for all SPC computations. Here, this meant normalising by the total number of peaks acquired at OK#4. The SPC is shown to be consistently greater at the measurement points in the corroded regions compared to the non-corroded, especially at the lower thresholds. There is no significant difference in SPC between COR and SCOR, except at the minimum threshold.

As stated in Section 2.2, the level of nonlinearity might be better indicated by considering the energy contained in the sidebands relative to the energy in the excitation frequencies (dominant peaks), that is, the nonlinearity parameter α as given by Equation (6). The parameter is determined using the same data used in the SPC method. For comparative purposes, the α values were normalised with respect to the maximum parameter value found at OK#4. As seen in the lower part of Figure 14 there is a more clear separation between the regions and α is found to be more than twice as high at SCOR#12 compared to OK#4 at low threshold levels. Interestingly, although COR and SCOR had almost the same SPC, the α is significantly smaller for COR. Beyond the threshold level of 0.03, both COR and SCOR exhibit lower α and they approach 0 before OK does. This indicates that the weaker nonlinearity in the
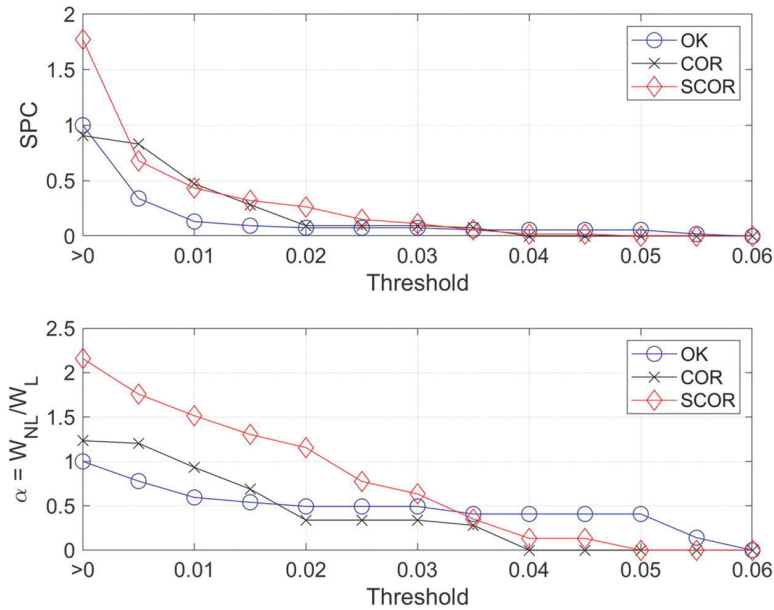
Figure 14. (Upper) SPC as a function of threshold varying from 0 to 0.06 of the maximum magnitude. (Lower) Parameter of nonlinearity a as a function of threshold normalised with respect to the maximum value for OK#4. Both parameters have been normalised by the respective maximum values found at point OK#4.

(Upper) The SPC graph shows that the greatest SPC at point twelve (SCOR) is approximately one and eight tenths times greater than the SPC at point four (OK). The corresponding SPC at point eleven is nine tenths of the SPC at point four. The SPC decreases exponentially until it reaches zero at the threshold value fifty-five tenths. (Lower) The a parameter value acquired at point twelve (SCOR) is two and two tenths greater than the corresponding value at point 4 (OK). The corresponding value at point eleven (COR) is one and two tenths greater than OK number four. The parameter value decreases in a linear fashion and reaches zero at the threshold value six tenths for OK, four tenths for COR, and five tenths for SCOR.

OK region causes the energy to be distributed to fewer frequency components, thus resulting in peaks with greater magnitudes but fewer sideband peaks in relation to those in the corroded regions. In the corroded regions, the energy is distributed to a greater number of frequencies and initially, the total energy contained in these peaks is greater than those at OK. As the threshold increases, the distributed energy is drastically reduced as the weaker but plentiful sidebands are ignored. Similarly, the uniformly corroded region COR had a similar SPC but the energy distributed to these peaks was lower than for SCOR. This indicates a clear step-wise increase in acoustical nonlinearity with an increasing grade of corrosion.

4.3. Comparing β′ , SPC, and α

Comparing the results gained from the pitch-catch measurements determining β' and those obtained from the transmission SPC and α measurements, it is found that the nonlinearity increases with increasing grade of corrosion. However, the increase is likely not as dramatic as

indicated by β' in Figure 11(f)). Due to the difficulty of accurately extracting echoes from the measurements on SCOR measurement points, efforts were not made towards determining attenuation correction factors. It is assumed that if attenuation correction was applied in the pitch-catch measurements, the β' values at SCOR (and COR) would likely drop and perhaps indicate a similar trend as shown in the α distribution in Figure 14. Regardless, there are identifiable signal differences between the specimen regions which is significant for NDT purposes in real-life engineering applications such as the inspection of CLPs.

As shown in the micro- and tomographs in Figures 4 and 5 respectively, the SCOR-type corrosion product has several defects from microscopic ($10^{-6}m$) to macroscopic ($> 10^{-3}m$). This makes it very challenging to determine the exact source of nonlinearity as there might be many different contributing factors, some of which may be related to stress concentration at crack tips, and stiffness asymmetry. Moreover, the presence of large defects may decrease the measured nonlinearity, thus causing a weaker contrast between the inspected regions. This hypothesis cannot be confirmed by the present work due to its qualitative nature, however, previous quantitative research into damage evolution has indicated such trends [28].

It is clear that the inspected corroded regions have very rough surfaces. The effect of the roughness on the measured nonlinearity parameters are not entirely clear. Scattering causes greater attenuation, and mode conversions contribute to more complex effects possibly skewing the nonlinearity. There may be additional effects whose impact on the results are unknown. Previous research has indicated that roughness variations smaller than the probing wavelength in the coupling media may increase the observed nonlinearity [41]. However, it is has also been shown that rough surfaces may affect measurement reliability negatively [42]. The effects from roughness variations that are in the same order or greater than the probing wavelength in the coupling media is not clear. In addition to the cracks and delaminations found in corrosion products, it is suspected that roughness caused by corrosion affects the signal content. Thus, creating considerable signal differences between a smooth (non-corroded) and rough (corroded) surface. These differences may be utilised for NDE purposes. An evaluation of these effects is outside the scope of this paper, but greatly encouraged.

5. Conclusions

This study demonstrates that severe corrosion products with internal defects such as cracks and delaminations with sizes in the orders of magnitude from micro- to macroscopic can be detected and possibly localised using nonlinear ultrasound. Three parameters of acoustic nonlinearity were studied. The relative parameter of quadratic nonlinearity β' is given by the ratio between the second harmonic amplitude and the fundamental amplitude squared. This parameter was measured by using a pitch-catch setup, which is the most realistic setup for the inspection of a containment wall. The sideband peak count (SPC) is a measure of the number of sideband peaks generated by a wide band excitation. The parameter α describes the energy distributed in the nonlinear sideband components relative to the linear excitation components. The SPC measurements were based on through-transmission measurements to ensure that internal defects were excited. All three parameters indicated a significant increase in nonlinearity in the region containing the shell-type corrosion product with cracks and delaminations. The

regular uniformly corroded region did not exhibit any significant increase in β', but both SPC and α indicated a small increase over the non-corroded region. Building upon these initial results, future work will investigate if the inherent nonlinearity caused by the heterogeneous nature of concrete will mask the nonlinearity from corroded plates. To this end, inspection of various concrete samples with embedded corroded steel plates will be carried out.

Disclosure statement

The authors declare that they have no known competing financial interests or personal relationships that could have appeared to influence the work reported in this paper.

ORCID

Markus Nilsson   http://orcid.org/0000-0002-6560-0029
Nils Rydén   http://orcid.org/0000-0001-7138-2622

CRediT authorship contribution statement

Markus Nilsson: Conceptualisation, Methodology, Software, Investigation, Formal analysis, Visualisation, Writing – Original Draft, Writing – Review & Editing.
Peter Ulriksen: Conceptualisation, Supervision, Funding acquisition, Resources, Writing – Review & Editing.
Nils Rydén: Conceptualisation, Supervision, Writing – Review & Editing.

References

[1] Swedish Radiation Safety Authority. Nuclear power; 2022. Available from: https://www.stralsakerhetsmyndigheten.se/en/areas/nuclear-power/
[2] Paek Y, Kim S, Yoon E, et al. Introduction of Containment Liner Plate (CLP) corrosion. In: Transactions of the Korean nuclear society spring meeting. Jeju, Korea: Korean Nuclear Society; 2018. p. 17–19.

[3] Dunn D, Pulvirenti A, Klein P. Containment liner corrosion. Vol. 2, 15th International Conference on Environmental Degradation of Materials in Nuclear Power Systems-Water Reactors 2011 Colorado Springs, CO, USA; 2011. p. 985–996.

[4] Renshaw JB, Lhota JR, Muthu N, et al. Thermographic inspection of pipes, tanks, and containment liners. AIP Conf Proc. 2015;1650(April 2015):290–297.

[5] Tešić K, Baričević A, Serdar M. Non-Destructive corrosion inspection of reinforced concrete using ground-penetrating radar: a review. Materials. 2021;14(4):1–20.

[6] Michel A, Pease BJ, Geiker MR, et al. Monitoring reinforcement corrosion and corrosion-induced cracking using non-destructive x-ray attenuation measurements. Cement Concr Res. 2011;41(11):1085–1094. DOI:10.1016/j.cemconres.2011.06.006.

[7] Zaki A, Chai HK, Aggelis DG, et al. Non-Destructive evaluation for corrosion monitoring in concrete: a review and capability of acoustic emission technique. Sensors (Switzerland). 2015;15(8):19069–19101. DOI:10.3390/s150819069.

[8] Zhu W, Rose JL, Barshinger JN, et al. Ultrasonic guided wave NDT for hidden corrosion detection. Res Nondestr Eval. 1998;10(4):205–225. DOI:10.1080/09349849809409629.

[9] Zhao X, Gao H, Zhang G, et al. Active health monitoring of an aircraft wing with embedded piezoelectric sensor/actuator network: I. Defect detection, localization and growth monitoring. Smart Mater Struct. 2007;16(4):1208–1217. DOI:10.1088/0964-1726/16/4/032.

[10] Rudenko OV. Giant nonlinearities in structurally inhomogeneous media and the fundamentals of nonlinear acoustic diagnostic techniques. Phys Usp. 2006;49(1):69–87.

[11] Rudenko OV, Korobov AI, Izosimova MY. Nonlinearity of solids with micro- and nanodefects and characteristic features of its macroscopic manifestations. Acoust Phys. 2010;56(2):151–157.

[12] Solodov I, Krohn N, Busse G. CAN: an example of nonclassical acoustic nonlinearity in solids. Ultrasonics. 2002;40(1–8):621–625.

[13] Jhang K-Y, Lissenden CJ, Solodov I, et al. Measurement of nonlinear ultrasonic characteristics. Singapore: Singapore Nature Singapore Pte Ltd; 2020.

[14] Matlack KH, Kim JY, Jacobs LJ, et al. Nonlinear Rayleigh waves to detect initial damage leading to stress corrosion cracking in carbon steel. AIP Conf Proc. 2012;1430(31):1452–1459.

[15] Zeitvogel DT, Matlack KH, Kim JY, et al. Characterization of damage due to stress corrosion cracking in carbon steel using nonlinear surface acoustic waves. AIP Conf Proc. 2013;1511(January 2013):1286–1293.

[16] Hogg SM, Anderson BE, Le Bas PY, et al. Nonlinear resonant ultrasound spectroscopy of stress corrosion cracking in stainless steel rods. NDT E Int. 2019;102(October 2018):194–198. DOI:10.1016/j.ndteint.2018.12.007.

[17] Jiao J, Fan Z, Zhong F, et al. Application of ultrasonic methods for early detection of intergranular corrosion in austenitic stainless steel. Res Nondestr Eval. 2016;27(4):193–203. DOI:10.1080/09349847.2015.1103922.

[18] Zhong F, Zhang C, Li W, et al. Nonlinear ultrasonic characterization of intergranular corrosion damage in super 304H steel tube. Anti-Corros Methods Mater. 2016;63(2):145–152. DOI:10.1108/ACMM-05-2014-1390.

[19] Korenska M, Matysik M, Vyroubal P, et al. Assessment of reinforcement corrosion using nonlinear ultrasonic spectroscopy. NDT in Progress 2009 - 5th International Workshop of NDT Experts, Proceedings Prague, Czech Republic; 2009. p. 143–151.

[20] Antonaci P, Bruno CL, Scalerandi M, et al. Effects of corrosion on linear and nonlinear elastic properties of reinforced concrete. Cement Concr Res. 2013;51:96–103. DOI:10.1016/j.cemconres.2013.04.006.

[21] Climent MÁ, Miró M, Carbajo J, et al. Use of non-linear ultrasonic techniques to detect cracks due to steel corrosion in reinforced concrete structures. Materials. 2019;12(5):813. DOI:10.3390/ma12050813.

[22] Arumaikani T, Sasmal S, Kundu T. Detection of initiation of corrosion induced damage in concrete structures using nonlinear ultrasonic techniques. J Acoust Soc Am. 2022;151(2):1341–1352.

[23] Féron D. Nuclear corrosion science and engineering. 22nd ed. Cambridge, UK: Woodhead Publishing Limited; 2012. p. 22.

[24] Kundu T, Eiras JN, Li W, et al. Fundamentals of nonlinear acoustical techniques and sideband peak count. In: Kundu T, editor. Nonlinear ultrasonic and vibro-acoustical techniques for nondestructive evaluation. Chapter 1. Cham, Switzerland: Springer Nature Switzerland; 2019. p. 1–88.

[25] Kundu T, editor. Nonlinear ultrasonic and Vibro-acoustical techniques for nondestructive evaluation. Cham, Switzerland: Springer Nature Switzerland AG; 2018.

[26] Nazarov VE, Sutin AM. Nonlinear elastic constants of solids with cracks. J Acoust Soc Am. 1997;102(6):3349–3354.

[27] Hedberg CM, Johnson E, Andersson SA, et al. Ultrasonic monitoring of a fiber reinforced plastic - Steel composite beam during fatigue. Vol. 2, Proceedings of the 6th European Workshop - Structural Health Monitoring 2012, EWSHM 2012 Dresden, Germany. 2012. p. 1254–1260.

[28] Donskoy D, Liu D. Vibro-Acoustic modulation baseline-free non-destructive testing. J Sound Vibr. 2021;492:115808. DOI:10.1016/j.jsv.2020.115808.

[29] Zaitsev VY. Nonlinear acoustics in studies of structural features of materials. MRS Bull. 2019;44(5):350–360.

[30] Kube CM, Arguelles AP. Ultrasonic harmonic generation from materials with up to cubic nonlinearity. J Acoust Soc Am. 2017;142(2):EL224–EL230. DOI:10.1121/1.4998139.

[31] Pantea C, Osterhoudt CF, Sinha DN. Determination of acoustical nonlinear parameter β of water using the finite amplitude method. Ultrasonics. 2013;53(5):1012–1019. DOI:10.1016/j.ultras.2013.01.008.

[32] Hafezi MH, Alebrahim R, Kundu T. Peri-Ultrasound for modeling linear and nonlinear ultrasonic response. Ultrasonics. 2017;80:47–57. DOI:10.1016/j.ultras.2017.04.015.

[33] Xu Y, Wang Q, Jiang X, et al. Nondestructive assessment of microcracks detection in cementitious materials based on nonlinear ultrasonic modulation technique. Constr Build Mater. 2021;267:121653. DOI:10.1016/j.conbuildmat.2020.121653.

[34] Chen XJ, Kim JY, Kurtis KE, et al. Characterization of progressive microcracking in Portland cement mortar using nonlinear ultrasonics. NDT E Int. 2008;41(2):112–118. DOI:10.1016/j.ndteint.2007.08.009.

[35] Neff D, Harnisch J, Beck M, et al. Morphology of corrosion products of steel in concrete under macro-cell and self-corrosion conditions. Mater Corros. 2011;62(9):861–871. DOI:10.1002/maco.201005861.

[36] Poupard O, L'Hostis V, Catinaud S, et al. Corrosion damage diagnosis of a reinforced concrete beam after 40 years natural exposure in marine environment. Cement Concr Res. 2006;36(3):504–520. DOI:10.1016/j.cemconres.2005.11.004.

[37] Köliö A, Honkanen M, Lahdensivu J, et al. Corrosion products of carbonation induced corrosion in existing reinforced concrete facades. Cement Concr Res. 2015;78:200–207. DOI:10.1016/j.cemconres.2015.07.009.

[38] Guyer RA, Johnson PA. Nonlinear mesoscopic elasticity: evidence for a new class of materials. Phys Today. 1999;52(4):30–36.

[39] Khodabandeloo B, Hedberg C, Berghuvud A. Resonance frequency measurements of a few materials for temperature variations resonance frequency measurements of a few materials for temperature variations analysis. Proceedings of the Baltic-Nordic Acoustic Meeting 2014 Tallinn, Estonia; 2014. June.

[40] Magda P, Stepinski T. Corrosion assessment using ultrasound. Diagnostyka. 2015;16(1):15–17.

[41] Yuan M, Dai A, Liao L, et al. Numerical study on surface roughness measurement based on nonlinear ultrasonics in through-transmission and pulse-echo modes. Materials. 2021;14(17):4855. DOI:10.3390/ma14174855.

[42] Chakrapani SK, Howard A, Barnard D. Influence of surface roughness on the measurement of acoustic nonlinearity parameter of solids using contact piezoelectric transducers. Ultrasonics. 2018;84:112–118. DOI:10.1016/j.ultras.2017.10.022.

Appendix B

Paper II

Nilsson, M., Huttunen-Saarivirta, E., Bohner, E. and Ferreira, M., (2023). Non-destructive evaluation of corrosion in steel liner plates embedded in concrete using nonlinear ultrasonics. *Construction and Building Materials*. Elsevier Ltd, *408(September),* p. 133691, doi: 10.1016/j.conbuildmat.2023.133691
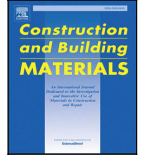
Non-destructive evaluation of corrosion in steel liner plates embedded in concrete using nonlinear ultrasonics

Markus Nilsson [a,*], Elina Huttunen-Saarivirta [b], Edgar Bohner [b], Miguel Ferreira [b]

[a] *Division of Engineering Geology, Faculty of Engineering, Lund University, Lund, Sweden*
[b] *VTT Technical Research Centre of Finland Ltd, Espoo, Finland*

ARTICLE INFO

ABSTRACT

Nuclear containment structures employ a leak-tight steel liner to avoid any unwanted particle release into the exterior environment. The steel liner can be embedded in concrete which creates large continuous areas where the steel plate is in direct contact with surrounding concrete. The impact of the aging of concrete structures due to the presence of structural discontinuities, such as the presence of foreign matter and a delamination gap at the embedded steel–concrete interface, is investigated for small laboratory-scale specimens manufactured with a novel inlay technique by nonlinear ultrasonic evaluation. A Total Damage Index (TDI) which combines several parameters related to acoustic wave distortion into a single damage index to rank the specimens is introduced. The findings in this work indicate that severe corrosion, the presence of foreign matter, and delamination gap in the steel–concrete interface can be detected using nonlinear ultrasonic techniques based on higher-harmonic analysis and modulation intensity using continuous ultrasonic probe excitation and an impactor to modulate the signal. The results obtained using the TDI are consistent with attenuation, a conventional parameter used in corrosion detection.

1. Introduction

Containment structures housing nuclear reactors shield the exterior environment from radioactive release in the event of an accident by employing several engineering barriers. One of the barriers is a gas-tight steel liner plate, which in certain structures is embedded in heavily reinforced concrete roofs and walls. As the liner plate is surrounded by an alkaline concrete environment, it should not undergo significant corrosion during the designed lifetime due to a protective passive film forming on the steel surface. However, cases have been described in the literature in which corrosion attacks have perforated the liner plate and even caused through-wall corrosion, due to the presence of embedded foreign matter in contact with the liner, or cavities in the concrete near the liner plate [1]. It is also acknowledged that substantial drying of the thick concrete walls may not occur until several decades after construction [2], which may result in cavities near the liner being partially filled with water (an electrolyte). Also, if in contact with ambient air from outside of the structure, the atmospheric CO_2 may react with concrete, resulting in its carbonation. The presence of foreign matter, delamination gap in the steel–concrete interface or concrete cavities near the steel liner may locally lower the pH level

of the environment at the steel surface, challenging the passivity and supply oxygen in other areas, facilitating localized corrosion of the steel liner plate at the location of lowered pH. As the corrosion attack is then concentrated on a small area of the otherwise passive steel surface, the leak tightness of the liner plate may be compromised long before the expected operating lifetime is reached. Additionally, the concrete may begin to crack around the corroded area due to the volumetric expansion by the formation of corrosion products, which further impairs the structural integrity of the concrete containment [3]. Particularly, the concrete cover depth is a meaningful parameter in defining the time to cracking [4]. However, when cracking is visually evidenced, the corrosion initiation stage has already passed and the degradation has progressed to the propagation phase [5]. It is therefore of paramount importance to be able to detect the initiated corrosion at the earliest possible stage by non-destructive means to implement adequate remedies.

Non-Destructive Testing (NDT) refers to a group of analysis techniques for evaluating the properties of a material, component, or structure without influencing its future serviceability. For example, conventional acoustic NDT methods typically rely on the generation of

Table 1
Concrete recipe used in casting of the concrete slabs.

Concrete mix for slabs		Weight (kg/m3)		Volume (dm3/m3)
Cement CEM II/B-M (S-LL) 42.5 N (Parainen)		380		123
Aggregates (dry)	0.1–0.6 mm	361.6	1808	672
	0.5–1.2 mm	180.8		
	1.0–2.0 mm	361.6		
	3.0–6.0 mm	542.3		
	0.0–8.0 mm	361.6		
Effective water content		175		175
Superplasticizer MasterGlenium SKY 600 (BASF)		6.1		5
Target air content		0		25

ultrasonic elastic waves in a specimen and then measuring the time of flight and attenuation [6]. NDT methods are widely used to examine the condition and structural integrity of civil engineering structures, including concrete structures. Nevertheless, the unique aspect of concrete is the heterogeneous nature of the material: concrete is a mixture of randomly arranged constituents with different shapes and physical properties. Therefore, the acoustic waves with frequencies in the MHz range that are required to detect small defects, like the initiation of internal high-temperature corrosion [7] are strongly attenuated in concrete. As a result, conventional acoustic methods may be limited in their ability to detect the early stages of deterioration in thick-walled concrete structures. For the evaluation of the steel–concrete bond in reinforced concrete structures there are some recent non-destructive techniques that have been proposed, such as ultrasonic pulse velocity [8], and the use of a rebound hammer [9]. However, the rebound hammer technique is not suited for the evaluation of bond quality for fully embedded steel liners, as the technique requires the steel component to be exposed to the environment. Since ultrasonic pulse velocity is measured point by point, evaluating the bond between large embedded steel liner plate surfaces and the surrounding concrete in, e.g., a containment building would require significant time and personnel resources. To overcome some of the key limitations associated with conventional and recent novel acoustic methods, nonlinear ultrasonics have emerged as a promising class of NDT techniques.

Nonlinear acoustic NDT methods are based on the principle that the signal distortion caused by small structural defects can occur even when the probing wavelength is significantly greater than the defect size, thus enabling the use of frequencies in the lower ultrasonic range (20–100 kHz). An additional benefit of these techniques is that they can often be utilized for global inspection, i.e., inspecting large areas or even entire components in a single measurement [10]. The elastic nonlinearity caused by small defects, such as cracks or the initiation of corrosion attacks, leads to amplitude-dependent effects, such as the generation of higher harmonics and various modulation phenomena [11–13]. Additional complex phenomena may occur, such as a chaotic noise-like behavior of nonlinear components [14] and slow non-equilibrium dynamics [15], which makes concrete inspection using these techniques demanding.

Despite the recognized challenges, studies utilizing nonlinear ultrasonics have indicated promising potential for detecting early stages of aging in concrete structures [16–21]. In particular, their capability of detecting the onset of corrosion in reinforcement bars (rebars) embedded in concrete has been acknowledged in several studies during the last decade [12,16,21–24]. However, the corrosion processes in these studies have been highly accelerated, introducing intensive uniform corrosion in the rebars after short test durations. In reality, the initiation and progress of corrosion may take years [25], even decades [26]. To the best of the authors' knowledge, no studies investigating slowly progressing corrosion in steel plates embedded in concrete and, in particular, the detection of minor to moderate localized corrosion attacks using these techniques have been reported up to date. This study bridges this gap by presenting results from novel corrosion acceleration experiments, thus widening the applicability of the techniques

and proposing data analysis approaches that may reveal the potential localized corrosion in critical components of nuclear power plants, such as the containment liner in the reactor containment building.

The present study investigates the corrosion of steel liner plates embedded in concrete and exposed to wetting-drying cycles for 2 years. The local conditions at the steel plate surface were varied using inlays of normal concrete, carbonated concrete, wood (foreign matter), and normal concrete with a gap, that was placed on the steel surface and embedded in concrete along with the steel liner. The target was to concentrate possible corrosion in the locations where these pieces are in contact with the steel. For additional specimens, the corrosion initiation and progress were slightly accelerated by adding chlorides and/or applying an impressed current. The manufacturing of specimens and the results from in-situ electrochemical measurements and post-exposure characterization of the steel plates with respect to the extent of attack have been reported elsewhere [27], yet the knowledge about the presence of corrosion and the nature of the steel–concrete interface is also employed here. This paper reports the performance of and results from ultrasonic inspection of the concrete specimens at the end of the 2-year exposure period using global nonlinear acoustic techniques based on harmonic generation and impact modulation. Some of the specimens did not feature any meaningful corrosion attacks, and these are used as reference points in the paper. A Total Damage Index (TDI) is proposed to combine several damage indices of the structure into a single indicator to estimate the extent of damage in the inspected concrete slabs or to evaluate the condition of the steel–concrete interface. This can be useful for triage inspections or when mapping the possible localized attack within a large structure.

2. Materials and methods

2.1. Materials and specimens

The specimens investigated in this work were concrete slabs that enveloped a steel liner plate aligned parallel to the surface of the concrete slab. If the plate was diagonally offset with respect to the surface plane then additional mode conversion could occur which might contaminate the results. Having the plates oriented vertically would offer the possibility to conduct measurements at each side of the plate. However, it is unlikely that such inspection scenarios would occur when the purpose is to evaluate a containment liner plate. Indeed, in reality, the surface of the liner plate is parallel to the concrete surface.

Each concrete slab, of the size of $350 \times 270 \times 80$ mm^3, was cast in two steps using the concrete mixture given in Table 1. First, a concrete layer of 25 mm was cast in a plastic mold and the steel liner plate was gently pressed into the concrete to ensure adhesion. The liner plate was of structural steel S355 (EN 10025-2) and featured dimensions of $300 \times 220 \times 5$ mm^3. Each steel plate contained a welded reinforcement bar ($\varnothing$6 mm) that stuck out of the concrete (to enable an electrical connection for electrochemical measurements, the results of which are reported elsewhere [27]). On the surface of each steel liner plate, inlays of concrete with varying characteristics and foreign matter were attached with the objective of initiating a possible corrosion

Fig. 1. Example of the concrete slab in the plastic mold. The welded reinforcement bar can be seen in the bottom right corner. On both left and right edges the edge of the stainless-steel mesh is visible.

attack underneath the inlay. The inlay materials were normal concrete, carbonated concrete, and oak wood. The diameter of the cylindrical concrete inlays was 45 mm, while the dimension of the wooden inlays was $35 \times 35 \times 20$ mm^3. Additionally, an inlay of normal concrete was manufactured and placed on the steel surface in such a way that a gap of a maximum of 1 mm was formed between the concrete inlay and the steel. Carbonated concrete inlays were obtained by subjecting inlays of normal concrete to carbonation treatment for 3 months in an atmospheric chamber. Some of the experiments were accelerated by the addition of chlorides (Cl$^-$) to the inlay concrete. The chlorides for the concrete inlays were added directly to the inlay concrete mix, at the content of 2.5% Cl$^-$ by cement mass. In turn, the wooden inlays were submerged in tap water that contained chlorides.

Some of the inlays contained a MnO$_2$ electrode, as a reference electrode for electrochemical measurements. On top of the steel plate-inlay system, a stainless-steel wire mesh (EN 1.4301, ∅3 mm) was placed to act as a counter electrode in the electrochemical measurements. Finally, a concrete cover of 50 mm was added to cover the steel plate, the inlays, and the electrodes. An example of the specimen is shown in Fig. 1. The cast concrete slabs were covered with plastic foil and regularly watered to ensure optimal curing conditions. They were then transported to a climate chamber with constant conditions, with a temperature of 20 °C and relative humidity (RH) of 65%. After casting, the slabs were allowed to dry for 8 weeks to increase the level of oxygen inside the concrete. After the drying period, the specimens were stored under the same constant conditions and watered once per week so that cyclic conditions of wetting and drying were achieved. Such conditions were maintained for 2 years to accelerate possible corrosion in the steel liner. In some of the experiments, further acceleration was obtained using an impressed current.

Aging-related deterioration of the concrete structures enveloping a steel liner can result from various conditions, such as carbonation of concrete as a result of reaction with the available atmospheric CO$_2$ (which lowers the concrete pH), the presence of embedded foreign matter such as a piece of wood (which typically feature lower pH than concrete but also introduces a new interface: steel–wood), and voids and/or delamination gap at the steel–concrete interface (which may enable the accumulation of, e.g., humidity). One significant environmental factor that contributes to the initiation of corrosion of steel in concrete is the presence of chloride ions. Altogether, these conditions enable two main corrosion scenarios for the embedded steel liner corrosion: 1) loss of passivity and 2) delamination-induced corrosion. In this study, several specimens were prepared to investigate the aging of concrete structures by utilizing the two proposed corrosion scenarios and examining the possible aging by nonlinear ultrasonic

techniques. Table 2 provides a list of specimens and the corresponding conditions investigated. Fig. 2 schematically illustrates the practical implementation of the conditions mentioned in Table 2.

After 2 years of exposure, the steel liner specimens were separated from the concrete cover. The steel specimens were photographed and subjected to analyses with respect to the extent of corrosion on the surfaces. The amount of surface corrosion was defined in absolute values (cm^2) and relative values (%). The results summarized in this work represent the relative values.

2.2. Data analysis and experimental setup for nonlinear ultrasonic measurements

Conventional acoustic methods for NDT, such as pulse-echo testing, rely on the transmission of high-frequency sound waves through a material, and the detection of the resulting echoes to assess the structural integrity. Conventional linear ultrasound techniques are widely used and effective in many applications, but the main limitation is the frequency-dependent sensitivity. To resolve small and subtle defects the methods require equally small wavelengths, thus often having probing frequencies exceeding several MHz. In contrast, nonlinear ultrasound offers improved sensitivity to microstructural changes even for probing wavelengths several orders of magnitude greater than the smallest detectable defect [28].

The intrinsic heterogeneity of concrete causes high levels of elastic nonlinearity even in an intact concrete structure. Therefore, it is important to include intact reference specimens in the test matrix. It is also known that some nonlinear features are clearly enhanced by the aging of concrete structures, e.g., by the presence of corrosion attacks [20, 23]. Corrosion of structural steel components embedded in concrete often results in the build-up of corrosion products at the steel surface. This essentially means a change from the original steel–concrete system into the steel-corrosion product-concrete system, which may result in the formation of a delamination gap or cracks in the bulk volume of the corrosion products that are parallel to the steel–concrete interface [29, 30]. Additionally, the corrosion products have a greater volume than the original metal, causing swelling pressure and subsequently micro- and macro-cracking in the surrounding concrete [16,21]. Cracks that often are filled with corrosion products cause strong local nonlinear elastic effects due to several factors, such as stress concentration at sharp crack tips [31], complex contact effects in closed and partially closed cracks [32], and thermal-elastic coupling [33]. The nonlinear effects are cumulative, meaning they distort increases over time and space [34]. Additionally, nonlinearity increases with an increasing number of defects in the examined media. However, this is only valid up to a certain damage level after which the nonlinearity has been shown to decrease [12,35]. The cumulative properties can be utilized for the inspection of large bulk material volumes, i.e., global inspection. Global inspection will not yield any spatial information about defect locations but is, instead, more suited for triage-type inspection.

The analysis procedure of nonlinear acoustic measurements can generally be divided into three steps: processing, extraction, and calculation. Processing covers the signal processing and estimation of spectra; extraction explains what spectral components or information to extract, and the final step is to calculate the sought parameters using the extracted data. In the following subsections, the methods employed in the present work are introduced and the data analysis procedures based on the steps are presented. Lastly, the experimental setup used for the nonlinear ultrasonic measurements in the present study is presented.

2.2.1. Analysis of higher harmonics

A simple scheme of the data analysis procedure towards higher harmonics can be seen in Fig. 3 following the three steps: processing, extraction, and calculation. To remove potential end effects, apodization using a Hanning window is employed in the time domain before

Table 2
A list of the specimens prepared for the present investigations.

Specimen	Scenario	Variable	Conditions
R	1	Reference	Normal concrete
RC	1	Reference with chlorides	Concrete inlay with added chlorides
PH	1	Concrete pH	Carbonated concrete inlay
PHI	1	Concrete pH, electrochemical acceleration	Carbonated concrete inlay, impressed current
PHCI	1	Concrete pH, added chlorides, electrochemical acceleration	Carbonated concrete inlay with added chlorides, impressed current
WC	1	Embedded wood, chlorides	Chlorides added to a piece of wood embedded in normal concrete
D	2	Delamination in steel–concrete interface	Delamination gap formed between steel and concrete inlay from normal concrete.
DC	2	Delamination, chlorides	Delamination gap formed between steel and concrete inlay, concrete inlay with added chlorides
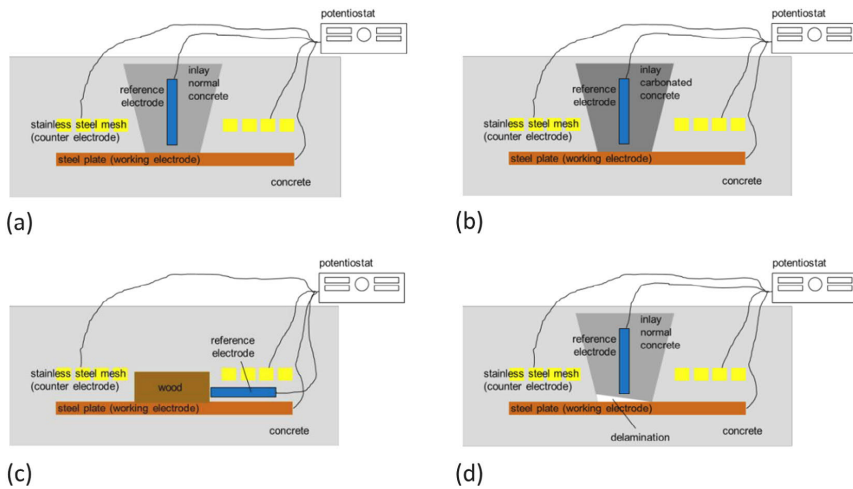
Fig. 2. Schematic of the implementation of the various corrosion scenarios: (a) Reference case; (b) inlay of carbonated concrete (low pH); (c) embedded foreign matter, here wood; (d) delamination gap in the steel–concrete interface.

the magnitude spectra are computed using the Fast Fourier Transform (FFT) algorithm. Using the spectrum, the magnitude of the fundamental frequency (f) component along with its harmonics (nf, $n = 2, 3, \ldots$) can be extracted. After the extraction, the parameters of harmonic nonlinearity are calculated.

To evaluate the level of aging-related changes in the structure, several indices can be used. In nonlinear ultrasonic inspections, so-called *damage indices* are often based on the ratio between the magnitude of the nonlinear component(s) over the probing wave component. The most commonly used parameter is called the relative parameter of *quadratic nonlinearity* (β'), which is a relative measure of the classical power-series type nonlinearity of the quadratic order [30,36]. β' is calculated by the measured magnitude of the second harmonic, A_2', over the first harmonic, A_1', squared (Eq. (1)).

$$\beta' = \frac{A_2'}{A_1'^2} \qquad (1)$$

For the parameter of *cubic nonlinearity*, which is less common in the literature, the corresponding parameter is δ', given by the third harmonic, A_3', over the first harmonic cubed (Eq. (2)).

$$\delta' = \frac{A_3'}{A_1'^3} \qquad (2)$$

The prime in the parameter notation indicates that the voltage signal amplitudes are used instead of displacement amplitudes. It is more convenient to use the signal voltage than to convert the signal into displacement using appropriate transfer functions when determining the relative parameters of nonlinearity, as such transfer functions must take the system parameters into account [37].

For global inspection, a continuous excitation can be used to insonify the entire volume. This will cause a level of intrinsic distortion due to internal scattering and mode conversion, effects that cannot be attributed to the inherent nonlinear elasticity of the inspected material. However, defects may amplify the measured distortion by several orders of magnitude greater than the intrinsic effects. Nevertheless, intrinsic distortion regardless of source may mask weak effects from nonlinear elasticity, which is the reason why it is beneficial to study several parameters in a single inspection.

2.2.2. Modulation spectroscopy

The analysis procedure for modulation spectroscopy is like the one for higher-harmonic analysis: a Hanning window is applied to the time signal prior to using the FFT to acquire a magnitude spectrum. The data indices corresponding to the sideband intervals are then extracted along with the information on the width of the probing component. These data indices are then used along with the trapezoidal rule to integrate
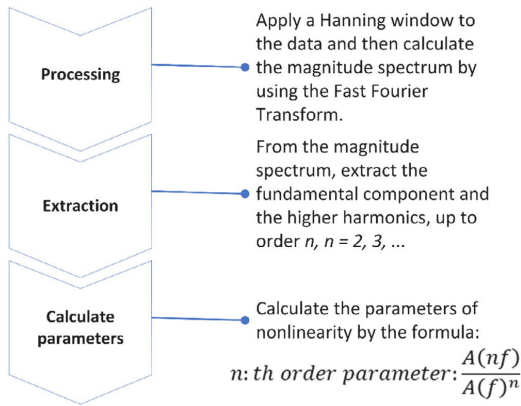
Fig. 3. Schematic three-step process for determining the global parameters of nonlinearity based on higher harmonics.
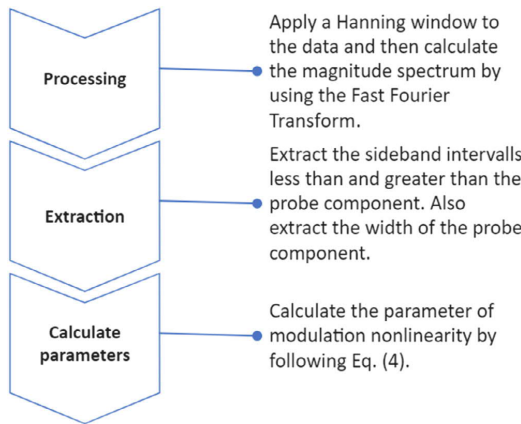

Fig. 4. Schematic illustration of the three-step process to extract and determine the modulation parameter γ.

the discrete data. A simple schematic of the procedure can be viewed in Fig. 4.

Continuous probe excitation enables the use of an additional excitation source to study frequency-mixing, which is a combination of amplitude- and frequency modulation by a strong source on a weaker probe. This can be achieved in many ways, for example, by using a second transducer at frequency $f_m << f_p$, where f_m and f_p are the modulation and probe frequencies, respectively. This will generate sum- and difference frequencies called sidebands around the probing frequency and the sidebands can be formulated by Eq. (3):

$$f_{sideband}^j = f_p \pm j f_m \tag{3}$$

where j is an integer greater than zero. To generate a wide spectrum of sidebands, the mechanical impulse from an impact can be used to excite several structural resonances at once. This phenomenon is illustrated in Fig. 5 for the case of a linear (a) and a nonlinear (b) interaction.

The level of nonlinearity, which is linked to the damage level, can be estimated by calculating the magnitude ratio of the sidebands over the probing component. The transient nature of the impact causes several frequencies to appear and in on-site inspections, these frequencies may

be unknown. To determine the probe and sideband energy, integration at relevant intervals can be used, as suggested by [38]. The parameter of modulation nonlinearity (γ) is therefore given by Eq. (4), where $Y(f)$ is the Fourier magnitude spectra of the recorded signal. The subscripts *Left* and *Right* denote the sideband regions at frequencies lower (left) and greater (right) than the probe frequency. Probe start and stop define the width of the probing frequency peak.

$$\gamma = \frac{\int_{f_{Left\,start}}^{f_{Left\,stop}} Y(f)\,df + \int_{f_{Right\,start}}^{f_{Right\,stop}} Y(f)\,df}{\int_{f_{Probe\,start}}^{f_{Probe\,stop}} Y(f)\,df} \tag{4}$$

2.2.3. Extraction of instantaneous modulation characteristics

A possible drawback of the modulation parameter γ (Eq. (4)) is that there is no separation between amplitude and frequency modulations, as the extraction of the magnitudes is done from a Fourier magnitude spectrum of the recorded signal. Fortunately, the Hilbert Transform (HT) can be used to extract the instantaneous modulation characteristics of a signal. However, the HT is mostly suited for mono-component or narrowband signals. The nonlinear interactions create multi-component signals, which makes the use of HT limited. To overcome this limitation, the Hilbert–Huang transform (HHT), proposed in the late 1990s, can be employed [39,40]]. The HHT is a data-driven signal processing method for nonlinear signals that combine Empirical Mode Decomposition (EMD) and the Hilbert transform. EMD decomposes the signal into a set of intrinsic mode functions (IMFs), which are localized and oscillatory intrinsic features of the signals. These properties mean that an IMF represents a carrier frequency (hence intrinsic mode) of a signal. The EMD procedure can be viewed schematically in a block diagram shown in Fig. 6.

The EMD procedure includes the following five steps:

(1) Identify all local maxima and minima of the input signal. Connect all the local extrema with two splines, commonly rational or cubic. These two curves define the upper and lower envelopes of the signal, respectively.
(2) Calculate the average between the upper and lower envelopes to obtain the *local mean* (m_i) of the signal component.
(3) Calculate the first component (c_1) of the EMD, which is obtained by subtracting the local mean, m_1, from the original signal x following (Eq. (5)):

$$c_1(t) = x(t) - m_1(t) \tag{5}$$

If the number of extrema and zero-crossings is equal or differs at most by one, and if the component has zero mean, it is considered an IMF.

(4) This process is repeated iteratively on the residual signal, given by $r_1 = x(t) - c_1(t)$, and $r_n = r_{(n-1)} - c_n$. Thus, the original signal is described by (Eq. (6)):

$$x(t) = \sum_{i=1}^{n} c_i(t) + r_n(t) \tag{6}$$

(5) The mode decomposition is finished when certain criteria have been met. The criteria can be defined by the user and be as simple as prescribing a set number of IMFs to extract. A more general criterion is that the procedure continues until the residual is a monotonic function from which no oscillatory features can be extracted [40].

The main difference in the procedure to analyze instantaneous characteristics (see Fig. 7 for an overview) lies in the use of a mode decomposition algorithm and the HT. The processing step is to apply a suitable filter to ensure reliable extraction using the mode decomposition. The parameters of interest are then calculated and analyzed further.

When decomposing a multi-component signal, like a nonlinear ultrasonic response, by using EMD some of the extracted intrinsic modes
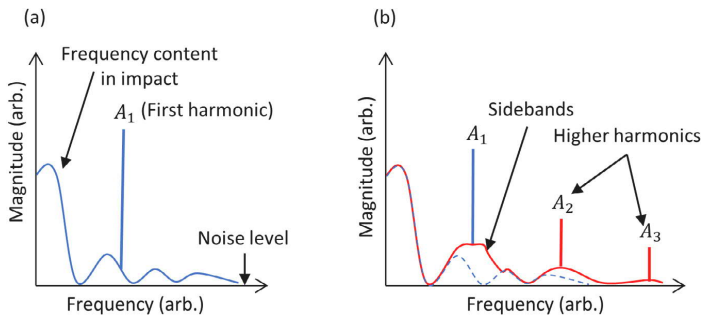
Fig. 5. Illustrations of magnitude spectra for simultaneous impact and continuous ultrasonic excitation in (a) the linear case were no frequency-mixing (modulation) occurs and (b) where material nonlinearity causes modulation and higher harmonic generation of the probing component. The dashed line in (b) represents the impact response in (a).
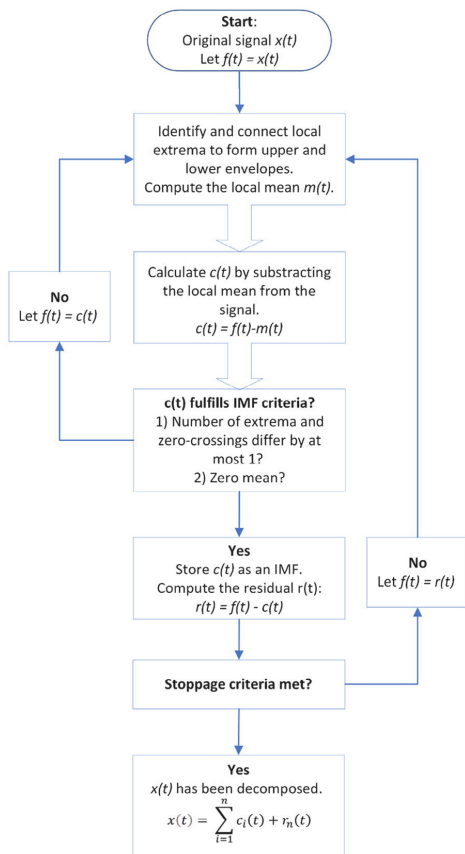

Fig. 6. Block diagram for the empirical mode decomposition process.

Fig. 7. The three-step procedure for analyzing instantaneous modulation phenomena.

the desired frequency. While IMFs acquired from the EMD process are not necessarily mono-component functions, they are likely more appropriate for the HT than the original signal. It is important to note that the spline techniques and boundary conditions associated with the process used to form the envelopes for the local mean can introduce erroneous end effects that must be considered during the final analyses [42]. A rigorous formulation of the EMD process and discussions of its limitations are beyond the scope of this work but interested readers are referred to [43,44]. Although similar decomposition methods to the EMD have been proposed recently [45,46], they are not considered in this work.

Let the HT of an extracted IMF $c(t)$ be $\hat{c}(t)$. The analytical signal is then given by (Eq. (7)):

$$y(t) = c(t) + j\hat{c}(t) = IA(t)e^{j\phi(t)} \tag{7}$$

where $IA(t)$ is the instantaneous amplitude and $\phi(t)$ is the instantaneous phase described by (Eqs. (8)–(9)):

$$IA(t) = \sqrt{c^2(t) + \hat{c}^2(t)} \tag{8}$$

and

$$\phi(t) = tan^{-1}\left[\frac{\hat{c}(t)}{c(t)}\right] \tag{9}$$

respectively. The instantaneous frequency $IF(t)$ can be obtained by differentiating the instantaneous phase and scaling by the sampling

can be analyzed for their instantaneous characteristics. EMD first extracts the shorter time-scale components, i.e., the highest frequency of the signal. To achieve reliable extraction of the desired component, it is recommended to filter the signal before the EMD process [41]. This technique helps to ensure that the first IMF extracted will contain

frequency used when acquiring the data, F_s, following (Eq. (10)):

$$IF(t) = \frac{F_s}{2\pi} \frac{d}{dt} \phi(t) \tag{10}$$

To get meaningful instantaneous frequency information, the instantaneous phase must be unwrapped prior to differentiation. Damage indices $DI_{Amplitude}$ and $DI_{Frequency}$ that use the standard deviation of the instantaneous amplitude and frequency to estimate modulation intensities have been suggested by [47]. The standard deviations are normalized with respect to the mean instantaneous amplitude and probe frequency and are presented as (Eqs. (11)–(12)):

$$DI_{Amplitude} = \frac{\sqrt{\frac{1}{N} \sum_{i=1}^{N} [IA(i) - \mu(IA)]^2}}{\mu(IA)} \tag{11}$$

$$DI_{Frequency} = \frac{\sqrt{\frac{1}{N} \sum_{i=1}^{N} [IF(i) - \mu(IF)]^2}}{F_{Probe}} \tag{12}$$

where $\mu(IA) = 1/N \sum_{i=1}^{N} IA(i)$ and $\mu(IF) = 1/N \sum_{i=1}^{N} IF(i)$ are the mean instantaneous amplitude and frequency, respectively, and N is the total number of digitized samples being analyzed.

2.2.4. Combining parameters – The total damage index

In nonlinear ultrasonic inspections, numerous parameters can be extracted from a single measurement conducted for the specimens. Studying each parameter separately may yield insights into the characteristics of the defects in the specimens. An example would be the separation between classical (typically integer harmonic generation) and nonclassical parameters (various modulation-based parameters), where the latter only arise from certain types of defects, such as cracks and other contact-type defects [11,31], and classical nonlinearity can be caused by anharmonicity in interatomic potentials [48], thus being an intrinsic effect. However, for aging damage detection purposes, combining multiple extracted parameters provide a more complete picture than separate indices alone, as intrinsic effects caused by classical nonlinearity are generally much smaller than the combined effects of various defects.

While the analysis of each parameter separately may provide valuable information, combining them into a Total Damage Index (TDI) can yield a more comprehensive understanding of the level of damage. Eq. (13) shows a general expression for the TDI, which can be obtained by normalizing and summing all previously proposed damage indices as well as any additional damage index or parameter acquired during an inspection.

$$TDI(S) = \frac{1}{K} \sum_{k=1}^{K} \frac{DI_k(S)}{max(DI_k)} \tag{13}$$

where $DI_k(S)$ is the k:th damage index, or parameter of nonlinearity, for the inspected specimen S, and K is the total number of damage indices included in the calculation. The denominator is simply the maximum value of the k:th damage index across the inspected specimen population found by identification. Combining the damage indices used in the present study, the TDI is given by Eq. (14) where i is the measurement point notation.

$$TDI(S)_i = \frac{1}{5} \left[\frac{\beta'_i(S)}{max(\beta'_i)} + \frac{\delta'_i(S)}{max(\delta'_i)} + \frac{\gamma_i(S)}{max(\gamma_i)} \right. $$
$$ \left. + \frac{DI_{Amplitude_i}(S)}{max(DI_{Amplitude_i})} + \frac{DI_{Frequency_i}(S)}{max(DI_{Frequency_i})} \right] \tag{14}$$

The range of the TDI, as for many other damage indices, is from 0 to 1, where 0 indicates an undamaged (as-received) state and 1 means that the specimen is severely damaged. Setting a threshold damage level requires several inspections for specimens with varying degrees of damage, based on which the threshold damage level can be grouped into selected categories. Before setting the thresholds, dividing the interval into four categories; low, minor, moderate, and severe,

Table 3
TDI intervals and corresponding damage levels.

TDI (Dimensionless)	Damage level
0–0.25	Low
0.25–0.50	Minor
0.5–0.75	Moderate
0.75–1.0	Severe

as seen in Table 3, could yield some initial guidance. Note, initial measurements conducted for intact specimens may yield erroneous conclusions using this categorization as the specimens will likely yield low parameter values, but when normalized they may yield high TDI even if their damage level is low. This observation highlights the need for including both damaged and intact specimens in the initial test matrix.

Due to the normalization process, the TDI is a qualitative measure of damage mainly suggested for use in triage-type inspections where several samples with similar characteristics are inspected. The TDI may also be used to map damage levels on large structures if their dimensions and composition do not vary greatly. The TDI is dimensionless, which enables the combination of parameters from several NDT methods to achieve a wide range of utilized phenomena gathered into a single parameter.

2.2.5. Experimental setup for the nonlinear ultrasonic measurements

The key components required for nonlinear acoustical measurements include ultrasonic transducers for generating and receiving the waves, a waveform generator to produce the excitation waveform, an amplifier to enhance the signal, and a data acquisition system to capture and subsequently analyze the response.

The experimental setup used to inspect the concrete slabs is shown in Fig. 8. The arbitrary waveform generator (AWG), an Agilent 33500B, was used to generate a continuous sinusoidal excitation at 1 $V_{peak\text{-}to\text{-}peak}$ amplitude and with a frequency of 36 kHz. The signal was amplified by an A.A. Lab Systems A-303 high voltage power amplifier to an amplitude of 35 $V_{peak\text{-}to\text{-}peak}$. The transducers used as transmitter and receiver (T and R in Fig. 9) were commercial Olympus X1021 contact transducers with a specified nominal frequency of 50 kHz, but in reality, closer to the frequency range of 36–38 kHz. The transducers were coupled to the specimen using grease.

An impactor consisting of a Phillips button head M4.5 × 15 mm screw attached to the end of a 370 mm long cable tie was used to excite structural resonant frequencies to achieve frequency-mixing. Impacts were performed at two locations situated in the proximity of the transmitter (location 1) and receiver (location 2), see Fig. 9. The impact event triggered the measurement, and the acquisition was set to acquire 100 kS before the trigger event. The signals were collected using a Measurement Computing USB-1602HS data-acquisition unit (DAQ) at a sampling rate of 2 MS/s collecting 200 kS. The measurement was controlled using software programmed in LabView. The data was post-processed (windowing, Fast Fourier transform, HHT, and more) using scripts developed in the MATLAB environment.

The surface roughness of the inspected concrete slabs was high, as seen in Fig. 9. The pronounced roughness may induce intrinsic signal distortion due to mode conversions among other effects. However, this characteristic was common to all inspected specimens, therefore the possible influence of surface roughness on the data is expected to be equal in all cases.

3. Results and discussions

3.1. The extent of corrosion and the nature of the steel–concrete interface

The results from the in-situ electrochemical measurements and post-exposure characterization of the concrete-embedded steel plate specimens is described in detail elsewhere [27]. The main finding was
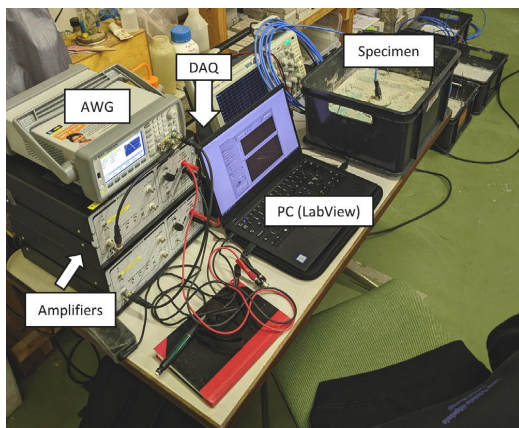
Fig. 8. Experimental setup used for the nondestructive inspections in this work.
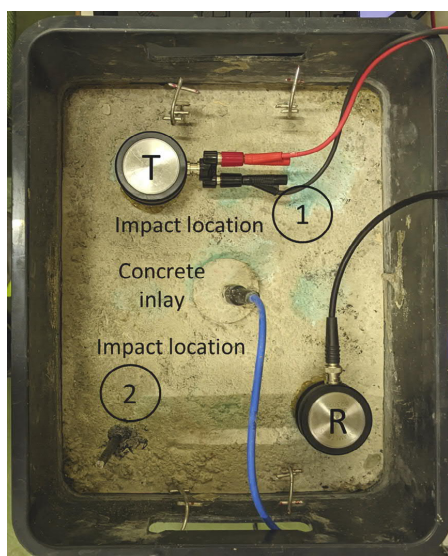

Fig. 9. Top view of one of the investigated specimens. Picture shows the location of transmitter (T) and receiver (R). Approximate locations for the impacts are shown as well.

that the specimens could be grouped into the following four categories according to the extent of corrosion detected on the surfaces, defined based on the average surface coverage by corrosion products (based on two or three parallel specimens): no corrosion, minor corrosion, moderate corrosion, and severe corrosion. Among the investigated specimens, the no corrosion category included specimens R and D, minor corrosion was detected in RC, PH, and DC, with moderate corrosion occurred in WC, and severe corrosion was observed in PHI and PHCI. The main findings from the corrosion experiments are summarized in Table 4.

The photographs of the specimens presented in Table 4 revealed that the corrosion attacks were indeed concentrated in areas underneath the inlay, i.e., in areas of the steel surface that are in direct contact with the inlay, as targeted. In some cases, corrosion also occurred at the outer periphery of the inlay. The presence of chlorides generally introduced a greater extent of corrosion. In the case of the reference specimens (R, RC), the presence of chlorides induced a corrosion attack essentially underneath the inlay, whereas in the case of specimens with the delamination gap (D, DC), corrosion attack in the presence of chlorides occurred both underneath the inlay and at the outer periphery of the inlay. In the case of specimens of carbonated concrete (PH) and inlay of wood with chlorides (WC), corrosion was concentrated on areas underneath the inlay. In the specimens subjected to an impressed current for the acceleration of corrosion (PHI, PHCI), corrosion attacks were detected both at the center of the specimen (underneath and around the inlay) and at the edges of the specimens.

Corrosion of the steel plate impairs the structural integrity of specimens by, e.g., deteriorating the bond at the steel–concrete interface. However, it has been acknowledged that steel corrosion at low levels may even slightly improve the bond strength between the steel and concrete due to increased surface roughness and good overall adhesion of rust to the steel surface, whereas further increases in the extent of corrosion may then dramatically lower the bond strength between the steel and the concrete [49,50]. Chai et al. [51] have shown for steel reinforcement in concrete that minor corrosion up to 1% mass loss leads to higher bond strength values between the steel and concrete than in the control case with no corrosion, whereas further increases in the extent of corrosion beyond 2.4% mass loss introduced bond failure. It is important to note that rebars have a ribbed structure that enhances mechanical adhesion through friction-locking, whereas regular steel plates have a smooth uniform surface and lack such capabilities. Therefore, it is suspected that the contribution of minor corrosion to adhesion might be greater in the case of plates compared to rebars.
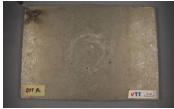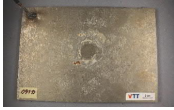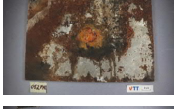
Based on the above, it could be expected that the interface between steel and concrete is intact in the specimens falling into no corrosion and minor corrosion categories, i.e., R, D, RC, PH, and DC. In contrast, bond failure could be expected in specimens falling into moderate corrosion and severe corrosion categories, i.e., for WC, PHI, and PHCI. However, the presence of the delamination gap (D, DC) introduced by the inlay geometry challenges the bond strength categorization purely based on the extent of corrosion. In these specimens, the bond strength is likely affected both by the presence of the geometrical gap and the extent of corrosion. In the case of wooden inlay (WC), it is also likely that the steel–wood interface exhibits different characteristics than the steel–concrete interface. Non-bonded steel–concrete or steel–wood interface may introduce contact-type elastic nonlinearity, a type of nonclassical nonlinearity known to manifest various strong nonlinear phenomena [52].

3.2. Nonlinear ultrasonic inspections

3.2.1. Harmonic analysis

Fig. 10(a) displays examples of the recorded voltage signals as a function of time for the reference specimen (R) and the specimen with a delamination gap and chlorides (DC). Fig. 10(b) and (c) depict the corresponding magnitude spectra before the impact ($0 - 0.04$ s) and the full signal, respectively. The impact clearly influences the signal by introducing additional energy at lower frequencies (from 100 s Hz to 20 kHz), which mixes with the ultrasonic wave. This effect is observable through the presence of sidebands around the probing frequency (36 kHz). The harmonic magnitudes from the measurements conducted at the two impact locations were extracted from the full signal spectra and are presented for all specimens in Fig. 11. The magnitudes of the first harmonics depicted in Fig. 11(a) indicate a trend where the specimens PHI, PHCI, DC, and WC, exhibit stronger attenuation, i.e., lower first harmonic magnitude, than R, RD, D, and PH. This trend was maintained regardless of the impact location as the fundamental magnitudes are equal in the two measurements. A similar attenuation trend cannot be observed when studying the higher-order harmonics shown in Fig. 11(b) and (c).

Table 4

The extent of corrosion detected in the steel specimens that were embedded in concrete.

Category	Maximum extent of corrosion, %	Specimens falling into the category with the extent of corrosion	Example of steel plate surface after the test
No corrosion	0.1	R: 0.12%	
		D: 0.08%	
Minor corrosion	1	RC: 0.51%	
		PH: 0.82%	
		DC: 0.59%	
Moderate corrosion	1–10	WC: 3.1%	
Severe corrosion	>50	PHI: 51.4%	
		PHCI: 76.9%	

The analysis of Fig. 11(b) reveals that the specimen featuring low-pH concrete denoted as PH, exhibited the highest magnitude of the second harmonic. The second harmonic for PH was more than 4 times greater than the corresponding levels for the specimens with similar fundamental magnitudes, specifically R, and D. This difference suggests a considerably greater degree of nonlinearity for PH, even though the level of attenuation remained comparable. The magnitudes of second harmonics were quite equal for most specimens: R, RC, D, PHI, DC, and WC. However, when considering the stronger fundamental levels observed in R, RC, and D, it became apparent that PHI, DC, and WC exhibited a higher level of quadratic nonlinearity. PHCI demonstrated the most pronounced nonlinearity based on the second harmonic analysis. Despite having fundamental levels comparable to DC and WC, PHCI exhibited a second harmonic magnitude that was more than twice as strong.

Upon analyzing the magnitudes of the third harmonics in Fig. 11(c), it became evident that the specimen with the delamination gap (D) exhibited the strongest third harmonic. PHCI followed closely, displaying slight variation between the two measurements. The weak fundamental magnitude of PHCI signifies strong cubic nonlinearity compared to the other specimens. While D had the strongest third harmonic among the inspected specimens, its strong fundamental magnitude indicates comparatively weak cubic nonlinearity. Similarly, R, RC, and PH exhibited quite strong third harmonics, however, since the corresponding fundamental is also strong their cubic nonlinearity was weak. In contrast, DC and WC exhibited low third harmonics and fundamental levels, implying moderate cubic nonlinearity, albeit weaker than PHCI. PHI exhibited similar third harmonic magnitudes to DC and WC but possessed a strong fundamental, thus resulting in weak cubic nonlinearity.

The observations made when studying the harmonic magnitudes were more noticeable when studying the corresponding relative parameters of quadratic (β') and cubic (δ') nonlinearity, defined by Eqs. (1) and (2) and shown in Fig. 12(a) and (b), respectively. PHCI stood out with the greatest values for both quadratic (1.2 V^{-1}) and cubic parameters (3.8 V^{-2}), indicating enhanced nonlinearity. DC and WC also exhibited notable nonlinearity with 0.97 V^{-1} and 1.1 V^{-1} for β' respectively, and correspondingly 1.8 V^{-2} and 1.2 V^{-2} for δ'. Among
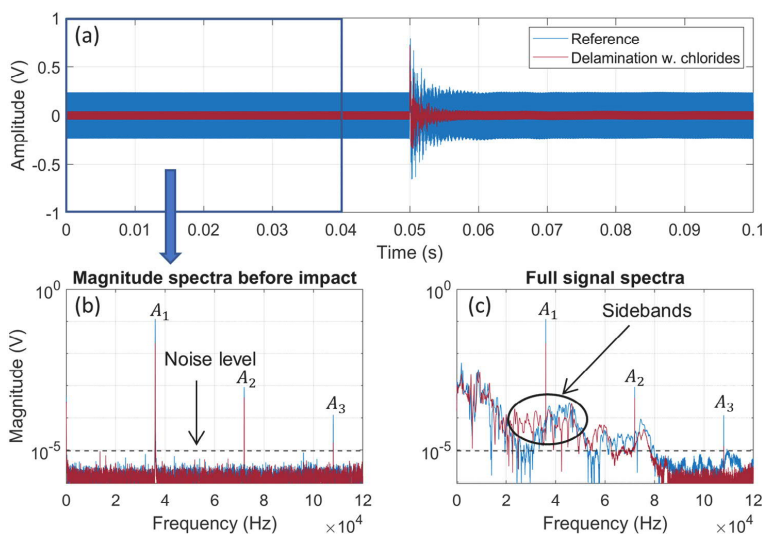
Fig. 10. Acquired signals for the reference specimen (R) and the specimen with a delamination gap with Cl⁻ (DC). (a) Acquired time signal. The box illustrates the time frame (0 – 0.04 s) from which the magnitude spectra before impact was calculated (b). (c) shows the spectra estimated using the entire signal.

the remaining specimens, R (0.066 V^{-1} and 0.073 V^{-2}), RC (0.0010 V^{-1} and 0.0028 V^{-2}), and D (0.041 V^{-1} and 0.10 V^{-2}) showed relatively lower values for both quadratic and cubic parameters, suggesting comparatively weaker nonlinearity. PH (0.14 V^{-1} and 0.024 V^{-2}), and PHI (0.083 V^{-1} and 0.069 V^{-2}), demonstrated weak to moderate values, with specimen PH displaying higher quadratic nonlinearity than cubic, while PHI exhibited slightly higher cubic nonlinearity. These findings highlight the varying degrees of distortion between the specimens, with PHCI, DC, and WC showcasing the most pronounced effects when strictly analyzing higher-order harmonics, followed by PH and PHI, while R, RC, and D exhibited weaker nonlinearity in comparison. Considering that specimens WC, PHI, and PHCI featured moderate to severe corrosion, hence likely a poor bond between the steel plate and concrete, and specimens D and DC contained a geometrical gap at the steel–concrete interface, the results of harmonic magnitudes quite nicely reflect the bond challenges at the steel–concrete interface, particularly for PHCI, DC, and WC. Therefore, the bond characteristics at the interface are suspected to be the likely origin of the enhanced distortion of the acoustic waves observed in these measurements.

The relative variation of the higher-order harmonics between the two measurements (locations 1 and 2) increased with increasing order of harmonics. This can likely be attributed to the low magnitudes of these harmonics, where even small variations led to significant variability. Interestingly, in most cases, the greatest magnitudes of the higher-order harmonics and the corresponding parameters of nonlinearity were observed when impacts were performed at location 1. This suggests that the measurements performed at the second location may have been conducted during a slow recovery phase, being influenced by the slow dynamic behavior common in complex nonlinear elastic materials, such as concrete.

3.2.2. Spectral analysis of impact modulation

The spectra in Fig. 10(c) illustrate the impact response combined with sideband generation for the two example specimens, R and DC. The modulation parameter γ was determined by integrating the magnitude spectra in the frequency interval of 20–50 kHz. The sidebands were in the intervals of 20–35.98 kHz and 36.02–50 kHz. The probe energy was visible between the sideband locations, in the frequency interval of 35.98–36.02 kHz. The modulation parameter γ, acquired

by striking the specimens at the two locations and defined based on Eq. (4), is shown in Fig. 13. The parameter values for specimens R, RC, and D ranged from 0.6 to 1.2 at location 1 and increased to a range of 0.6 to 2.8 at location 2. For PH, PHI, and PHCI, the values ranged from 0.8 to 1.9 at location 1, and from 0.8 to 1.3 at location 2. In the case of DC and WC, significantly higher modulation parameter values were observed, with values of 5.5 and 9.7 for DC at locations 1 and 2, respectively, and values of 14 and 5.6 for WC.

For specimens DC and WC, the trends detected in the damage parameter γ were consistent with those obtained for the damage parameters β' and δ', the values were clearly higher than for the other specimens. However, the γ parameter did not indicate as high damage levels for the specimen PHCI as the parameters for harmonic distortion (β' and δ') did. Furthermore, PHI and PHCI had similar parameter values, indicating similar damage levels, which is consistent with the results from the characterization of the extent of corrosion (Table 4). These findings demonstrate that the extent of corrosion is not the sole factor influencing the distortion of ultrasonic waves. It is evident that the specimens DC and WC exhibited different steel–concrete interface characteristics compared to the remaining specimens: the presence of the delamination gap and the steel–wood interface introduced non-bonded mechanical contacts, which are known to strongly contribute to nonlinear effects [32,48,53]. This may also explain why specimen D, falling within the no corrosion category, exhibited a stronger nonlinearity than specimen PH, which exhibited moderate corrosion.

3.2.3. Analysis of instantaneous modulation characteristics

To assist the EMD, the signals were band-pass filtered around the probing frequency with a bandwidth of 15 kHz to remove unwanted higher frequency components, such as higher harmonics, which could complicate the EMD process. Fig. 14(a–b) shows the first extracted IMF from the example time signals shown in Fig. 10(a). It is clear from the IMFs that the filtering and EMD process did not remove the characteristic peaks caused by the impact. This implies that the IMFs were not true mono-component signals but exhibited wide-band modulation caused by the impact. The curves also revealed significant amplitude differences between the IMFs, which were expected due to the increase in attenuation previously observed for DC. However, an additional interesting observation could be made from the IMF plots.
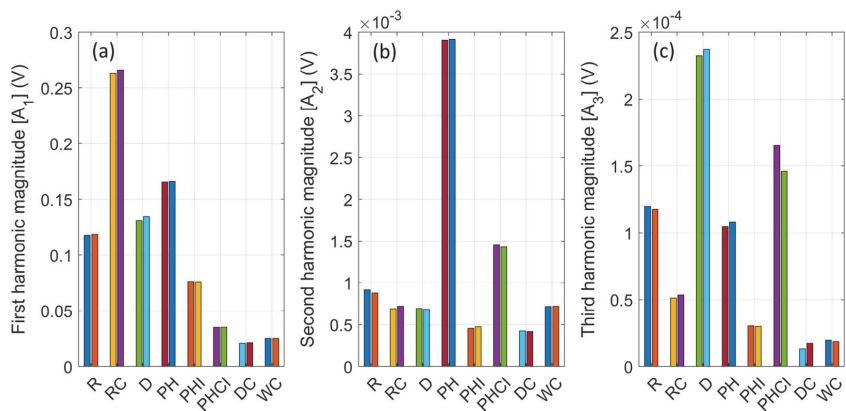
Fig. 11. First (a), second (b), and third (c) harmonic magnitudes for all specimens. Two bars are presented for each specimen. The left bar is data from measurements with impact at location 1, whereas the bar to the right is from impact at location 2.
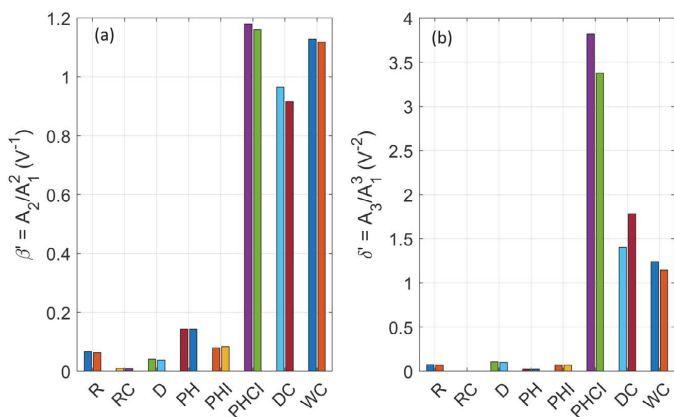

Fig. 12. Parameter of quadratic (a) and cubic nonlinearity (b). Each specimen presents two bars, the left bar is data from impact at location 1, the right bar is data from impact at location 2.
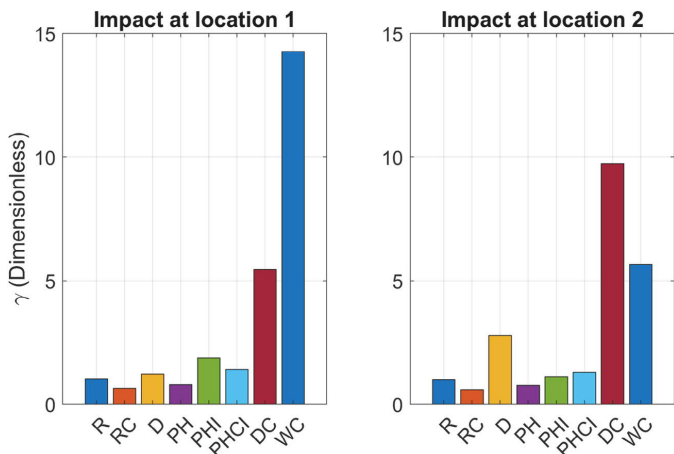

Fig. 13. The modulation parameter γ for the inspected specimens.
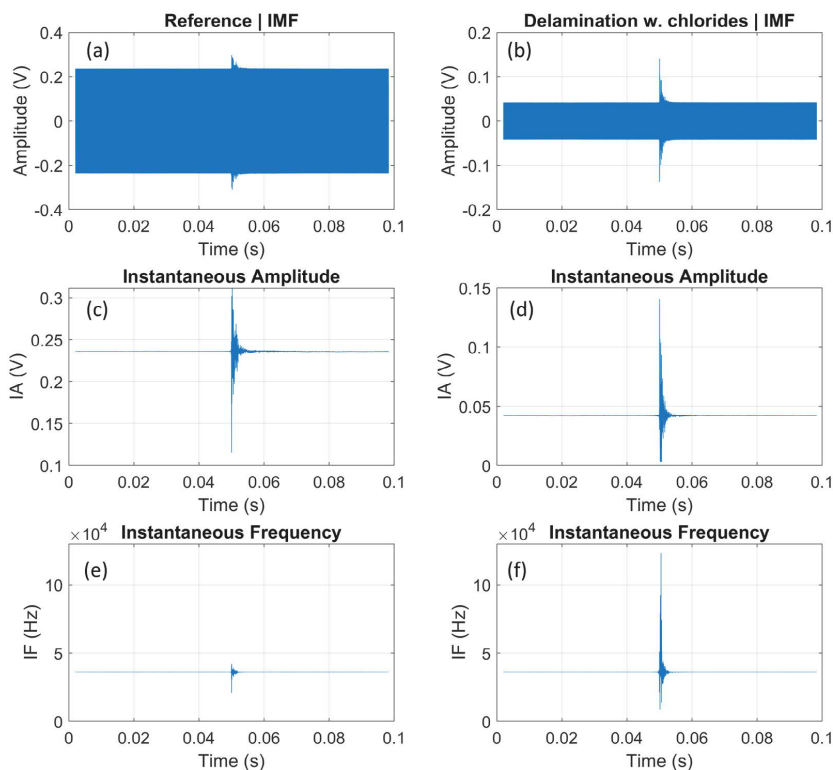
Fig. 14. (a) Probe component IMFs for the reference specimen (R) and (b) the specimen containing delamination and added chlorides (DC). Corresponding instantaneous amplitude (c – d) and frequency (e – f).

The magnitude of the impact peak in relation to the probing wave amplitude could be viewed as a measure of amplitude modulation because of the localized property of the IMF. The IMF plots seemingly indicate that the reference specimen (R) was weaker modulated by the impact than the specimen DC simply because of the attenuation differences. To study the actual effects of the impact modulation phenomena separately, the instantaneous amplitude (IA) and frequency (IF) signals were obtained by using the HT and Eqs. (8) and (10), respectively.

The instantaneous amplitude (IA) signals are plotted in Fig. 14(c–d). No modulation was observed for the specimens before the impact, which was expected. The results disclosed that the impact did modulate the signal significantly; however, it was difficult to assess the intensity from the IA plots alone. The filtering process evidently retained the modulation frequencies above the cut-off frequency, and the magnitude of instantaneous frequency (IF) varied between the specimens. IF curve for specimen R, Fig. 14(e), revealed evidently weaker modulation than for specimen DC, the corresponding IF curve for which is shown in Fig. 14(f). The IMF for specimen DC exhibited exceedingly pronounced broad-banded frequency modulation compared to the IF obtained for specimen R.

The modulation intensity is illustrated by plotting the damage indices calculated using Eqs. (11)–(12) in Fig. 15. The damage indices of amplitude modulation ($DI_{Amplitude}$) are depicted for all specimens in Fig. 15(a) and (b) and represent the results acquired from the impact at locations 1 and 2, respectively. For specimens R, RC, and PH, the $DI_{Amplitude}$ ranged from 0.011 to 0.017 at both impact locations; these were the lowest values detected among the studied specimens. The corresponding values for D, PHI, and PHCI were 0.025 to 0.038 at

location 1 and 0.021 to 0.050 at location 2. For DC the values were 0.078 and 0.19 at locations 1 and 2, and for WC the corresponding values were 0.32, and at location 2 the $DI_{Amplitude}$ was lowered to 0.08.

The values for the damage index for frequency modulation ($DI_{Frequency}$) are depicted in Fig. 15(c) and (d). The values ranged from 0.0028 to 0.0072 at location 1 for specimens R, RC, and PH, and 0.0047 to 0.0059 at location 2. For D, PHI, and PHCI the range was 0.012 to 0.030 at location 1 and 0.0059 to 0.03 at location 2. The corresponding values for DC were 0.043 and 0.042, and 0.035 and 0.023 for WC.

Interestingly, the trend observed for the modulation parameter γ that indicated weak modulation for all specimens except for DC and WC was also observed for the parameters $DI_{Amplitude}$ and $DI_{Frequency}$, albeit with some interesting variations. Specimens R, RC, and PH, all with no or minor corrosion (Table 4) and likely intact steel–concrete interface, exhibited overall weak modulation in the analyses of all these parameters. The specimens with severe corrosion, PHI and PHCI, behaved quite consistently with respect to modulation parameter γ and the damage index for amplitude modulation. The values for parameters of γ and $DI_{Amplitude}$ were relatively low, but those for $DI_{Frequency}$ were at a moderate level indicating enhanced sensitivity of the frequency modulation phenomenon. Also, specimen D featured parallel trends, i.e., low overall γ and $DI_{Amplitude}$ but moderate $DI_{Frequency}$, yet there were differences between the values obtained at impact locations 1 and 2 so that the values at impact location 2 were clearly higher than at impact location 1. Finally, the highest values for all three parameters: γ, $DI_{Amplitude}$, and $DI_{Frequency}$ were detected for the specimens DC and WC. However, the significant differences between the indices γ and $DI_{Amplitude}$ observed for DC and WC with respect to PHI and PHCI

are eliminated when studying $DI_{Frequency}$, here the difference between the specimens is comparatively small. A possible explanation for the variation between γ and $DI_{Frequency}$ is that γ is restricted to 20–50 kHz whereas no bandwidth restriction is employed during the analysis of $DI_{Frequency}$, only the influence of harmonics was removed due to the EMD-process. Previous work has indicated that amplitude modulation is more sensitive to the presence of defects than frequency modulation is [47], although our findings clearly indicate that this is not universally true. It is important to consider the aspect of the variability of impact strength as this will largely impact the instantaneous amplitude, but the effects on frequency modulation are not as clear.

PHI, PHCI, DC, and WC exhibit similar frequency modulation at location 1, whereas the frequency modulation for PHI and PHCI halved in intensity when impacted at location 2. On the other hand, specimen D demonstrates a general increase in modulation intensity at location 2, which aligns with the observation for γ. This behavior might be explained by the impacts being in regions closer to local defects at the locations showing elevated modulation intensities here. For PHI that would be location 1, and for D location 2. Considering that corrosion occurred under the inlay in all cases, it would be reasonable to assume that the impact locations may not significantly affect the result as the location of the defects should be consistent across all specimens. However, due to the variability of corrosion-induced roughness and the circular contact of the inlay, the non-bonded contacts and various other defects may arise in seemingly random sectors of the circular region. Referring back to Fig. 9, we observe that the impact locations are opposite to each other, indicating that the impacts primarily affect the closest sectors of the inlays. Certainly, the impacts generate omnidirectional elastic waves and thus affect the entire specimen volume but the greatest wave amplitudes within the volume are found in the direct path from the source locations. Injecting energy close to defects causes them to act as more intense nonlinear sources due to the comparatively higher amplitudes activating the defects, thereby influencing the results. This reasoning is strengthened by the fact that the specimens with likely intact steel–concrete interfaces, i.e., R, RC, and PH, do not exhibit such pronounced impact location-based variability. It is important to note that the results may also have been affected by various complex nonclassical nonlinear elastic effects such as noise-like variability and instability of modulation components [14]. Similar speculations have been made in previous studies on this subject [16,54].

3.2.4. Combined results using the total damage index

The TDI for specimen S at location i was calculated using Eq. (14). The values for TDI for the specimens defined at impact locations 1 and 2 are depicted in Fig. 16(a) and (b), respectively. By using the TDI, the specimens can be effectively categorized according to their level of damage. For instance, for specimens R, RC, and PH, the TDIs at both measurement locations were below 0.1. Therefore, these specimens are categorized as having a low damage level, see Table 3. Even the specimen PHI which exhibited slightly greater TDI values: 0.2 at location 1 and 0.11 at location 2, also fell into the group of "low level of damage". Further, specimen D featured the TDIs of 0.1 at location 1 and 0.26 at location 2. The latter value brings the specimen into the group of "minor damage level" (Table 3). Specimen PHCI systematically exhibited TDI values exceeding 0.5 but lower than 0.75 in both measurement locations, being therefore grouped into "moderate damage level", see Table 3. Ultimately, specimens DC and WC exhibited TDIs greater than 0.5 at both measurement locations, with TDI values in one of the two measurements exceedingly as high a value as 0.8. Therefore, it is evident that these specimens belonged to the group of "severe damage level" (Table 3). By using the TDI classification, it is evident that the grouping of the specimens by damage level is less cumbersome compared to relying on studying each damage index separately. This highlights the strength of using combined damage indices and inspection result fusing using the TDI.

Based on the results, it is evident that the discontinuities introduced to the slabs in the form of wood (WC) and delamination (D & DC) induced strong waveform distortion. As discussed previously, this may be caused by the new type of interface, steel–wood interface, and the delamination gap, in the concrete structure. The delamination gap itself was filled by water (times of wetting) and air (times of drying) during the wetting-drying cycles. It is expected that the media in the delamination gap did not significantly contribute to any type of localized nonlinearity, however, the contact areas around the gap may be partially non-bonded (particularly specimen DC) which creates localized elastic contacts. The embedded wooden piece cannot bond to the steel surface in the same manner as concrete, and it is possible that the concrete may have difficulties in bonding to the wooden surfaces, as well. The presence of a kissing bond in any of the interfaces would certainly affect the local elastic properties, thus inducing nonlinear effects. The capability to differentiate between steel–concrete interface characteristics is a very promising result for the employed nonlinear ultrasonic techniques, as embedded foreign matter and delamination between steel and concrete have been reported in connection with liner damage [1].

The concrete slab containing the most severely corroded steel liner, PHCI (see Table 4), demonstrated a moderate level of damage according to the TDI. Without periodical inspection during the exposure period, two speculations regarding the observations can be made. The damage may have exceeded the level where measured nonlinearity would reach its maximum, a phenomenon known to occur in severely damaged specimens [12,35]. However, this is unlikely considering that no macro-cracking was observed in the concrete. In terms of harmonic distortion, PHCI exhibited greater levels of harmonics compared to DC and WC. Conversely, the other severely corroded specimen PHI demonstrated a low TDI but exhibited strong instantaneous frequency modulation yet weak harmonic distortion. Although the specimen PHI suffered from a corrosion attack covering a large surface area, the extent was "only" 2/3 of that in PHCI (Table 4) which was clearly reflected in the results. It is quite possible that the corrosion products formed in the specimens PH and PHI were insufficiently voluminous (i.e., too thin) to induce cracking in the surrounding concrete and possibly only blocked the gaps formed by surface roughness in the interface, thus not challenging the bond strength in the steel–concrete interface.

The insets in Fig. 16(a) and (b) show the normalized inverse magnitude of the fundamental frequency component A_1 (magnitudes shown in Fig. 11(a)) for measurements with impacts at locations 1 and 2, respectively. The inverse magnitude here acts as a proxy for attenuation, a widely used parameter in corrosion detection [6]. By purely studying the trend seen in the inset figures, it is evident that a similar pattern to that depicted in the TDI distributions is shown. Interestingly, previous work has indicated that attenuation measurements were more sensitive to corrosion-induced damage than the nonlinear technique called Scaling Subtraction Method was when measurements were performed using a transmitter and receiver on the same side [22], as the measurements are performed in the present work. Our work indicates similar sensitivity when using globally measured parameters, both attenuation and parameters of nonlinearity. Furthermore, our work suggests that frequency modulation is very sensitive to corrosion-induced bond failure which is reflected in the TDI. If through-transmission measurements were performed on a specimen with completely non-bonded concrete–steel–concrete interfaces, it is quite possible that attenuation would be a far greater indicator of disbonding compared to nonlinear evaluation. This is because the ultrasonic waves would likely face difficulties propagating through the air-filled voids caused by completely non-bonded interfaces. Therefore, the recorded signals would likely have very weak amplitudes.
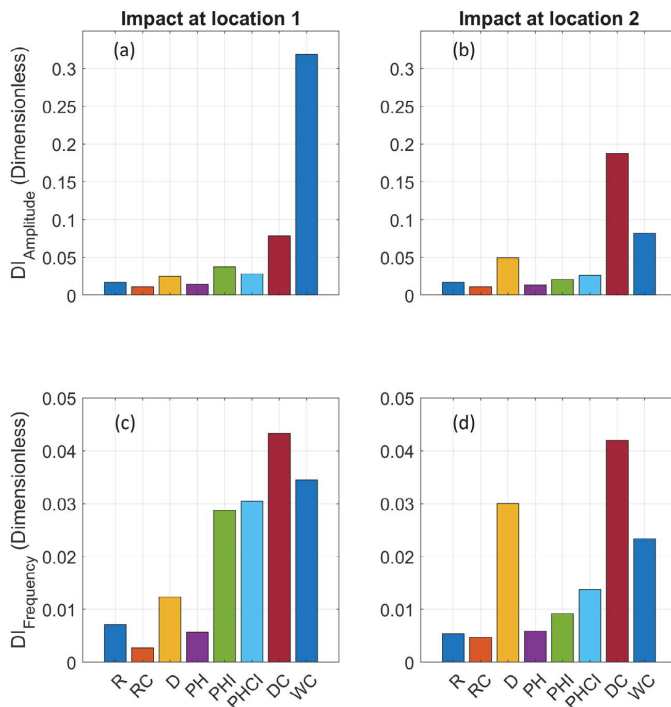
Fig. 15. Damage indices extracted from instantaneous modulation characteristics. Amplitude modulation (a – b) and frequency modulation (c – d) for all studied specimens.
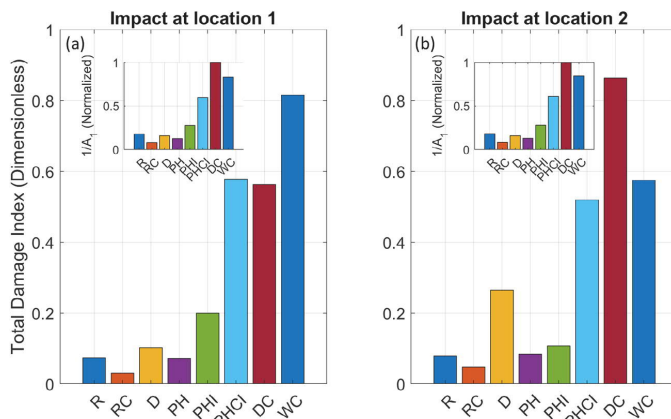

Fig. 16. Total Damage Index for all inspected specimens for measurements with impacts at location 1 (a) and location 2 (b). The inset figures display the inverse of the magnitude of the fundamental component to show that the similar patterns seen in the TDI is reflected in the attenuation of the fundamental component.

4. Recommendations for future work

To further validate and expand the applicability of our approach, we recommend conducting experiments on larger concrete specimens with coarse-grained constituents. Additionally, future research should explore the synergy of combining results from nonlinear ultrasonic evaluation with complementary inspection techniques using the TDI, thus enhancing the accuracy and reliability of structural assessments. The recommendations are summarized in three items:

(1) Future work is recommended to employ both acoustic (e.g., ultrasonics, impact echo, and more) and possibly electrical (e.g., resistivity) measurements and combine the results into a TDI to achieve a richer parameter, thus achieving more reliable and accurate evaluation of the structural integrity of the object under examination.

(2) When performing accelerated corrosion of embedded steel liner plates the damage evolution could be monitored by the use of

linear and nonlinear ultrasonic evaluation, and electrochemical measurements during the corrosion process. If adequately small specimens are manufactured, it would be possible to X-ray the specimens exhibiting a strong damage response to better understand the nature of the steel–concrete interface and any damage induced in the concrete due to corrosion expansion. This would also yield a better understanding of the response from the ultrasonic measurements.

(3) It would be beneficial to examine larger specimens with coarse-grained constituents and varying embedment depth of the steel liner to approach real-world applications. The novel inlay-technique presented here and in more detail in Ref. [27] could assist in producing localized accelerated corrosion in large specimens. The difference in results between through-transmission and measurements using one-sided access would also be of interest to investigate.

5. Conclusions

In this work, we have conducted a comprehensive investigation using non-destructive nonlinear ultrasonic evaluation techniques on small laboratory-scale concrete slabs containing a steel liner. Our research involved the assessment of steel–concrete interface discontinuities, including the presence of foreign matter, delamination gap, and various extents of corrosion. The corrosion was achieved by employing a novel concrete-inlay technique which allowed the corrosion to occur in a defined anodic area at a slowly accelerated state, thus approaching naturally occurring corrosion in its various forms. By the use of a global inspection technique featuring a single probing location with two impact locations, we employed higher-harmonic analysis, impact-based modulation spectroscopy, and the separation of modulation phenomena by the use of the Hilbert–Huang transform (HHT). The related damage indices were combined into a Total Damage Index (TDI) to enable an intuitive classification of the inspected specimens by their damage level. The results presented in this paper enable the following conclusions to be drawn:

(1) The combination of higher-harmonic analysis and modulation intensity analysis, into a Total Damage Index (TDI), represents a promising approach to evaluate structural damage in concrete slabs. The presence of discontinuities at the steel–concrete interface, attributed to foreign matter, delamination gap, or severe corrosion, consistently yielded high TDI values (exceeding 0.5). These results strongly indicate the potential of nonlinear ultrasonic techniques and the integration of related damage indices into a TDI to detect early-stage structural deterioration by corrosion and discontinuities in laboratory-scale concrete slabs.

(2) This study demonstrated the utility of the HHT for isolating frequency modulation, which revealed waveform distortion consistent with the level of discontinuities at the steel–concrete interface. The isolation of frequency modulation is suspected to reduce the effects of varying impact strength which would affect isolated amplitude modulation greatly in impact-based modulation measurements.

(3) By the use of a global inspection technique, we have shown that nonlinear ultrasonic techniques can be combined with conventional methods, i.e. attenuation measurements, via the introduction of the inverse magnitude of the fundamental frequency component of the ultrasonic probe wave which acted as a proxy for attenuation. The TDI results obtained through our approach exhibited consistency with indications derived from attenuation estimations, reinforcing the efficacy of our method in identifying foreign matter, delamination gaps, or severe corrosion at the steel–concrete interface. This approach highlights the synergy of combining conventional and nonlinear ultrasonic evaluation as well as the strength of global inspection techniques.

In summary, our research not only presents a novel and effective method for evaluating structural damage in concrete but also indicates the potential of nonlinear ultrasonic techniques. The introduction of the novel concrete-inlay corrosion procedure makes this study, to the best of our knowledge, the first to investigate the detection of slowly progressed localized minor to moderate corrosion in concrete-embedded steel plates using nonlinear ultrasonic evaluation. By focusing on laboratory-scale concrete slabs, we provide a foundation for future investigations on larger and more complex concrete structures. We anticipate that the integration of our findings with conventional NDT approaches and the further refinement of nonlinear ultrasonic methods will contribute to a more reliable and accurate assessment of the structural integrity of complex concrete structures.

CRediT authorship contribution statement

Markus Nilsson: Writing – review & editing, Writing – original draft, Visualization, Methodology, Investigation, Funding acquisition, Formal analysis, Conceptualization. **Elina Huttunen-Saarivirta:** Writing – review & editing, Resources, Funding acquisition, Conceptualization. **Edgar Bohner:** Writing – review & editing, Resources, Funding acquisition, Conceptualization. **Miguel Ferreira:** Writing – review & editing, Resources, Funding acquisition, Conceptualization.

Declaration of competing interest

The authors declare that they have no known competing financial interests or personal relationships that could have appeared to influence the work reported in this paper.

Data availability

Data will be made available on request.

Acknowledgments

References

[1] D. Dunn, A. Pulvirenti, P. Klein, Containment liner corrosion, in: Proceedings of the 15th International Conference on Environmental Degradation of Materials in Nuclear Power Systems — Water Reactors, Vol. 2, Springer International Publishing, Cham, 2011, pp. 1037–1049, http://dx.doi.org/10.1007/978-3-319-48760-1_63, URL: http://link.springer.com/10.1007/978-3-319-48760-1_63.

[2] M. Oxfall, Climatic Conditions Inside Nuclear Reactor Containments - Evaluation of Moisture Condition in the Concrete Within Reactor Containments and Interaction with the Ambient Compartments (Doctoral dissertation), Lund University, 2016.

[3] D. Féron, Nuclear Corrosion Science and Engineering, No. 22, twenty second ed., Woodhead Publishing, 2012, p. 463, http://dx.doi.org/10.1533/9780857095343,

[4] Y. Xu, Y. Song, Chemical-mechanical transformation of the expansion effect for nonuniform steel corrosion and its application in predicting the concrete cover cracking time, Cem. Concr. Compos. 127 (March 2021) (2022) 104376, http://dx.doi.org/10.1016/j.cemconcomp.2021.104376, https://linkinghub.elsevier.com/retrieve/pii/S0958946521004431.

[5] M. Otieno, J. Ikotun, Y. Ballim, Experimental investigations on the influence of cover depth and concrete quality on time to cover cracking due to carbonation-induced corrosion of steel in RC structures in an urban, inland environment, Constr. Build. Mater. 198 (2019) 172–181, http://dx.doi.org/10.1016/j.conbuildmat.2018.11.215, https://linkinghub.elsevier.com/retrieve/pii/S0950061818329106.

[6] P. Magda, T. Stepinski, Corrosion assessment using ultrasound, Diagnostyka 16 (1) (2015) 15–17.

[7] H. Liu, L. Zhang, H.F. Liu, S. Chen, S. Wang, Z.Z. Wong, K. Yao, High-frequency ultrasonic methods for determining corrosion layer thickness of hollow metallic components, Ultrasonics 89 (January) (2018) 166–172, http://dx.doi.org/10.1016/j.ultras.2018.05.006.

[8] M. Saleem, H. Gutierrez, Using artificial neural network and non-destructive test for crack detection in concrete surrounding the embedded steel reinforcement, Struct. Concr. 22 (5) (2021) 2849–2867, http://dx.doi.org/10.1002/suco.202000767, URL: https://onlinelibrary.wiley.com/doi/10.1002/suco.202000767.

[9] M. Saleem, A. Hosoda, Latin hypercube sensitivity analysis and non-destructive test to evaluate the pull-out strength of steel anchor bolts embedded in concrete, Constr. Build. Mater. 290 (2021) 123256, http://dx.doi.org/10.1016/j.conbuildmat.2021.123256, https://linkinghub.elsevier.com/retrieve/pii/S0950061821010163.

[10] J. Jin, M.G. Moreno, J. Riviere, P. Shokouhi, Impact-based nonlinear acoustic testing for characterizing distributed damage in concrete, J. Nondestruct. Eval. 36 (3) (2017) 51, http://dx.doi.org/10.1007/s10921-017-0428-2, URL: http://link.springer.com/10.1007/s10921-017-0428-2.

[11] V. Zaitsev, V. Gusev, B. Castagnede, Luxemburg-Gorky effect retooled for elastic waves: A mechanism and experimental evidence, Phys. Rev. Lett. 89 (10) (2002) 2–5, http://dx.doi.org/10.1103/PhysRevLett.89.105502.

[12] M.Á. Climent-Llorca, M. Miró-Oca, P. Poveda-Martínez, J. Ramis-Soriano, Use of higher-harmonic and intermodulation generation of ultrasonic waves to detecting cracks due to steel corrosion in reinforced cement mortar, Int. J. Concr. Struct. Mater. 14 (1) (2020) http://dx.doi.org/10.1186/s40069-020-00432-x.

[13] V. Marcantonio, D. Monarca, A. Colantoni, M. Cecchini, Ultrasonic waves for materials evaluation in fatigue, thermal and corrosion damage: A review, Mech. Syst. Signal Process. 120 (2019) 32–42, http://dx.doi.org/10.1016/j.ymssp.2018.10.012.

[14] I.Y. Solodov, B.A. Korshak, Instability, chaos, and "memory" in acoustic-wave–crack interaction, Phys. Rev. Lett. 88 (1) (2002) 3, http://dx.doi.org/10.1103/PhysRevLett.88.014303.

[15] M. Bentahar, A. Di Bella, C. Mechri, S. Montresor, M. Scalerandi, X. Yu, Exploiting slow dynamics effects for damage detection in concrete, Front. Built Environ. 6 (June) (2020) 1–10, http://dx.doi.org/10.3389/fbuil.2020.00064.

[16] M. Miró, J.N. Eiras, P. Poveda, M. Climent, J. Ramis, Detecting cracks due to steel corrosion in reinforced cement mortar using intermodulation generation of ultrasonic waves, Constr. Build. Mater. 286 (2021) 122915, http://dx.doi.org/10.1016/j.conbuildmat.2021.122915.

[17] S. Basu, A. Thirumalaiselvi, S. Sasmal, T. Kundu, Nonlinear ultrasonics-based technique for monitoring damage progression in reinforced concrete structures, Ultrasonics 115 (April) (2021) 106472, http://dx.doi.org/10.1016/j.ultras.2021.106472.

[18] F. Ouvrier-Buffet, J.N. Eiras, V. Garnier, C. Payan, N. Ranaivomanana, B. Durville, C. Marquie, Linear and nonlinear resonant ultrasonic techniques applied to assess delayed ettringite formation on concrete samples, Constr. Build. Mater. (2021) 121545, http://dx.doi.org/10.1016/j.conbuildmat.2020.121545.

[19] S. Miele, P.M. Karve, S. Mahadevan, V. Agarwal, Diagnosis of internal cracks in concrete using vibro-acoustic modulation and machine learning, Struct. Health Monit. 21 (5) (2022) 1973–1991, http://dx.doi.org/10.1177/14759217211047901, URL: http://journals.sagepub.com/doi/10.1177/14759217211047901.

[20] J. Zhao, J. Wu, K. Chen, Feasibility of application for the SHG technology of longitudinal wave in quantitatively evaluating carbonated concrete, Appl. Sci. (Switzerland) 12 (24) (2022) http://dx.doi.org/10.3390/app12413009.

[21] M.-Á. Climent, M. Miró, J.-N. Eiras, P. Poveda, G. de Vera, E.-G. Segovia, J. Ramis, Early detection of corrosion-induced concrete micro-cracking by using nonlinear ultrasonic techniques: Possible influence of mass transport processes, Corros. Mater. Degrad. 3 (2) (2022) 235–257, http://dx.doi.org/10.3390/cmd3020014.

[22] P. Antonaci, C.L. Bruno, M. Scalerandi, F. Tondolo, Effects of corrosion on linear and nonlinear elastic properties of reinforced concrete, Cem. Concr. Res. 51 (2013) 96–103, http://dx.doi.org/10.1016/j.cemconres.2013.04.006.

[23] M.Á. Climent, M. Miró, J. Carbajo, P. Poveda, G. de Vera, J. Ramis, Use of non-linear ultrasonic techniques to detect cracks due to steel corrosion in reinforced concrete structures, Materials 12 (5) (2019) http://dx.doi.org/10.3390/MA12050813.

[24] T. Arumaikani, S. Sasmal, T. Kundu, Detection of initiation of corrosion induced damage in concrete structures using nonlinear ultrasonic techniques, J. Acoust. Soc. Am. 151 (2) (2022) 1341–1352, http://dx.doi.org/10.1121/10.0009621.

[25] B. Díaz, B. Guitián, X. Nóvoa, M. Pérez, The effect of long-term atmospheric aging and temperature on the electrochemical behaviour of steel rebars in mortar, Corros. Sci. 140 (September 2017) (2018) 143–150, http://dx.doi.org/10.1016/j.corsci.2018.06.007, https://linkinghub.elsevier.com/retrieve/pii/S0010938X17317171.

[26] G.S. Duffó, W. Morris, I. Raspini, C. Saragovi, A study of steel rebars embedded in concrete during 65 years, Corros. Sci. 46 (9) (2004) 2143–2157, http://dx.doi.org/10.1016/j.corsci.2004.01.006.

[27] E. Huttunen-Saarivirta, E. Bohner, A. Trentin, M. Ferreira, A closer look at the corrosion of steel liner embedded in concrete, Cem. Concr. Compos. (105280) (2023) 105280, http://dx.doi.org/10.1016/j.cemconcomp.2023.105280, URL: https://linkinghub.elsevier.com/retrieve/pii/S0958946523003542.

[28] V.Y. Zaitsev, L.A. Matveev, A.L. Matveyev, On the ultimate sensitivity of nonlinear-modulation method of crack detection, NDT E Int. 42 (7) (2009) 622–629, http://dx.doi.org/10.1016/j.ndteint.2009.05.001, URL: http://dx.doi.org/10.1016/j.ndteint.2009.05.001.

[29] D. Neff, J. Harnisch, M. Beck, V. L'Hostis, J. Goebbels, D. Meinel, Morphology of corrosion products of steel in concrete under macro-cell and self-corrosion conditions, Mater. Corros. 62 (9) (2011) 861–871, http://dx.doi.org/10.1002/maco.201005861.

[30] M. Nilsson, P. Ulriksen, N. Rydén, Nonlinear ultrasonic characteristics of a corroded steel plate, Nondestruct. Test. Eval. 38 (3) (2023) 456–479, http://dx.doi.org/10.1080/10589759.2022.2123481, https://www.tandfonline.com/doi/full/10.1080/10589759.2022.2123481.

[31] O.V. Rudenko, A.I. Korobov, M.Y. Izosimova, Nonlinearity of solids with micro- and nanodefects and characteristic features of its macroscopic manifestations, Acoust. Phys. 56 (2) (2010) 151–157, http://dx.doi.org/10.1134/S1063771010020053.

[32] I. Solodov, N. Krohn, G. Busse, CAN: an example of nonclassical acoustic nonlinearity in solids, Ultrasonics 40 (2002) 621–625.

[33] D. Broda, W.J. Staszewski, A. Martowicz, T. Uhl, V.V. Silberschmidt, Modelling of nonlinear crack-wave interactions for damage detection based on ultrasound - A review, J. Sound Vib. 333 (4) (2014) 1097–1118, http://dx.doi.org/10.1016/j.jsv.2013.09.033, URL: http://dx.doi.org/10.1016/j.jsv.2013.09.033.

[34] S.L. Garrett, Nonlinear acoustics, in: Understanding Acoustics - An Experimentalist's View of Acoustics and Vibration, Vol. 1, first ed., Springer Cham, 2017, pp. 815–870, http://dx.doi.org/10.1007/978-3-319-49978-9.

[35] G. Zhao, M. Jiang, Y. Luo, W. Li, Q. Sui, Comparison of sensitivity in nonlinear ultrasonic detection based on lamb wave phase velocity matching mode, Nondestruct. Test. Eval. 38 (2) (2022) 297–312, http://dx.doi.org/10.1080/10589759.2022.2121394.

[36] K.H. Matlack, J.Y. Kim, L.J. Jacobs, J. Qu, Review of second harmonic generation measurement techniques for material state determination in metals, J. Nondestruct. Eval. 34 (1) (2015) http://dx.doi.org/10.1007/s10921-014-0273-5.

[37] Kyung-Young Jhang, C.J. Lissenden, I. Solodov, Y. Ohara, V. Gusev, in: K.-Y. Jhang, C.J. Lissenden, I. Solodov, Y. Ohara, V. Gusev (Eds.), Measurement of Nonlinear Ultrasonic Characteristics, in: Springer Series in Measurement Science and Technology, Springer Singapore, Singapore, 2020, http://dx.doi.org/10.1007/978-981-15-1461-6, URL: http://link.springer.com/10.1007/978-981-15-1461-6.

[38] X.J. Chen, J.Y. Kim, K.E. Kurtis, J. Qu, C.W. Shen, L.J. Jacobs, Characterization of progressive microcracking in Portland cement mortar using nonlinear ultrasonics, NDT E Int. 41 (2) (2008) 112–118, http://dx.doi.org/10.1016/j.ndteint.2007.08.009.

[39] N.E. Huang, Z. Shen, S.R. Long, M.C. Wu, H.H. Snin, Q. Zheng, N.C. Yen, C.C. Tung, H.H. Liu, The empirical mode decomposition and the hubert spectrum for nonlinear and non-stationary time series analysis, Proc. R. Soc. A 454 (1971) (1998) 903–995, http://dx.doi.org/10.1098/rspa.1998.0193.

[40] N.E. Huang, Z. Wu, A review on Hilbert-Huang transform: Method and its applications to geophysical studies, Rev. Geophys. 46 (2) (2008) RG2006, http://dx.doi.org/10.1029/2007RG000228, URL: http://rcada.ncu.edu.tw/reference010.pdf, http://doi.wiley.com/10.1029/2007RG000228.

[41] Y. Chen, M.Q. Feng, A technique to improve the empirical mode decomposition in the Hilbert-Huang transform, Earthq. Eng. Eng. Vib. 2 (1) (2003) 75–85, http://dx.doi.org/10.1007/BF02857540, URL: http://link.springer.com/10.1007/BF02857540.

[42] Z. He, Y. Shen, Q. Wang, Boundary extension for Hilbert–Huang transform inspired by gray prediction model, Signal Process. 92 (3) (2012) 685–697, http://dx.doi.org/10.1016/j.sigpro.2011.09.010, https://linkinghub.elsevier.com/retrieve/pii/S0165168411003100.

[43] A. Zeiler, R. Faltermeier, I.R. Keck, A.M. Tome, C.G. Puntonet, E.W. Lang, Empirical mode decomposition - an introduction, in: The 2010 International Joint Conference on Neural Networks, Vol. 1, IJCNN, IEEE, 2010, pp. 1–8, http://dx.doi.org/10.1109/IJCNN.2010.5596829, URL: http://ieeexplore.ieee.org/document/5596829/.

[44] M.C. Peel, G.G. Pegram, T.A. McMahon, Empirical mode decomposition: Improvement and application, in: MODSIM07 - Land, Water and Environmental Management: Integrated Systems for Sustainability, Proceedings, 2007, pp. 2996–3002.

[45] D. Iatsenko, Nonlinear Mode Decomposition, in: Springer Theses, Springer International Publishing, Lancaster University, UK, Cham, 2015, http://dx.doi.org/10.1007/978-3-319-20016-3, URL: https://link.springer.com/10.1007/978-3-319-20016-3.

[46] G. Tu, X. Dong, S. Chen, B. Zhao, L. Hu, Z. Peng, Iterative nonlinear chirp mode decomposition: A Hilbert-Huang transform-like method in capturing intra-wave modulations of nonlinear responses, J. Sound Vib. 485 (2020) 115571, http://dx.doi.org/10.1016/j.jsv.2020.115571, https://linkinghub.elsevier.com/retrieve/pii/S0022460X2030403X.

[47] H.F. Hu, W.J. Staszewski, N.Q. Hu, R.B. Jenal, G.J. Qin, Crack detection using nonlinear acoustics and piezoceramic transducers—instantaneous amplitude and frequency analysis, Smart Mater. Struct. 19 (6) (2010) 065017, http://dx.doi.org/10.1088/0964-1726/19/6/065017, URL: https://iopscience.iop.org/article/10.1088/0964-1726/19/6/065017.

[48] R.G. Maev, F. Seviaryn, Applications of non-linear acoustics for quality control and material characterization, J. Appl. Phys. 132 (16) (2022) 161101, http://dx.doi.org/10.1063/5.0106143, https://pubs.aip.org/jap/article/132/16/161101/2837589/Applications-of-non-linear-acoustics-for-quality.

[49] X. Fu, D. Chung, Effect of corrosion on the bond between concrete and steel rebar, Cem. Concr. Res. 27 (12) (1997) 1811–1815, http://dx.doi.org/10.1016/S0008-8846(97)00172-5, https://linkinghub.elsevier.com/retrieve/pii/S0008884697001725.

[50] S. Sajedi, Q. Huang, Probabilistic prediction model for average bond strength at steel–concrete interface considering corrosion effect, Eng. Struct. 99 (2015) 120–131, http://dx.doi.org/10.1016/j.engstruct.2015.04.036, https://linkinghub.elsevier.com/retrieve/pii/S0141029615002928.

[51] X. Chai, H. Shang, C. Zhang, Bond behavior between corroded steel bar and concrete under sustained load, Constr. Build. Mater. 310 (July) (2021) 125122, http://dx.doi.org/10.1016/j.conbuildmat.2021.125122, https://linkinghub.elsevier.com/retrieve/pii/S0950061821028671.

[52] Y. He, Y. Xiao, Z. Su, Y. Pan, Z. Zhang, Contact acoustic nonlinearity effect on the vibro-acoustic modulation of delaminated composite structures, Mech. Syst. Signal Process. 163 (June 2021) (2022) 108161, http://dx.doi.org/10.1016/j.ymssp.2021.108161, URL: https://linkinghub.elsevier.com/retrieve/pii/S0888327021005409.

[53] D. Donskoy, A. Sutin, A. Ekimov, Nonlinear acoustic interaction on contact interfaces and its use for nondestructive testing, NDT E Int. 34 (4) (2001) 231–238, http://dx.doi.org/10.1016/S0963-8695(00)00063-3, URL: https://linkinghub.elsevier.com/retrieve/pii/S0963869500000633.

[54] C.R. Courtney, B.W. Drinkwater, S.A. Neild, P.D. Wilcox, Factors affecting the ultrasonic intermodulation crack detection technique using bispectral analysis, NDT E Int. 41 (3) (2008) 223–234, http://dx.doi.org/10.1016/j.ndteint.2007.09.004, URL: https://linkinghub.elsevier.com/retrieve/pii/S0963869507001120.

Appendix C

Paper III

Nilsson, M., Ulriksen, P. and Rydén, N. (2024). Nonlinear Wave Modulation for the Evaluation of Corroded Steel Plates Embedded in Concrete. *Journal of Advanced Concrete Technology*. Japan Concrete Institute, Vol. 22, pp. 545 – 560, doi:10.3151/jact.22.545

Scientific paper

Nonlinear Wave Modulation for the Evaluation of Corroded Steel Plates Embedded in Concrete

Markus Nilsson[1*], Peter Ulriksen[2] and Nils Rydén[3]

Abstract

Corrosion of steel components embedded in concrete is detrimental to the structural integrity and their intrinsic function, such as the leak tightness of containment liners in nuclear reactor containment buildings. Detection of embedded liner corrosion is a challenging task due to the concrete heterogeneity and the large dimension of containment buildings. This initial study explores early-stage detection using nonlinear wave modulation on corroded liner plates embedded inside small lab-scaled concrete cylinder specimens. The liners were corroded before being embedded in concrete to minimize the risk of concrete cracking, allowing for a focused exploration of early-stage detection capabilities. Impact-based modulation and Luxembourg-Gorky-type cross-modulation techniques were employed. Impact-based modulation uses a hammer impact to introduce a strong perturbation on a weak probe signal, analyzed with the Hilbert-Huang transform. Cross-modulation uses a second amplitude-modulated ultrasound to transfer modulation onto the weaker probe, analyzed via spectral analysis. Initial results indicate that impact-based frequency modulation is not highly sensitive to corrosion products alone and may not effectively identify specimens without concrete defects. However, impact-induced amplitude modulation is more responsive to corrosion and cracks in concrete. Cross-modulation shows strong sensitivity to crack-like defects and embedded severe corrosion but may not be optimal for early-stage corrosion detection due to inherent concrete cracks. Further research is needed to evaluate nonlinear ultrasonic techniques applied to larger concrete specimens and under realistic conditions before making practical recommendations.

1. Introduction

Evaluating the structural integrity of concrete structures is inherently challenging due to their heterogeneous composition, which causes high attenuation of excitations and intricate scattering. This is especially true in critical environments such as nuclear reactor containment buildings, which consist of heavily reinforced concrete and typically a steel liner. The liner may be surface mounted (inside) or be embedded and covered by concrete with a thickness upwards to 1 m. The purpose of the liner is to ensure that the containment building act as a leak-tight barrier against radioactive particle release, which is why its leak-tightness is very important to maintain. Li and Gong (2023) have shown that degradation of the liner by corrosion can seriously affect the leak-tightness of the structure to the point where leakage might occur even at low pressure under accident conditions. It is therefore critical for the prolongation of existing reactors to be able

to detect corrosion in concrete-embedded steel liners before through-wall corrosion occurs, and if it has, to locate the damaged area for remedial measures.

Steel should not undergo severe corrosion when embedded in concrete because the alkaline environment keeps the steel surface in a passive state. However, high levels of chlorides, concrete carbonation, or embedded foreign matter may all contribute to increased risk of deterioration (Miyazato and Otsuki 2010; Dunn *et al.* 2011; Otieno *et al.* 2019). In addition to affecting the properties of the liner itself, corrosion causes a volumetric expansion of the liner within the concrete which can induce cracking, thus severely impact the structural integrity of the concrete (Otieno *et al.* 2019; Liang and Wang 2020). Due to the many negative implications of concrete-embedded steel components it is important to evaluate techniques to nondestructively evaluate and detect early-stage corrosion in embedded steel.

Nonlinear acoustical methods have proven capable of detecting various flaws in concrete structures through several studies (Chen *et al.* 2008; Korenska *et al.* 2009; Leśnicki *et al.* 2011; Dahlen *et al.* 2015; Ongpeng *et al.* 2016; Shokouhi *et al.* 2017; Climent-Llorca *et al.* 2019; Genovés *et al.* 2019; Miele *et al.* 2020; Basu *et al.* 2021; Xu *et al.* 2022) but little work has been done on evaluating the state of the embedded components themselves. However, methods based on nonlinear frequency-mixing that utilizes a pump-probe excitation scheme have shown promising indications for detecting steel corrosion-induced damage in concrete (Donskoy *et al.* 1998; Climent-Llorca *et al.* 2020, 2022).

---

[1]Doctoral student, Division of Engineering Geology, Faculty of Engineering, Lund University, Lund, Sweden. *Corresponding author,
E-mail: markus.nilsson@tg.lth.se
[2]Researcher, Division of Engineering Geology, Faculty of Engineering, Lund University, Lund, Sweden.
[3]Associate Professor, Division of Engineering Geology, Faculty of Engineering, Lund University, Lund, Sweden.

The most common frequency-mixing method is called Vibro-Acoustic Modulation, coined by Donskoy and Sutin (1998), or Nonlinear Wave Modulation Spectroscopy (NWMS) (Van Den Abeele *et al.* 2000). The method uses a comparatively low-frequency continuous vibration to modulate a higher frequency probing wave. Instead of using a continuous perturbation to modulate the probe signal, an impactor can be used to achieve a wide-banded modulation by transient excitation (Donskoy and Sutin 1998; Eiras *et al.* 2016). The strong 'pump' modulates a weaker 'probe' due to local elastic nonlinearities caused by the presence of defects (Broda *et al.* 2014; Pieczonka *et al.* 2015).

Defects such as cracks, delaminations, and contacts are associated with embedded corrosion, and they often have sizes much smaller than the probing wavelength. This makes detection with conventional ultrasonic techniques challenging. However, such defects demonstrate strong elastic nonlinearity which distorts acoustic waves, even with wavelengths several orders of magnitude greater than the defect size. The nonlinearity often deviates from classical power-law stress-strain dependence and the associated phenomena are termed nonclassical (Zaitsev 2019). Some nonclassical nonlinear phenomena include clapping Hertzian nonlinearity, as suggested by Zaitsev *et al.* (2011), hysteretic nonlinearity (Guyer and Johnson 1999), slow dynamics and the associated relaxation phenomenon (Johnson and Sutin 2005), and amplitude-dependent dissipation (Zaitsev *et al.* 2005; Fillinger *et al.* 2006). The combined effects from various nonlinear phenomena can be exploited to achieve highly sensitive methods for non-destructive evaluation (Zaitsev *et al.* 2009).

An experimentally interesting nonclassical phenomenon is the elastic wave analogue of the Luxembourg-Gorky (LG) effect initially observed in radio waves by Tellegen (1933). The LG effect is essentially cross-modulation where a strong amplitude-modulated wave transfers modulation information to a weaker probing wave, thus generating sidebands around the probing spectral component (Zaitsev *et al.* 2002a, 2002b, 2005; Osika *et al.* 2023). This cross-modulation method offers a way to examine strictly nonclassical modulation without being influenced by classical power-law nonlinearity which typically occurs simultaneously as various nonclassical phenomena (Johnson and Sutin 2005).

Previous work on the use of nonlinear acoustic methods to nondestructively evaluate the state of concrete specimens containing corroding components has mainly focused on studying methods to detect reinforcement corrosion achieved by highly accelerated corrosion processes (Antonaci *et al.* 2013; Climent-Llorca *et al.* 2020, 2022; Miró *et al.* 2021). Such gross corrosion indeed introduces pronounced cracking in the surrounding concrete which is certainly beneficial for the nonlinear ultrasonic methods applied. However, it may not always be the case that severe cracking can be detected before significant deterioration has already occurred as the time for

cracks to develop is related to the concrete cover (Otieno *et al.* 2019; Xu and Song 2022). A recent study by Nilsson *et al.* (2023a) examined slowly progressed localized corrosion and used nonlinear ultrasonic techniques to evaluate the state of the examined specimens. It was hypothesized that clean steel surfaces may have a weaker bond to the concrete whereas corroded surfaces may cause greater bond strength due to friction locking, a phenomenon utilized in reinforcement bars by their ribbed structure, although in a significantly greater scale. The study also indicated that frequency modulation, when separated using the Hilbert-Huang transform (Huang *et al.* 1998), was particularly sensitive to corrosion-related defects.

It is clear that corrosion indeed introduces features in the concrete specimens that may produce elevated nonlinear response. Corrosion products themselves introduce features that may elevate the nonlinearity locally due to the many cracks and delaminations present in corrosion products (Zhong *et al.* 2016; Bentahar *et al.* 2023; Nilsson *et al.* 2023b). However, it is not clear whether the defects cause significantly elevated nonlinearity when the corrosion is embedded in concrete. The present study aims to evaluate this by examining concrete cylinders with embedded liners of varying degrees of corrosion. It is assumed that the rolling process used when manufacturing steel plates creates surface-plane parallel internal structures which, when the plate corrodes, expands into disbonds and cracks. It is suspected that such features may contribute to elevated and pronounced nonlinearity in concrete specimens prior to concrete cracking. To build upon previous research, the cylinder specimens in the present work were inspected using two methods: impact-based modulation to examine instantaneous modulation as suggested by Nilsson *et al.* (2023a), and Luxembourg-Gorky cross-modulation to isolate a nonclassical phenomenon. The results from the impact measurements are analyzed by studying instantaneous modulation characteristics by utilizing the Hilbert-Huang transform, whereas the cross-modulation analysis is performed by typical spectroscopy, i.e., studying the recorded signal in the frequency domain and extracting the magnitude of the probe and its sideband components.

This investigation presents a novel approach to detecting early-stage corrosion of steel liners embedded in concrete by using advanced nonlinear wave modulation techniques in small-scale lab specimens. Unlike conventional methods that may struggle with the complexities of concrete's heterogeneity and the large scale of containment structures, this study focuses on the early detection of corrosion using impact-based modulation and Luxembourg-Gorky-type cross-modulation. By corroding the liners before embedding them in concrete, the study isolates the effects of early-stage corrosion from concrete cracking, thus allowing for a clearer assessment of detection capabilities. This research advances the field by highlighting the strengths and limitations of these methods in detecting specific types of damage, setting the

Table 1 Nonlinear wave modulation methods.

Method	Modulation source	Relevant characteristics	Studied parameter(s)
Impact-based instantaneous modulation	Impact from hammer.	Wideband modulation. Separation of AM & FM	Frequency modulation ($DI_{Frequency}$) & Amplitude modulation ($DI_{Amplitude}$)
Cross-modulation	Continuous amplitude-modulated ultrasound.	Narrowband modulation. Isolation of nonclassical modulation.	Modulation index (α)

stage for future applications in larger, more realistic settings.

2. Methods: Nonlinear wave modulation for non-destructive evaluation

The present study utilized the study of instantaneous modulation characteristics (Section 2.1) including the separation of amplitude and frequency modulation (AM & FM), and nonclassical cross-modulation (Section 2.2). The methods are summarized in **Table 1**. The essence of both methods is to introduce a high-amplitude perturbation which conditions the defects within the specimens causing nonlinear phenomena to occur. To effectively record the effects of the perturbations it is advised to employ a continuous probing wave so the disturbance can reach a steady state and thus induce minimal nonequilibrium effects. This makes amplitude extractions more reliable. The continuous nature of the signal also provides a narrow probe component which facilitates good separation of modulation components in the frequency domain.

2.1 Studying impact-based modulation using instantaneous characteristics

When exciting a structure with a transient, such as a mechanical impulse, the specimen is excited in a broad-banded fashion and commonly the specimen resonant frequencies are particularly excited. This results in high-amplitude vibrations which may perturb 'soft' defects such as cracks and delaminations, and the results of such perturbations can be probed by using a weak ultrasonic excitation. The downside is that the frequencies that modulate the probing wave are likely unknown unless rigorous modal analysis has been performed on the object under examination. This makes the extraction of the magnitude of modulation components in frequency domain difficult to perform reliably as spurious components from noise and/or other disturbances may be included in the analysis. Additionally, it is not possible to separate the modulation phenomena by amplitude or frequency modulation, rather the effects are combined. Fortunately, an alternative way to study the impact-based modulation has been suggested by Hu *et al.* (2010) and successfully implemented for corrosion evaluation by Nilsson *et al.* (2023a) where the instantaneous amplitude and fre-

quency were extracted by using the Hilbert-Huang transform (HHT) which enabled the study of the amplitude and frequency modulation separately over time. The study by Hu *et al.* (2010) indicated that instantaneous amplitude modulation is more sensitive to crack length when compared to frequency modulation.

The HHT uses empirical mode decomposition (EMD) to decompose an originally broad-banded signal into several intrinsic components called intrinsic mode functions (IMF) (Huang *et al.* 1998; Huang and Wu 2008). The reasoning behind using the HHT is that the Hilbert transform (HT) is most suitable for analyzing mono-component signals, or at least narrowband signals. By extracting the IMF corresponding to the probing wave by using EMD, the influence of various harmonics and noise can be eliminated. To improve the robustness of the HHT, it is recommended that the signal being decomposed is band-pass filtered around the frequency range of interest (Chen and Feng 2003). This should be performed because the EMD extracts the highest frequency component first. Nonlinear ultrasonic signals likely contain higher harmonics which may then affect the extracted IMF's. By filtering the signal it is ensured that the mode of interest is extracted first and effectively. A rigorous description of the HHT and its related processes is outside the scope of this work but readers interested in the HHT in general are referred to (Huang and Wu 2008); for in-depth descriptions of the EMD and its limitations, the authors recommend Peel *et al.* (2007) and Zeiler *et al.* (2010). A basic sketch showing the entire HHT process can be viewed in **Fig. 1**.

The result of the HHT is one or several narrow-banded IMF's which admit a proper HT, and thus the extraction of instantaneous amplitude and frequency is facilitated. Assume that the extracted IMF is denoted $c(t)$, then the analytical signal is expressed by Eq. (1).

$$y(t) = c(t) + j\hat{c}(t) = IA(t)e^{j\phi(t)} \tag{1}$$

where $\hat{c}(t)$ is the HT of $c(t)$, $IA(t)$ is the instantaneous amplitude of the analytical signal $y(t)$, and $\phi(t)$ is the instantaneous phase given by Eqs. (2) and (3) respectively:

$$IA(t) = \sqrt{c^2(t) + \hat{c}^2(t)} \tag{2}$$

$$\phi(t) = \tan^{-1}\left[\frac{\hat{c}(t)}{c(t)}\right] \qquad (3)$$

To obtain the instantaneous frequency (IF) we simply differentiate $\phi(t)$ with respect to time and scale by the sampling rate (F_s) used when digitizing the data:

$$IF(t) = \frac{F_s}{2\pi}\frac{d}{dt}\phi(t) \qquad (4)$$

To investigate and compare the modulation intensity, Hu *et al.* (2010) have suggested damage indices (DI) given by the standard deviation for the instantaneous characteristic normalized by the mean value. For the amplitude modulation, this is the mean amplitude before the perturbation was introduced, for the frequency modulation, the mean value is simply the probing frequency. The expressions for these DI can be viewed in Eqs. (5) and 6):

$$DI_{Amplitude} = \frac{\sqrt{\frac{1}{N}\sum_{i=1}^{N-1}\left[IA(i) - \mu(IA)\right]^2}}{\mu(IA)} \qquad (5)$$

$$DI_{Frequency} = \frac{\sqrt{\frac{1}{N}\sum_{i=1}^{N-1}\left[IF(i) - F_{probe}\right]^2}}{F_{probe}} \qquad (6)$$

where N is the number of samples being analyzed, and $\mu(IA)$ is the mean instantaneous amplitude before the perturbation. It is therefore required to collect data before

the impact is recorded. The HHT does suffer from erroneous end effects which may contaminate the results unless they are excluded or mitigated by various techniques (He *et al.* 2012).

2.2 Exploiting nonclassical cross-modulation using spectral analysis

It has been argued for many years that the classical power-series type nonlinearity based on anharmonicity in the interatomic elastic potential does not adequately describe certain phenomena experimentally observed in solids containing crack-like defects (Zaitsev 2019). One of many interesting nonclassical phenomena is the cross-modulation effect where an amplitude-modulated wave with a strong amplitude can modulate another weaker wave by its 'pumping' modulation, thus transferring energy to a different carrier frequency. This phenomenon, known as the 'Luxembourg-Gorky' (LG) effect, involved nonlinear ionospheric alterations caused by powerful radio transmissions. Initially observed in the 1930s by Tellegen (1933) and later confirmed in Nizhny Novgorod by Zaitsev *et al.* (2002a, 2002b), it continues to be a subject of research (Carozzi 2000; de Boer and Vester 2018).

The LG effect is assumed to be caused by nonlinear dissipation caused by the absorption of ionospheric plasma (Ginzburg and Gurevich 1960; Bailey 1965). The acoustical analogue of the LG effect is caused by a type of nonlinear dissipation that is not caused by friction or hysteresis (Osika *et al.* 2023). Recently, Osika *et al.* (2023) have proposed an analytical model of the LG effect in shear horizontal waves based on viscoelasticity and their results have some interesting implications. One
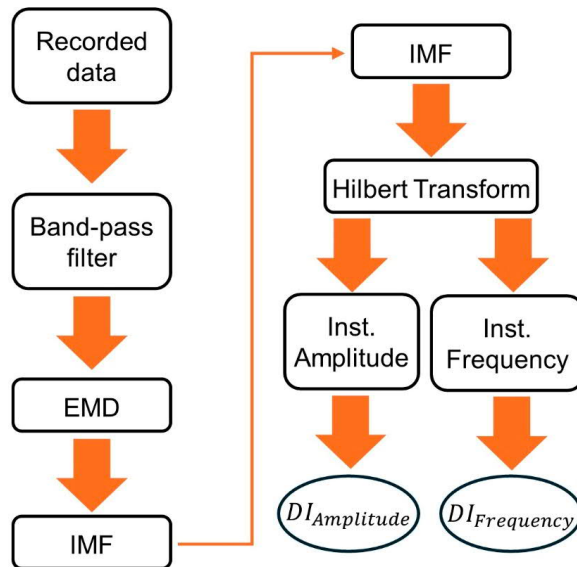

Fig. 1 Basic sketch of the Hilbert-Huang transform process.

of which is that the modulation intensity was shown to be far greater when the modulation transfer occurred from a high-frequency pumping wave to a lower-frequency probe wave as the opposite case did not generate any pronounced modulation transfer. This modulation scheme is applied in the current work to assess LG modulation using longitudinal waves.

If a linear medium is excited by a probing signal with the frequency F_{probe} and at the same time by an amplitude-modulated signal with the carrier frequency F_{pump}, that is modulated by the frequency, F_m these are the only spectral components expected to be found in the frequency domain of the recorded signal, which is illustrated in **Fig. 2(a)**. If the medium is instead quadratically nonlinear, new spectral components will be generated and this is illustrated in **Fig. 2(b)** where it is clear that a second harmonic of the probing frequency has been generated, accompanied by modulation side bands. However, no cross-modulation product is to be found. In the third case, **Fig. 2(c)**, the cross-modulation components have been included for illustrative purposes. To evaluate the intensity of cross-modulation the modulation index α, given by Eq. (7) can be used:

$$\alpha = \frac{\sum_{i=1}^{I} \left(A_{i,\,left} + A_{i,right} \right)}{A_{probe}} \quad (7)$$

where $A_{i,\,left}$ and $A_{i,right}$ are the magnitudes of the ith order sidebands to the left and right of the probing frequency, I is the highest order of modulation components being included, and A_{probe} is the magnitude of the probing frequency.

3. Experimental investigation

3.1 Specimen preparation

Several small lab-scaled concrete cylinders were prepared to investigate acoustic nonlinearity caused by embedded corrosion. To investigate damage evolution, plates of varying corrosion grades were prepared. In the present work, one plate without any corrosion was to be used as a reference, referred to as "OK". The other plates had uniform corrosion (COR), uniform corrosion with a shell-type corrosion product glued on top (SCOR), and lastly, a thin shell-type corrosion product (Shell). The plates used for the cylinder insets were cut into 90 mm diameter discs from larger plates using a water jet, which enables precise cutting. The resulting discs can be viewed in **Fig. 3** and the specimen notation and meaning can be viewed in **Table 2**. The reason to include the red (high oxygen and water exposure) shell-type corrosion product is that it has interesting cracking characteristics shared with black (typically limited oxygen and low moisture
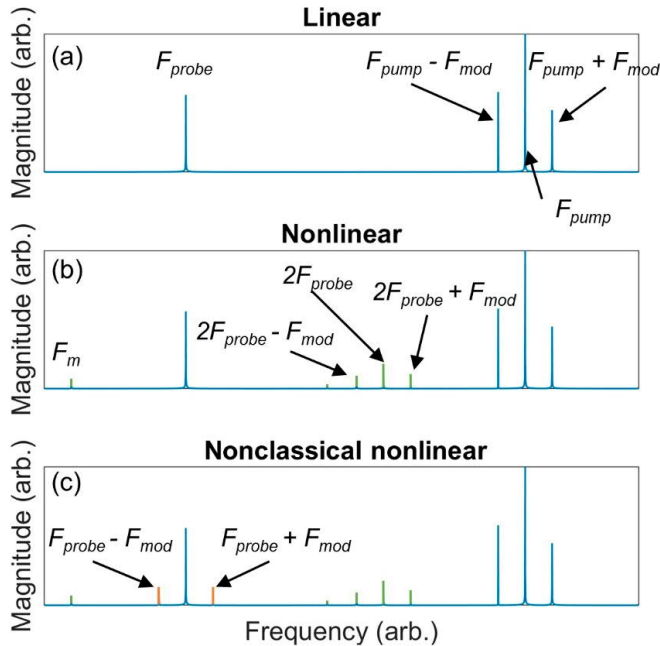

Fig. 2 Illustration of magnitude spectra for different cases. (a) Linear case where only the excitation signal components are present. (b) Quadratically nonlinear (classical) case, note the generation of probe harmonic and the modulation frequency. (c) The case of nonclassical cross-modulation by the high-frequency pump on the lower frequency carrier.

Table 2 Specimen notation and meaning.

Specimen notation	Cylinder containing
Concrete	No steel plate
OK	Pristine steel plate
COR	Uniformly corroded plate
SCOR	Uniformly corroded with shell-type corrosion
Shell	Only the corrosion shell.

Table 3 Concrete mix.

Concrete component	Mass (kg/m^3)
Cement	302
Coarse aggregate (4-8 mm)	302
Fine aggregate (0-2 mm)	604
Water	130

exposure) corrosion products found in an embedded containment liner plate in a nuclear power plant. X-ray tomography (resolution 13 µm) of these two types of corrosion products can be seen in **Fig. 4** and it is clear that the red shell-type (a) corrosion product and the black containment liner corrosion (b) shares internal cracking characteristics.

To ensure that the plate discs remain stationary during the concrete casting process certain measures were taken. The plates were glued to cylindrical shells of expanded steel mesh with a material thickness of 2.8 mm using a polyurethane-based sealant, see **Figs. 5(a)** and **(5b)**. The expanded steel cylinders were 250 mm in height which gave the full length of the concrete cylinders. The inner diameter of the expanded steel cylinders matched the disc diameters to ensure tight fixation. PVC pipes with an inner diameter of 100 mm with a stopper on one end were used as casting molds.

The concrete recipe for the cylinders in the present work can be viewed in **Table 3**. The cement used was

Fig. 3 The plate discs that were embedded in concrete. From left to right: OK (non-corroded), COR (uniform corrosion); SCOR (uniform corrosion with a layer of shell-type corrosion product glued on top); Shell (only shell-type corrosion product).
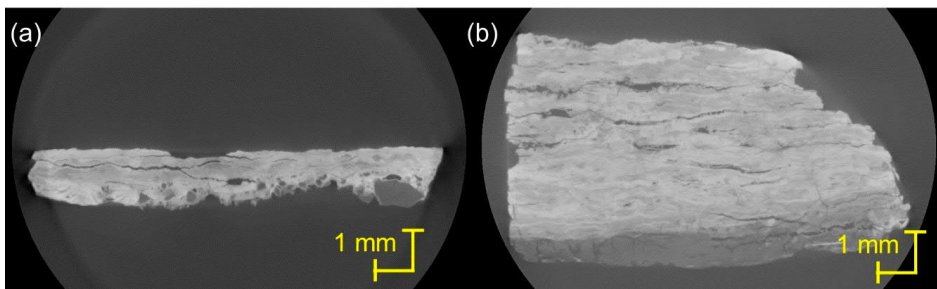
Fig. 4 (a) X-ray tomography of a corrosion product of the shell-type considered in the present work (red hydrated oxide type). (b) Tomograph of a corrosion product from an embedded containment liner plate found in a nuclear power plant (black corrosion from limited oxygen and moisture).

Portland-limestone cement, CEM II/A-LL 42.5 R. The resulting water-to-cement ratio was 0.43. The components were mixed in a regular cement mixer for roughly 5 minutes. The PVC pipes were then filled to about half

Fig. 5 (a) and (b) The plate discs were attached to cylinders of expanded metal (steel) before casting. The discs were adhered using silicone. (c) The cylinders were cast at full length (250 mm) and cured. (d) After being cured for 5 weeks the cylinders were cut to 200 mm by removing 25 mm from both ends of the concrete cylinders.

of their height, and then the expanded metal cylinders with the plate discs were carefully placed in the mold. To enable the expanded metal cylinder to slowly immerse into the concrete slurry by its own weight, a shaking table was used. During immersion, the brittle shell corrosion product for specimen Shell was destroyed, leaving multiple smaller pieces distributed in the concrete volume. Nevertheless, the specimen was decided to be included in the work to investigate the effects of small corrosion products. While shaking, the expanded metal cylinders slowly set at the bottom of the PVC mold. This procedure also allowed the concrete to fill the holes in the expanded metal mesh. When the expanded steel cylinder had been set in the bottom, additional concrete was poured into the mold until the pillar length of 250 mm was achieved. The molds were then shaken for several minutes using the aforementioned shake table to consolidate the concrete. To finalize the casting process, a plastic film was placed inside the pipe on the surface of the fresh concrete, as seen in **Fig. 5(c)**. After the concrete had cured for 5 weeks, the ends of the concrete cylinders were removed by cutting off 25 mm at each end, resulting in a total length of 200 mm with the embedded plates centered in the cylinders and less rough surfaces for proper transducer mounting.

X-ray tomographs (XCT) of the Concrete, OK, and SCOR specimens were obtained using a RX Solutions EasyTom150 tomograph with 64 µm resolution. Snapshots from the reconstruction be viewed in **Fig. 6**. These three specimens were selected for X-ray imaging due to their particular relevance to our evaluation. Limited resources necessitated focusing on these key specimens. Features with low density, such as pores and cracks, appear dark in the XCT images, while high-density features,
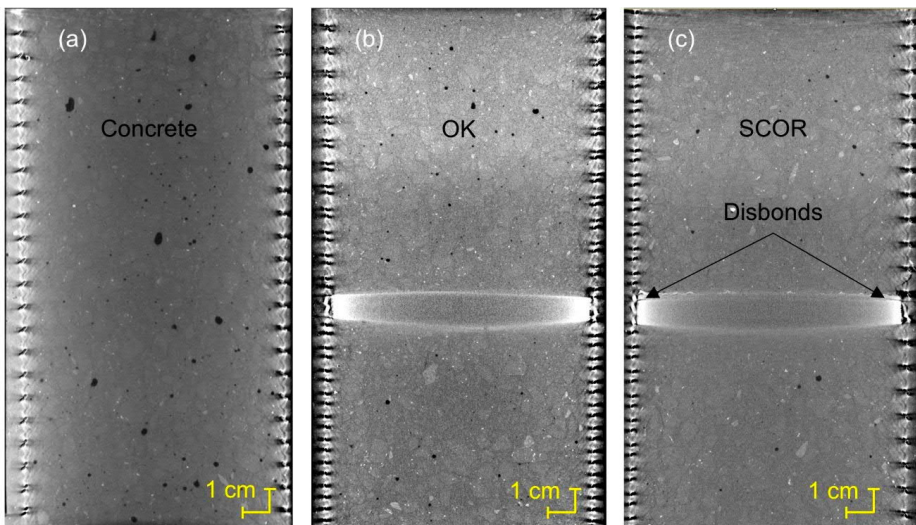

Fig. 6 X-ray tomography of some of the specimens. (a) Concrete: no steel plate inside. (b) OK: pristine plate. (c) SCOR: uniformly corroded steel with a corrosion shell on the top surface. The plates appear thicker in the center because the periphery is closer to the detector than at the edges.

such as steel, appear bright. It is clear from **Fig. 6(a)** that the specimen with no plate (Concrete) contains quite many pores, some with sizes similar to the coarse aggregates. Specimens OK [**Fig. 6(b)**] and SCOR [**Fig. 6(c)**] contain considerably fewer pores and the steel-concrete interface appears to be intact from these snapshots. By looking closely at **Fig. 6(c)** a hint of disbonding between the plate and the shell corrosion can be observed. Although the steel-concrete interface for specimen OK appears to be largely intact, **Fig. 7**, which represents a zoomed-in part of a different snapshot from the reconstruction, reveals that the specimen in fact contains cracks and an inclusion near the steel-concrete interface. Similar defects were not identified in the reconstructions for specimens Concrete and SCOR specimens.

3.2 Measurement setups
3.2.1 Impact-modulation measurements
The experiment setup used to measure impact-based modulation on an ultrasonic probe wave can be viewed in **Fig. 8**. In the present work, the probe wave actuator (Tx1) was an Olympus X1021 contact transducer generating longitudinal waves with a claimed nominal frequency of 50 kHz. However, the frequency which yielded the least variation in excitation level between the inspected specimens was 52.380 kHz. This frequency was selected as the probing frequency. The probe signal used was a continuous sinusoidal wave with a peak-to-peak amplitude of 0.1 V_{pp} generated from an Agilent 33500B waveform generator and amplified to a voltage amplitude of 3.5 V_{pp} by using an A.A Labs A-303 voltage amplifier. It is important to keep the probing wave amplitude relatively weak to not induce a strong nonlinear response by

the probing wave. The ultrasound was received by an Olympus X1021 transducer (Rx) to keep the sensitivity around the probing frequency high. The actuator and receiver were coupled to the specimens by using lithium-based grease. The specimens were impacted with a PCB 086D05 ICP impact hammer equipped with a force sensor (sensitivity 0.23 mV/N) and a hard tip (PCB 084B03) to generate a wide band of modulation frequencies. The impact hammer was driven by a PCB 480E09 ICP conditioner set to a x1 gain. The signals were digitized using a Measurement Computing USB-1602HS data acquisition unit with 16-bit resolution and 2 MS/s sampling rate collecting 200 kS and using a 40 kS pretrigger to properly catch the entire impact event. The entire measurement was controlled by a PC using software developed in Lab-VIEW, and post-processing (digital filtering, HHT, and calculating damage indices) was conducted using MATLAB code.

3.2.2 Cross-modulation measurements
To examine the cross-modulation effect caused by a strong and comparatively high frequency amplitude-modulated (AM) wave on a weak lower frequency probing wave, a setup very similar to the one presented in Section 3.2.1 was used. Here, the second source (Tx2) is an Olympus X1019 contact transducer with a claimed nominal frequency of 180 kHz. However, the frequency which yielded the most consistent and strongest excitation level for all specimens was 178 kHz. The amplitude-modulated continuous pump wave had an excitation amplitude of 1 V_{pp} which after amplification using a second A.A Labs A-303 amplifier was 35 V_{pp}. It is important not to use too high excitation levels as this might introduce
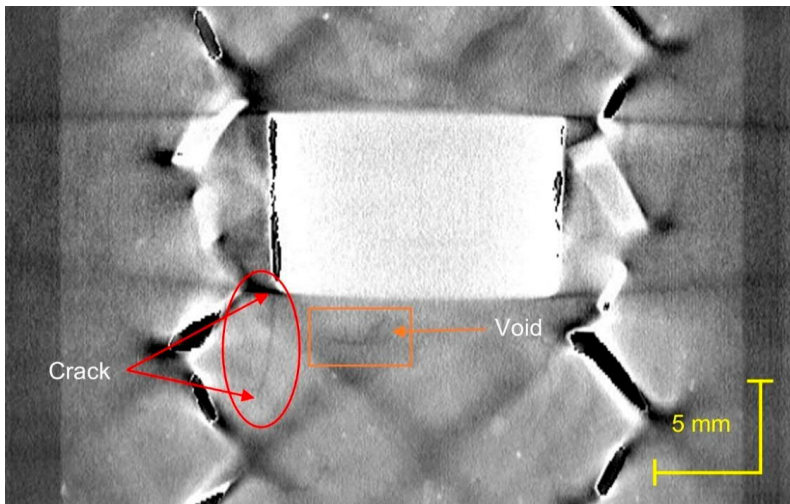

Fig. 7 Defects found within specimen OK. A crack from the bottom surface of the embedded plate is highlighted by a red circle. A yellow square indicates an inclusion with a crack propagating towards the circled crack.

spurious system and adhesive nonlinearities that may contaminate the measurements. The carrier frequency for the AM wave was 178 kHz and the modulation frequency (F_{mod}) was set to 0.100 kHz with a modulation depth of 100%. The probing wave specifications were once again set to 52.380 kHz and 0.1 V_{pp} (3.5 V_{pp} after amplification) using the same X1021 transducer. The transducers were coupled to the specimens using lithium-based grease. The data was digitized into 200 kS using a sampling rate of 2 MS/s and no pretrigger acquisition.

4. Results and discussion

4.1 Impact-based modulation
The signals recorded from the impact-based modulation experiments were band-pass filtered with the pass frequency of 32.380 kHz and stop frequency of 72.380 kHz, i.e., a 40 kHz bandwidth around the probing frequency component. The stopband attenuation was −60 dB at 28.055 kHz and 78.500 kHz respectively. After filtering the signals, the Empirical Mode Decomposition (EMD) process extracted intrinsic mode functions (IMFs) representing the probe component and the corresponding instantaneous amplitude and frequency (IA & IF) were extracted using the Hilbert Transform (HT).

The IA and IF are plotted for the inspected specimens in **Fig. 10**. When studying the IA and IF from these plots, the difference between the specimens is evident. The Concrete specimen which has no embedded plate, exhibits very little amplitude deviation from the equilibrium state after the impact perturbation, which is seen in **Fig. 10(a)**. When studying the instantaneous amplitude for specimen OK [**Fig. 10(c)**], a slight deviation from the equilibrium amplitude is observed. This indicates that the impact has conditioned the specimen and momentarily affected its material properties. This is a nonclassical nonlinear effect arising from slow dynamics (TenCate *et al.* 2000; Carrión *et al.* 2021). When the conditioning stops a sudden drop in the instantaneous amplitude is observed, followed by a recovery process that is logarithmic in time.

The slow dynamics effect is even more evident for specimens COR and SCOR as observed in **Figs. 10(e)** and **10(g)**, respectively. Here, the amplitude drops quite significantly and does not appear to approach the equilibrium amplitude as fast as specimen OK does. This indicates a strong level of nonclassical hysterical nonlinearity present for specimen COR and SCOR. It is particularly interesting that COR exhibits strong equilibrium deviation since the level of impact is the lowest for all specimens at 2387 N. The impact force for OK (2752 N) and SCOR (2771 N) are more comparable, however, the
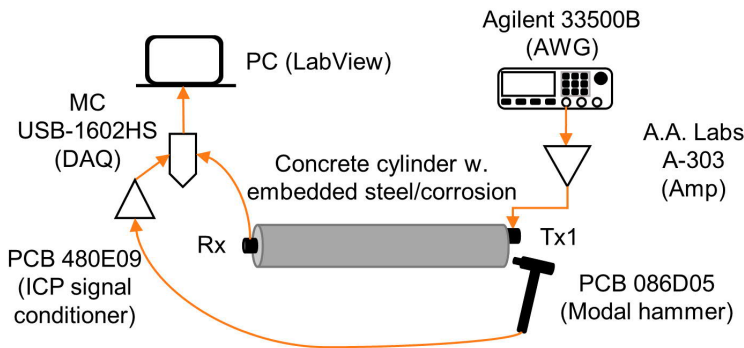

Fig. 8 Schematic illustration of the impact-modulation setup.
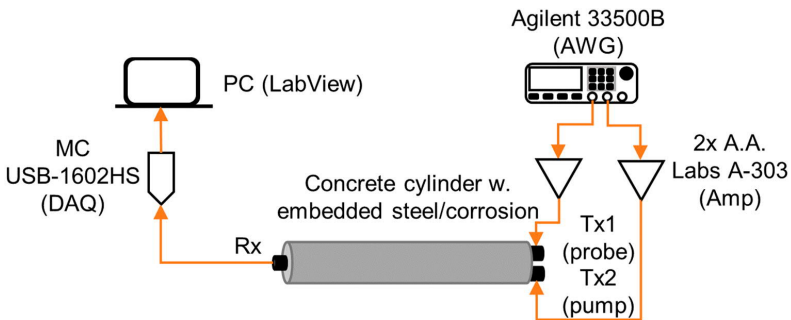

Fig. 9 Schematic illustrating the setup used for the pump-probe measurements.

nonequilibrium effects are more pronounced for SCOR. It is important to consider the impact force for each measurement as the effects that are probed are amplitude dependent. The impact forces are presented in **Fig. 11**.

The instantaneous frequency modulation seen in **Figs. 10(b)**, **10(d)**, **10(f)**, **10(h)**, and **10(j)** show that the frequency modulation is on the order of a few kHz for all specimens except SCOR. However, OK and COR appear to have a longer reverberation time than the Concrete and Shell specimens. SCOR exhibits modulation on several tens of kHz. The instantaneous modulation plots clearly indicate that SCOR exhibits the overall strongest nonlinear response whereas OK and COR are intermediate, while the Concrete and Shell specimens exhibit the weakest responses.

To quantify the modulation intensity across the specimen population, we utilized the damage indices described by Eqs. (5) and (6). The results of $DI_{Amplitude}$ and
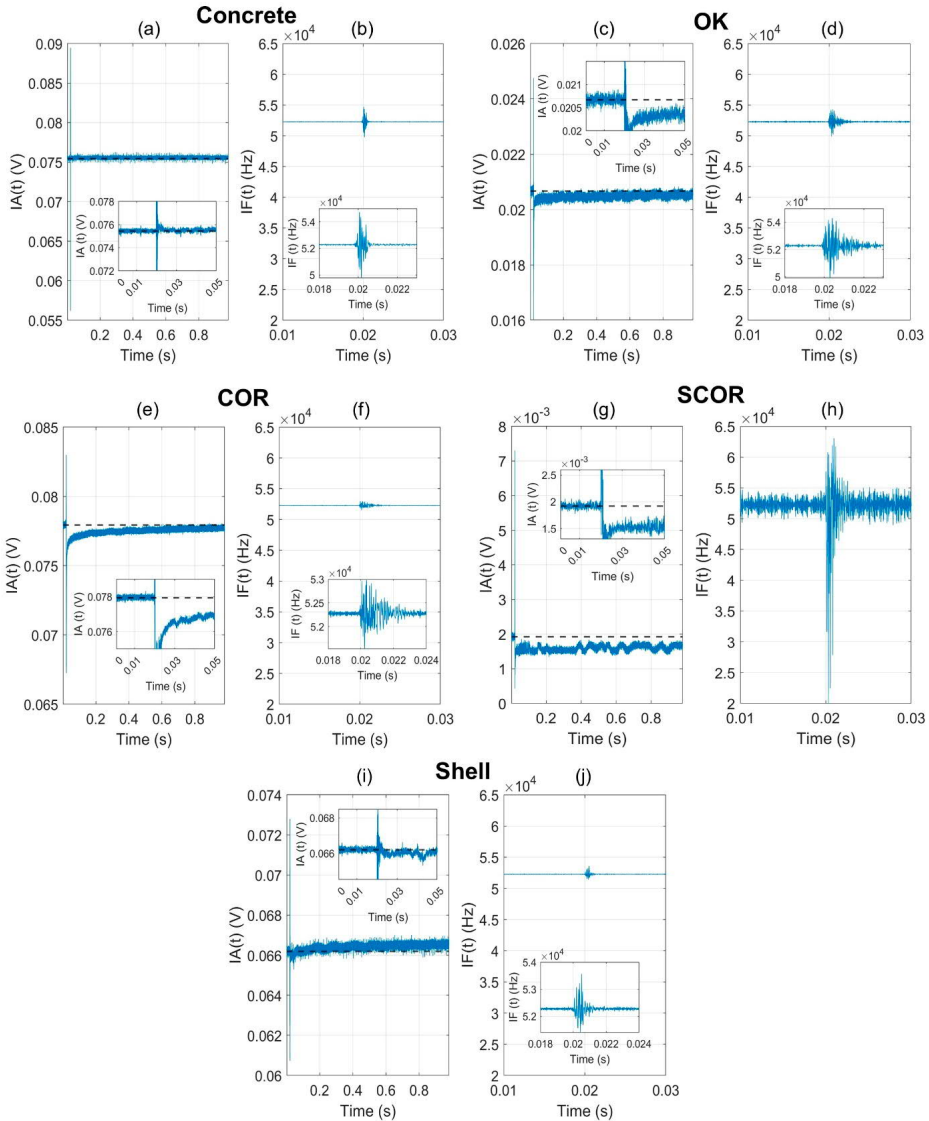
Fig. 10 Instantaneous amplitude (a),(c), (e), (g), (i) and frequency (b), (d), (f), (h), (j) for the inspected specimens. The dashed line in the instantaneous amplitude plots correspond to the mean amplitude at equilibrium. Note that the plots for instantaneous frequency have been zoomed in to illustrate the instantaneous modulation more clearly.

$DI_{Frequency}$ are depicted in **Figs. 12(a)** and **12(b)**, respectively. To mitigate end effects, we excluded data near the ends, considering only the range $0.001 \leq t \leq 0.099$.

As expected from the plots in **Fig. 10**, specimen SCOR exhibits the strongest amplitude modulation, with a value of 0.18. The second strongest modulation is observed for specimen OK at 0.011, followed by COR at 0.0077, Shell at 0.0041, and Concrete at 0.0030. Despite the impact force being similar (with a difference of approx. 20 N), the intensity of amplitude modulation is approximately 16 times greater for SCOR than for OK. Notably, specimen COR, with the lowest impact force of 2387 N, exhibits the third strongest amplitude modulation, more

than twice the intensity magnitude compared to Concrete. Both Concrete and Shell specimens show similar levels of amplitude modulation, although Concrete had an impact force of 2548 N compared to Shell's 2607 N.

A previous study by Hu *et al.* (2010) indicated that amplitude modulation is more sensitive to crack length than frequency modulation. This sensitivity is particularly interesting in the case of specimen OK, which contains some cracking (see **Fig. 7**) and exhibits the second-highest $DI_{Amplitude}$.

When examining the damage index for frequency modulation, as shown in **Fig. 12(b)**, a similar trend to amplitude modulation is observed. The SCOR specimen
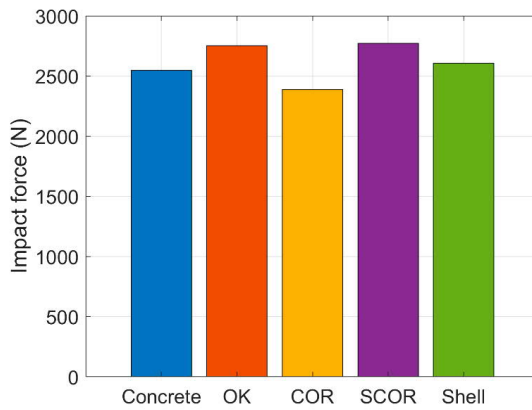
Fig. 11 Maximum impact force measured for each specimen.
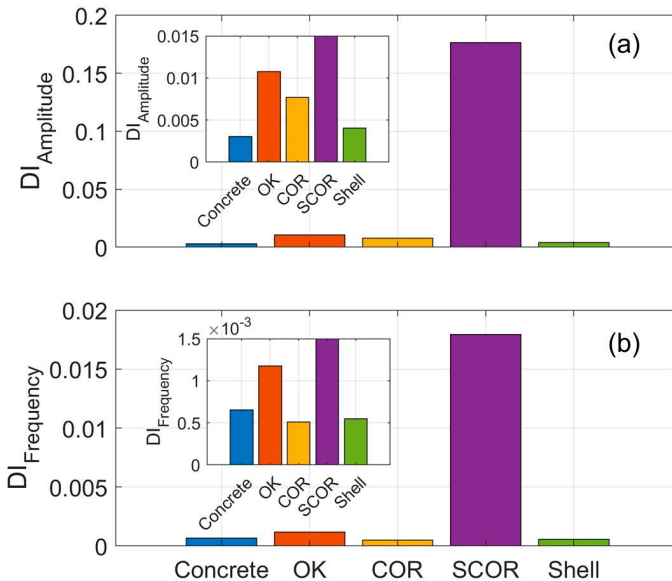
Fig. 12 Damage indices for (a) amplitude modulation and (b) frequency modulation.

demonstrates the strongest frequency modulation with an intensity of 0.018, followed by OK at 0.0012. However, the frequency modulation for Concrete (0.00065) is stronger than COR (0.00051), which exhibits the weakest modulation among the inspected specimens. The damage index for Shell is slightly greater than OK at 0.00055.

These results indicate that the presence of weak corrosion, as observed in the COR specimen, does not significantly elevate the nonlinear response, although some increase compared to the reference (Concrete) is observed. This observation is consistent with the findings of Nilsson *et al.* (2023b) who also noted that corrosion similar to that in SCOR, characterized by disbonds and other defects in the corroded volume, substantially affected the measurements. Although the corrosion product in Shell is similar to the corrosion product in SCOR, it does not produce an elevated nonlinear response in terms of amplitude and frequency modulation using the current technique. Possibly due to the lack of complex contact interactions to its host plate as is likely present for SCOR. Additionally, the destruction of the thin sheet may have affected the results. Observe that the plates were corroded pre-embedment which means that there are no corrosion-related defects in the concrete itself. Defects such as cracks or alterations to the steel-concrete interface would otherwise be expected to occur due to the volumetric expansion of the corrosion products. Previous studies by Nilsson *et al.* (2023a) indicated that frequency modulation was particularly sensitive to corrosion defects, this is not observed in the present results.

The presence of defects in specimen OK meant that no pristine reference specimen with an embedded plate was included in the study. As these nonlinear ultrasonic methods are qualitative, it is challenging to ascertain trends observed relative to a pristine specimen. However, the defects in OK enabled the observation that the concrete defects indeed affect the results regardless of the condition of the embedded plate.

4.2 Luxembourg-Gorky cross-modulation

To examine the modulation transfer from the high-frequency (178 kHz) amplitude-modulated pumping wave to the lower frequency (around 52 kHz) probing wave, the acquired time signals were windowed using a Hanning window. The Fourier transform is obtained by using the FFT. The resulting spectra are shown in **Fig. 13**. The spectra shows that LG-type cross-modulation was observed for all inspected specimens. The spectra shows that the first-order cross-modulation components with the greatest magnitudes are those for SCOR, Shell and OK, closely followed by COR. Notably, specimen SCOR is the only specimen which exhibits second-order cross-modulation, meaning that distinct components on the frequencies $F_{probe} \pm 2F_{mod}$ were generated. As the cross-modulation phenomenon is associated with nonlinear dissipation it is interesting to consider the magnitude of the probing signal. As clearly illustrated by **Fig. 13**, specimens OK and SCOR exhibit the weakest magnitude of the probing signal yet at the same time they have the strongest modulation components. This indicates that these specimens exhibit the strongest level of this type of nonclassical nonlinear dissipation.

The cross-modulation intensity can be illustrated by determining the modulation index (α) by using Eq. (7). By including first- and second-order cross-modulation components the modulation indices shown in **Fig. 14** are obtained. It is clear that specimen SCOR exhibits the strongest level of the acoustic analogue of the LG effect with a modulation index of 0.0096 followed by specimen OK at 0.0060. Specimens COR and Shell exhibit very
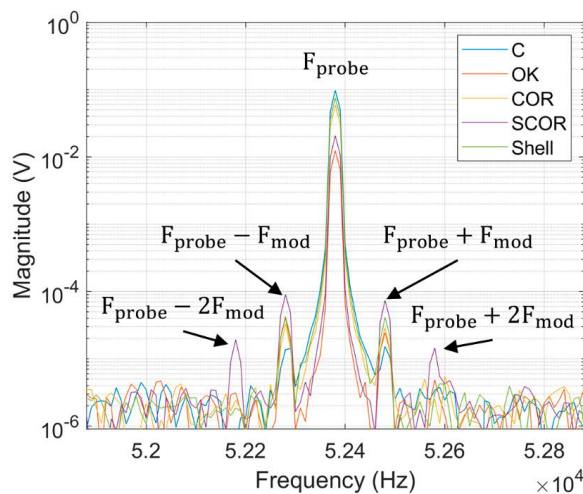

Fig. 13 Spectra around the probing frequency. Note the first- and second-order cross-modulation components for specimen SCOR.
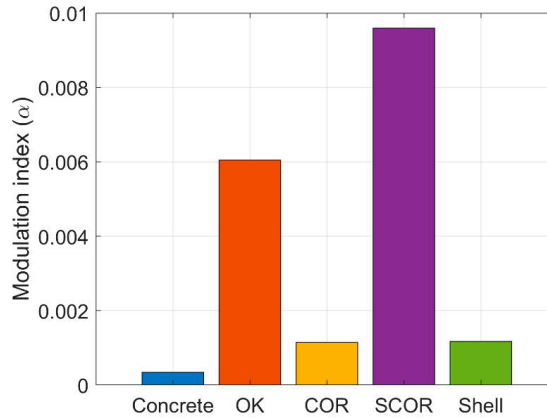
Fig. 14 Modulation index (α) for all inspected specimens.

similar levels of cross-modulation at the modulation indices 0.0011 and 0.0012 respectively. The specimen without any embedded steel plate, Concrete, had an approximate modulation index of 0.00034, which is much lower than the remaining population.

The nonclassical modulation indicates that the specimen without any embedded plate, Concrete, exhibits the weakest nonclassical nonlinearity. This was also indicated by the observations made in Section 4.1 concerning the comparatively weak amplitude deviation from equilibrium. Specimens COR and Shell exhibit similar levels of nonlinearity which agrees with the observations made for the impact-based measurements in Section 4.1, albeit much weaker cross-modulation compared to OK and SCOR is observed. It is interesting to observe that Concrete and Shell are likely more comparable than the rest of the specimens due to the destruction of the corrosion product in Shell. The elevated modulation index for Shell hints at detection capabilities for small corrosion products distributed in a volume. However, the present investigation has insufficient data to confirm this.

It is interesting that OK and SCOR exhibit more similar modulation intensities for the cross-modulation compared to the impact-based modulation. Granted, the cross-modulation effect is a strictly nonclassical phenomenon whereas the impact-based modulation evidently generated both fast and slow nonlinear response, which includes classical and nonclassical nonlinearities of various forms. It is possible that the cracking in specimen OK shown in **Fig. 7** is the cause of the pronounced nonlinear effects observed for the current measurement. Interestingly, these cracks are evidently significantly larger than the crack-like defects in the SCOR corrosion product. It is known that when cracks grow above a certain level, the nonlinearity starts to decrease (Donskoy and Liu 2021) which might explain these observations. This result highlights the sensitivity of nonclassical nonlinear phenomena. However, this remarkable sensitivity makes employing the techniques in real-world applications challenging. In particular when inspection of concrete structures is of interest because cracking is expected to occur during drying and aging due to creep and shrinkage effects. The cross-modulation effect may arise from nonlinear dissipation, This can be described by using nonfrictional, nonhysterical damping which is typical for viscoelastic materials (Osika *et al.* 2023). Considering that concrete can be modelled as a viscoelastic material (Mei and Wang 2020) it might therefore not be suitable to use such nonclassical ultrasonic methods for the inspection of concrete-embedded components. In contrast, it could be interesting to exploit cross-modulation for the monitoring of creep-induced damage and concrete cracking because of viscoelastic behavior.

5. Conclusions

Nonlinear elastic wave modulation has been investigated to evaluate corrosion in nuclear containment liners embedded in concrete. The examined cylindrical concrete specimens contained a pristine plate, a uniformly corroded plate, a uniformly corroded plate with a thin sheet of severely cracked corrosion products called shell corrosion, and the thin shell corrosion which unfortunately cracked during casting. In addition to the plate-containing specimens, a specimen without an embedded plate was manufactured. The embedded plate discs of a corroded nature were corroded before being cast in concrete to investigate whether the corrosion products introduce a sufficiently strong nonlinear response to not be masked by inherent nonlinearity from the surrounding concrete. The results enable the following conclusions to be made:

1. The impact-based measurements performed in this work demonstrate that impact-induced amplitude modulation is elevated for specimens containing corrosion. However, the modulation is more sensitive to the presence of defects, such as cracks in concrete, than to corroded steel alone when the concrete remains

unaffected. The SCOR specimen exhibited the strongest amplitude modulation, indicating that corrosion characterized by disbonds, and other defects significantly affects the nonlinear response. Despite some concrete cracking, the OK specimen showed only moderate amplitude modulation, suggesting that the sensitivity to defects is not straightforward.

2. The impact-induced frequency modulation is not significantly sensitive to the presence of corroded steel embedded in concrete when the concrete itself is unaffected. While the SCOR specimen showed the strongest frequency modulation, the presence of weak corrosion in other specimens, like COR, lead to a weaker frequency modulation compared to the concrete reference specimen. This indicates that frequency modulation may not be a reliable indicator of corrosion in the absence of concrete defects.

3. Nonclassical cross-modulation measurements indicated remarkable sensitivity to concrete cracking and embedded corrosion with disbonds and cracks. The nonclassical modulation did not yield strong indications for the specimen with a uniformly corroded steel plate (COR) nor for the specimen containing the distributed thin shell corrosion (Shell). This indicates that the nonclassical phenomenon, regardless of its remarkable sensitivity to cracking, might not be optimal for evaluating the condition of early-stage degradation of concrete-embedded nuclear containment liners. The method might be more appropriate for evaluating concrete cracking. It is possible that cross-modulation measurements could be used in future research investigating gross corrosion of steel components embedded in concrete, as gross corrosion may introduce concrete cracking.

The experiments focused on small lab-scale specimens, indicating the need for further evaluation. Future studies should perform experiments on larger-scale containment building mock-ups before application in real power plants. Such mock-ups should include both early-stage and severely corroded steel plates, as well as various defect conditions, to investigate the ultimate sensitivity and reliability of nonlinear ultrasonic methods in detecting containment liners embedded in concrete.

Acknowledgements

References

Antonaci, P., Bruno, C. L. E., Scalerandi, M. and Tondolo, F., (2013). "Effects of corrosion on linear and nonlinear elastic properties of reinforced concrete." *Cement and Concrete Research*, 51, 96-103.

Bailey, V. A., (1965). "Some nonlinear phenomena in the ionosphere." *Journal of Research of the National Bureau of Standards, Section D: Radio Science*, 69D(1), 9-24.

Basu, S., Thirumalaiselvi, A., Sasmal, S. and Kundu, T., (2021). "Nonlinear ultrasonics-based technique for monitoring damage progression in reinforced concrete structures." *Ultrasonics*, 115, 106472.

Bentahar, M., Petitmangin, A., Blanc, C., Chabas, A., Montresor, S., Niclaeys, C., Elbartali, A., Najjar, D., Duccini, R., Jean, M., Nowak, S., Pires-Brazuna, R. and Dubot, P., (2023). "Does atmospheric corrosion alter the sound quality of the bronze used for manufacturing bells?" *Materials*, 16(13), 4763.

Broda, D., Staszewski, W. J., Martowicz, A., Uhl, T. and Silberschmidt, V. V., (2014). "Modelling of nonlinear crack-wave interactions for damage detection based on ultrasound - A review." *Journal of Sound and Vibration*, 333(4), 1097-1118.

Carozzi, T. D., (2000). "*Radio waves in the ionosphere : Propagation, generation, and detection* (IRF Scientific report 272*)*." Uppsala, Sweden: Uppsala University.

Carrión, A., Genovés, V., Pérez, G., Bittner, J., Popovics, J. S., Payá, J. and Gosálbez, J., (2021). "Effects of slow dynamics and conditioning on non-linear hysteretic material assessment using impact resonance acoustic spectroscopy." *Mechanical Systems and Signal Processing*, 150, 107273.

Chen, X. J., Kim, J. Y., Kurtis, K. E., Qu, J., Shen, C. W. and Jacobs, L. J., (2008). "Characterization of progressive microcracking in Portland cement mortar using nonlinear ultrasonics." *NDT and E International*, 41(2), 112-118.

Chen, Y. and Feng, M. Q., (2003). "A technique to improve the empirical mode decomposition in the Hilbert-Huang transform." *Earthquake Engineering and Engineering Vibration*, 2(1), 75-85.

Climent-Llorca, M. Á., Miró, M., Carbajo, J., Poveda, P., de Vera, G. and Ramis-Soriano, J., (2019). "Use of non-linear ultrasonic techniques to detect cracks due to steel corrosion in reinforced concrete structures." *Materials*, 12(5), 813.

Climent-Llorca, M. Á., Miró, M., Eiras, J.-N., Poveda, P., de Vera, G., Segovia, E.-G. and Ramis-Soriano, J., (2022). "Early detection of corrosion-induced concrete micro-cracking by using nonlinear ultrasonic techniques: Possible influence of mass transport processes." *Corrosion and Materials Degradation*, 3(2), 235-257.

Climent-Llorca, M. Á., Miró, M., Poveda, P. and Ramis-Soriano, J., (2020). "Use of higher-harmonic and intermodulation generation of ultrasonic waves to detecting cracks due to steel corrosion in reinforced cement mortar." *International Journal of Concrete Structures and Materials*, 14(1), 52.

Dahlen, U., Ryden, N. and Jakobsson, A., (2015). "Damage identification in concrete using impact non-

linear reverberation spectroscopy." *NDT and E International*, 75, 15-25.

de Boer, P. T. and Vester, M., (2018). "Sideband asymmetry in ionospheric cross modulation." *Radio Science*, 53(5), 640-655.

Donskoy, D. M. and Liu, D., (2021). "Vibro-acoustic modulation baseline-free non-destructive testing." *Journal of Sound and Vibration*, 492, 115808.

Donskoy, D. M. and Sutin, A. M., (1998). "Vibro-acoustic modulation nondestructive evaluation technique." *Journal of Intelligent Material Systems and Structures*, 9(9), 765-771.

Donskoy, D. M., Ferroni, K., Sutin, A. and Sheppard, K., (1998). "A nonlinear acoustic technique for crack and corrosion detection in reinforced concrete." In: R. E. Green, Ed. *Nondestructive Characterization of Materials*. Boston, Massachusetts, USA: Springer, 555-560.

Dunn, D., Pulvirenti, A. and Klein, P., (2011). "Containment liner corrosion." In: J. T. Busby, G. Ilevbare and P. L. Andresen, Eds. *Proc. 15th International Conference on Environmental Degradation of Materials in Nuclear Power Systems - Water Reactors*, Colorado Springs, Colorado, USA 7-11 August 2011. Cham, Switzerland: Springer International Publishing, 1037-1049.

Eiras, J. N., Vu, Q. A., Lott, M., Payá, J., Garnier, V. and Payan, C., (2016). "Dynamic acousto-elastic test using continuous probe wave and transient vibration to investigate material nonlinearity." *Ultrasonics*, 69, 29-37.

Fillinger, L., Zaitsev, V. Y., Gusev, V. and Castagnède, B., (2006). "Nonlinear relaxational absorption/transparency for acoustic waves due to thermoelastic effect." *Acta Acustica united with Acustica*, 92(1), 24-34.

Genovés, V., Carrión, A., Escobar, D., Gosálbez, J., Monzó, J., Borrachero, M. V. and Payá, J., (2019). "Nonlinear acoustic spectroscopy and frequency sweep ultrasonics: Case on thermal damage assessment in mortar." *Journal of Nondestructive Evaluation*, 38(3), 1-14.

Ginzburg, V. L. and Gurevich, A. V., (1960). "Nonlinear phenomena in a plasma located in an alternating electromagnetic field." *Soviet Physics Uspekhi*, 3(1), 115-146.

Guyer, R. A. and Johnson, P. A., (1999). "Nonlinear mesoscopic elasticity: Evidence for a new class of materials." *Physics Today*, 52(4), 30-36.

He, Z., Shen, Y. and Wang, Q., (2012). "Boundary extension for Hilbert-Huang transform inspired by gray prediction model." *Signal Processing*, 92(3), 685-697.

Hu, H. F., Staszewski, W. J., Hu, N. Q., Jenal, R. B. and Qin, G. J., (2010). "Crack detection using nonlinear acoustics and piezoceramic transducers - Instantaneous amplitude and frequency analysis." *Smart Materials and Structures*, 19(6), 065017.

Huang, N. E. and Wu, Z., (2008). "A review on Hilbert-Huang transform: Method and its applications to geophysical studies." *Reviews of Geophysics*, 46(2), RG2006.

Huang, N. E., Shen, Z., Long, S. R., Wu, M. C., Snin, H. H., Zheng, Q., Yen, N. C., Tung, C. C. and Liu, H. H., (1998). "The empirical mode decomposition and the Hilbert spectrum for nonlinear and non-stationary time series analysis." *Proceedings of the Royal Society A: Mathematical, Physical and Engineering Sciences*, 454(1971), 903-995.

Johnson, P. and Sutin, A., (2005). "Slow dynamics and anomalous nonlinear fast dynamics in diverse solids." *The Journal of the Acoustical Society of America*, 117(1), 124-130.

Korenska, M., Matysik, M., Vyroubal, P. and Pospisil, K., (2009). "Assessment of reinforcement corrosion using nonlinear ultrasonic spectroscopy." In: P. Mazal, Ed. *Proc. NDT in Progress 2009 - 5th International Workshop of NDT Experts*, Prague, Czech Republic 12-14 October 2009. New York, USA: Curran Associates, Inc., 143-151.

Leśnicki, K. J., Kim, J. Y., Kurtis, K. E. and Jacobs, L. J., (2011). "Characterization of ASR damage in concrete using nonlinear impact resonance acoustic spectroscopy technique." *NDT and E International*, 44(8), 721-727.

Li, X. and Gong, J., (2023). "Effects of steel liner corrosion on the leak-tightness of prestressed concrete containment structure under severe accident loads." *Annals of Nuclear Energy*, 180, 109487.

Liang, Y. and Wang, L., (2020). "Uncertain factors relating to the prediction of corrosion-induced cracking of concrete cover." *Journal of Advanced Concrete Technology*, 18(11), 699-715.

Mei, S. and Wang, Y., (2020). "Viscoelasticity: A new perspective on correlation between concrete creep and damping." *Construction and Building Materials*, 265, 120557.

Miele, S., Karve, P., Mahadevan, S. and Agarwal, V., (2020). "*Concrete structure health monitoring using vibro-acoustic testing and machine learning* (Report no. INL/EXT 20-59914)." Idaho, USA: Idaho Operations Office of the US Department of Energy.

Miró, M., Eiras, J. N., Poveda, P., Climent-Llorca, M. Á. and Ramis-Soriano, J., (2021). "Detecting cracks due to steel corrosion in reinforced cement mortar using intermodulation generation of ultrasonic waves." *Construction and Building Materials*, 286, 122915.

Miyazato, S. and Otsuki, N., (2010). "Steel corrosion induced by chloride or carbonation in mortar with bending cracks or joints." *Journal of Advanced Concrete Technology*, 8(2), 135-144.

Nilsson, M., Huttunen-Saarivirta, E., Bohner, E. and Ferreira, M., (2023a). "Non-destructive evaluation of corrosion in steel liner plates embedded in concrete using nonlinear ultrasonics." *Construction and Building Materials*, 408, 133691.

Nilsson, M., Ulriksen, P. and Rydén, N., (2023b).

"Nonlinear ultrasonic characteristics of a corroded steel plate." *Nondestructive Testing and Evaluation*, 38(3), 456-479.

Ongpeng, J. M. C., Oreta, W. C. and Hirose, S., (2016). "Effect of load pattern in the generation of higher harmonic amplitude in concrete using nonlinear ultrasonic test." *Journal of Advanced Concrete Technology*, 14(5), 205-214.

Osika, M., Ziaja-Sujdak, A., Radecki, R. and Staszewski, W. J., (2023). "The Luxembourg-Gorky effect for elastic shear horizontal guided waves - Analytical and numerical modelling." *International Journal of Engineering Science*, 193, 103933.

Otieno, M., Ikotun, J. and Ballim, Y., (2019). "Experimental investigations on the influence of cover depth and concrete quality on time to cover cracking due to carbonation-induced corrosion of steel in RC structures in an urban, inland environment." *Construction and Building Materials*, 198, 172-181.

Peel, M. C., Pegram, G. G. S. and McMahon, T. A., (2007). "Empirical mode decomposition: Improvement and application." In: L. Oxley and D. Kulasiri, Eds. *Proc. MODSIM07 - Land, Water and Environmental Management: Integrated Systems for Sustainability*, Christchurch, New Zealand 10-13 December 2007. Canberra, Australia: Modelling and Simulation Society of Australia and New Zealand, 2996-3002.

Pieczonka, L., Klepka, A., Martowicz, A. and Staszewski, W. J., (2015). "Nonlinear vibroacoustic wave modulations for structural damage detection: An overview." *Optical Engineering*, 55(1), 011005.

Shokouhi, P., Rivière, J., Lake, C. R., Le Bas, P. Y. and Ulrich, T. J., (2017). "Dynamic acousto-elastic testing of concrete with a coda-wave probe: Comparison with standard linear and nonlinear ultrasonic techniques." *Ultrasonics*, 81, 59-65.

Tellegen, B. D. H., (1933). "Interaction between radio-waves?" *Nature*, 131, 840.

TenCate, J. A., Smith, E. and Guyer, R. A., (2000). "Universal slow dynamics in granular solids." *Physical Review Letters*, 85(5), 1020-1023.

Van Den Abeele, K. E.-A., Johnson, P. A. and Sutin, A., (2000). "Nonlinear elastic wave spectroscopy (NEWS) techniques to discern material damage, Part I: Nonlinear wave modulation spectroscopy (NWMS)." *Research in Nondestructive Evaluation*, 12(1), 17-30.

Xu, Y. and Song, Y., (2022). "Chemical-mechanical transformation of the expansion effect for nonuniform steel corrosion and its application in predicting the concrete cover cracking time." *Cement and Concrete Composites*, 127, 104376.

Xu, Y., Jiang, X., Fan, Y., Wang, Q. and Zhang, H., (2022). "Microcrack detection in thermally damaged concrete based on broadband frequency coupling of nonlinear ultrasonic modulation." *Journal of Materials in Civil Engineering*, 34(3), 04021473.

Zaitsev, V. Y., (2019). "Nonlinear acoustics in studies of structural features of materials." *MRS Bulletin*, 44(5), 350-360.

Zaitsev, V. Y., Gusev, V. and Castagnede, B., (2002a). "Luxemburg-gorky effect retooled for elastic waves: A mechanism and experimental evidence." *Physical Review Letters*, 89(10), 2-5.

Zaitsev, V. Y., Gusev, V. and Castagnède, B., (2002b). "Observation of the 'Luxemburg-Gorky effect' for elastic waves." *Ultrasonics*, 40, 627-631.

Zaitsev, V. Y., Matveyev, L. A. and Matveyev, A. L., (2009). "On the ultimate sensitivity of nonlinear-modulation method of crack detection." *NDT and E International*, 42(7), 622-629.

Zaitsev, V. Y., Matveev, L. A. and Matveyev, A. L., (2011). "Elastic-wave modulation approach to crack detection: Comparison of conventional modulation and higher-order interactions." *NDT and E International*, Elsevier, 44(1), 21-31.

Zaitsev, V. Y., Nazarov, V. E., Tournat, V., Gusev, V. E. and Castagnède, B., (2005). "Luxemburg-Gorky effect in a granular medium: Probing perturbations of the material state via cross-modulation of elastic waves." *Europhysics Letters*, 70(5), 607-613.

Zeiler, A., Faltermeier, R., Keck, I. R., Tome, A. M., Puntonet, C. G. and Lang, E. W., (2010). "Empirical mode decomposition - An introduction." In: *Proc. 2010 International Joint Conference on Neural Networks (IJCNN)*, Barcelona, Spain 18-23 July 2010. New York, USA: Institute of Electrical and Electronics Engineers, N-0296.

Zhong, F., Zhang, C., Li, W., Jiao, J. and Zhong, L., (2016). "Nonlinear ultrasonic characterization of intergranular corrosion damage in super 304H steel tube." *Anti-Corrosion Methods and Materials*, 63(2), 145-152.

Appendix D

<div align="right">

Paper IV

</div>

Nilsson, M., Ulriksen, P. and Rydén, N. (2024). Ultrasonic imaging of concrete-embedded corroded steel liners using linear and nonlinear evaluation. *Nondestructive Testing and Evaluation*. Taylor & Francis, 1-29, doi: 10.1080/10589759.2024.2402889

170

Taylor & Francis
Taylor & Francis Group

Ultrasonic imaging of concrete-embedded corroded steel liners using linear and nonlinear evaluation

Markus Nilsson, Peter Ulriksen and Nils Rydén

Division of Engineering Geology, Faculty of Engineering, Lund university, Lund, Sweden

ABSTRACT

This study explores the efficacy of horizontally polarised shear (SH) waves in ultrasonic inspection of concrete-embedded steel liner plates, focusing on corrosion detection. SH-waves are found to significantly improve the localisation and potential dimensional assessment of embedded plate-like structures compared to compressional (P) waves, as evidenced by SH C-scans. Anomalies corresponding to severe corrosion are discernible in SH C-scans, whereas they are minimally visible in P-wave scans. Nonlinear evaluation explores harmonic-based imaging, including second harmonic generation (SHG) and third harmonic generation. Nonlinear SH-wave evaluation accurately locates the most severely corroded embedded plate, whereas comparative P-wave evaluations fail. However, potential FFT sidelobe contamination in the results warrants consideration. These results suggest a promising use for nonlinear waveform distortion in SH-wave-based corrosion detection though conclusive evidence of the source of SHG is uncertain. Experiments utilised an automatic scanner system for consistent control. The concrete specimen investigated herein contained pre-corroded plates which hint at heightened nonlinear effects when corrosion occurs post-embedment due to corrosion-induced cracking. These findings encourage further investigation into SH-waves for nonlinear ultrasonic detection of concrete-embedded steel liner plates and the development of instrumentation tailored to such methods.

1. Introduction

Corrosion of steel components embedded in concrete remains a challenge in terms of prevention, detection, and remediation. When steel corrodes, the structural integrity of the component is affected greatly [1,2] and if the component is embedded in concrete, it may severely affect the concrete by a swelling pressure, causing the concrete to crack and spall [3]. However, before severe cracking occurs it may be of interest to detect embedded components suffering from the onset of severe corrosion to plan adequate remedies before failure occurs. This is the case for leak-tight steel liner plates in large pressure vessels such as the reactor containment in Nuclear Power Plants (NPPs). If the liner is

embedded in concrete, it is not possible to assess the integrity of the component visually, hence there is a need for non-destructive imaging means.

Ultrasound has been used for several decades to image the interior of various media [4–6]. The development of ultrasonic techniques has been greatly affected by its pronounced use in clinical examinations [7] and for material inspection [8,9]. Typically, ultrasonic techniques measure the amount of energy scattered back to the receiver and the time it takes for the scattered signal to arrive. This yields an indication of how strongly the signal reflects, which is an indirect measurement of the acoustic impedance of the material, and the location of the scatterer if the sound velocity of the media is known. Typically, defects, such as cracks, offer a large impedance difference compared to the host material which causes strong reflections. However, the sound beam transmitted into a material is generally quite spread with the majority of the energy focused on the main lobe in the middle of the beam, and then some energy is spread to the sides in so-called side lobes. These side lobes may generate unwanted reflections causing a cluttered image. In biomedical applications, this was avoided by imaging tissue receiving the second harmonic, i.e. twice the fundamental frequency of the ultrasound signal. This is advantageous because the weak side lobes will not generate any pronounced second harmonics as the nonlinear effects are finite (high but limited) amplitude phenomena.

Although the second harmonic imaging technique works well in tissue, the increase in attenuation and scattering effects from defects in solids may yield erroneous indications if only the magnitude of the second harmonic is studied. Thankfully, defects such as cracks and corrosion have been shown to induce local nonlinear elastic regions which enhances the nonlinear effects [10,11]. For longitudinal waves, it is common to quantify the nonlinearity by using the ratio between the second harmonic magnitude and the fundamental harmonic squared, called the relative parameter of quadratic nonlinearity [12]. Acoustic nonlinearity is also much less dependent on the probing wavelength, meaning that subwavelength defects can be detected [10,13–15]. The second harmonic generation (SHG) for longitudinal waves is a quadratically nonlinear phenomenon [16] that is expected to occur to a certain extent in most solids due to weak anharmonicity of the interatomic potential (material nonlinearity) [17–20], and solids containing crack-like defects due to contact nonlinearity [21]. The SHG is also an effect of finite strain (geometrical nonlinearity) which is unaffected by material properties [22,23]. Additionally, the SHG may also be affected by the piezoelectric coupling via electro-mechanical nonlinearity [24]. There are evidently many factors that can affect the SHG for longitudinal waves, thus the sensitivity of defect detection is reduced, while measurement complexity increases to reduce these effects. Interestingly, transverse waves such as horizontally polarised shear waves (SH-waves) commonly used for ultrasonic inspection of concrete [25] typically does not generate second harmonics [26,27] but may do so under specific circumstances due to complex nonlinear interactions [28].

The use of bulk SH-waves for concrete inspection has been shown to exhibit various advantages compared to the use of longitudinal (P) waves due to the comparative reduction of attenuation and backscattering in SH-waves [29,30] and their non-dispersive nature [31]. As the particle displacement for SH-waves is oriented perpendicular to the wave front, such waves are suspected to be more sensitive to frictional interfaces given that the interface is parallel to the displacement field [26]. Additionally,

when it comes to the nonlinear characteristics, the SH-waves differ from the P-waves in that the second (even) harmonics are only generated for nonclassical interactions in frictional interfaces, e.g. for an oblique crack [32], or when a tangential prestress is present in the interface [28]. An effect of this is that SHG in SH-waves is therefore immune to such things as adhesive nonlinearity [32], and even classical material non-linearity [31]. These factors suggest that the SHG for SH-waves may serve as a valuable tool for the inspection of interfacial defects such as changes to the steel–concrete interface in embedded steel liners due to corrosion.

Although the advantageous characteristics of the SHG in SH-waves have been reported since the early 2000's [26], there is a very limited amount of experimental work on the matter. To the author's knowledge, this is the first report of its kind looking into the feasibility of using SHG imaging utilising SH-waves for the detection of concrete-embedded corroded steel liner plates. The authors also failed to find any literature that covers work on ultrasonic imaging of embedded steel plates that have undergone corrosion. However, related work on reinforcement corrosion [33,34] and non-imaging studies on embedded steel liners [35] do exist. Our work is therefore, to the best of our knowledge, novel in two aspects: ultrasonic imaging of corroded steel plates embedded in concrete; and in using SHG imaging with SH-waves. Additionally, the nonlinear evaluation presented herein includes the third harmonic as well. The third harmonic is expected to be effectively generated for SH-waves in heterogeneous media due to the resonant properties with the fundamental frequency [27,28,36]. The measurements were conducted using an XY-scanner, and the results are compared to P-wave measurements.

2. Ultrasonic evaluation by imaging

2.1. Principles of ultrasound imaging

Ultrasound utilises high-frequency acoustic waves to inspect various media such as concrete and steel, as well as various biological materials. Typically, an electrical pulse is sent to a piezoelectric material which converts the electrical charge into mechanical stress and vice versa, thus elastically deforming the piezo which generates acoustic waves whose characteristics depend on the design of the transducer. The excitation must be of a transient nature to achieve spatial resolution. The generated waves are directed into the object under examination and when the wave encounters interfaces with an acoustic impedance differing from the host material the waves undergo partial reflection and transmission. For heterogeneous materials such as concrete, which have randomly arranged constituents with a wide range of sizes, e.g. aggregates, and pores, the absorption and scattering of ultrasound is significant. This causes ultrasound to attenuate effectively and also generates many spurious reflections that may be referred to as *structural noise*. These effects can be reduced by increasing the excitation wavelengths, at the cost of spatial resolution. Previous studies have reported advantages of the use of SH-waves over P-waves due to reduced attenuation and scattering, i.e. structural noise [29].

By recording the amplitude and Time-of-Flight (ToF) of the backscattered signals, the boundaries between materials with varying impedance may be imaged by intensity (amplitude) and location (by the ToF). A single measurement of the

magnitude and ToF (A-scan) of a reflected incident wave is typically not sufficient to adequately assess the integrity of the object under examination. Therefore, it is common to conduct a series of measurements in a line or a grid to create multiple A-scans from which a 2-D depth profile (B-scan) or a 2-D section at a certain depth (C-scan) can be created by using the envelope of the A-scans. Such images may yield valuable information about the internals of critical components and areas of interest that may need additional inspection can be identified. When conducting measurements on concrete specimens, the presence of structural noise might render ToF estimations of the signal of interest challenging due to the difficulty of arrival time picking. There have been significant efforts made to automate the picking of the ToF, some of which are presented in Section 2.2.

As reflections occur when an incident wave interacts with an interface with a change in impedance, it is important to reduce the impedance difference between the transducer face and the object under examination to maximise the amount of energy that is transmitted into the material. To achieve this there must usually be a thin layer of a suitable couplant between the surface of the material and the transducer face to minimise the impedance difference. However, applying a couplant introduces an additional source of uncertainty as there may be micro-inhomogeneities in the couplant and the layer may be uneven. For ultrasonic concrete inspection, the fortunate invention of Dry-Point-Contact (DPC) transducers in the late 1980s has eliminated the need of a couplant and thus made concrete imaging using DPC transducers an effective tool in the NDT arsenal [25]. There are nowadays commercial instruments based on the use of DPC transducers and advanced imaging processing techniques such as synthetic aperture focusing technique (SAFT) to improve image qualities [30].

2.2. Arrival time estimation techniques

Picking the arrival times is important for the extraction of relevant parts of the signal. The echoes corresponding to the tone burst must be extracted with near-zero start and end points and contain an integer number of periods for the reliable extraction of the second harmonic [12]. Naturally, when conducting inspections of large structures using scanning techniques there will be a large number of signals to analyse. To manually pick the arrival times for all measurements would be an incredibly time-consuming and tedious task, and the picks may be subjective, thus differing between operators. Considerable efforts have therefore been put into the development of methods to (semi-)automatically pick the arrival time or ToF (henceforth used interchangeably) of a wide range of signals using various techniques [37–43]. The least complex picking methods are based on picking the arrival time by using an amplitude threshold [37] and are therefore very sensitive to noise. However, such threshold techniques offer great flexibility due to their simplicity, and they can therefore easily be adapted to the situation. The following subsections describe three methods that can be used to estimate the arrival of an ultrasonic echo. The methods are based on cross-correlation, the Akaike's information criterion, and the third method is an amplitude-threshold-based method proposed

by the authors for the extraction of tone bursts by studying the zero-crossings within a prescribed time window.

2.2.1. Estimation of arrival time by cross-correlation

Picking methods based on cross-correlation use a reference signal to represent the signal of interest to find at which point in time the highest correlation is found between the reference signal and the recorded data [39,40,43]. These techniques are usually robust with regards to noise suppression and low-amplitude signals as they only look for the signal of interest given by the reference [40]. However, if the analysed signal is distorted due to scattering, mode conversions, or nonlinear material properties, the ToF estimation may become biased and return incorrect estimates [44].

The cross-correlation $R_{f(t)g(t)}(\tau)$ (see Eq. (1)) between the reference signal $f(t)$, and the received signal $g(t)$ can be used to estimate the ToF of $g(t)$ by finding the time τ which corresponds to the maximum cross-correlation.

$$R_{f(t)g(t)}(\tau) = \int_{-\infty}^{\infty} f(t)g(t+\tau)dt \tag{1}$$

When dealing with discrete signals, it is preferable to utilise the fast Fourier Transform (FFT) to compute the cross-correlation. In terms of FFT, the cross-correlation at the discrete sample n is given by Eq. (2):

$$R_{f(n)g(n)}(n) = FFT^{-1}\{FFT[f(n)]FFT[g(n)]^*\} \tag{2}$$
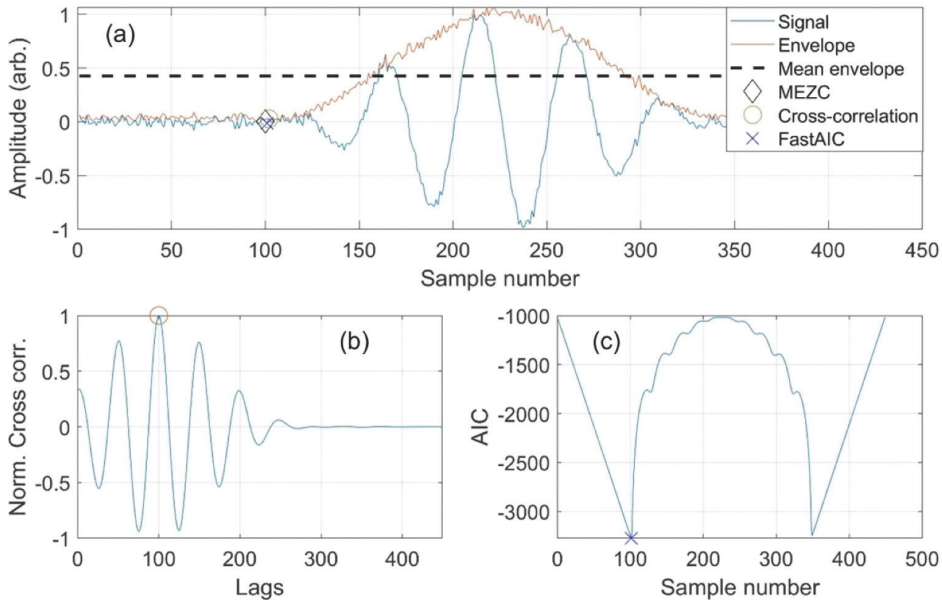
Figure 1. Illustration of the arrival time picking methods. (a) A 5-cycle sinusoidal tone burst with an SNR of 20 dB along with the arrival time picks for each method. (b) Normalized cross-correlation between the signal in (a) and a reference signal. (c) Fast AIC of the signal in (a).

where * is the complex conjugate and FFT^{-1} is the inverse FFT. The sample n which yields the maximum $R_{f(n)g(n)}(n)$ gives the ToF estimation, see Figure 1. As the cross-correlation method depends on the reference signal, it is important that the reference indeed represents the expected received signal. When exciting a transducer with an electrical pulse, it would be required to determine the response of the transducer, e.g. by constructing a theoretical model of the transducer and its response [40]. The excitation signal in the present work is a Hanning-windowed tone burst, and indeed a model of this signal can be used as a reference due to the forced vibration by this excitation form. Details of the excitation signals are provided in Section 3.2.

2.2.2. Akaike's information criterion for arrival time estimation

Methods based on the Akaike information criterion (AIC) [38,41,42] operate on the assumption that the arrival time is a transition point between two separate stationary processes [41]. Naturally, this causes the methods to be very sensitive to noise, equipment-based crosstalk, and spurious reflections as the local processes would be greatly influenced by such effects; however, by the appropriate use of adaptive windows and phase correction techniques, the robustness can be improved [41]. The AIC for a discrete record of N samples, $x(n)$, $(n = 1, 2, \ldots, N)$ is given by Eq. (3)

$$AIC(k) = k \times \lg\{Var(x[1,k])\} + (N - k - 1) \times \lg\{Var(x[k+1,N])\} \qquad (3)$$

where k is the discrete samples, i.e. $k \in [1, N]$, and $Var(x[1,k])$ and $Var(x[k+1,N])$ represent the variance of the segments of data within the two windows. The time windows must be slid once per sampling point, and the variance must be recalculated for each step. This leads to a computationally inefficient algorithm due to large amount of multiplication when applied to a large amount of signals, for example, when scanning large structures. To combat this, the FastAIC algorithm has been proposed [42] and is given by Eq. (4)

$$FastAIC(k) = k \times \lg\left(\frac{1}{k}s_{k2} - 2\bar{x}\frac{1}{k}s_{k1} + \bar{x}^2\right) + (N - k - 1)$$
$$\times \lg\left(\frac{1}{N-k} \times (s_m - s_{k2}) - \frac{2\bar{x}}{N-k} \times (N\bar{x} - s_{k1}) + \bar{x}^2\right) \qquad (4)$$

where $s_{k1} = \sum_{n=1}^{k} x(n)$, $s_{k2} = \sum_{n=1}^{k} x(n)^2$, $\bar{x} = (1/N)\sum_{n=1}^{N} x(n)$, $s_m = \sum_{n=1}^{N} x(n)^2$, $x(n)$ is the discrete signal. The advantage over this algorithm compared to eq. (3) is that when N is fixed there is only a need to calculate $\bar{x}$ and s_m once which indeed reduces the number of computations [42]. The arrival time is estimated at the sample k that corresponds to the global minimum of the AIC or FastAIC, see Figure 1. However, when analysing ultrasonic signals acquired from arrays, there may be surface waves that reach the sensor before the expected direct reflection. To avoid false estimations of the arrival time, an adaptive window which is a rough estimate within which the ToF is expected can be used. The minimum within this window is then the estimated ToF.

2.2.3. Proposed mean envelope zero-crossing method

In this work, we have adopted an amplitude-threshold picking technique that uses the mean envelope of a signal within an adaptive window to find the zero-crossing which represents the first estimate of the arrival. This zero-crossing typically occurs one period after the actual time of arrival, so the method uses this first estimate to look for an additional zero-crossing occurring a period before the estimated pick. This new estimate is then used to extract the tone burst by finding the end point by searching for a zero-crossing with the same inclination (rising or falling edge) occurring after the duration of the tone burst; this ensures that an integer number of periods are extracted. The duration is given by the nominal frequency and the number of cycles in the burst. In essence, the processing steps to extract a tone burst are as follows.

> *Step 1*: Define the time window within which the ToF is expected to occur and with sufficient duration to capture several periods of the tone burst. It is preferred if the end of the window is given by the start point plus the expected duration of the signal of interest. The start of the time window can be identified by studying B-scans. Remove the DC-offset if present. Compute the envelope of the signal within the time window.

> *Step 2*: Find the zero-crossing which occurs before the mean-value of the envelope from Step 1. Search for the zero-crossing occurring one period before the mean envelope crossing point. This is the estimated time of arrival (ToF). Determine the slope orientation of the zero-crossing, i.e. is the signal increasing (rising edge) or decreasing (falling edge) locally with time.

> *Step 3*: Use the tone burst duration and the slope orientation to find the zero-crossing which corresponds to the end of the tone burst. An integer number of periods is given when the slope orientation is equal at the start and end of the extracted signal.

The method is intuitively termed Mean Envelope Zero-Crossing (MEZC), and its working principle to find the ToF is illustrated in Figure 1 where a 5-cycle 40 kHz sinusoidal tone burst with a Signal-to-Noise Ratio (SNR) of 20 dB is used as the example signal. The signal 'arrives' at the 100th sample. For the sake of completeness, MEZC is compared with a regular cross-correlation technique and is shown in Figure 1(b) where a tone burst without noise is used as reference. The maximum correlation indicates the arrival time. The Fast-AIC method as suggested by Long et al. [42] is shown in Figure 1(c) where the global minimum indicates the arrival time. The second minimum indicates the next transition of processes, i.e. the end of the tone burst. In this particular example, both MEZC and the cross-correlation technique accurately detect the arrival time at sample 100, whereas the Fast-AIC method picks at sample 101. However, as signal complexity increases, the robustness of the cross-correlation and AIC techniques fail, which will be illustrated in the results given in Section 4.2.

The MEZC method described here is tailored to the specific application reported herein and its performance depends greatly on the mean value of the envelope. For longer tone bursts, the mean value increases, and it is therefore possible that the first estimate is erroneous. The method is therefore only currently proven for specific cases in the present work.

2.3. Nonlinear ultrasonics

2.3.1. Higher harmonic generation in horizontally polarized shear bulk waves

The generation of integer multiples of the fundamental frequency (*f*) of an incident wave is called *harmonic generation*. The mechanisms that govern the generation of even harmonics differ from the generation of odd harmonics. Odd harmonics, which are odd multiples of the fundamental frequency (*3f, 5f,* . . .) are to a certain extent generated for many types of signal distortion. Clipping is one of such signal distortions which is caused by reaching the limited dynamic range of the system. The even harmonics (*2f, 4f,* . . .) are only generated when there is an asymmetry between the positive and negative half-periods in the received signal. An example of waveform asymmetry is the 'clapping' effect commonly discussed in longitudinal wave interaction with microcracks [21,45]. When the microcrack is opened it cannot support elastic wave rarefaction (tension), but the compressive part can propagate and potentially close the crack. The crack stiffness governs the local compressive stress limit, because when closing occurs the maximum stress is reached which in itself causes the aforementioned clipping effect. When the crack is closed tension is supported, however, the tension may cause the crack to open once again. As such, there is an asymmetry between the maximum levels of compressive and tensile stress being supported by the crack locally. This type of stiffness asymmetry causes both even and odd harmonic generation among other effects [46]. This reasoning can also be applied to SH-waves; however, the crack orientation plays a large role in how strong the generation of even harmonics is [32]. If the crack is oriented vertically, i.e. in the direction of a wave propagation, or horizontally, i.e. in the direction of the particle displacement, there will be no clapping effect. However, if the crack is oblique, the crack is expected to cause an asymmetrical stiffness due to a variation of the contact force at the crack interface due to negative/positive shear forces [32].

Recent work has commented on the second-harmonic generation (SHG) for SH-waves [28] where the authors performed a rigorous analysis of Contact Acoustic Nonlinearity (CAN) [21] and found that SHG may arise for SH-waves in the presence of tangential prestress in the contact region due to a form of stiffness asymmetry. Assume that an incident SH-wave interacts with a contact region that is subjected to a tangential prestress. The contact naturally has friction that limits sliding, and the friction is typically modelled to be equal in the positive and negative directions. If the incident shear stress is oriented in the same direction as the tangential prestress, the relative stress threshold that the incident SH-wave needs to overcome to achieve sliding, i.e. the friction, decreases. Naturally, when the shear stress from the incident transverse wave is in the opposite direction, the stress threshold will increase as the wave would need to overcome both the prestress and the friction. This causes an asymmetry between the positive and negative half-periods of the transverse wave as the maximum supported stress is not equal. When no prestress is present, the maximum shear stress that can be supported is equal to the limiting friction, above which sliding occurs and once again inducing the clipping effect. As this limiting friction is equal for both half-periods, a symmetrical stiffness is achieved.

The above brief discussion introduces circumstances where even, and in particular second, harmonic generation for SH-waves is possible. Oblique cracks and the presence of tangential prestress in a frictional interface facilitate the SHG, both of which are related to CAN [21]. It is therefore suspected that SH-wave SHG is sensitive to

changes to the contact interface between steel plates and concrete, in particular when the plates are severely corroded. The contact interface that is formed by steel-corrosion product-concrete offers complex contact mechanics due to the randomly distributed surface roughness of the corrosion products and the properties of the corrosion products themselves. The SH-wave SHG is therefore particularly interesting when inspecting structures with considerable prestress, such as NPP containment buildings [47], and particularly the steel liner plate within. Previous work on using nonlinear ultrasonic evaluation of embedded steel plate corrosion has indicated changes to the nonlinear response due to such features [35]. The experimental work presented here aims to investigate the feasibility of using harmonic generation to image contact interface anomalies that occur between embedded steel plates and concrete due to corrosion.

2.3.2. Parameters of nonlinearity based on harmonic generation

Because of attenuation and scattering effects of internal discontinuities and the challenges of consistent transducer coupling, it is not common to use the magnitude of the generated harmonics in NDT applications because this might yield erroneous conclusions regarding the state of a specimen. This is because undamaged materials will likely attenuate less, which results in stronger harmonics. Conversely, the damaged regions will attenuate the signals which leads to a reduction in the observed harmonics. It is therefore more common to study various parameters of the nonlinearity, in particular what is called the *relative parameter of the quadratic nonlinearity* (β') which is given by the ratio of the magnitude of the second harmonic (A_2) over the fundamental magnitude squared (A_1^2), see Eq. (5). The parameter is *relative* because it is a derivative of the *absolute parameter of quadratic nonlinearity* and typically uses the magnitude of the voltage signals from the transducers rather than a calibrated displacement signal [12]. These parameters are essentially a measure of the energy distribution from the fundamental component to the harmonic of interest. It is therefore expected that regions exhibiting strong nonlinearity will have reduced levels of the fundamental component and this effect is reflected in the parameter value. In addition to the quadratic parameter, the parameter of *cubic* order (δ') can be used to qualitatively quantify the distribution of energy to the third harmonic (A_3), which is given by Eq. (6).

$$\beta' = \frac{A_2}{A_1^2} \tag{5}$$

$$\delta' = \frac{A_3}{A_1^3} \tag{6}$$

3. Specimen and measurement methodology

3.1. Concrete slab specimen containing corroded steel plates

The specimen used was a concrete slab contained within a heavy-duty plastic container designed to hold a maximum load of 4300 kg, see Figure 2(a) for the tub before casting, (b) for the appearance of the slab surface after 5 years and (c) for a view of the reinforced bottom which shows no sign of buckling. The inner dimensions of the plastic tub were $1100 \times 710 \times 420$ mm^3 as seen in the schematic in Figure 3. Observe the symmetric nature
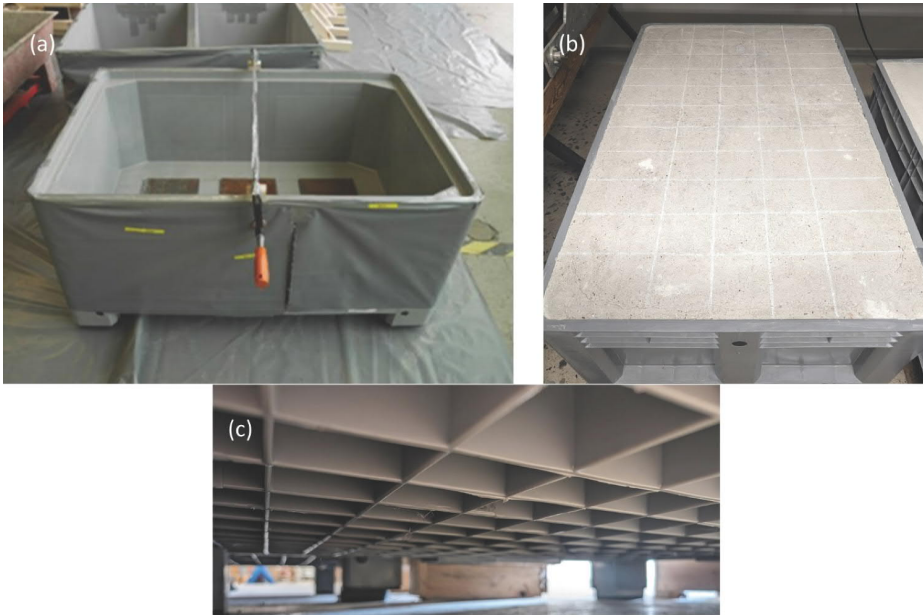
Figure 2. (a) Plastic container used as a mould for the concrete specimen. (b) Specimen after 5 years. (c) Reinforced bottom shows no indication of buckling.
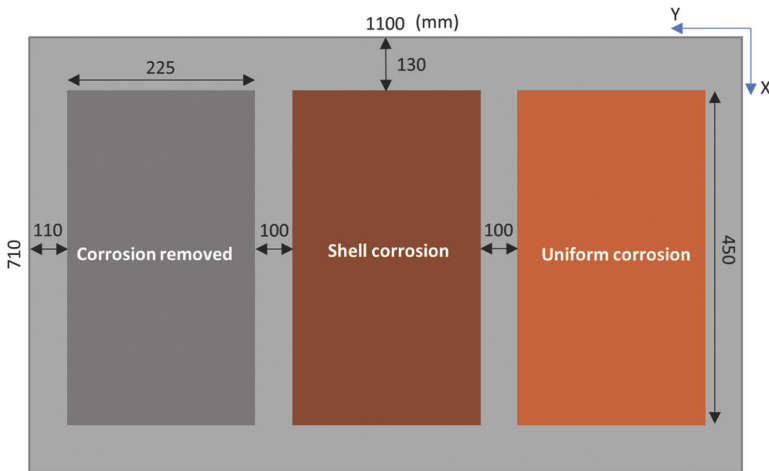

Figure 3. Schematic illustration of the placement of the steel plates at the bottom of the concrete slab.

of the specimen design. The specimen is symmetric along its horizontal and vertical centres and the only differing factors are the characteristics of the embedded plates. An additional factor that may affect the results is that the walls of the plastic tub and the plates are only separated by approximately 110–130 mm on each side, which is roughly equal to the transducer dimensions (see Section 3.2). The concrete from the contractor was specified as C35/45 SF2 WC 0.50 with a maximum aggregate size of 16 mm and was cast in

Figure 4. Surface cracks along the boundary of the specimen.

April 2018. This means that the specimen was well cured for some time when the experiments described herein were performed (fall 2023). This means that curing effects such as shrinkage have affected the slab. This is evidenced by the surface cracking along the boundary as shown in Figure 4. When the slab was cured, its surface was smoothened by mechanical grinding. This process resulted in a levelled surface; however, the procedure also revealed pores that now cause small inhomogenities in the surface. There is no buckling of the backwall. This is expected considering that the load of the concrete, which is approximately 800 kg if a density of 2400 kg/m^3 is assumed, is well below the limit of 4300 kg. Buckling would result in a non-horizontal backwall which would greatly
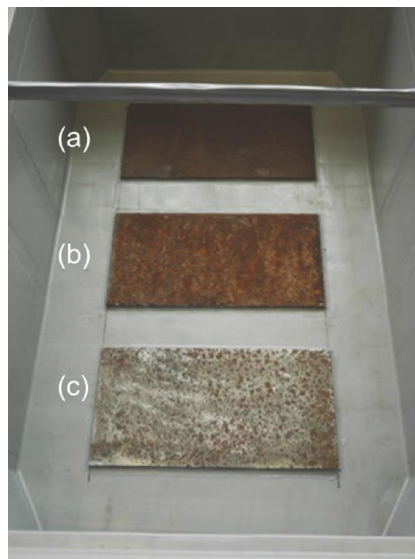
Figure 5. Steel plates at the bottom of the plastic tank. (a) Uniformly corroded plate. (b) Uniformly corroded plate with shell-type corrosion. (c) Corroded plate grounded to remove corrosion.
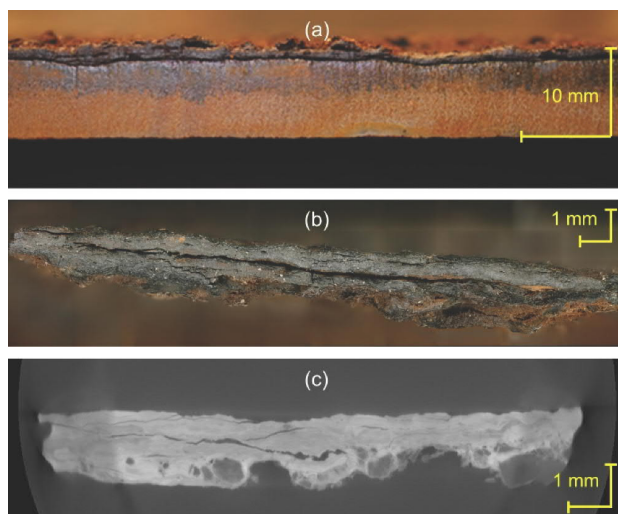
Figure 6. (a) Cross-sectional view of a uniformly corroded plate with shell-type corrosion. Note the delamination between the corrosion shell and steel plate and also note the cracking in the corrosion shell. (b) Stitched microscopy of the cross-section of a piece of shell corrosion. (c) X-ray tomography of a piece of shell corrosion.

affect the results. Instead, it is the surface roughness of the plates that may induce non-horizontal reflectors.

At the bottom of the plastic tub, three steel plates measuring 225×450 mm^2 with a nominal thickness of 8 mm were adhered and sealed by the use of silicone along their edges to avoid the lifting of the plates due to concrete slurry finding its way underneath during casting. The embedded plates were cut from a larger specimen to keep the bulk properties (almost) equal. The steel plates that were embedded are a typical uniformly corroded plate, a uniformly corroded plate with a corrosion shell on top, and the third plate was initially uniformly corroded but the corrosion has been removed by grinding, Figure 5 shows the plates at the bottom of the plastic tub. The middle plate with the corrosion shell is of particular interest due to the shell-type corrosion product. Figure 6 shows the characteristics of shell corrosion from the same host plate as the three embedded plates were cut from. The shell is typically locally delaminated from the bulk of the steel plate (a), severely cracked (b–c), contains voids (a–c), and indeed exhibits a significant surface roughness (a–c). Such corrosion has been shown to cause substantial waveform distortion when excited by ultrasound [10,48]. The delamination characteristics of the shell-corrosion create a steel-corrosion product interface, and when embedded in concrete an additional interface is formed in the region. This creates a steel-corrosion-concrete interface that certainly has complex contact conditions, partially due to the significant surface roughness of the corrosion product which indeed should affect the conditions for elastic wave interaction in the interface. However, such effects are more likely to be pronounced when corrosion occurs post-embedment. The uniformly corroded plate does not exhibit any delamination between the steel and corrosion products, therefore, the

contact interface is corrosion-concrete. The ground plate has very little corrosion and is therefore mostly characterised by a steel–concrete interface.

The choice to embed steel plates that were already corroded was made to minimise the risk of concrete damage caused by the swelling of corrosion products. This results in the possibility of assessing the feasibility of detecting the very early onset of corrosion which is suspected to challenge the interfacial conditions between the steel plate and concrete [35]. Furthermore, it is known that the concrete cover is one of the most influential parameters when defining the corrosion-induced concrete cracking [49]. For thick-walled structures, cracking might not occur until the corrosion is severe. However, when cracking occurs, the nonlinear response is expected to increase significantly, which has been confirmed by previous studies covering reinforcement bar corrosion [33,34,50], although the effects on SH-waves are not completely explored. The delamination between the shell-corrosion layer and the steel itself may also be a source of enhanced nonlinearity due to contact nonlinearity.

3.2. Measurement setup

The schematic of the experimental setup used for the automatic scanning of the specimen can be viewed in Figure 7. The measurement series is controlled by a PC running in the MATLAB environment. The software controls the waveform generation, positioning of the XY-scanner (see Figure 8), and the pneumatic actuators lifting and lowering the dual-aperture array. This allows automatic scanning which eliminates operator dependency leading to consistent measurements for both SH- and P-wave measurements. To measure SH-waves, the ACS M2502 DPC fixed dual-aperture array was used, and for longitudinal wave (P) measurements the ACS
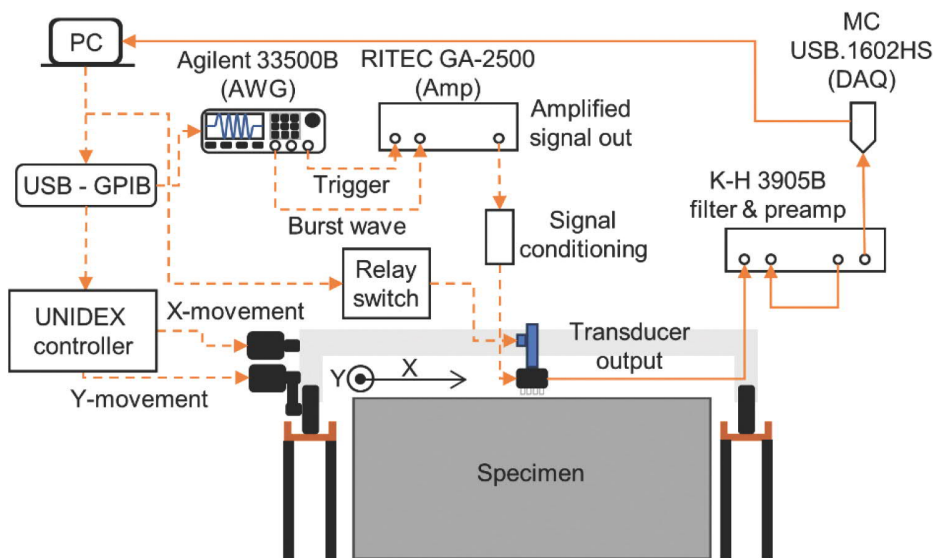
Figure 7. Schematic illustrating the experimental setup used for the automatic scanning. Dashed lines indicate control signals and bold lines indicate measurement data.

Figure 8. The concrete slab specimen and the xy-scanner used to control the ACS M2502 fixed dual aperture array.

M2503 was used. Each fixed dual-aperture array has 24 spring-loaded transducers where 12 of the transducers are connected in parallel as transmitters and the other 12 as parallel receivers. The apertures are fixed, meaning that there is no programmatical switching between the transmitters and receivers. The manufacturer claims nominal frequencies of 50 kHz for the M2502 (SH) and 100 kHz for the M2503 (P). The dimensions of the apertures are 140 mm in length and 100 mm in width, and each sensor is separated by 20 mm. Additional information about the arrays can be found in Ref. [51]. Low-frequency antennas are used because the smaller wavelengths that are generated by waves with greater frequencies may interact more strongly with the various constituents within the concrete matrix. This would cause significant structural noise and spurious distortion. An additional benefit of using arrays is that the non-uniformity of the surface caused by the presence of pores and other inhomogeneities only affects the measurement to a small degree compared to the case of using a single transducer. The excitation waveforms that were used were a $1\,V_{pp}$ Hanning windowed sine burst with five cycles and a fundamental frequency of 40 kHz for the SH-wave and 80 kHz for the P-wave. The excitation frequencies were selected on the basis of the highest measured amplitude. The signals were amplified using a gated amplifier from RITEC (GA-2500) set to a power level of 8.2. The output from the amplifier was terminated with a 50 Ω high-power load, and the signals were then fed through a 100 kHz low-pass filter in two stages. This was done to reduce the signal distortion coming from the amplification process. This resulted in an excitation tone burst with a maximum peak-to-peak amplitude of about 600 V measured into 50 Ω. The received signal was bandpass-filtered by a Krohn-Hite Model 3905B programmable filter to remove high-frequency noise. The lower cut-off was 20 kHz and upper 150 kHz for the SH-wave measurements, and 60 kHz and 300 kHz for the P-wave. The received signal was also amplified by 60 dB. Each measurement was repeated 16 times for averaging purposes. The measured grid was 62 points across (X) and 98 along (Y) the sample, resulting in a total of 6076 measurement points. Each measurement was spaced 1 cm apart in both X- and Y-directions. When the probe was lowered onto the specimen, the measurement was paused for a second to reduce non-equilibrium
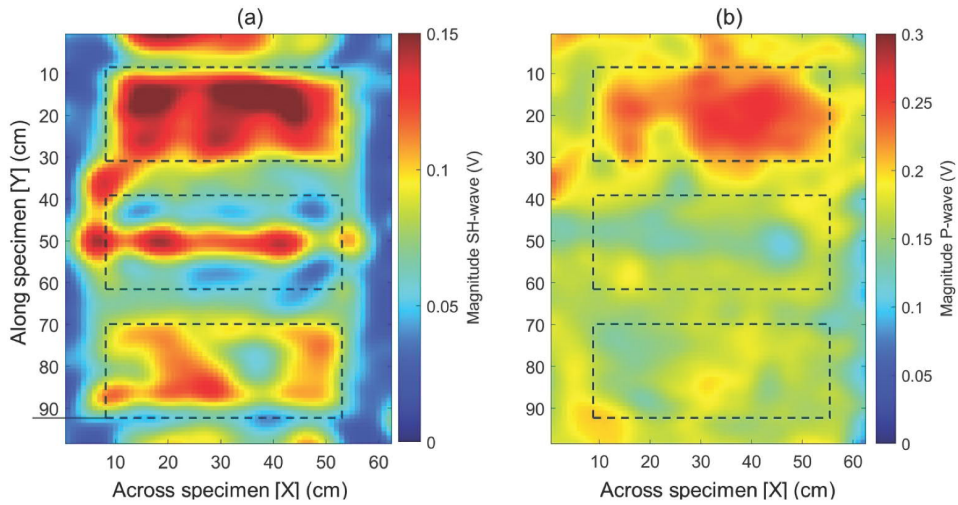
Figure 9. C-scan results from (a) SH-wave antenna at $t = 400$ μs (b) P-wave at $t = 232$ μs. Dashed rectangles indicate the approximate locations of the embedded steel plates. Top: uniformly corroded plate; middle: shell-corroded plate; bottom: ground plate.

effects; similarly, each measurement for the averaging was paused for a second between. This causes a single automatic scan to take approximately 20 hours, which certainly could be reduced.

4. Results and discussion

4.1. Linear evaluation – C-scans

Two separate types of C-scans were obtained from the measurements presented in Sec. 3.2. The SH envelope C-scan extracted at $t = 400$ μs is shown in Figure 9(a) and the corresponding P-wave C-scan which was extracted at $t = 232$ μs is shown in (b). These times correspond to the approximate maximum envelope magnitude for the respective signals which are suspected to be the first echo from the steel plate or the bottom of the plastic tub. Due to the comparatively small thickness of the plates (~8 mm) relative to the wavelength of one period within the tone burst (~60 mm for SH, ~50 mm for P), it is challenging to ascertain the origin of the reflections. Dashed rectangles are included to illustrate the expected locations of the embedded steel plates. The P-wave C-scan does not show any clear indication of the locations of the embedded plates. The only embedded plate that seems to generate strong P-reflections is the uniformly corroded plate. Conversely, the comparative SH C-scan that is shown in Figure 9(a) illustrates quite clear localisation of the uniformly corroded plate (top) and the ground plate (bottom) where it is essentially possible to estimate the dimensions of the plates. However, no clear indication of the boundaries for the severely shell-type corroded steel plate (middle) is seen from the C-scan. Rather, it appears that the middle plate has a ridge-like structure which is highly unlikely. Instead, it is possible that the topmost corrosion product is delaminated along the edges of the plate and in contact in the

middle. It can be argued that the SH scan appears symmetrical which is not surprising considering the design of the specimen; however, the three plates clearly give three distinctly different responses for the SH scan. Such different responses are not observed for the P-wave scan, and neither is the C-scan particularly symmetrical in its appearance. The P-wave measurements cannot successfully resolve the plates because the probing wavelength being far too long as the displacement field is oriented in the propagation direction. The SH-wave perturbs the plates perpendicular to its incidence, which evidently appears to induce greater sensitivity to horizontal structures within the concrete compared to P-waves at similar wavelengths. This strongly highlights the advantage of SH-wave ultrasonics over P-waves, at least for the application at hand. The SH C-scan does not indicate that the top plate is particularly corroded, which may be due to an enhanced adhesion between the concrete and steel plate due to the roughness of the plate surface. Concrete would likely adhere to a perfectly smooth surface, but some roughness may increase adhesion. If corrosion occurred post-embedment, it is possible that the interface would be affected which indeed might cause signal attenuation in weakly uniformly corroded regions as well. This reasoning is supported by the fact that the ground plate appears to have a weaker bond than the uniformly corroded plate, which is indicated by the magnitude differences in these regions. These results indicate the advantage of SH-waves over P-waves for the evaluation of concrete interfaces, it also appears that SH-waves show anomalies where the most severely corroded plate is located further highlighting the potential of SH ultrasonics.

4.2. Estimating time of arrival for signal extraction

To extract higher harmonics automatically and reliably from the tone-burst reflections from the steel plates or bottom of the plastic tub, it is important to have robust signal
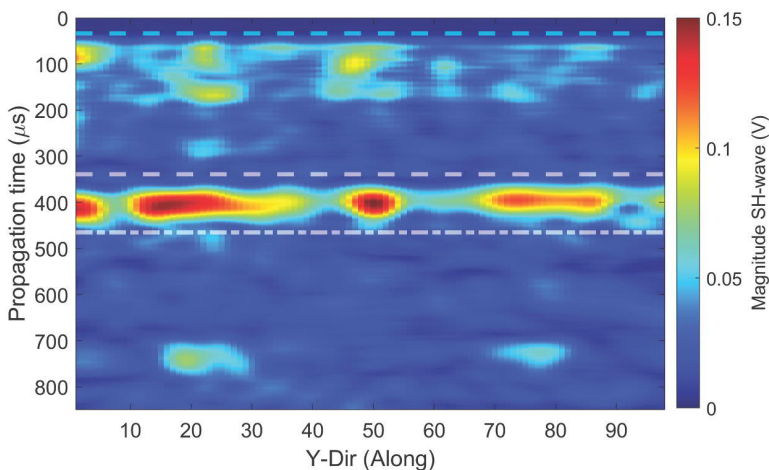
Figure 10. SH B-scan along X-line 20. The cyan line indicates the approximate arrival of the surface waves (34 µs). The white dashed line indicates the start of the time window (340 µs) used for extraction of the time of arrival of the sh-waves. The black dashed line indicates the time corresponding to the start of the time window plus the duration of the tone burst (465 µs).
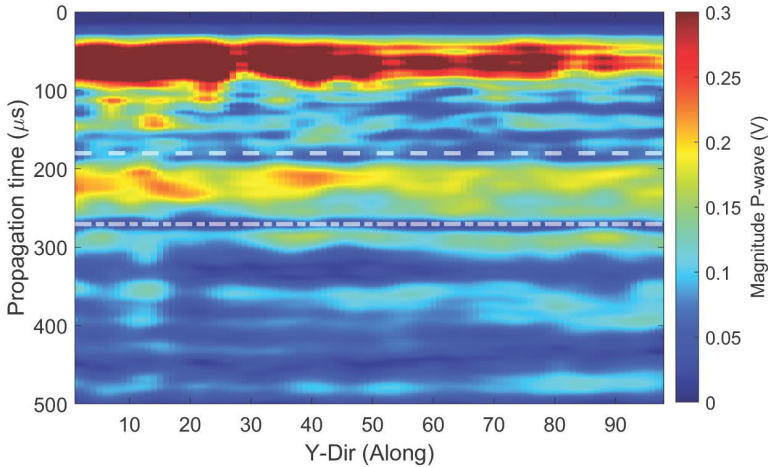
Figure 11. P-wave B-scan along X-line 20. Dashed line indicates the start of the time window (181 μs), dash-dotted line indicates the end of the time window (271 μs).

extraction methods as discussed in section 2.2. To start off, we study the SH-wave B-scan along the profile line X = 20 which shown in Figure 10. The topmost response (cyan dashed line) in Figure 10 which arrives at approximately 34 μs is assumed to be the direct surface wave between transmitters and receivers. If we assume that the wave travels from the centre of the transmitting half of the antenna to the centre of the receivers, the distance would be 70 mm [51]. This results in an estimated average surface wave velocity of approximately 2100 m/s, which is reasonable for concrete. However, it is interesting to note that the surface wave does not appear to be uniform along the surface. This is likely due to varying surface conditions because of the grinding procedure. Some transducers may not be in complete contact because of the pores, as such, the surface wave effect is affected. The P-wave B-scan in Figure 11 does, however, show much more uniform response. The wave of interest, however, is the first echo from the steel plates or bottom of the plastic tub. In the SH B-scan in Figure 10, this echo arrives at approximately 340 μs (white dashed line in Figure 10), which is set as the start of the adaptive window. Note that this is not the final time of arrival but rather a first estimate. The end of the time window is given by the start plus the expected duration of the tone burst, which equates to 465 μs, as shown by the white dash-dotted line in Figure 10. The corresponding echo for the P-wave measurements (Figure 11) occurs at around 181 μs and the end is at 271 μs. It is immediately observed that the reflection patterns differ greatly between the two polarisations. The P-wave B-scan does not yield any clear indications of differing characteristics between the plates. Rather, the response is comparatively uniform, whereas the SH-wave B-scan shows three distinctly different responses pertaining to the three plates. This agrees with the observations made in the C-scans in Figure 9 and suggests that the P-wave measurements only reflect the very backwall whereas the SH-wave measurements are indeed affected by the characteristics of the embedded plates.

In both Figures 10 and 11, the thickness of the plates (8 mm) is not distinctly resolved by clear arrival time differences between the plates. Although the SH-wave B-scan suggests some time differences at specific locations (Y = 0–10, 30–40, 60–70, and 90–98), no such
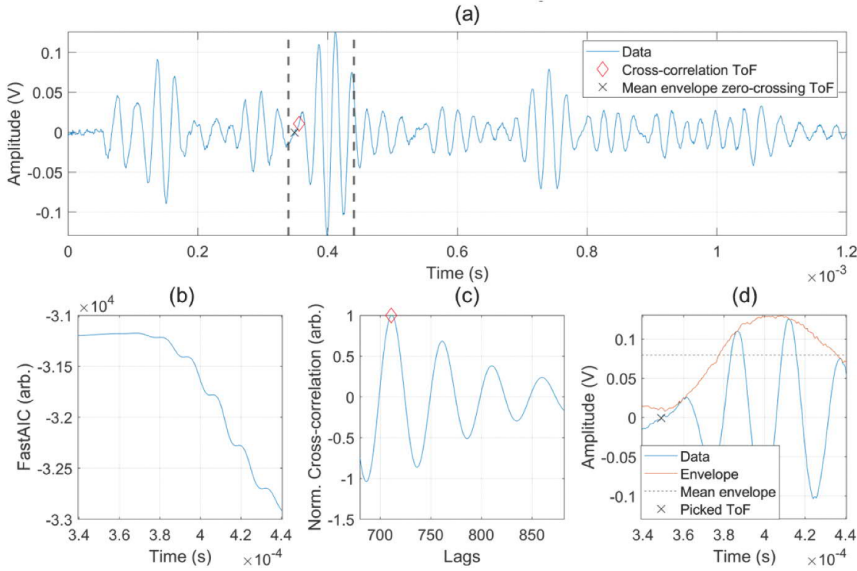
Figure 12. (a) a typical SH ultrasonic signal. The dashed vertical lines indicate the area within the search for an arrival time will occur. The markers indicate estimated time of arrival by the cross-correlation technique (red diamond) and MEZC (black cross). (b) FastAIC undefined within the time window, no minima found. (c) Normalized cross-correlation of which the maxima indicate the time of arrival. (d) Illustration of the Mean-Envelope zero-crossing technique.

differences are evident in the P-wave B-scan. This effect arises due to the relatively long wavelength of the probing waves (approximately 5 cm) compared to the plate thickness. Given this wavelength-to-thickness ratio, it is not feasible to expect the 5 cm acoustic wavelength to resolve a thickness as fine as 8 mm. Notably, the signal levels between the plates in SH C-scans (as shown in Figure 9) are weaker, facilitating plate localisation. This observation highlights the potential of using comparatively low probing frequencies for detecting embedded corrosion during single-sided ultrasonic measurements on large civil engineering structures.

The application of the methods to estimate the ToF described in Section 2.2 on a single SH-signal (X = 20, Y = 50) is shown in Figure 12, where (a) shows the waveform being analysed with the vertical-dashed lines illustrating the time window and markers correspond to the estimated arrival times. The signal appearance illustrates the need of the time window used for extraction, as there is some structural noise just before the start of the time window. Such features may complicate the ToF estimation and ultimately the signal extraction for nonlinear evaluation. This is clearly illustrated in Figure 12(b) where the AIC of the signal within the time window is shown. It appears that the AIC does not detect any change of processes in the provided window as there is no clear minimum, which means that no arrival time can be estimated. However, the AIC appears to signal a change towards the end due to the decreasing trend of the AIC. The cross-correlation technique, however, successfully identifies the maximum correlation within the time window and thus provides an estimated arrival time, the principle of which is shown in Figure 12(c). The proposed MEZC method is illustrated in Figure 12(d) which also
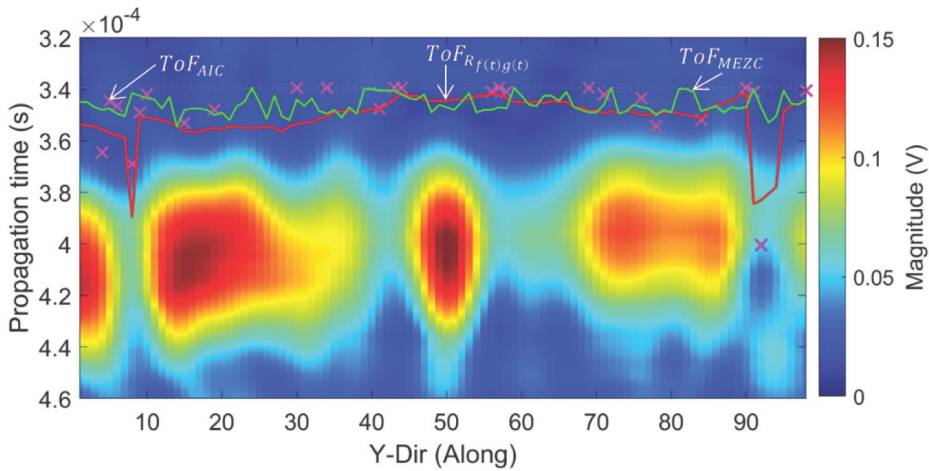
Figure 13. Zoomed in B-scan from Figure 10 showing the results of the three ToF-picking methods. Magenta crosses are the points from the FastAIC method. Observe that the FastAIC method did not find picks for all points in Y. The red line indicates all ToF picks from the cross-correlation method. The green line is the picks from the MEZC method.

identifies a ToF. The estimated arrival times for each method are plotted in Figure 12(a) as markers. Observe that the cross-correlation estimation is somewhat later than the MEZC one, and indeed a zero-crossing is found with the MEZC method.

Figure 13 shows the zoomed in view of the adaptive window in the B-scan from Figure 10 and shows the arrival time picks for the AIC method, cross-correlation technique, and MEZC. Observe that the AIC method (magenta crosses) could not extract arrival times for all signals, and the cross-correlation technique (red solid line) estimates the arrival time erroneously for several points which is indicated by the sudden spikes. The MEZC picks (green solid line) indicate some variation, but the estimations are within reasonable ranges for all points. Reliable extraction of the reflected signals is important as poor estimations may cause considerable sidelobes when performing an FFT on the signal, which may contaminate the extraction of harmonics. By using the MEZC picks, the estimated average shear wave velocity is approximately 2400 m/s, which is reasonable for concrete and coincides well with the surface wave estimate. Only the MEZC method was used to extract signals for the entire SH- and P-wave scans due to the errors shown for the AIC and cross-correlation methods.

4.3. Nonlinear evaluation

The tone bursts for all measurement points are extracted by using the MEZC method and the given knowledge of the tone-burst duration and adding one period to the end. Examples of the three SH-wave signals and the estimated start and end of the tone bursts are shown in Figure 14. Observe that the three signals have similar amplitudes. All extracted signals were windowed using a Hanning window to ensure zero start and end points and to reduce leakage effects compared to other window functions [12]. The magnitude spectra (see Figure 15) were computed from which the magnitudes of the
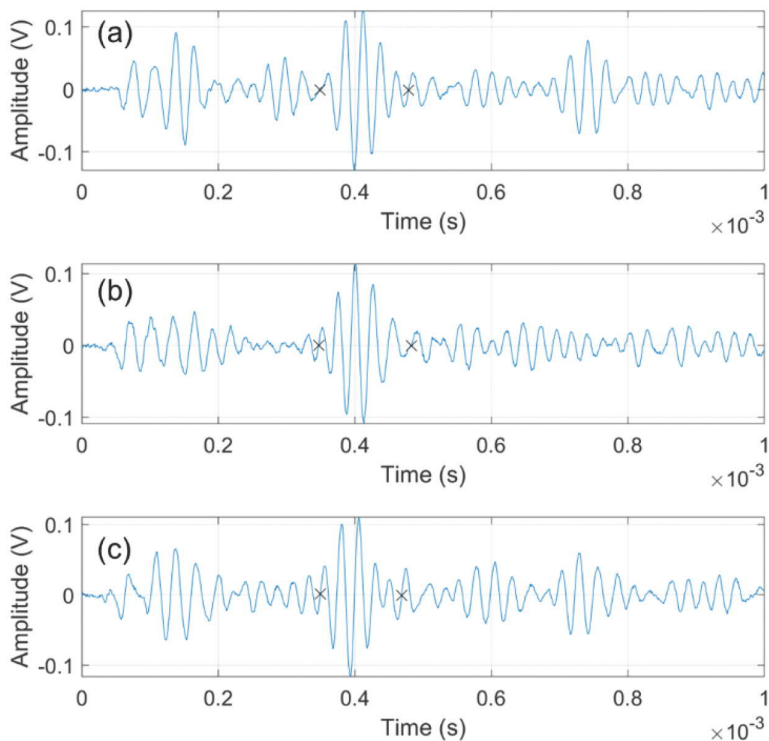
Figure 14. Recorded SH signals at X = 20 and (a) Y = 20 (middle of uniformly corroded plate), (b) Y = 50 (middle of shell corroded plate), and (c) Y = 80 (middle of ground plate). Black x's illustrate the start and end points used for tone burst extraction.
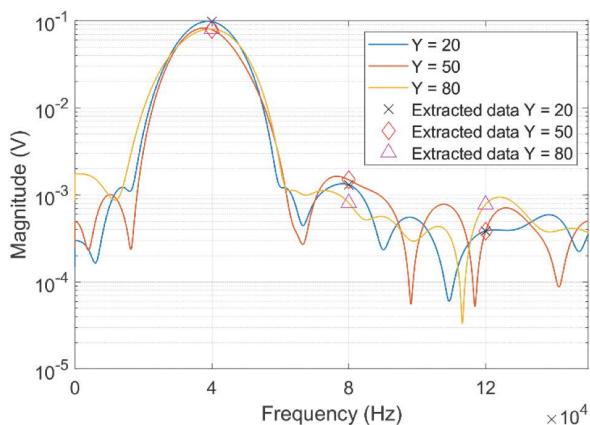

Figure 15. Magnitude spectra for the SH signals shown in Figure 14. Markers illustrate the extracted magnitudes for the fundamental (~40 kHz), second (~80 kHz), and third (~120 kHz) harmonics.

fundamental component and higher harmonics can be extracted. By studying the spectra in Figure 15 it appears that the second harmonics are generated for Y = 20, and Y = 50, which correspond to the approximate locations of the uniformly corroded plate and shell corroded plate, respectively. However, there appears to be some sidelobe contamination for the measurement at Y = 50 as there is no clear peak at 80 kHz. The second harmonic for Y = 80, i.e. the ground plate, is even less clear. The reason for this may be identified already in Figure 14(b,c) if the extracted waveforms are studied closely. The end of the tone bursts appears to contain some interference. It is possible that this causes increased sidelobes that interfere and cause an increased baseline spurious 'harmonic' which contaminates the result. This illustrates the complexity of signal extraction for the current application. Similar challenges are observed when studying the third harmonic at 120 kHz. There is no clearly generated peak at 120 kHz, but rather skewed peaks due to FFT sidelobes. This means that the extracted 'harmonics' likely contain some spurious information. However, as the signals are of a similar appearance and magnitude, the sidelobes should be similar for the measurements and the actual harmonics cause an increase in the magnitude locally. These are only 3 out of 6076 measurement points, and no conclusion should be made strictly from these observations. To study the distribution of the signal distortion for all extracted signals, we map the relative quadratic (Figure 16) and cubic (Figure 17) parameters of nonlinearity similar to a C-scan.

The distribution of the parameter corresponding to the SHG, β' (Eq. (5)), can be viewed in Figure 16 for (a) SH-wave and (b) P-wave analysis. It is immediately observed that the boundaries of the scanned region appear to cause strong waveform distortion, an effect which may be attributed in part to cracks that have formed due to shrinkage. Such cracks are known to exist due to the observed surface cracking shown in Figure 4. An additional factor may be the plastic–concrete interface which may cause spurious effects
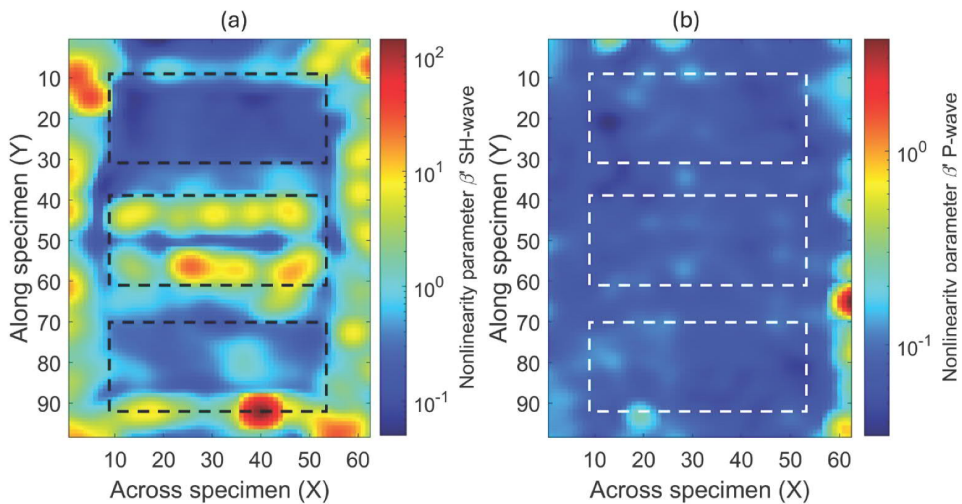

Figure 16. Maps showing the nonlinearity parameter related to second harmonic generation (β') for (a) SH-wave measurements and (b) for P-wave measurements. Dashed rectangles illustrate the approximate locations of the embedded steel plates. Top: uniformly corroded plate; middle: shell-corroded plate; bottom: ground plate.
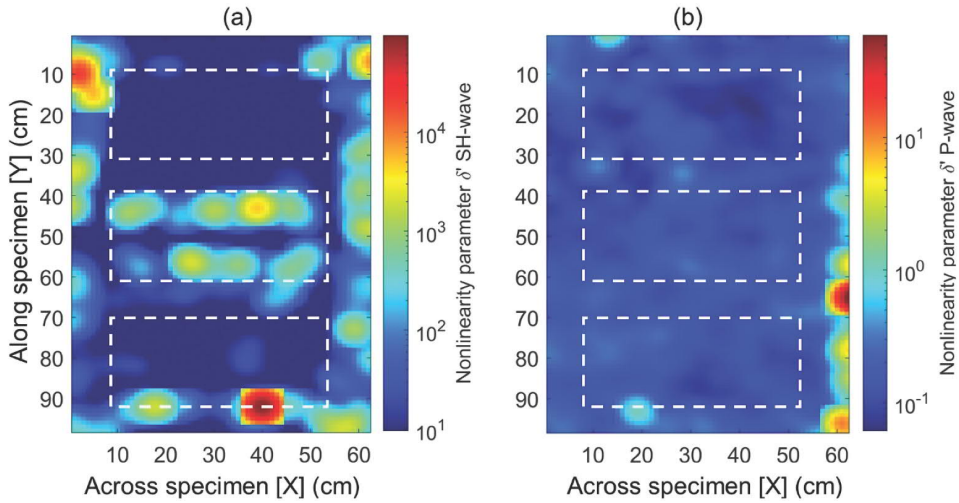
Figure 17. Maps showing the nonlinearity parameter related to third harmonic generation (δ') for (a) SH-wave measurements and (b) for P-wave measurements. Dashed rectangles illustrate the approximate locations of the embedded steel plates. Top: uniformly corroded plate; middle: shell-corroded plate; bottom: ground plate.

which contaminate the measurements. The effects near the boundary appear for the P-wave results as well; however, they are not as distinct as for the SH-wave counterpart due to the seemingly random distribution of parameter peaks within the scanned region.

By studying the parameter values in the expected plate regions in Figure 16(a), which are marked by dashed rectangles, it is observed that only the middle region, i.e. the shell-corroded plate, that exhibits clearly elevated β' in its region. The maximum value of β' within the region of the shell-corroded plate is 24. It is also observed that at X = 20, Y = 50 (corresponding to Figure 14(b)) we can see that the β' value is low compared to some areas within the region corresponding to the shell-corroded plate location. Moreover, the elevated levels of β' follow the boundaries of the shell-corroded plate and therefore allow its localisation. Interestingly, a giant increase in β' is observed in the ground plate area, around X = 40, Y = 92 with a maximum of 138. We cannot ascertain the cause of this immense increase in β', but it is highly unlikely that the structure of the embedded steel plate is the culprit because of its uniform structure. Another strong β' response is seen at X = 4, Y = 11 where the maximum value is 35. This region is very close to the boundary of the scanned area, so the distortion may be caused by geometrical effects. This strong increase of β' near the boundary is also observed at X = 56, Y = 96, which is also quite likely caused by spurious boundary reflections and interference.

Recalling the SH C-scan in Figure 9(a) it is observed that Figure 16(a) is essentially the inverse of Figure 9(a). This is because the β' is evaluated with the squared magnitude of the fundamental harmonic (A_1) in the denominator (see Eq. (5)). Small changes to A_1 will therefore impact β' more than the second harmonic will. Furthermore, it is suspected that the higher harmonics are attenuated more effectively than the fundamental, which further emphasises the effect that the fundamental amplitude has on the parameter estimation. This effect is expected to be even more pronounced for strongly attenuated

materials such as concrete and corrosion. Attenuation correction factors can be used to correct for certain effects [52]; however, this requires a reliable extraction of the second echo and its corresponding harmonic magnitudes. Such reliable extractions are not possible for all measurement points in the present work. This is indicated by the B-scan in Figure 10 from which it can be seen that only second reflections that are possible to discern from noise are located near two of the three plates. Erroneous extraction of the second echo can cause overestimations of the parameter values, hence the omitted attenuation correction. Additionally, the previously observed sidelobe contamination may affect the absolute value of the parameter(s).

If the focus is momentarily shifted towards the comparative P-wave measurements, it is observed that no clear plate localisation can be distinguished from the distribution in Figure 16(b). The region with the distribution of the highest parameter value is the ground plate (bottom rectangle), specifically the upper left corner of the plate. However, the centre region appears to have the most uniform distribution of β'. It is very difficult to distinguish any clear pattern that may be connected to the status of the embedded plates. Compared to the SH results, the P-wave is considerably less informative.

To compare the SHG with a different index that is based on waveform distortion, the relative parameter of cubic nonlinearity (δ') was extracted. This parameter uses the third harmonic and the fundamental cubed, see Eq. (6). The parameter is interesting for SH-waves as the third harmonic is expected to be generated by both classical and nonclassical nonlinear interactions and is therefore expected to be generated in part by the heterogeneous nature of concrete, whereas this is not expected for the SHG. The distribution of δ' for the SH-wave scan is presented in Figure 17(a,b) for the P-wave scan. It is immediately observed that the boundary effects appear to have been reduced in (a), which may be because of the major increase in the order of magnitude of the maximum values in (a). Here, δ' assumes values greater than 1500, with a giant maximum of 91,000 at X = 40, Y = 92, which also exhibited the maximum for β'. Compared to β', the cubic parameter is more than 2 orders of magnitude greater (nearly 3 for the maximum value). The maximum value of δ' in the shell-corroded region reaches as high as 4700. However, the distribution of δ' in this middle region is not as smooth as β', once again possibly due to the enormous range of parameter magnitudes.

For the P-wave results in Figure 17(b), the magnitude is of the same order as for the corresponding P-wave β' values. It is also not possible to discern the plate locations or to evaluate the status of the embedded steel plates from the P-wave map. Conversely, the SH results appear similar to the β' map in Figure 16(a) and therefore successfully detect the shell-corroded plate. The uniformly corroded plate does not appear to cause considerable waveform distortion. It should be noted that the maps do not show isolated elastic nonlinearity, but rather bulk waveform distortion that may be caused by many different effects. The contact between the concrete and steel plates varies in smoothness depending on the roughness of the embedded plate surface. The roughness is expected to increase with corrosion severity. A rough surface is known to cause an increased waveform distortion [53]. Very rough surfaces also cause local oblique incidence, which further affects attenuation by increased absorption and indeed mode conversion itself [54], which could explain some of the observed increase in attenuation at the severely corroded region. Furthermore, the rough asperities that are created by severe voluminous corrosion affect the nonlinearity in the contact interface even further by CAN [21]. This

agrees with the observations made in the present work as the shell corrosion is much more voluminous than the uniform corrosion, thus also inducing stronger waveform distortion. Similar observations were made in a previous work by the authors [10]. However, the bulk properties of the shell corrosion should not be neglected. The gross damage in the shell corrosion can indeed cause elevated nonlinear response due to the vast amount of cracks and delaminations that are present. Notably, it has been observed that the damage-related nonlinearity typically decreases at gross levels of damage [55], which may reduce the impact of the damage level of the shell corrosion itself. There is, however, another characteristic of the shell corroded plate that may explain certain effects, namely the delamination of the shell corrosion from its host plate. If it is completely delaminated, the air gap would cause a strong reflection that would interfere with the incident wave, causing it to distort. This would also explain the ridge-like response for the shell corroded plate because if the middle of the plate is not completely delaminated, this effect would be greatly reduced. Additionally, this effect cannot be present for the other plates as they are not expected to have any delaminated surfaces. It is therefore suspected that the main contributors to waveform distortion in the present work are the contact interface between the embedded plates and the concrete cover, and the delamination between the steel plate and the shell corrosion. Together they form very strong indicators of severe corrosion.

The results herein indicate that anomalies in the contact interface between steel plate and concrete due to corrosion could possibly be detected using parameters based on waveform distortion, given that the corrosion is sufficiently severe. This agrees with previous work that has investigated the harmonic generation due to rough interfaces between two solids [56]. Interestingly, the experiments conducted indicate that nonclassical SHGs for contact-type anomalies that are typically not expected to be generated for SH-waves might occur. This effect is enhanced by the strong third harmonics which produces large δ' values. It is suspected that the effects of nonlinear waveform distortion would increase if corrosion had occurred post-embedment in prestressed structures, as the interface is more likely to be affected under such circumstances and it is possible that oblique cracking may occur along with other effects. Due to the uncertainty of the interface characteristics in the present case it is not possible to ascertain the exact mechanics of the observed phenomena. The results obtained from the present study along with its uncertainties encourage further investigation of the use of the nonlinear distortion of ultrasonic SH-waves for the detection of contact interface anomalies.

5. Conclusions

This work has demonstrated the advantages of using horizontally polarised shear (SH) waves for ultrasonic inspection of the status of concrete-embedded steel liner plates, with an emphasis on corrosion detection. It is observed that SH-waves can effectively locate and possibly dimension embedded plate-like structures in traditional envelope C-scans, which does not seem to be particularly effective when using comparative compressional (P) waves. Furthermore, it is possible to observe anomalies in the SH C-scan, which corresponds to the location of the most severely corroded steel plate included in the specimen. Our work highlights that while performing ultrasonic measurements there is

good reason to perform both conventional processing and nonlinear evaluation of the signals to get more information from a single measurement.

The reported work is among the first to experimentally study second harmonic generation (SHG) for SH-waves, a phenomenon traditionally not expected to occur. However, recent theoretical advances have indicated that contact-type defects and anomalies can facilitate their generation. The observations in the present work do not conclusively confirm SHG due to steel plate corrosion, and there is evidence indicating FFT sidelobe contamination in the results. Nevertheless, the parameter map of nonlinearity corresponding to SHG accurately indicates the location of the most severely corroded plate embedded in the specimen, as does the parameter based on the third harmonic. The comparable P-wave results do not facilitate any evaluation of the status of the embedded steel liner plates, thus highlighting the use of SH-waves for concrete inspection. This further suggests promising applications of nonlinear waveform distortion of SH-waves for the detection and localisation of concrete-embedded steel liner corrosion. The experiments were performed on a specimen containing pre-corroded steel plates, and the nonlinear effects are therefore suspected to be even greater when corrosion occurs post-embedment since the swelling of corrosion products may cause cracking. Certain structures that contain concrete-embedded steel liners, such as containment buildings in nuclear power plants, may also be prestressed, an additional factor that may contribute to elevated levels of nonclassical nonlinearities for SH-wave interaction with frictional interfaces. The remaining uncertainties in the present work encourage further investigation of the use of SH-waves for nonlinear ultrasonic evaluation and the development of suitable instrumentation for such methods.

Acknowledgments

Disclosure statement

No potential conflict of interest was reported by the author(s).

Funding

Data availability statement

Data will be made available upon reasonable request.

Author contributions

Markus Nilsson: Conceptualisation, methodology, software, investigation, formal analysis, visualisation, writing – original draft, writing – review & editing.
Peter Ulriksen: Conceptualisation, supervision, funding acquisition, resources, test specimen, writing – review & editing.
Nils Rydén: Conceptualisation, supervision, writing – review & editing.

References

[1] Sajedi S, Huang Q. Probabilistic prediction model for average bond strength at steel–concrete interface considering corrosion effect. Eng Struct. 2015;99:120–131. doi: 10.1016/j.engstruct.2015.04.036

[2] Li X, Gong J. Effects of steel liner corrosion on the leak-tightness of prestressed concrete containment structure under severe accident loads. Ann Nucl Energy. 2023;180:109487. doi: 10.1016/j.anucene.2022.109487

[3] Broomfield JP. Corrosion of steel in concrete, 3rd ed. London: CRC Press; 2022.

[4] Zatar WA, Nguyen HD, Nghiem HM. Ultrasonic pitch and catch technique for non-destructive testing of reinforced concrete slabs. J Infrastruct Preserv Resil. 2020;1 (1):12. doi: 10.1186/s43065-020-00012-z

[5] Chen Q, Zhang C, Zhao J, et al. Recent advances in emerging imaging techniques for non-destructive detection of food quality and safety. TrAC Trends Anal Chem. 2013;52:261–274. doi: 10.1016/j.trac.2013.09.007

[6] Waag RC, Gramiak R. Methods for ultrasonic imaging of the heart. Ultrasound Med Biol. 1976;2(3):163–170. doi: 10.1016/0301-5629(76)90033-8

[7] Yu Y, Feng T, Qiu H, et al. Simultaneous photoacoustic and ultrasound imaging: a review. Ultrasonics. 2024;139:107277. doi: 10.1016/j.ultras.2024.107277

[8] Xu X, Ran B, Jiang N, et al. A systematic review of ultrasonic techniques for defects detection in construction and building materials. Measurement. 2024;226:114181. doi: 10.1016/j.measurement.2024.114181

[9] Yun H, Rayhana R, Pant S, et al. Nonlinear ultrasonic testing and data analytics for damage characterization: a review. Measurement. 2021;186:110155. doi: 10.1016/j.measurement.2021.110155

[10] Nilsson M, Ulriksen P, Rydén N. Nonlinear ultrasonic characteristics of a corroded steel plate. Nondestruct Test Eval. 2023;38(3):456–479. doi: 10.1080/10589759.2022.2123481

[11] Rudenko OV, Korobov AI, Izosimova MY. Nonlinearity of solids with micro- and nano-defects and characteristic features of its macroscopic manifestations. Acoust Phys. 2010;56 (2):151–157. doi: 10.1134/S1063771010020053

[12] Kyung-Young J, Lissenden CJ, Solodov I, et al. Measurement of nonlinear ultrasonic characteristics. Singapore: Springer Singapore; 2020.

[13] Zhang M, Chen R, Zheng L, et al. Electromagnetic ultrasonic signal processing and imaging for debonding detection of bonded structures. Measurement. 2022;205:112106. doi: 10.1016/j.measurement.2022.112106

[14] Sun M, Zhang S, Zhang G, et al. Detection and evaluation of fatigue cracks using a nonlinear ultrasonic sideband peak count technique with a pulse-echo experimental method. J Sound Vib. 2024;583:118429. doi: 10.1016/j.jsv.2024.118429

[15] Zhang C, Pan Q, Liu T, et al. Nonlinear ultrasonic C-Scan imaging for contact-type defects in diffusion-bonded joints—A case study. Materials (Basel). 2024;17(6):1288. doi: 10.3390/ma17061288

[16] Matlack KH, Kim JY, Jacobs LJ, et al. Review of second harmonic generation measurement techniques for material state determination in metals. J Nondestruct Eval. 2015;34(1). doi: 10.1007/s10921-014-0273-5

[17] Cantrell JH. Crystalline structure and symmetry dependence of acoustic nonlinearity parameters. J Appl Phys. 1994;76(6):3372–3380. doi: 10.1063/1.357463

[18] Zaitsev VY, Nazarov VE, Talanov VI. "Nonclassical" manifestations of microstructure'induced nonlinearities: new prospects for acoustic diagnostics. Usp Fiz Nauk. 2006;176(1):97. doi: 10.3367/ufnr.0176.200601g.0097

[19] Williams CL, Lear MH, Shokouhi P. A review of the microstructural contributions to the acoustic nonlinearity parameter measured with longitudinal and Rayleigh wave second harmonic generation in metals. NDT E Int. 2024;142:103027. doi: 10.1016/j.ndteint.2023.103027

[20] Korshak BA, Solodov IY, Ballad EM. DC effects, sub-harmonics, stochasticity and "memory" for contact acoustic non-linearity. Ultrasonics. 2002;40(1–8):707–713. doi: 10.1016/S0041-624X(02)00241-X

[21] Solodov IY, Krohn N, Busse G. CAN: an example of nonclassical acoustic nonlinearity in solids. Ultrasonics. 2002;40(1–8):621–625. doi: 10.1016/S0041-624X(02)00186-5

[22] Zarembo LK, Krasilnikov VA. Nonlinear phenomena in the propagation of elastic waves in solids. Sov Phys Usp. 1971;13(6):778–797. doi: 10.1070/PU1971v013n06ABEH004281

[23] Rudenko OV. Giant nonlinearities in structurally inhomogeneous media and the fundamentals of nonlinear acoustic diagnostic techniques. Physics-Uspekhi. 2006;49(1):69–87. doi: 10.1070/PU2006v049n01ABEH005876

[24] Jiang W, Cao W. Second harmonic generation of shear waves in crystals. IEEE Trans Ultrason Ferroelectr Freq Control. 2004;51(2):153–162. doi: 10.1109/TUFFC.2004.1320763

[25] Dinh K, Tran K, Gucunski N, et al. Imaging concrete structures with ultrasonic shear waves —technology development and demonstration of capabilities. Infrastructures. 2023;8(3):53. doi: 10.3390/infrastructures8030053

[26] O'Neill B, Maev RG, Severin F. Distortion of shear waves passing through a friction coupled interface. In: 2000 IEEE Ultrasonics Symposium. Proceedings. An International Symposium (Cat. No.00CH37121), Ames, Iowa. IEEE; 2000. p. 819–822.

[27] Liu Y, Chillara VK, Lissenden CJ, et al. Third harmonic shear horizontal and Rayleigh lamb waves in weakly nonlinear plates. J Appl Phys. 2013;114(11):114908. doi: 10.1063/1.4821252

[28] Chen H, Feng Z, Tao L, et al. On the emergence of the second harmonic shear horizontal wave in presence of tangential prestress. J Sound Vib. 2023;557:117732. doi: 10.1016/j.jsv.2023.117732

[29] Shevaldykin VG, Samokrutov AA, Kozlov VN. Ultrasonic low-frequency transducers with dry dot contact and their applications for evaluation of concrete structures. In: 2002 IEEE Ultrasonics Symposium, 2002. Proceedings, Munich, Germany. IEEE; 2002. p. 793–798.

[30] De La Haza AO, Samokrutov AA, Samokrutov PA. Assessment of concrete structures using the Mira and Eyecon ultrasonic shear wave devices and the SAFT-C image reconstruction technique. Constr Build Mater. 2013;38:1276–1291. doi: 10.1016/j.conbuildmat.2011.06.002

[31] Osika M, Ziaja-Sujdak A, Radecki R, et al. Nonlinear modes in shear horizontal wave propagation–analytical and numerical analysis. J Sound Vib. 2022;540:117247. doi: 10.1016/j.jsv.2022.117247

[32] Wen F, Shan S, Cheng L. Immunity of the second harmonic shear horizontal waves to adhesive nonlinearity for breathing crack detection. Struct Heal Monit. 2022;21(5):2340–2353. doi: 10.1177/14759217211057138

[33] Climent M-Á, Miró M, Eiras J-N, et al. Early detection of corrosion-induced concrete micro-cracking by using nonlinear ultrasonic techniques: possible influence of Mass transport processes. Corros Mater Degrad. 2022;3(2):235–257. doi: 10.3390/cmd3020014

[34] Arumaikani T, Sasmal S, Kundu T. Detection of initiation of corrosion induced damage in concrete structures using nonlinear ultrasonic techniques. J Acoust Soc Am. 2022;151(2):1341–1352. doi: 10.1121/10.0009621

[35] Nilsson M, Huttunen-Saarivirta E, Bohner E, et al. Non-destructive evaluation of corrosion in steel liner plates embedded in concrete using nonlinear ultrasonics. Constr Build Mater. 2023;408:133691. doi: 10.1016/j.conbuildmat.2023.133691

[36] Wen F, Shan S, Cheng L. Third harmonic shear horizontal waves for material degradation monitoring. Struct Heal Monit. 2021;20(2):475–483. doi: 10.1177/1475921720936983

[37] Kurz JH, Grosse CU, Reinhardt H-W. Strategies for reliable automatic onset time picking of acoustic emissions and of ultrasound signals in concrete. Ultrasonics. 2005;43(7):538–546. doi: 10.1016/j.ultras.2004.12.005

[38] Li C, Huang L, Duric N, et al. An improved automatic time-of-flight picker for medical ultrasound tomography. Ultrasonics. 2009;49(1):61–72. doi: 10.1016/j.ultras.2008.05.005

[39] Khyam MO, Ge SS, Li X, et al. Highly accurate time-of-flight measurement technique based on phase-correlation for ultrasonic ranging. IEEE Sens J. 2017;17(2):434–443. doi: 10.1109/JSEN.2016.2631244

[40] Sunol F, Ochoa DA, Garcia JE. High-precision time-of-flight determination algorithm for ultrasonic flow measurement. IEEE Trans Instrum Meas. 2019;68(8):2724–2732. doi: 10.1109/TIM.2018.2869263

[41] Bao Y, Jia J. Improved time-of-flight estimation method for acoustic tomography system. IEEE Trans Instrum Meas. 2020;69(4):974–984. doi: 10.1109/TIM.2019.2908704

[42] Long Y, Lin J, Li B, et al. Fast-aic method for automatic first arrivals picking of microseismic event with multitrace energy stacking envelope summation. IEEE Geosci Remote Sens Lett. 2020;17(10):1832–1836. doi: 10.1109/LGRS.2019.2952571

[43] Herter S, Youssef S, Becker MM, et al. Machine learning based preprocessing to ensure validity of cross-correlated ultrasound signals for time-of-flight measurements. J Nondestruct Eval. 2021;40(1):1–9. doi: 10.1007/s10921-020-00745-7

[44] Angrisani L, Lo Moriello R S. Estimating ultrasonic time-of-flight through quadrature demodulation. IEEE Trans Instrum Meas. 2006;55(1):54–62. doi: 10.1109/TIM.2005.861251

[45] Richardson JM. Harmonic generation at an unbonded interface—I. Planar interface between semi-infinite elastic media. Int J Eng Sci. 1979;17(1):73–85. doi: 10.1016/0020-7225(79)90008-9

[46] Zaitsev VY, Matveev LA, Matveyev AL. Elastic-wave modulation approach to crack detection: comparison of conventional modulation and higher-order interactions. NDT E Int. 2011;44(1):21–31. doi: 10.1016/j.ndteint.2010.09.002

[47] Norris WE, Naus DJ, Graves HL. Inspection of nuclear power plant containment structures. Nucl Eng Des. 1999;192(2–3):303–329. doi: 10.1016/S0029-5493(99)00125-9

[48] Nilsson M, Ulriksen P, Rydén N. Studies into the Use of non-linear ultrasound to detect corroded steel plates embedded in concrete. In: Al-Neshawy F, Ferreira M, and Bohner E, et al. editors. Proceedings of the International Conference on Non-destructive Evaluation of Concrete in Nuclear Applications, Espoo, Finland. Aalto University; 2023. p. 259–267.

[49] Xu Y, Song Y. Chemical-mechanical transformation of the expansion effect for nonuniform steel corrosion and its application in predicting the concrete cover cracking time. Cem Concr Compos. 2022;127:104376. doi: 10.1016/j.cemconcomp.2021.104376

[50] Miró M, Eiras JN, Poveda P, et al. Detecting cracks due to steel corrosion in reinforced cement mortar using intermodulation generation of ultrasonic waves. Constr Build Mater. 2021;286:122915. doi: 10.1016/j.conbuildmat.2021.122915

[51] Maack S, Küttenbaum S, Bühling B, et al. Low frequency ultrasonic dataset for pulse echo object detection in an isotropic homogeneous medium as reference for heterogeneous materials in civil engineering. Data Br. 2022;42:108235. doi: 10.1016/j.dib.2022.108235

[52] Jeong H, Barnard D, Cho S, et al. Receiver calibration and the nonlinearity parameter measurement of thick solid samples with diffraction and attenuation corrections. Ultrasonics. 2017;81:147–157. doi: 10.1016/j.ultras.2017.06.020

[53] Chakrapani SK, Howard A, Barnard D. Influence of surface roughness on the measurement of acoustic nonlinearity parameter of solids using contact piezoelectric transducers. Ultrasonics. 2018;84:112–118. doi: 10.1016/j.ultras.2017.10.022

[54] Yuan M, Dai A, Liao L, et al. Numerical study on surface roughness measurement based on nonlinear ultrasonics in through-transmission and pulse-echo modes. Materials (Basel). 2021;14(17):4855. doi: 10.3390/ma14174855

[55] Climent MÁ, Miró M, Carbajo J, et al. Use of non-linear ultrasonic techniques to detect cracks due to steel corrosion in reinforced concrete structures. In: Materials (Basel). Vol. 12. 2019. doi: 10.3390/MA12050813

[56] Korobov AI, Kokshaiskii AI, Shirgina NV, et al. Generation of higher acoustic harmonics at a flat rough interface between two solids. Acoust Phys. 2017;63(5):524–530. doi: 10.1134/S1063771017040066

NONLINEAR ULTRASONIC EVALUATION FOR CORROSION ASSESSMENT OF STEEL PLATES EMBEDDED IN CONCRETE

This thesis evaluates nonlinear ultrasonic methods for detecting and assessing corrosion in embedded containment liners. Ultrasonic testing uses sound waves above the human audible range to image internal structures. However, in concrete, high-frequency sound waves are quickly absorbed, necessitating the use of low-frequency waves, which reduces the ability to resolve small defects. Nonlinear ultrasonic evaluation offers a solution. Defects like cracks cause elastic nonlinearity, leading to waveform distortion. This distortion creates new frequency components in the sound wave, allowing for the detection of defects regardless of the wave's frequency. The strength of these new components relative to the original frequency provides a measure of damage in the material.

The research, conducted on small-scale laboratory specimens, primarily focused on pre-corroded steel plates. The results demonstrate that nonlinear evaluation can locate and assess corrosion in embedded plates, with more severe corrosion yielding stronger nonlinear indications. Additionally, the method shows potential for detecting embedded foreign objects, such as wood, and separations between the plate and concrete. The findings suggest that combining conventional and nonlinear ultrasonic imaging techniques can provide a better understanding of a structure's damage state. However, further experiments on more realistic specimens are necessary to fully evaluate the methods' detection capabilities. These experiments should consider the challenges posed by intrinsic concrete micro-cracking, coarse aggregates, reinforcement, and large dimensions typical in nuclear power plants.

Energiforsk